UNIVERSIDAD AUTÓNOMA DE MADRID
Facultad de Ciencias
Departamento de Física Teórica

Measurements of the internal structure of jets using subjets in NC DIS at HERA

Submitted in partial fullfilment of the requirements
for the degree 'Doctor en Ciencias Físicas' by

Elías Ron
Supervisors : Claudia Glasman and Juan Terrón

9/3/2010

UNIVERSIDAD AUTÓNOMA DE MADRID
Facultad de Ciencias
Departamento de Física Teórica

Medidas de la estructura interna de jets mediante subjets en NC DIS en HERA

Entregado como requisito parcial de el título
de 'Doctor en Ciencias Físicas' por

Elías Ron
Directores de tesis : Claudia Glasman and Juan Terrón

9/03/2010

Dedicado a mi familia y, en especial, a mis padres.

Que el cielo exista, aunque nuestro lugar sea el infierno.

J.L. Borges (Deutsches Requiem).

Introduction

Jet production in the deep inelastic scattering (DIS) of a electron (or a positron) and a proton provides an excellent testing ground for the properties of the nuclear-strong interactions. Quantum chromodynamics (QCD), the quantum field theory that describes the dynamics of the strong interactions in terms of quarks and gluons, has proved in the last 36 years to be a very succesful theoretical framework capable of describing adequately the data obtained in a large variety of experiments in many different physical contexts. In this sense, HERA has set a milestone. Its characteristics have allowed physicists to closely examine QCD and its properties. A large quantity of very stringent tests of the validity of QCD as the theory of the strong interactions have been performed at HERA and QCD has so far resisted.

This document presents two recent analyses of jet production in neutral current (NC) DIS carried out in the context of the ZEUS Collaboration, both of which examine the extent up to which QCD correctly describes the internal strucure of jets that have a large transverse energy. The fundamental assumption contained in both analyses is that the energy flow that ultimately constitutes the internal structure of the jets mimics the underlying dynamics of parton radiation, which is expected to be described by QCD in its perturbative regime, pQCD. The analyses presented here study the substructure of jets by means of subjets, which are jet-like structures reconstructed within jets at a given resolution scale. The first analysis focuses on those jets in which two subjets are reconstructed. Measurements of normalised differential cross sections with respect to subjet variables sensitive to the pattern of parton radiation are presented. As well, the evolution of these cross sections with the energy scale is studied. The measurements are compared with the predictions of pQCD and it is examined whether an adequate description of the main features of parton radiation is achieved. In the second analysis, those jets with three subjets at a given resolution scale are examined also by measuring normalised differential cross sections with respect to subjet variables. The production of jets with three subjets provides a testing ground for the underlying color dynamics of QCD since the cross sections as functions of the subjet variables are sensitive to the color factors of the gauge group. This is studied by comparing the measured cross sections to theoretical predictions based on different gauge symmetry groups.

In chapter 1 the main aspects of the theoretical framework underlying the work presented are introduced, with some supporting experimental verification. A description of the DIS regime as well as its role as the motivating physical context that gave rise to QCD is given. A brief description of quantum field theory, quantum chromodynamics and some of its features, such as assymptotic freedom, the phenomenon of confinement and the dynamics of partons in ep scattering is also

presented.

In chapter 2 jets are introduced and the related physics is covered. The definition of a jet in terms of reconstruction algorithms is first presented. The physics of jets as described by pQCD follows and in the last part of the chapter subjets are defined; several theoretical notions of subjet physics, such as subjet multiplicity, and previous subjet studies by the ZEUS collaboration are presented.

In chapter 3 a description of the analyses and the motivation behind them is given. The subjet variables are defined and the proposed measurements are presented. The kinematic ranges in which jets are reconstructed and the resolution scales at which subjets are investigated are also introduced. In the last section of the chapter, the studies of the underlying gauge symmetry of the strong interactions performed at LEP as well as those at HERA are mentioned, which sets the motivation for the related study presented in this work.

Chapter 4 covers the description of HERA and of the ZEUS detector. HERA is an electron proton synchrotron collider with a center-of-mass energy of $\sqrt{s} = 320$ GeV, giving way to momentum transfers bewteen the electron and the constituents of the proton well within the predictive capabilities of pQCD. ZEUS is a multipurpose detector at one of the interaction points at HERA. It consists of a number of different detectors layered around the collision vertex, whose aim is to record as much information as possible about the collisions. Thus, ZEUS is a powerful tool for the study of QCD.

In chapter 5, the fixed-order pQCD calculations performed in order to compare data and theory are presented. It is explained how these calculations are done and which programs are used to perform them. The predictions of pQCD of the normalised differential cross sections as functions of the subjet variables are presented for both analyses. In the last part of the chapter the different sources that contribute to the theoretical uncertainties are discussed.

Monte Carlo (MC) event generators are introduced in chapter 6. The MC simulations are used to understand and correct jet and subjet measurements for detector effects. They also contain a phemenological model to describe the process of hadronization, which permits the correction of the pQCD calculations for parton-to-hadron effects and enables the comparison of the data and theoretical expectations at the same level.

In chapter 7 a detailed description of how the data samples were selected is given. A comparison of several distributions of interest between the MC simulations and data is presented as well. The comparisons legitimize the use of the MC simulations for estimating the systematic uncertainties in the measurements and obtaining the necessary corrections to the subjet cross sections. All these correction factors as well

the sources of systematic uncertainty in the measurements are shown in chapter 8. Due to the large amount of plots that correspond to this chapter, some of them have been moved to the Appendix to avoid a cumbersome reading.

In chapter 9 the results are presented. The normalised differential cross sections with respect to the subjet variables are shown for both analyses together with the theoretical expectations as dictated by pQCD. For the two-subjet analysis, the evolution of the subjet cross sections with the energy scale is also presented. For the three-subjet analsysis, special attention is given to the sensitivity of the subjet cross sections to the underlying symmetry structure.

Finally, a brief summary of the most relevant aspects and most important conclusions of the presented work is given.

The work presented in this thesis has led to the following publications:

- ZEUS Collaboration, S. Chekanov et al., *Subjet distributions in deep inelastic scattering at HERA*, *The European Physical Journal* **C63** (2009), 527.
- ZEUS Collaboration, S. Chekanov et al., *Three-subjet distributions in neutral current deep inelastic scattering*, ZEUS-prel-09-007, contributed paper to the International Europhysics Conference on High Energy Physics, Krakow, Poland, 2009.

The author has also contributed to the following publications:

- ZEUS Collaboration, S. Chekanov et al., *Multi-jet cross sections in charged current $e^{\pm}p$ scattering at HERA*, *Physical Review* **D78** (2008), 032004.
- ZEUS Collaboration, S. Chekanov et al., *Jet substructure in neutral-current deep inelastic ep scattering at high Q^2 with HERA II*, contributed paper to the International Conference on High Energy Physics, Philadelphia, USA, 2008.

This work has been carried out in the frame of the ZEUS Collaboration through the High Energy Physics Group of the Universidad Autónoma de Madrid. The author was financially supported by the Spanish Ministry of Education and Science.

Introducción

La producción de chorros de hadrones (jets) en el régimen de dispersión profundamente inelástica (DIS) de electrones (o positrones) y protones constituye un excelente campo de pruebas para testar las propiedades de la interacción nuclear fuerte. La cromodinámica cuántica, la teoría cuántica de campos que describe la dinámica de la interacción fuerte en términos de quarks y gluones, ha demostrado ser durante los últimos 36 años un marco teórico capaz de describir los datos obtenidos en una gran variedad de experimentos en diferentes contextos físicos. En este sentido, HERA marca un antes y un después. Dadas sus características, ha permitido comprobar la validez de QCD en situaciones muy exigentes y hasta la fecha QCD ha resistido el embite.

Este documento presenta dos análisis recientes acerca de producción de jets en corrientes neutras (NC) DIS en el contexto de la colaboración ZEUS. Ambos análisis examinan en qué medida QCD es capaz de describir la estructura interna de jets con un valor alto de energía transversa. La hipótesis fundamental sobre la que descansa este trabajo es que el flujo de energía que en última instancia constituye los jets está determinado por la dinámica de radiación partónica subyacente, la cual se espera que sea describible por QCD en su régimen perturbativo (pQCD). Los análisis aquí presentados estudian la estructura interna de los jets en términos de subjets, que son estructuras análogas a los jets reconstruidas dentro de los mismos. El primer análisis presentado examina la estructura interna de aquellos jets en los cuales exactamente dos subjets son reconstruidos a un determinado valor de la escala de resolución y_{cut}. Se obtienen medidas de la sección eficaz diferencial normalizada como función de variables de subjet, las cuales son sensibles a los detalles de la radiacion partónica. Además, se estudia la evolución de estas secciones eficaces con la escala de energía. Estas medidas son comparadas con las predicciones de pQCD y se examina en qué medida pQCD es capaz de proporcionar una descripción adecuada de los aspectos más importantes de la radiación partónica. En el segundo análisis se estudian aquellos jets en los cuales tres subjets son reconstruidos a un valor determinado de la escala de resolución. Se miden secciones eficaces diferenciales normalizadas como función de variables de los subjets. Estas secciones eficaces son sensibles a los factores de color del grupo de simetría gauge subyacente, por lo que este análisis permite estudiar la estructura gauge de las interacciones fuertes.

En el capítulo 1 se presentan los aspectos fundamentales del andamiaje teórico que subyace a los estudios presentados en este trabajo. Se describe el régimen DIS así como su rol como el contexto físico que dio lugar a QCD. Se proporciona también una breve descripción de teoría cuántica de campos, QCD y alguno de sus aspectos más relevantes, como la libertad asintótica, el fenómeno de confinamiento

y la dinámica de los partones en procesos de dispersión *ep*.

En el segundo capítulo se introduce el concepto de jet. Se presenta su definición en términos de algoritmos de reconstrucción así como la física relacionada con la producción de jets en el contexto de QCD perturbativa. En la última parte de este capítulo se presenta el concepto de subjet y se muestran algunos aspectos teóricos relacionados como la multiplicidad de jets, así como estudios de física de subjets realizados previamente por la colaboración ZEUS.

En el capítulo 3 se da una descripción de los análisis presentados en este trabajo y de su motivación. Se presentan los rangos cinemáticos en los que los jets son reconstruidos así como la escala de resolución a la cual se reconstruyen los subjets. En la última parte del capítulo se mencionan estudios previos realizados por LEP y ZEUS acerca de la simetría gauge subyacente en la interacción fuerte.

En el cuarto capítulo se describe HERA y el detector ZEUS. HERA es un sincrotrón electrón-protón con una energía del centro de masas de $\sqrt{s} = 320$ GeV, lo cual permite transferencias de momento entre el electrón y los constituyentes del protón en un rango dentro del dominio descriptivo de pQCD. ZEUS es un detector multipropósito en uno de los puntos de interacción de HERA. Consiste de un número de detectores organizados alrededor del punto de colisión, y cuyo objetivo es obtener la mayor información posible acerca las colisiones. Por tanto, ZEUS es una herramienta extremadamente eficaz para el estudio de QCD.

En el capítulo 5 se presentan los cálculos de pQCD a orden fijo que permiten comparar las medidas con las predicciones teóricas de QCD. Se menciona cómo se llevan a cabo estos cálculos y también cuáles son los programas con los que se realizan. Se presentan las predicciones para las secciones eficaces diferenciales normalizadas como función de las variables de subjets para los dos análisis. En la última parte del capítulo se presentan las diferentes fuentes que contribuyen a la incertidumbre asociada a las predicciones teóricas.

En el sexto capítulo se presentan los generadores de eventos Monte Carlo (MC). Las simulaciones MC se usan para entender y corregir los efectos que introduce el detector en las medidas de producción de jets y subjets. Así mismo, estas simulaciones incluyen modelos fenomenológicos para describir el fenómeno de la hadronización, lo cual permite una comparación de los datos y las expectativas teóricas al mismo nivel.

El capítulo 7 cubre los criterios de selección de la muestra sobre la que se realizan los análisis, tanto los rangos cinemáticos como los cortes de limpieza y eliminación de background. Se muestran comparaciones entre las simulaciones Monte Carlo y datos, las cuales legitimizan el posterior uso de las simulaciones para corregir los datos por los efectos del detector y la obtención de incertidumbres sistemáticas. Todos los

correspondientes factores de corrección se muestran el el capítulo 8. Debido a que la cantidad de figuras de esta sección es grande, la mayoría de ellos se muestran en el apéndice con el objetivo de facilitar la lectura.

En el capítulo 9 se presentan los resultados. Se muestran las secciones eficaces diferenciales con respecto a las variables de subjet para los dos análisis junto con las predicciones teóricas de pQCD. Para el análisis de dos subjets, también se muestra la evolución de las secciones eficaces con la escala de energía. Para el análisis de tres subjets, se incluyen los estudios acerca de la sensibilidad de las secciones eficaces al grupo de simetría gauge subyacente.

Finalmente, se da un breve resumen de los aspectos más relevantes y las conclusiones más importantes del trabajo presentado.

El trabajo presentado en esta tesis ha dado lugar a las siguientes publicaciones:

- ZEUS Collaboration, S. Chekanov et al., *Subjet distributions in deep inelastic scattering at HERA*, *The European Physical Journal* **C63** (2009), 527.
- ZEUS Collaboration, S. Chekanov et al., *Three-subjet distributions in neutral current deep inelastic scattering*, ZEUS-prel-09-007, artículo de contribución a International Europhysics Conference on High Energy Physics, Cracovia, Polonia, 2009.

El autor también ha contribuido a las siguientes publicaciones:

- ZEUS Collaboration, S. Chekanov et al., *Multi-jet cross sections in charged current $e^{\pm}p$ scattering at HERA*, *Physical Review* **D78** (2008), 032004.
- ZEUS Collaboration, S. Chekanov et al., *Jet substructure in neutral-current deep inelastic ep scattering at high Q^2 with HERA II*, artículo de contribución a International Conference on High Energy Physics, Filadelfia, EEUU, 2008.

Este trabajo ha sido llevado a cabo en el contexto de la colaboración ZEUS dentro del grupo experimental de física de altas energías de la Universidad Autónoma de Madrid. El autor ha sido financiado por el Ministerio de Educación y Ciencia.

Contents

Chapter 1

Theoretical background

In this chapter, the most relevant aspects of the theoretical framework underlying the work presented here are reviewed. There are three main concepts which are especially relevant for these analyses. The first one is deep inelastic *ep* scattering (DIS), which is the regime in which the studies were performed. The second is Quantum Field Theory (QFT) and most specifically Quantum Chromodynamics (QCD), the theoretical framework that best describes the physics of the nuclear-strong interactions. QCD allows for a perturbative approach (pQCD) which adequately describes the behaviour of strong-interacting particles in a wide variety of situations. The last pillar of this work is the concept of a jet. In this work, the internal structure of jets of hadrons is studied, which provides an excellent testing ground for the validity of pQCD in a very demanding physical context.

1.1 Deep inelastic scattering and the parton model

In an interacting quantum field theory, the interactions take place through the exchange of particles. In *ep* collisions, where the initial lepton interacts with one of the constituents of the proton, the interaction can either be electromagnetic, when a photon is exchanged, or nuclear-weak, in which case a W boson or a Z boson is exchanged. The exchanging of an electrically neutral particle (either the photon or the Z) is commonly referred to as a neutral-current interaction (NC), while the exchange of a W would be a charged-current (CC) interaction. Both processes take place at HERA and have been extensively studied.

Deep inelastic scattering is the regime where the exchanged boson has a momentum q such that $Q^2 \equiv -q^2$ is large compared with the energy scale at which partons are bound into hadrons, Λ_{QCD}. If the exchanged boson is a photon, this regime is the one in which the photon has a large virtuality.

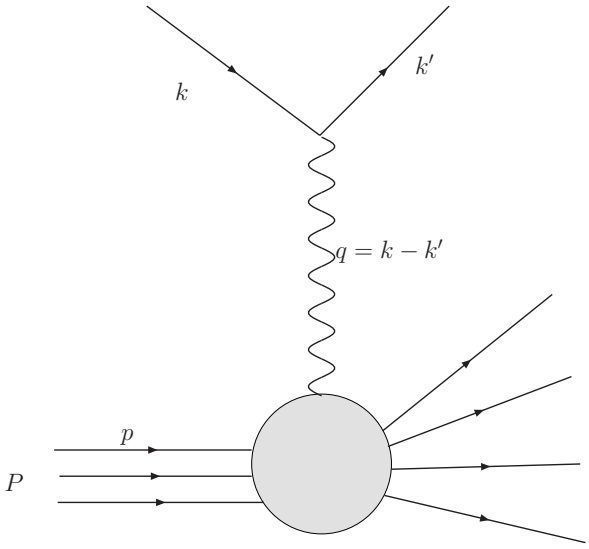

Figure 1.1: A Deep Inelastic *ep* Scattering process involving an electron with 4-momentum k and a proton with 4-momentum P.

The first experiments to test the nuclear-strong force turned out to be a box full of surprises. One should expect a strongly bounded state of whatever particles are inside of it. The first proton-proton collisions, at a energy of around 10 GeV produced a large number of pions. The measured spatial distribution of the produced pions was completely unexpected. A strongly-bounded state of pions should allow for internal particles to have large transverse momenta which would induce large transverse-momentum pions. However, the pions were produced almost entirely along the collision axis. It looked as if the particles inside the hadrons had momenta collinear with that of the hadrons. That is, as if they were esentially loose inside of them, a very contradicting assumption.

In the late 1960s the SLAC experiments began, and there it was seen that the total cross section of scattering of electrons from protons was comparable to what would have been if the proton was an elementary particle and the scattering proceeded according to the QED expectations, alhough very rarely did a whole proton emerge from the scattering process.

So in one hand, there was plenty of evidence of electromagnetic hard scattering but no evidence of strong-interaction hard scattering taking place. Bjorken and Feynman proposed then the parton model, where the proton is a loosely-bounded compound of a few constituents, which they called partons. It was postulated that partons do not exchange large momenta through interactions and that some of them have the electromagnetic interactions of elementary fermions.

This rather naive picture already imposes strong constraints on the cross section

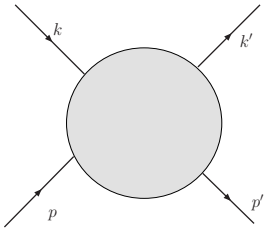

Figure 1.2: Mandelstam variables of the electron-parton interaction.

for deep inelastic scattering. To see this, let's imagine the hard scattering of an electron and one of the partons, as shown in Fig. 1.1 and recall that the square of the invariant matrix element in the massless limit is:

$$\frac{1}{4}\sum_{spins}|M^2| = \frac{8e^4Q_i^2}{\hat{t}^2}\left(\frac{\hat{s}^2+\hat{u}^2}{4}\right),$$

where $\hat{t}$, $\hat{s}$ and $\hat{u}$ are the Mandelstam variables:

$$\hat{s} = (p+k)^2 = (p'+k')^2,$$
$$\hat{t} = (k-k')^2 = (p-p')^2,$$
$$\hat{u} = (p'-k)^2 = (p-k')^2,$$

where the four momenta are depicted in Fig. 1.2.

Trying to relate the Mandelstam variables to measurable quantities one finds that $\hat{t}$ is equal to $-Q^2$, where Q^2 is defined as:

$$Q^2 \equiv -q^2.$$

It is also found that $\hat{s}$ is:

$$\hat{s} = (p+k)^2 = 2p\cdot k = 2\xi P\cdot k = \xi s, \tag{1.1}$$

where s is the square of the electron-proton center-of-mass energy. The quantity ξ can also be determined from measurements assuming that the electron-parton scattering is elastic. Then, neglecting the mass of the scattered parton and taking ξ to represent the fraction of the proton's momentum carried by the parton, one obtains:

$$m_{parton}^2 \approx 0 \approx (p+q)^2 = 2p\cdot q + q^2 = 2\xi P\cdot q - Q^2$$

and therefore,

$$\xi = x \tag{1.2}$$

where x is the Bjorken variable defined as:

$$x \equiv \frac{Q^2}{2P \cdot q}. \tag{1.3}$$

Both Q^2 and x are measurable quantities in each interaction, so the double-differential cross section with respect to these variables is a measurable quantity. The prediction of the parton model reads:

$$\frac{d^2\sigma}{dxdQ^2} = \sum_i f_i(x) Q_i^2 \cdot \frac{2\pi\alpha^2}{Q^4} \left[1 + \left(1 - \frac{Q^2}{xs}\right)^2\right], \tag{1.4}$$

where the functions $f_i(\xi)$ are the *parton distribution functions* in the proton and they express the probability of finding a parton within the proton with a fraction ξ of its momentum. These are not calculable functions from first principles in QCD, as we shall see they involve non-perturbative effects. Nonetheless they can be obtained from experimental fits and their evolution with Q^2 can be calculated.

The constraint induced by this model on the cross section is now manifest; by removing the kinematic factor

$$\frac{1}{Q^4}\left[1 + \left(1 - \frac{Q^2}{xs}\right)^2\right]$$

one obtains a quantity that depends only on x and is independent of Q^2, a behaviour known as Bjorken scaling. It means that the structure of the proton is the same regardless on how hard the electromagnetic interaction is. This was the behaviour exhibited by the data taken at SLAC.

Before hadrons were identified as bound states of fermions, an explanation of the hadron spectrum was searched for. Gell-Mann and Zweig had proposed in 1963 a model where three species of elementary particles existed, which they called quarks. The three kinds were the quarks *up*, *down* and *strange*. Mesons were thought to be bound states of quarks and antiquarks, while baryons were bound states of three quarks, such as the proton, which was thought to be a bound state of quarks *uud*. This model had a great success predicting the existence of hadrons that had not been discovered at that time, but it also presented some problems. In the first place, since the proton is a bound state of three quarks, they must have fractional charges, which imply that a combination like *uuu* would have a fractional charge too, but no particles with fractional charges were found. As well, the spectrum of baryons required that the wavefunction of the three quarks should be totally

symmetric under the interchange of the quark spin and flavor quantum numbers, which would imply a totally symmetric wave function for fermions.

An additional quantum number was then proposed, called color. It was postulated that the wavefunction of baryons and mesons should be antisymmetric under the interchange of the color quantum numbers. This was achieved with the combinations:

$$\bar{q}^i q_i, \tag{1.5}$$

$$\epsilon^{ijk} q_i q_j q_k \tag{1.6}$$

$$\epsilon^{ijk} \bar{q}_i \bar{q}_j \bar{q}_k \tag{1.7}$$

where the sum runs over 3 different colors, called *red*, *blue* and *green*, and ϵ^{ijk} is the antisymmetric matrix in 3 dimensions. Baryons and mesons are then invariant under a new internal $SU(3)$ global symmetry, of which color is the conserved charge. The previous combinations yield invariant quantities under $SU(3)$ transformations. This set of assumptions worked really well but it raised many questions, perhaps the most obvious of which is: by which mechanism is the color invariance realised? The key to these concerns came from DIS experiments and the subsequent development of Quantum Chromodynamics, a quantum field theory based on the gauge invariance under the action of the non-Abelian group $SU(3)$.

1.2 Quantum Field Theory

Local field theory is a useful idealization. The only known framework in which the quantum mechanical interactions of a finite number of types of particles in ordinary space-time are described is a local quantum field theory characterized by a local Lagrangian density, where the interactions are described by products of fields at the same space-time point.

Interactions amongst fields arise as a consequence of the so-called gauge invariace. The statement of gauge invariance simply asserts that any event, that is, the value of a given field at any space-time point, possesses a space of internal properties the value of which are independently chosen from its neighbours. This is more commonly rephrased as the freedom to change the phase of the fields by an arbitrary quantity that depends on the space-time point. Mathematically, this induces the existence of a field, the gauge field, which in turn possesses the right properties under phase transformations so that the dynamics is left unchanged. In a field such as the quark field, the continous set of values of its phase which are mathematically related by the action of the group $SU(3) \times SU(2) \times U(1)$ yield the same dynamics

and, therefore, this implies the interaction with three different gauge fields, gluons, W-Z bosons and photons, which means that quarks are sensitive to the strong, weak and electromagnetic interactions.

1.2.1 Renormalized perturbation theory

Quantum field theory does not account for the physics at arbitrarily small distances; it is commonly regarded as an effective low-energy approximation. This fact usually presents itself as infinities in the results of calculations, which brings up the necessity for the mathematical tools known as regularization and renormalization. When this is done, the physics at small distances is modified in some way to make the theory well-defined. The dependence on the short-distance physics which we do not know about is then incorporated into a set of parameters that can be related to physical quantities at measurable distances. Renormalizable theories are those in which a finite number of parameters are required to absorb all the dependence on short-distance physics. This usually means to re-express the parameters that appear in a Lagrangian, the so-called bare parameters, in terms of measurable quantities, the so-called physical parameters.

In renormalized perturbation theory, the goal is to absorb the divergences into the unobservable parameters of the theory, the bare parameters. To accomplish this, the perturbative expansion is conveniently modified so that these unobservable quantities do not appear explicitly in the Feynman rules. The absorption of the infinite shifts between bare and physical parameters are included in the so-called counterterms, extra terms in the Lagrangian giving rise to extra Feynman diagrams. There is no unique way of performing these operations and, therefore, theories are only well defined when it is manifestly stated the conditions by which they are renormalized. Generally, the set of conditions that are needed to properly define the theory are imposed at a certain energy scale M. One then speaks of M as the renormalization scale, which is regarded as the energy scale at which the theory is defined.

1.2.2 The Callan-Symanzik Equation

The relation between changes in the renormalization of the scale M and the corresponding shifts in the coupling constant and field strength are described in terms of the Callan-Symanzik equation.

Let $G^{(n)}$ be the connected $n-$point function computed in renormalized perturbation theory:

$$G^{(n)}(x_1, \cdots, x_n) = \langle \Omega \mid T\phi(x_1)\phi(x_2) \cdots \mid \Omega \rangle_{connected}$$

and now let's assume a shift in the renormalization scale M. There is a corresponding shift in the coupling constant α and the field strength such that the Green's functions remain fixed:

$$M \to M + \delta M,$$
$$\alpha \to \alpha + \delta\alpha$$
$$\phi \to (1 + \delta\eta)\phi$$

Defining the dimensionless parameters:

$$\beta \equiv \frac{M}{\delta M}\delta\alpha; \qquad \gamma \equiv -\frac{M}{\delta M}\delta\eta, \tag{1.8}$$

one obtains the Callan-Symanzik equation:

$$\left[M\frac{\partial}{\partial M} + \beta(\alpha)\frac{\partial}{\partial\alpha} + n\gamma(\alpha)\right] G^{(n)}(\{x_i\}; M, \alpha) = 0 \tag{1.9}$$

This equation shows that there are two universal functions $\beta(\alpha)$ (the so-called β function) and $\gamma(\alpha)$ (known as the anomalous dimension), related to the shifts in the coupling constant and field strength, that compensate for the shift in the renormalization scale M. The precise meanings of γ and β can be obtained by writing their definitions in a more suitable manner, by re-expressing them in terms of the bare parameters of the perturbation theory: the strength field rescaling factor Z, the bare coupling α_0 and the cut-off Λ. In doing so, one obtains:

$$\gamma(\alpha) = \frac{1}{2}\frac{M}{Z}\frac{\partial}{\partial M}Z. \tag{1.10}$$

So one sees that the dimensionless parameter $\gamma(\alpha)$ is related to the field strength rescaling. One also obtains:

$$\beta(\alpha) = M\frac{\partial}{\partial M}\alpha\mid_{\alpha_0,\Lambda}. \tag{1.11}$$

Thus the β function is the rate of change of the renormalized coupling at the scale M corresponding to a fixed bare coupling.

The easiest way to compute the β function from the Callan-Symanzik equation is to begin with explicit perturbative expressions for some conveniently chosen Green's functions and impose that the Callan-Symanzik equation is satisfied. The dependence on the scale M in the Green's functions comes from the counterterms that are needed to cancel the logarithmic divergences, and because of this the β function is related to these counterterms. To lowest order, the Callan-Symanzik equation can be written in terms of the counterterms needed to cancel the logarithmic divergences:

$$\beta(\alpha) = \alpha M \frac{\partial}{\partial M}(-\delta_1 + \delta_2 + \frac{1}{2}\delta_3). \tag{1.12}$$

This expression is useful to calculate the β function for a non-Abelian theory such as QCD, as we shall see in the next sections.

1.3 The renormalization group equation

Solving the Callan-Symanzik for the two-point Green's function at momentum p and coupling constant λ gives:

$$G^{(2)}(p,\lambda) = \mathcal{G}(\bar{\lambda}(p;\lambda))exp\left(-\int_{p'=M}^{p'=p} dlog(p'/M)\cdot 2[1-\gamma(\bar{\lambda}(p';\lambda))]\right), \tag{1.13}$$

where $\mathcal{G}$ is a function to be determined and $\bar{\lambda}(p;\lambda)$ is a quantity that solves the following equation:

$$\frac{d}{dlog(p/M)}\bar{\lambda}(p;\lambda) = \beta(\bar{\lambda}). \tag{1.14}$$

This differential equation describes the rate of change of a modified coupling constant $\bar{\lambda}(p;\lambda)$ as a function of momentum. The rate of change is precisely the β function, which is reminiscent of equation (1.11). $\bar{\lambda}(p)$ is known as the running coupling constant and equation (1.14) is the so-called renormalization group equation.

The ordinary Feynman perturbation series for a Green's function depends both on the coupling constant λ and on the dimensionless parameter $log(-p^2/M^2)$. Thus, even if the coupling constant was small, the perturbative expansion could be badly behaved if the ratio p^2/M^2 was large. The Callan-Symanzik equation applied to the Green's functions, like in equation (1.13), reorganizes these dependences into two factors. The first one involves the function $\mathcal{G}$. The determination of this function must be done by matching the perturbation series in λ of $G^{(2)}(p)$. The result (1.13) instructs us to take the ordinary perturbative expansion for the Green's function but with the coupling constant replaced by the effective coupling constant $\bar{\lambda}(p)$. Therefore, the running coupling constant is the effective coupling constant that arises as a consequence of the renormalization of the theory. This is the quantity that is measurable in experiments and, as we see, its precise value depends on the energy scale at which they are performed. The sign of the β function will also play a crucial role in the dynamics of QCD; a positive β function corresponds to an effective coupling constant which increases as the momentum increases, whereas for $\beta(\lambda) < 0$

the opposite behaviour arises. An effective coupling that gets weaker as the energy of the interaction increases is precisely what asymptotic freedom is about.

The second factor in equation 1.13 corresponds to the accumulated field strength rescaling of the correlation function from the reference point M to the actual momentum of the process p.

1.4 Non-abelian Gauge Theory

Non-abelian theories are described in terms of the Yang-Mills Lagrangian:

$$\mathcal{L} = -\frac{1}{4}(F^a_{\mu\nu})^2 + \bar{\psi}(i \not{D} - m)\psi, \tag{1.15}$$

where the index a runs over the generators of the non-abelian group G, and the fermion multiplet ψ belongs to an irreducible representation r of G. The field strength $F^a_{\mu\nu}$ is:

$$F^a_{\mu\nu} = \partial_\mu A^a_\nu - \partial_\nu A^a_\mu + g f^{abc} A^b_\mu A^c_\nu, \tag{1.16}$$

where f^{abc} are the structure constants of G. For a non-Abelian theory $f^{abc} \neq 0$ and, thus, the term $(F^a_{\mu\nu})^2$ contains terms proportional to A^3 and A^4. That is, there are products of the boson fields at the same space-time point which means that the bosons interact with each other. This is the fundamental fact that gives rise to the negative value of the β function.

The Feynman rules for this Lagrangian are derived from a functional integral over the fields ψ, $\bar{\psi}$ and A^a_μ. To define the functional integral, the Faddeev-Popov method constrains the overcounting of gauge degrees of freedom by inserting into the functional integral the identity:

$$1 = \int \mathcal{D}\alpha(x)\delta(G(A^\alpha))det\left(\frac{\delta G(A^\alpha)}{\delta\alpha}\right), \tag{1.17}$$

which implements the gauge-fixing condition $G(A) \equiv \partial_\mu A^\mu = 0$. The first non-Abelian feature appears here. The determinant in equation 1.17 is not independent of A, unlike in an Abelian theory. The Faddeev-Popov method represents this determinant as a functional integral over a set of anticommuting fields belonging to the adjoint representation of the group:

$$det\left(\frac{\delta G(A^\alpha)}{\delta\alpha}\right) = \int \mathcal{D}c\mathcal{D}\bar{c}\, \exp\left[i\int d^4x \bar{c}(-\partial^\mu D_\mu)c\right]. \tag{1.18}$$

The fields c are the so-called ghosts. They must be treated as additional particles in the computation of Feynman diagrams. The ghost Lagrangian is:

$$\mathcal{L} = \bar{c}^a(-\partial^2\delta^{ac} - g\partial^\mu f^{abc}A^b_\mu)c^c. \tag{1.19}$$

Thus, the full non-Abelian Lagrangian, including the non-trival effects of this gauge-fixing method, is:

$$\mathcal{L} = -\frac{1}{4}(F^a_{\mu\nu})^2 - \frac{1}{2\xi}(\partial^\mu A^a_\mu)^2 + \bar{\psi}(i\not{D} - m)\psi + \bar{c}^a(-\partial^\mu D^{ac}_\mu)c^c. \tag{1.20}$$

1.4.1 The β function in a non-Abelian theory

Given the Lagrangian, one is now able to calculate the contributions to the fermion-boson vertex, the fermion self-energy and the boson self-energy. These contributions are needed to evaluate the counterterms which are needed to regularize the one-loop divergences that one encounters, which give the lowest-order contribution to the β function as shown in equation 1.12. This gives:

$$\beta(\alpha) = -\frac{\alpha^3}{(4\pi)^2}\left[\frac{11}{3}C_2(G) - \frac{4}{3}n_f C(r)\right], \tag{1.21}$$

where n_f is the number of flavors, $C(r)$ is the Casimir operator in the r representation of the fermions and $C_2(G)$ is defined in terms of the structure constants:

$$f^{acd}f^{bcd} = C_2(G)\delta^{ab}.$$

Of special notice is the negative sign of equation 1.21. For small values of n_f, the β function of a non-Abelian gauge theory exhibits the asymptotic freedom that is required for a correct description of the strong interactions.

1.5 Quantum Chromodynamics

When Bjorken scaling was first discovered, no asymptotically free field theories in four dimensions were known. In the early 1970s such theories were discovered and they were based on non-Abelian gauge invariance. Within this new theoretical framework, the quarks were assumed to be bound together by vector bosons, called gluons.

However, these new gauge theories predicted that, although asymptotic freedom was a present feature, the running coupling would never be zero, as the experimental Bjorken scaling seemed to suggest. Therefore, if these theories were to correctly describe the strong interactions, small deviations from the scaling behaviour should be detected. In the 1970s this picture was indeed revealed, variations of the parton distribution functions over a logarithmic scale in Q^2 were observed.

Before non-Abelian gauge theories came into play, the color quantum number had already been proposed, as previously discussed. Then, as soon it was realised that a gauge symmetry was needed, it was natural to assign it to the existing color $SU(3)$ global symmetry, promoting it to a local, or gauge, symmetry.

Unlike photons and the electromagnetic interaction, the gluons carry the charge of the strong interaction, thus coupling to themselves. This is the fundamental feature of non-Abelian gauge theories that explains why only color-invariant combinations of quarks are observed. It is found that the cost of separating a color-singlet state into colored components grows proportionally to the separation. However, a force of this kind can be weak at short distances, providing a mechanism for asymptotic freedom at high energies while bounding quarks inside hadrons.

1.5.1 Color $SU(3)$

We previously stated that hadrons are built out of spin-$\frac{1}{2}$ quarks and integer-spin gluons, and that the quarks possess a degree of freedom called color:

$$q = \begin{pmatrix} q_{red} \\ q_{green} \\ q_{blue} \end{pmatrix} \tag{1.22}$$

Quantum Chromodynamics is the context in which this emerges as a consequence of the underlying $SU(3)$ symmetry. Fermions are objects that transform in the fundamental representation under the action of the group, which for $SU(N)$ is a N-dimensional representation. In addition, QCD has eight bosonic fields A^a_μ which transform according to the adjoint representation of $SU(3)$ under the action of the group. They are called gluons or gauge bosons of the strong interaction. The groups $SU(N)$ have $N^2 - 1$ generators in their fundamental and adjoint representations, and thus the number of gluons in $SU(3)$ is eight.

The dynamics of a gauge theory such as QCD are completely defined by the commutation relations between its group generators T^i:

$$[T^i, T^j] = i \sum_k f^{ijk} T^k \tag{1.23}$$

where f^{ijk} are the structure constants. In perturbative calculations, the average (sum) over all possible color configurations in the initial (final) states leads to the appearance of combinatoric factors C_F, C_A and T_F, which are defined by the relations:

$$\sum_{k,\eta} T^k_{\alpha\eta} T^k_{\eta\beta} = \delta_{\alpha\beta} C_F \tag{1.24}$$

$$\sum_{j,k} f^{jkm} f^{jkn} = \delta^{mn} C_A \tag{1.25}$$

$$\sum_{\alpha\beta} T^m_{\alpha\beta} T^n_{\beta\alpha} = \delta^{mn} T_F \tag{1.26}$$

These color factors C_F, C_A, and T_F represent the fundamental strengths of the gluon radiation from quarks, the triple-gluon vertex, and the gluon splitting into a quark-antiquark pair respectively, as depicted in Fig. 1.3.

Figure 1.3: The relative squared amplitudes of the vertices of the theory are dictated by the underlying symmetry group through the color factors.

For $SU(N)$, the predicted values of the color factors are:

$$C_A = N \qquad C_F = \frac{N^2 - 1}{2N} \text{ and} \qquad T_F = \frac{1}{2} \tag{1.27}$$

where N is the number of color charges.

1.5.2 The running of α_s

The expression for the β function in equation 1.21 gives, for $N = 3$:

$$\beta(\alpha) = -\frac{b_0 \alpha^3}{(4\pi^2)}, \tag{1.28}$$

with $b_0 = 11 - \frac{2}{3} n_f$ and n_f the number of quark flavors. The renormalization group equation 1.14 gives the expression for the effective coupling constant, which is usually called $\alpha_s(Q)$:

$$\alpha_s(Q) = \frac{\alpha_s}{1 + (\frac{b_0 \alpha_s}{2\pi}) log\left(\frac{Q}{M}\right)}, \tag{1.29}$$

where $\alpha_s \equiv \alpha^2/4\pi$ is the coupling constant at $Q = M$.

It is usual to remove the explicit dependence on the renormalization scale M in favour of a mass scale Λ which satisfies:

$$1 = \alpha^2 \frac{b_0}{8\pi^2} log\left(\frac{M}{\Lambda}\right). \tag{1.30}$$

With this definition, the running strong coupling constant is now:

$$\alpha_s(Q) = \frac{2\pi}{b_0 log\frac{Q}{\Lambda}} \tag{1.31}$$

In Fig. 1.4 the running of $\alpha_s(Q)$ is depicted.

There are several things worth noticing. In the first place, equation 1.31 shows very clearly the fact that, as Q^2 increases, $\alpha_s(Q^2)$ decreases as $log(Q^2)^{-1}$. QCD therefore exhibits the property that it is needed for any theory to describe the strong interactions, asymptotic freedom. It is also worth mentioning the dimensional transmutation that has taken place. The quantum theory is not characterized by a dimensionless parameter, but by a dimensional parameter Λ. It is the scale at which $\alpha_s(Q)$ becomes strong as Q^2 decreases. This means that one should expect that hadrons typically have a size determined by the length $\sim 1/\Lambda$, which is the length at which the interaction between them would become strong. Experimental measurements of Λ yield a value of $\Lambda \approx 200$ MeV, which corresponds to the size of the light hadrons.

Experimental determinations of the running of the strong coupling constant are now abundant and it has been well established that the running as predicted by QCD reproduces the experimental data. Figure 1.5 shows how HERA has been very powerful in determining the value of $\alpha_s(M_Z)$ through many different physics processes.

1.5.3 The confinement of quarks

One of the pieces of the puzzle that was presented at the beginning of section 1.1 is solved with the advent of the non-Abelian quantum field theory QCD. As we just saw, the effective coupling of this theory is consistent with the phenomena of asymptotic freedom. The other piece of the puzzle is: what keeps quarks confined inside hadrons? Intuitively, a coupling constant that grows strong as the energy of the interaction decreases seems to be the required behaviour for confinement to arise, but no analytic proof exists yet that QCD is a confining theory. Confinement is, in a way, the responsible feature that makes quarks and gluons impossible to detect in isolation. However, it is more accurate to state that it is the fact that light quarks are much lighter than Λ what actually makes QCD complicated. If,

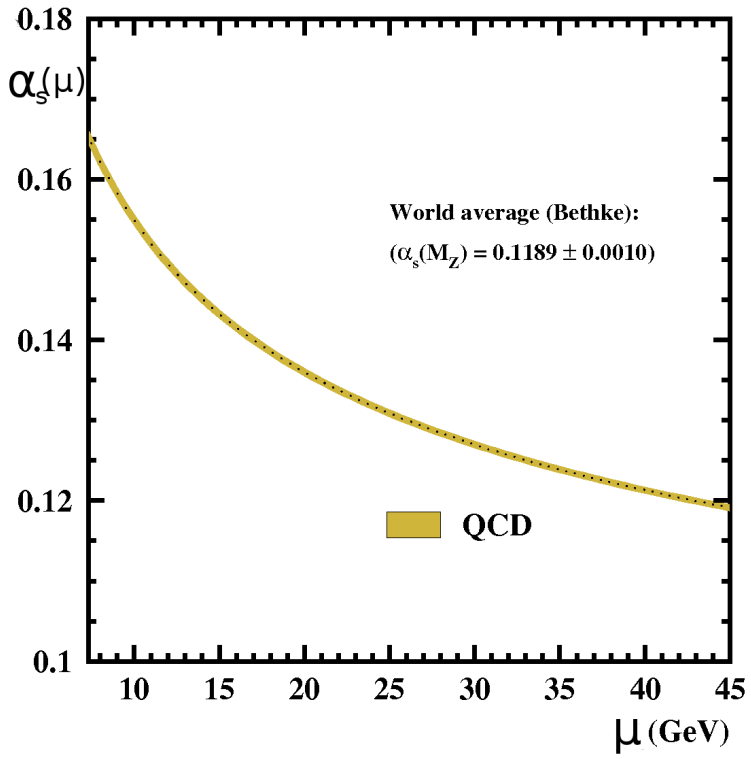

Figure 1.4: Perturbative QCD prediction for the scale dependence of $\alpha_s(\mu)$ for the value of $\alpha_s(M_Z) = 0.1189 \pm 0.001$, corresponding to the current world average.

for example, the ratio of the light quarks' mass and Λ were such that the effective coupling constant at the mass of the proton were:

$$\alpha_s(m_p) = \alpha_{em},$$

where α_{em} is the electromagnetic coupling constant, then some interesting features would appear. In the first place, since the chromodynamic forces would be as weak as the electromagnetic ones, the proton mass would be roughly three times the quark mass (assuming $m_u = m_d$ in this scenario). Thus, the quark mass would be:

$$m_q \approx m_p/3 \approx 300 \text{ MeV}.$$

The proton radius would simply be the Bohr radius $(\alpha_s m_q)^{-1} \approx 10^{-11}$cm, which is roughly 100 times bigger than in our world. Interestingly, this is still significantly smaller than the size of the atom so the chemistry of this scenario would not be significantly changed.

However, in this hypothetical world, the distance at which the strong coupling constant would become strong would now be:

$$\frac{1}{\Lambda} = exp\left(\frac{2\pi}{b_0\alpha_s(m_p)}\right)\frac{1}{m_p} \approx 10^{20}\text{cm},$$

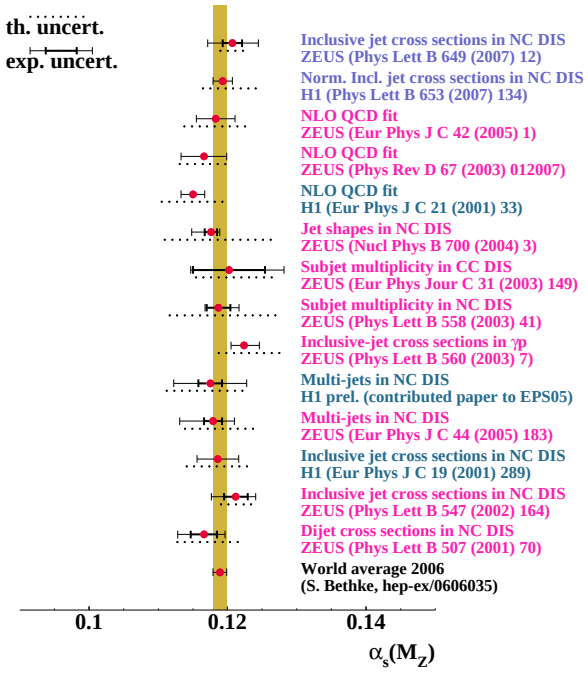

Figure 1.5: A compilation of determinations of $\alpha_s(M_Z)$ made at HERA.

which means that, if particle collisions were made by some creatures living in that universe, the effects of confinement, although present, would be the last thing in their minds as they would be really hard to measure.

1.6 QCD and Deep Inelastic Scattering

Once the theoretical framework of quantum field theory was established to describe the strong interactions, the machinery of Feynman diagrams and the perturbative approach was ready to be used in the study of deep inelastic scattering of electrons and protons.

Consider a process like the one shown in Fig. 1.6. If the squared invariant momentum transfer Q^2 is large, the quark is ejected from the proton in a manner that cannot be balanced by subsequent soft processes. However, these processes create gluons and other quark-antiquark pairs that eventually neutralize the color and cause the struck quark to materialize as a jet of hadrons. When the total invariant mass of the hadronic final-state system is large, the process is referred to as deep inelastic scattering.

To derive a first approximation to the cross section, consider this reaction in the

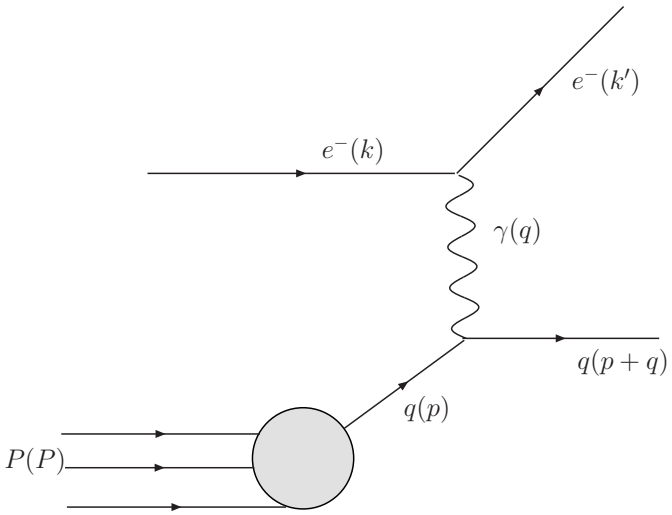

Figure 1.6: Kinematics of a DIS process at lowest order.

electron-proton center-of-mass frame. Let's assume that the center-of-mass energy is large enough to ignore the mass of the proton. In this frame, the proton constituents are then almost collinear with the momentum of the proton. This is because a constituent of the proton can acquire transverse momentum with respect to the proton's momentum only by the exchange of a hard transverse gluon, a process which is supressed by a factor α_s. This means that, at lowest order in pQCD, the momentum of the constituents is related to that of the proton by:

$$p = \xi P. \tag{1.32}$$

The cross section for e^-p scattering is then given, at lowest order in α_s, by the cross section for electron-quark scattering at a given fraction of the proton's momentum ξ (depicted in Fig. 1.6) multiplied by the probability that the proton contains a quark at that value ξ and integrated over all possible values of ξ. The cross section is then given by:

$$\sigma(e^-(k)p(P) \to e^-(k') + X) = \int_0^1 d\xi \sum_f f_f(\xi)\sigma(e^-(k)q_f(\xi P) \to e^-(k') + q_f(p')). \tag{1.33}$$

That is, the expression that was obtained in section 1.1 for the cross section in the parton model is recovered by QCD at lowest order in α_s. It was argued then that in the parton model the parton distribution functions depend only in the quantity ξ, a behaviour known as Bjorken scaling. Now it is easy to guess that the deviations from the scaling behaviour will arise as a consequence of the higher-order terms in

the perturbative expansion.

It is often convenient to represent the cross section in equation 1.4 in terms of dimensionless combinations of kinematic variables. The variable x is already dimensionless, the other choice is:

$$y \equiv \frac{2P \cdot q}{2P \cdot k} = \frac{2P \cdot q}{s}. \tag{1.34}$$

It is worth noting that, in the frame where the proton is at rest:

$$y = \frac{q^0}{k^0}. \tag{1.35}$$

The variable y is thus the fraction of the incident electron's energy that is transferred to the hadronic system and, thus, $0 \leq y \leq 1$.

If follows that

$$Q^2 = xys,$$

so that the following change of variables can be made:

$$d\xi \, dQ^2 = dx \, dQ^2 = x \, s \, dx \, dy,$$

and the differential cross section becomes:

$$\frac{d^2\sigma}{dxdy}(e^- p \to e^- X) = \left(\sum_f x f_f(x) Q_f^2 \right) \frac{2\pi\alpha^2 s}{Q^4} \left[1 + (1-y)^2 \right]. \tag{1.36}$$

The dependence on y in the factor $[1 + (1-y)^2]$ reflects the helicity of the interacting particles and it is specific to the scattering of electrons from massless fermions, which gave evidence that the partons involved in deep inelastic scattering processes were fermions at a time when it was not yet clear.

The range of x, Q^2 and y available in an experiment depends on its characteristics. At HERA, the kinematic range is quite wide in both x and Q^2, ranging from values of x as low as $x \sim 10^{-6}$ in the case of ZEUS. Likewise, interactions with a Q^2 between 10^{-1} GeV^2 and larger than 10^4 GeV^2 are available at HERA. A schematic representation of the kinematic plane x-Q^2 can be seen in Fig. 1.7.

The convolution of the parton distribution functions with the cross section of electron and quark scattering is known as factorisation. The philosophy behind factorisation is simply to write the hard interaction of high-energy processes as a perturbative expansion in α_s. These processes are not sensitive to the details of the long-distance physics involved such as the description of the incoming hadron and

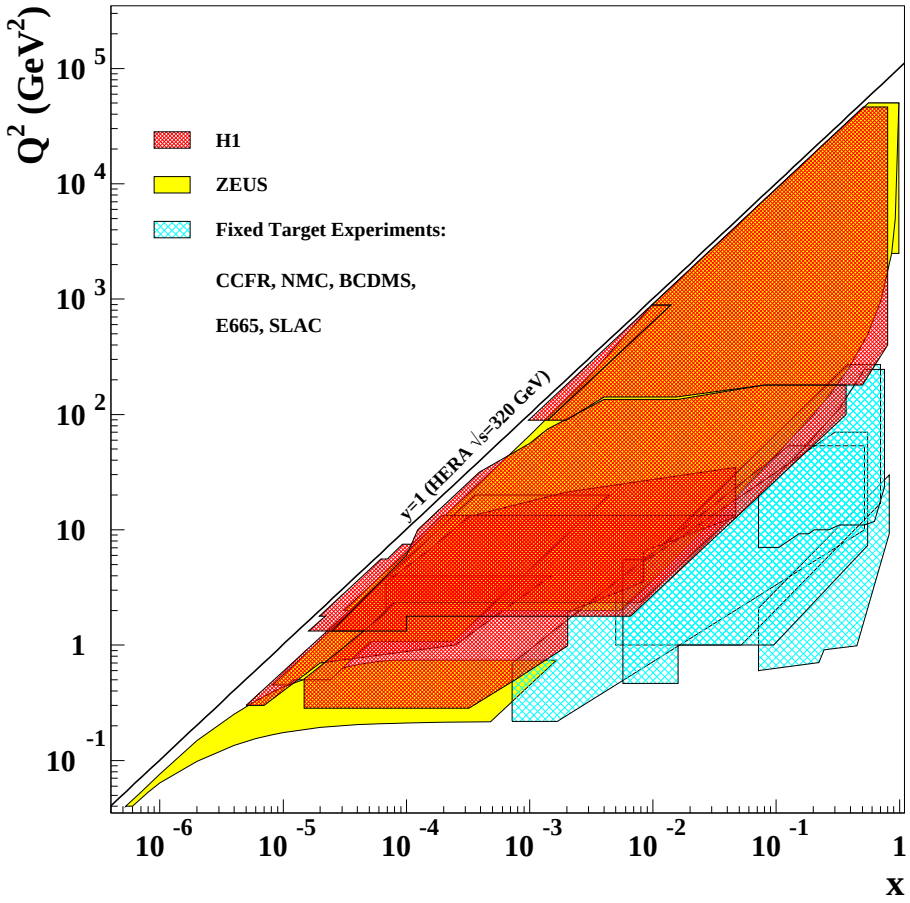

Figure 1.7: The regions of the kinematic plane covered by the ZEUS and H1 experiments at HERA. The regions covered by fixed-target experiments are also depicted for comparison.

thus they factorise out of the hadron physics description. The energy scale which separates what is called the hard interaction from the rest of the process is known as the factorisation scale, usually denoted by μ_F. A parton that is emitted with a transverse momentum smaller than μ_F is considered to be a part of the hadron structure and therefore absorbed into the parton distribution function. The cross section for lepton-hadron scattering is then expressable as:

$$\sigma(P_l, P_h) = \sum_i \int d\xi f_i(\xi, \mu_F^2) \bar{\sigma}(P_l, \xi P_h, \alpha_s(\mu_R), \mu_R, \mu_F), \tag{1.37}$$

where P_l (P_h) are the incoming lepton's (hadron's) momentum.

The parton distribution functions (PDFs) in the proton are not calculable from first principles in QCD and have to be extracted from experimental results. This can be done because of the universality of the factorisation procedure. The obtained PDFs in one experiment can be used in another to make predictions. However, the evolution of the PDFs with the scale Q^2 can be predicted within QCD when the

scale is large. The evolution of the PDFs with the scale is slow in this case and the perturbative approach can be used.

The ZEUS collaboration has performed several extractions of the proton PDFs [1, 2]. In these analyses, a reference value Q_0 is chosen and the PDFs are parametrized at that value. The parameterization used has the form:

$$xf(x) = p_1 x^{p_2}(1-x)^{p_3}(1+p_4 x),$$

where p_i are the parameters to be extracted. The distributions are then subjected to the evolution with the scale as predicted by the DGLAP [3–7] equations (see next section) so that values of the structure functions as well as predictions for other observables are obtained.

In the analyses presented, the ZEUS-S PDFs were used [1], which included HERA data as well as fixed-target data to constrain the fits at high x and provide information on the valence distributions and the flavor composition of the sea. The kinematic range covered by the data input to the fits is $6.3 \times 10^{-5} \leq x \leq 0.65$ and $2.5 \leq Q^2 \leq 30000$ GeV^2.

In Fig. 1.8(a) the ZEUS-S PDFs as functions of x at $Q^2 = 10$ GeV^2 are shown. In Fig. 1.8(b), a comparison with the PDFs as extracted by the MRST [8] and CTEQ [9] collaborations is shown.

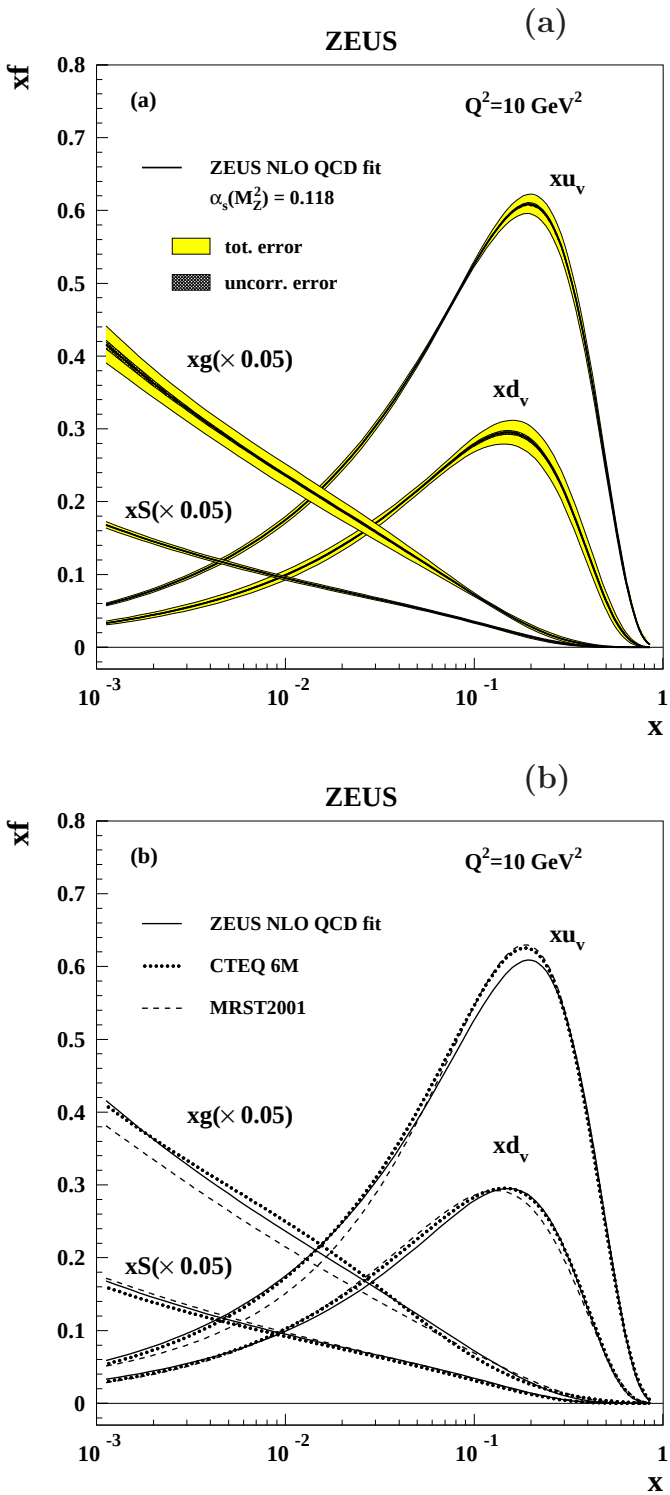

Figure 1.8: **(a)** The gluon, sea, and u and d valence distributions extracted from the standard ZEUS-S NLO QCD fit at $Q^2 = 10$ GeV^2. **(b)** Comparison with the extractions performed by the MRST and CTEQ collaborations.

1.6.1 Parton Evolution

Moving into the next order in α_s inmediately hits the problem of the zero-mass singularities. Unlike the case of e^+e^- annihilation, mass singularities and soft-gluon singularities do not cancel out because of the presence of initial-state partons. This is the fact that induces logarithmic violations of the Bjorken scaling. In QCD, the emission of a collinear gluon costs a factor:

$$\alpha_s(Q^2) log \frac{Q^2}{\Lambda^2}, \tag{1.38}$$

which is a quantity $\mathcal{O}(1)$. Therefore, out of the roughly $(n!)^2$ Feynman diagrams involved in a process with n participating particles, the ones corresponding to collinear emissions are the maximally enhanced ones since:

$$(\alpha_s log Q^2)^n = \mathcal{O}(1).$$

The procedure by which these enhanced contributions are selected out of all the contributing diagrams is known as the leading-log approximation (LLA) [10, 11]. These diagrams correspond to the emission of n succesive gluons with increasing virtuality. Figure 1.9 shows one of the contributing diagrams that are logarithmically enhanced. A quark, initially with a momentum fraction x_0, emits n gluons as it moves into more virtual square masses and lower momentum fractions. This has an interesting physical interpretation. Since the intermediate quarks are increasingly more virtual as the diagram moves towards the scattering, it seems natural to intepret them as components of the physical quark when the particle is analyzed at succesively smaller distances. That is, a quark scattered at one resolution can be resolved at a finer scale as an even more virtual quark and a number of gluons and other quarks. Thus, it seems logical to include these logarithmics enhancements due to collinear emission inside of the parton distribution functions. By doing this, the PDFs acquire the momentum dependence just discussed, the partons looks differently depending on the scale at which they are observed and, therefore, scaling violations arise. However, since the scale dependence is logarithmic, an approximate Bjorken scaling is still observed.

A fundamental ingredient in the ability to take into account the dominant contributions at all orders is the strong ordering of the succesive emissions $|k_0|^2 << |k_1|^2 << ... << |k_n|^2$. Physically, this is justified by the fact that quark-gluon multiplication processes happen at larger space-time distances than the hard interaction. With this separation it is possible to describe quark and gluon cascades in terms of independent splitting processes.

This resummation of enhanced logarithmic terms leads to a set of equations

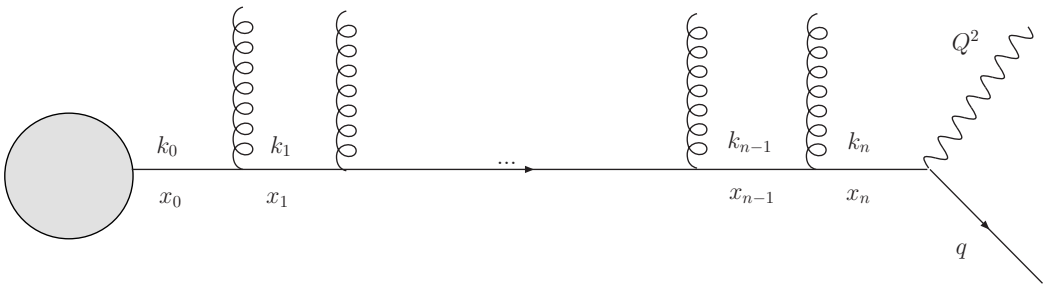

Figure 1.9: Succesive gluon emissions from a quark before it undergoes a deep inelastic process.

that describe the evolution of the parton distribution functions in the energy range where perturbation theory can be applied. The set of equations are known as the DGLAP equations. The equations essentially state that the parton distribution functions evolve pertubatively with the scale Q according to the convolution of two ingredients. The first one is the present configuration of the PDFs at that scale, in which the resummation of collinear emission previously discussed is present, and the second one is the parton emission which can proceed through the three different vertices (at leading order in α_s) shown in Fig. 1.10 (four vertices are shown, but two of them are identical). The differential probability of a parton $p1$ emitting a parton $p2$ with a fraction z of its momentum is described in terms of the splitting functions $P_{p1}^{p2}(z)$. In QCD there are four different possibilities, all of them also shown in Fig. 1.10. With these ingredients, one can write the set of differential equations that govern the evolution of the parton distribution functions:

$$\frac{d}{dlogQ} f_g(x,Q) = \frac{\alpha_s(Q^2)}{\pi} \int_x^1 \frac{dz}{z} \left\{ C_F P_q^g(z) \sum_f [f_f(\frac{x}{z},Q) + f_{\bar{f}}(\frac{x}{z},Q)] + C_A P_g^g(z) f_g(\frac{x}{z},Q) \right\}, \tag{1.39}$$

$$\frac{d}{dlogQ} f_f(x,Q) = \frac{\alpha_s(Q^2)}{\pi} \int_x^1 \frac{dz}{z} \left\{ C_F P_q^q(z) f_f(\frac{x}{z},Q) + T_F P_g^q(z) f_g(\frac{x}{z},Q) \right\}, \tag{1.40}$$

$$\frac{d}{dlogQ} f_{\bar{f}}(x,Q) = \frac{\alpha_s(Q^2)}{\pi} \int_x^1 \frac{dz}{z} \left\{ C_F P_q^q(z) f_{\bar{f}}(\frac{x}{z},Q) + T_F P_g^q(z) f_g(\frac{x}{z},Q) \right\}. \tag{1.41}$$

Here $f_f(\xi)$ and $f_g(\xi)$ represent the quark and gluon distribution functions inside a proton.

In chapter 6 a Monte Carlo event generator which simulates the resummation of the enhanced logarithmic terms by a succession of parton branchings is discussed. It

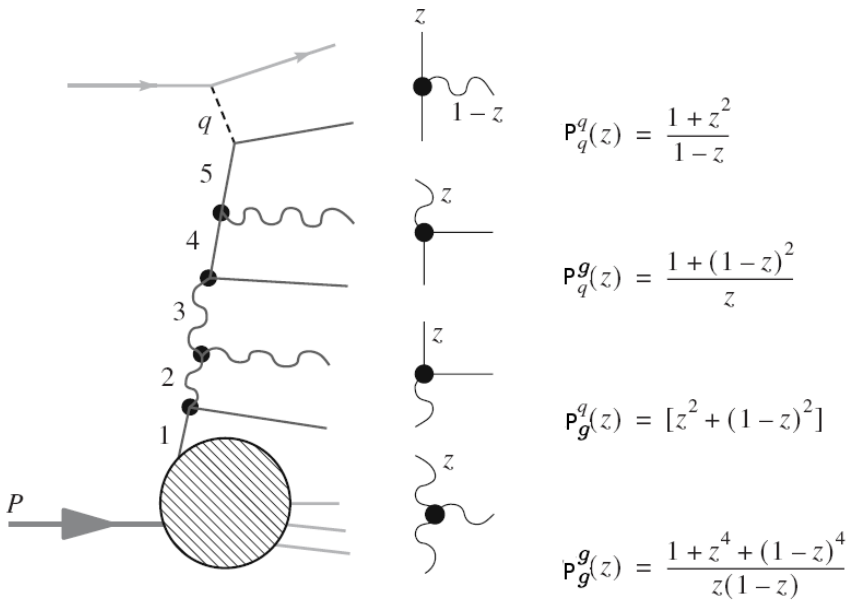

Figure 1.10: Parton splitting functions.

uses a numerical approach to the evolution equations based on the so-called Sudakov form factor:

$$\Delta_i(t) = exp\left[-\int_{t_0}^{t}\frac{dt'}{t'}\sum_j\int dz\frac{\alpha_s}{2\pi}P_i^j(z)\right], \tag{1.42}$$

where P_i^j represents the splitting functions.

One can then write the set of differential equations for the evolution of the f_i as

$$t\frac{\partial}{\partial t}\left(\frac{f_i}{\Delta_i}\right) = \frac{1}{\Delta_i}\sum_j\int\frac{dz}{z}\frac{\alpha_s}{2\pi}P_j^i(z)f_j(x/z,t). \tag{1.43}$$

The Sudakov form factor expresses the probability that parton i does not branch between the scales t_0 and t and it sums enhanced virtual and real contributions to all orders.

In the formulation of the DGLAP equations, $f_f(\xi)$ and $f_g(\xi)$ represented the quark and gluon distribution functions inside a proton. However, certain combinations of PDFs are preferred in terms of which the cross sections are usually expressed. To obtain this expression, let's consider a process like the one shown in Fig. 1.1. The leptonic contribution to the process can be calculated using the standard Feynman rules.

$$L_e^{\mu\nu} = \frac{1}{2} Tr((\not{k}' + m)\gamma^\mu(\not{k} + m)\gamma^\nu) \tag{1.44}$$

On the other hand, since the cross section has to be Lorentz-invariant, the general expression will have to be of the form:

$$d\sigma \sim L^e_{\mu\nu} W^{\mu\nu}, \tag{1.45}$$

where $W^{\mu\nu}$ represents the Lorentz structure of the target, which is a priori unknown, but can be constrained with the aid of Lorentz invariance and current conservation. In the first place, it must be a combination of the independent inputs to the physical process, the momenta p and q. With this requirement, the most general expression containing two free Lorentz indices is:

$$W^{\mu\nu} = -W_1 g^{\mu\nu} + \frac{W_2}{M^2} p^\mu p^\nu + iW_3 \epsilon^{\mu\nu\rho\sigma} p_\rho q_\sigma + \frac{W_4}{M^2} q^\mu q^\nu + \frac{W_5}{M^2}(p^\mu q^\nu + q^\mu p^\nu), \tag{1.46}$$

where M is the mass of the proton. The Ward Identity comes into role now following the conservation law:

$$\partial_\mu W^{\mu\nu} = 0$$

from which the Ward Identity asserts that q_μ can be dotted into $W^{\mu\nu}$:

$$q_\mu W^{\mu\nu} = 0$$

so that the expression is further constrained. Thus, only three of the five initial inelastic structure functions of equation 1.46 are independent. It is common to write:

$$F_1(x, Q^2) = MW_1(x, Q^2), \tag{1.47}$$

$$F_2(x, Q^2) = \frac{Q^2}{2Mx} W_2(x, Q^2) \tag{1.48}$$

and

$$xF_3(x, Q^2) = \frac{Q^2}{2M} W_3(x, Q^2). \tag{1.49}$$

The functions F_i are the combinations of PDFs we were after; they are admixtures of the f_f and f_g. The function F_3 is a parity-violating contribution and it is only present when a Wor Z boson is the exchanged particle and thus the contribution from this term is important only at high values of Q^2.

Thus, in the limit where the parton masses can be ignored, the general NC DIS cross section can be written as:

$$\frac{d^2\sigma}{dxdQ^2}(e^{\pm}p) = \frac{4\pi\alpha^2}{xQ^4}[xy^2F_1 + (1-y)F_2 \mp y(1-\frac{1}{2}y)xF_3] \tag{1.50}$$

In Fig. 1.11, measurements of the structure function F_2 at HERA by the experiments ZEUS and H1 are shown. It can be seen that there is indeed a dependence of F_2 with the scale Q^2, which is especially important at low x.

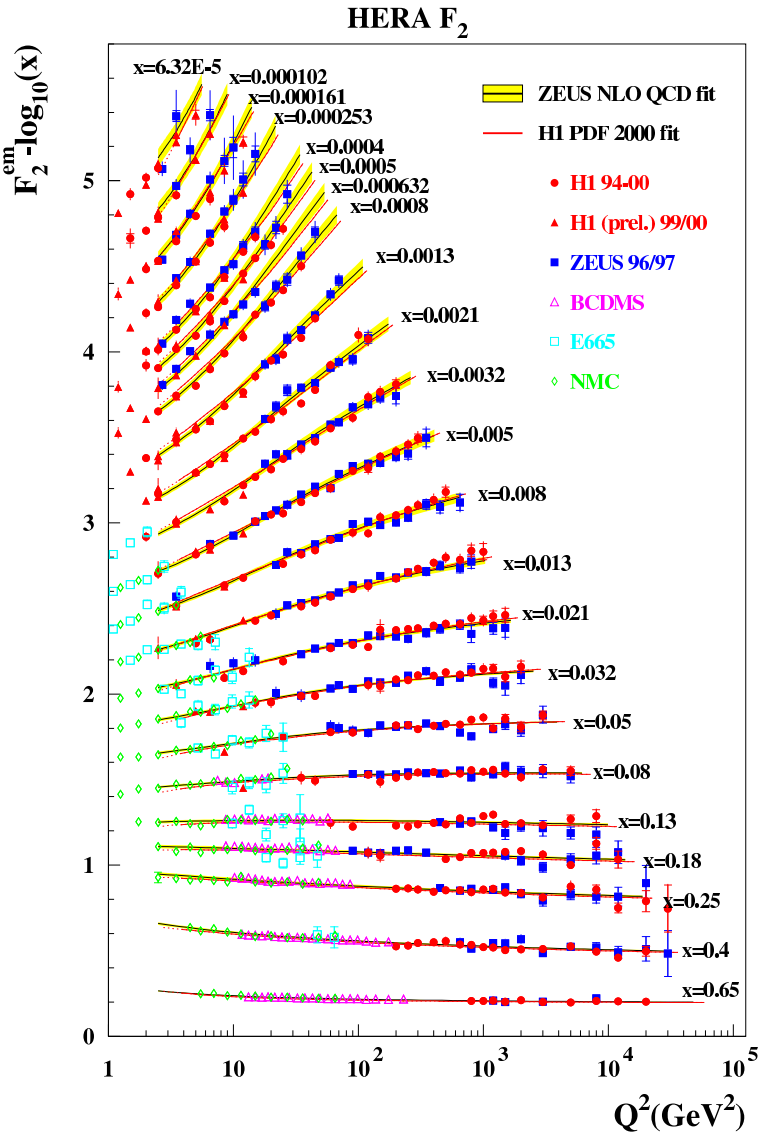

Figure 1.11: Summary of measurements of F_2 at HERA.

Chapter 2

Jet physics

In section 1.5.3 the phenomenon of confinement was discussed. As it was argued, the fact that QCD is a non-Abelian theory and that the mass of the quarks is significantly smaller than Λ, makes it impossible to observe a completely isolated colored object. When the distance between two color-connected objects is larger than the fundamental scale $1/\Lambda$ it is energetically favorable to create a quark-antiquark pair so that the initial partons evolve into a system of hadrons. These are the jets.

Thus, ultimately what the experimentalist observes is a jet of hadrons. Therefore, the ability to relate the observations to the underlying hard interaction has to be done in terms of the elements that are observed in the detection process, like the energy of the hadrons or their spatial distribution. That is, the concept of jet has to be defined precisely in an unambiguous manner so that a theory of hard interactions can be compared to the data obtained in an experiment. As we shall see in the next section, a jet is defined as the end-product of an interative process that runs over a set of input objects (final-state particles, energy deposits in a calorimeter, etc), known as a jet reconstruction algorithm.

2.1 Jet algorithms

The precise details of an optimal jet algorithm are subject to specifics of the experiment where it is going to be used. However, there is a set of attributes that any jet algorithm should have. In order to perform comparisons of the predictions of QCD with the data, the end-products of the theoretical calculations are also fed into the jet algorithm, which reconstructs jets of partons (see chapter 7). On the other hand, it is necessary for certain Feynman diagrams to give the same jet configurations in order to make collinear and infrared divergences go away. Thus, for any theoretical calculation of jet production that aims to make sensible predictions, this type of cancellations should take place after the application of the jet reconstruction algorithm

to the final partons of the pQCD calculations. If this is the case, the algorithm is said to be collinear and infrared safe.

It is also desirable that it has little sensitivity to hadronization corrections, since the smaller they are, the better the correspondence between the measurements of the jets of hadrons and the underlying dynamics of the partons.

It also should exhibit certain invariances. In hadron-induced reactions, the quantities involved in the definition of distances have to be invariant under longitudinal boosts along the collision axis. This is especially important in an experiment like HERA, where the center-of-mass energy of the hard interaction depends on the fraction of the momentum of the proton that the struck quark carries, which varies in an event-by-event basis.

The algorithm that was used for the studies presented in this work was the k_T-cluster algorithm [12] in its longitudinally-invariant inclusive mode [13]. A schematic representation of how the algorithm works can be found in Fig. 2.1. It is infrared and collinear safe, and it makes use of the longitudinally-invariant quantities E_T, $\Delta\eta$ and ϕ. It is also an algorithm that has several advantages over other common reconstruction algorithms such as the cone algorithm [14]. It yields smaller hadronization factors and it is also less influenced by soft particles than the cone algorithm.

It proceeds according to the following steps:

- For every pair of objects i and j (e.g. final-state partons, final-state hadrons or energy deposits in the calorimeter), the distance d_{ij} between them is found according to:

$$d_{ij} = min\{E_{T,i}^2, E_{T,j}^2\} \left[(\eta_i - \eta_j)^2 + (\phi_i - \phi_j)^2\right],$$

  where $E_{T,i}$, η_i and ϕ_i are the transverse energy, pseudorapidity and azimuthal angle of the $i-$th object.

- For collisions involving incoming hadron beams, one also has to define a closeness measure to the beam direction to ensure that the resulting cross sections obey the factorization theorem. For every object i, the closeness to the beam direction is defined according to

$$d_i = E_{T,i}^2 \cdot R^2,$$

  where R is commonly known as the radius of the jet. In this work, it is set to unity. Recent analyses by ZEUS have studied the radius-dependence of the inclusive jet production in NC DIS [15, 16].

- The smallest value of all $\{d_{ij}, d_i\}$ is considered. If this is one of the d_{ij} the two objects are merged into a new one following the recombination scheme:

$$E_{T,k} = E_{T,i} + E_{T,j}; \qquad \eta_k = \frac{1}{E_{T,k}} \left(\eta_i E_{T,i} + \eta_j E_{T,j}\right); \qquad \phi_k = \frac{1}{E_{T,k}} \left(\phi_i E_{T,i} + \phi_j E_{T,j}\right).$$

  This recombination scheme is known as the Snowmass convention [17]. If, however, the minimum is one of the d_i, then that object is considered as a protojet and it is no longer considered in the iteration process.

- This process is repeated until no object remains, that is until it is satisfied that:

$$d_i < d_{ij}$$

  for all i and j. All the objects have been clustered into protojets at this point.

- Jets are selected from the sample of protojets by imposing a cut on the transverse energy of the protojets to disentangle the end-products of the hard interaction.

One also has to specify the system of reference where jets are reconstructed. In the analyses presented here, this was the laboratory frame. In jet physics at HERA, jets are commonly reconstructed in the Breit frame [18, 19]. However, a reconstruction in the Breit frame would not allow for studies of jet substructure at next-to-leading order in the three-subjet analysis, as will be explained in section 5.1.

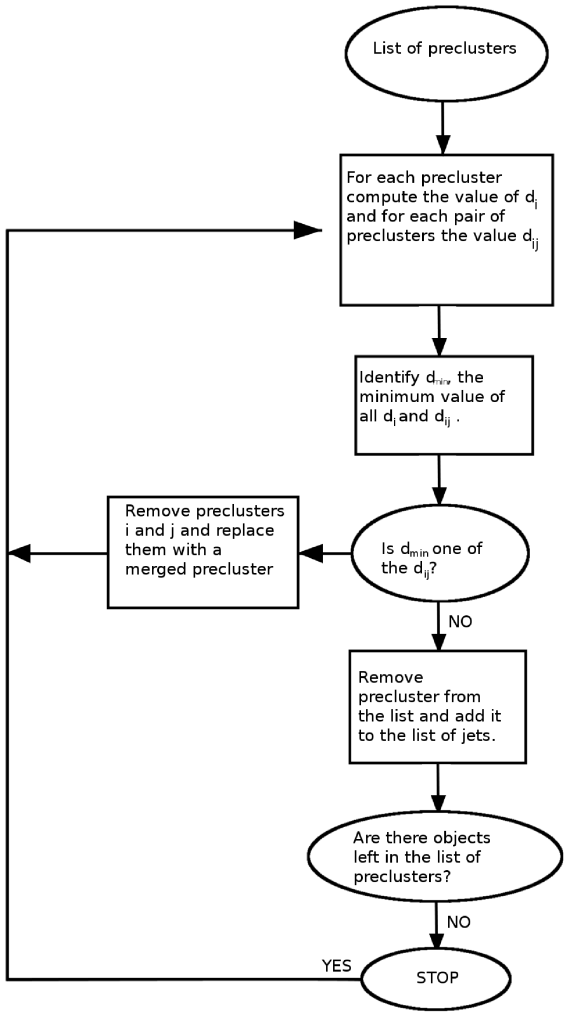

Figure 2.1: A schematic representation of the k_T cluster algorithm in its longitudinally-invariant mode.

2.2 Perturbative jet physics

Jets of hadrons, which ultimately are what hit the detectors, arise as a consequence of the non-perturbative phenomenon of color confinement. For this reason alone, the applicability of pQCD even to hard processes is far from obvious. However, the data obtained in many years of experiments with QCD jets clearly show that the broad features of hadronic jet systems, calculated at the parton level, agree surprisingly well with the measured ones. This demonstrates the dominant role of the perturbative phase of jet evolution and supports the hypothesis of Local Parton-Hadron Duality (LHPD) [20, 21]. The fundamental assumption is that the conversion of partons into hadrons occurs at a low virtuality scale, which is independent of the scale of the primary hard process, and involves only low-momentum transfers.

The analytical perturbative approach (APA), which combines pQCD with the LHPD hypothesis, attempts to describe the structure of multi-hadronic final states with the minimal reference to the dynamics of fragmentation. In this framework, the dominant source of multihadron production in hard processes is gluon bremsstrahlung. The produced hadrons bear information about the underlying dynamics at small distances, so that the distributions of the color-singlet hadrons in the final state are governed by the dynamics of the parton-shower system and, in particular, by the flow of color numbers.

Gluon brehmstrahlung off a quark, which plays the key role in QCD jets, has a differential spectrum given by:

$$d\omega^{q\to q+g} = \frac{\alpha_s(k_\perp)}{4\pi} 2C_F \left[1 + \left(1 - \frac{k}{p}\right)^2\right] \frac{dk}{k} \frac{dk_\perp^2}{k_\perp^2}, \tag{2.1}$$

where k is the gluon four-momentum.

At a large emission angle, which contributes to the multijet topology, and large energy E one would have:

$$k_\perp \sim k \sim E \to w \sim \frac{\alpha_s}{\pi} << 1.$$

That is, a small probability to emit a gluon-jet. At the same time, quasi-collinear emissions and soft partons, which constitute the bulk of radiation, will not lead to additional jets but will instead populate the original jet with secondary partons influencing the particle multiplicity and other jet characteristics such as its substructure:

$$k_\perp << k << E \to w \sim \alpha_s log^2 E \sim 1$$

Therefore, it is of tantamount importance to take into account the effects of these soft-emissions. The physics involved in this regime were discussed in section 1.6.1 in the context of parton distribution functions.

2.2.1 Coherent branching

Coherence phenomena are an intrinsic property of any gauge theory. In QCD, color coherence can be separated into two regions: intrajet and interjet coherence [10, 11]. Intrajet coherence deals with coherent efects in partonic cascades, resulting on average in the angular ordering of the sequential parton branching inside jets.

In addition to the logarithmic enhancements that come from collinear parton emission, there are also enhancements which arise from soft gluon emission. The enhancement factor appears in the external lines of Feynman diagrams, which means

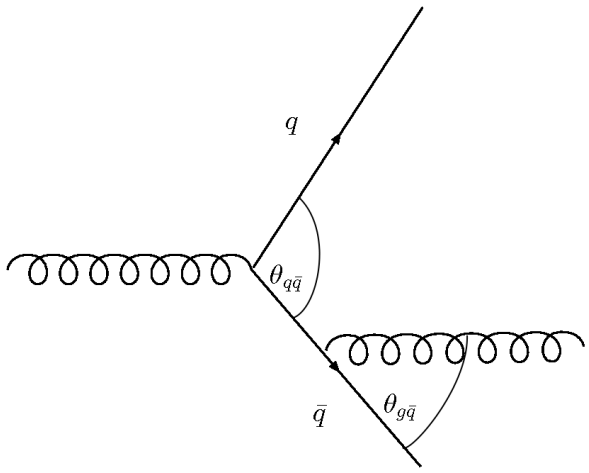

Figure 2.2: Due to the coherence effects, the final-state gluon is emitted with $\theta_{g\bar{q}} < \theta_{q\bar{q}}$.

that when the coherent sum is taken to calculate the cross section, there will be a term which is a sum over all pairs of lines $\{i, j\}$:

$$d\sigma_{n+1} = d\sigma_n \frac{d\omega}{\omega} \frac{d\Omega}{2\pi} \frac{\alpha_s}{2\pi} \sum_{i,j} C_{ij} W_{ij}, \tag{2.2}$$

where $d\Omega$ is the element of solid angle for the emitted gluon, C_{ij} is a color factor to be computed and the radiation function W_{ij} is given by:

$$W_{ij} = \frac{\omega^2 p_i \cdot p_j}{p_i \cdot q \, p_j \cdot q} = \frac{1 - v_i v_j cos\theta_{ij}}{(1 - v_i cos\theta_{iq})(1 - v_j cos\theta_{jq})} \tag{2.3}$$

where q is the gluon's momentum.

The quantity W_{ij} can be separated into two terms:

$$W_{ij} = W_{ij}^{[i]} + W_{ij}^{[j]},$$

where

$$W_{ij}^{[i]} = \frac{1}{2} \left(W_{ij} + \frac{1}{1 - cos\theta_{iq}} - \frac{1}{1 - cos\theta_{jq}} \right).$$

The funtion $W_{ij}^{[i]}$ possesses the property of angular ordering, by which the angular integration in equation 2.2 gives:

$$\begin{aligned} \int_0^{2\pi} \frac{d\phi_{iq}}{2\pi} W_{ij}^{[i]} &= \frac{1}{1 - cos\theta_{iq}} \text{ if } \theta_{iq} < \theta_{ij} \\ &= 0 \text{ otherwise} \end{aligned} \tag{2.4}$$

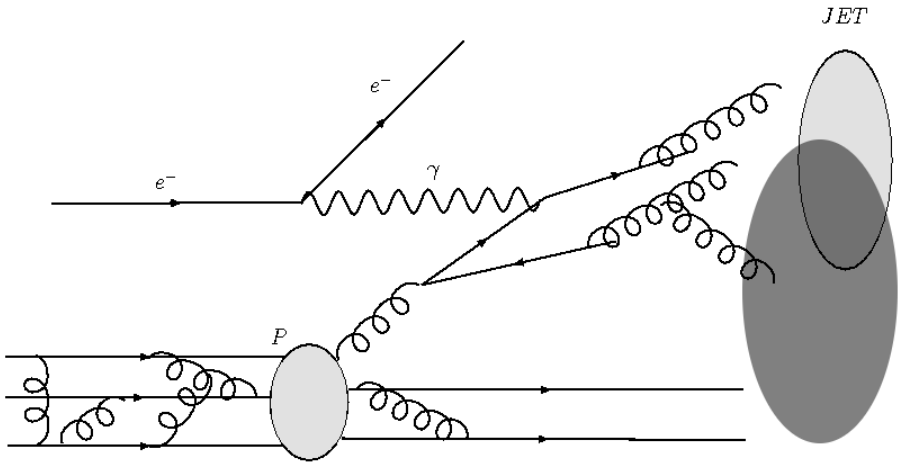

Figure 2.3: Color-coherence effects between initial and final states in DIS ep scattering. Due to these effects, the soft radiation is restricted to the region between the jet and the color-connected proton remnant, depicted as the dark-grey area.

That is, this term yields a contribution to soft-gluon emission from the external legs $\{i, j\}$ which is confined in a cone centered along the direction of i and delimited by the direction of j ($\theta_{iq} < \theta_{ij}$). Of course, the same argument works for $W_{ij}^{[j]}$. Thus, succesive soft-gluon emissions from external lines exhibit the phenomenon of angular ordering (AO), depicted in Fig. 2.2.

A color-coherence phenomenon that will be studied in the work presented here is the coherence between initial and final states. In this case, the effects manifest themselves by esentially restricting the region where soft partons are emitted to the one between the two color-connected partners in the event, which in this case are the proton remnant and the jet. A schematic representation is given in Fig. 2.3, where the dark-grey area represents the region where the soft emissions are to be expected.

2.3 Subjets

Subjets are jet-like structures resolved within jets [22–25]. The clustering algorithm is re-applied to the objects that have been clustered together in a jet with a dimensionless resolution parameter y_{cut}.

Having selected a particular jet, the k_T-cluster algorithm was re-applied to all the particles belonging to it until it is satisfied that

$$d_{ij} > y_{cut} \left(E_T^{jet}\right)^2; \tag{2.5}$$

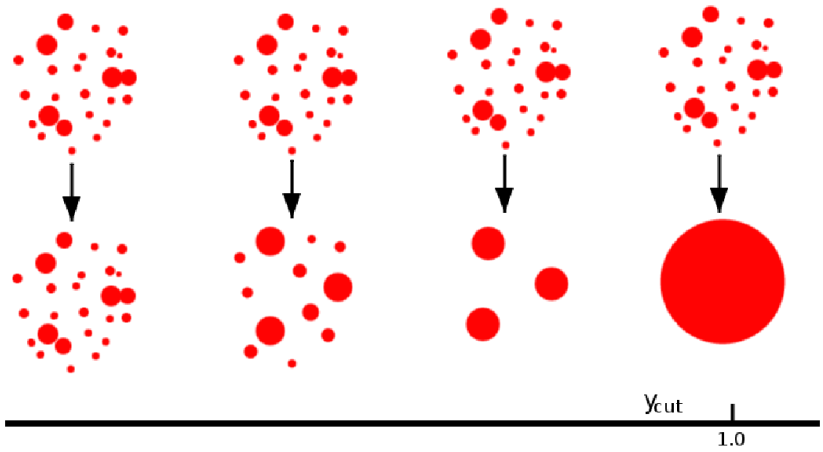

Figure 2.4: The resolution parameter y_{cut} determines how many subjets are resolved within a given jet.

the remaining particles after this condition is satisfied for all $\{i, j\}$ are called subjets. The parameter y_{cut} determines how many subjets are resolved within a given jet (see Fig. 2.4. When y_{cut} increases there are less pairs of clusters that satisfy equation 2.5 and, thus, the multiplicity of subjets decreases with increasing y_{cut}. In the limit of $y_{cut} = 1$ one obtains only one subjet which is the jet itself, since the requeriment $d_{ij} > \left(E_T^{jet}\right)^2$ was satisfied for the algorithm to reconstruct the given jet. For very small values of y_{cut} one would be able to resolve the individual hadrons if the detector had enough resolution.

The most interesting region is the intermediate region where the resolution scale is large enough for perturbation theory to be valid but small enough for accessing non-trivial values of multiplicity of subjets.

2.3.1 Subjet multiplicity

The mean subjet multiplicity in a QCD calculation at a fixed order depends on the number of partons that constitute the jet and the resolution scale y_{cut}. All partons inside the jet may be clustered together as well in a single subjet if the resolution scale y_{cut} is large, or all of them may be resolved into different subjets if y_{cut} is small enough. The mean subjet multiplicity is defined to be

$$\langle n_{sbj} \rangle = \frac{N_{jets}(sbj = 1) + 2N_{jets}(sbj = 2) + ...}{N_{jets}} = 1 + A_1\alpha_s + A_2\alpha_s^2 + ... \qquad (2.6)$$

At $\mathcal{O}(\alpha_s)$ one has two partons in the final state that may be clustered together by the jet definition. The non-trivial contribution to the subjet mutiplicity occurs

when the two partons are resolved into different subjets upon the re-application of the algorithm with the resolution parameter y_{cut}.

Given the recombination scheme used, the jet variables are given in terms of the subjet variables as

$$E_T^{jet} = E_T^{sbjet_1} + E_T^{sbjet_2} \tag{2.7}$$

$$\phi^{jet} = \frac{E_T^{sbjet_1}\phi^{sbjet_1} + E_T^{sbjet_2}\phi^{sbjet_2}}{E_T^{jet}} \tag{2.8}$$

$$\eta^{jet} = \frac{E_T^{sbjet_1}\eta^{sbjet_1} + E_T^{sbjet_2}\eta^{sbjet_2}}{E_T^{jet}}. \tag{2.9}$$

The two-body phase space $\{(E_T^{sbjet_1}, \eta^{sbjet_1}, \phi^{sbjet_1}), (E_T^{sbjet_2}, \eta^{sbjet_2}, \phi^{sbjet_2})\}$ can be parametrized in terms of the jet variables $\{E_T^{jet}, \eta^{jet}, \phi^{jet}\}$, the energy fraction $z = E_T^{sbjet_2}/\ (E_T^{sbjet_1} + E_T^{sbjet_2})$, the rescaled transverse momentum

$$y = k_\perp^2/(E_T^{jet})^2 = z^2\left[(\eta^{sbjet_1} - \eta^{sbjet_2})^2 + (\phi^{sbjet_1} - \phi^{sbjet_2})^2\right]$$

and ψ, an angle defined in the $\eta - \phi$ plane [23]. The quantity $k_\perp$ is the transverse momentum of subjet 2 relative to subjet 1 and it is assumed that $E_T^{sbjet_1} > E_T^{sbjet_2}$. This quantity must be greater that $\sqrt{y_{cut}}E_T^{jet}$ for the two subjets to be resolvable. With these definitions, the following relations hold:

$$E_T^{sbjet_1} = (1-z)E_T^{jet}, \tag{2.10}$$

$$\phi^{sbjet_1} = \phi^{jet} + \sqrt{y}sin\psi \tag{2.11}$$

$$\eta^{sbjet_1} = \eta^{jet} + \sqrt{y}cos\psi \tag{2.12}$$

$$E_T^{sbjet_2} = zE_T^{jet}, \tag{2.13}$$

$$\phi^{sbjet_2} = \phi^{jet} - \sqrt{y}sin\psi\frac{1-z}{z}, \tag{2.14}$$

$$\eta^{sbjet_2} = \eta^{jet} - \sqrt{y}cos\psi\frac{1-z}{z}. \tag{2.15}$$

The kinematic limits that the resolvability of the two subjets imposes are

$$0 < \psi < 2\pi \tag{2.16}$$

$$y_{cut} < y < 1/4 \tag{2.17}$$

$$\sqrt{y} < z < 1/2 \tag{2.18}$$

Using the above parameterizations and kinematic limits, one is able to perform theoretical calculations on the number of subjets produced. For example, the two-

subjet fraction $N_{jets}(sbj = 2)/N_{jets} = R_2$ is the ratio of the cross section of two-parton production in the particular case that the two final-state partons are resolved into two subjets at a given y_{cut} over the cross section of inclusive jet production:

$$R_2 = \frac{d\sigma^{2subjets}}{d\sigma^{jet}}$$

This can be calculated numerically with the two-body phase-space parameterization given above.

In general, one finds that the probability of finding a n-subjet event goes like $P_n \sim \alpha_s^{n-1}$. At small y_{cut} the leading term at the order α_s^m, where $m \geq n-1$, is $ln^{2m}y_{cut}$. These leading logarithmic terms must be summed to all orders in α_s for the perturbative approach to make sense. The next-to-leading logarithms ($ln^{2m-1}y_{cut}$) must also be taken into account to have a result which is of leading-order accuracy, since each extra power of α_s contributes with two logarithms. These extra next-to-leading logarithms contain essential contributions from soft gluons that are radiated off the incoming partons, as shown in studies performed in the context of hadron collisions [25]. However, due to the lack of resummed calculations for the processes considered here, the studies have been limited to sufficiently large y_{cut} values so that a fixed-order calculation is precise enough.

Studies of subjet mutiplicity have already been performed by ZEUS [26, 27]. It was found that next-to-leading order QCD calulations were able to adequately describe the data and an extraction of α_s was made. Two of the main results are shown in Fig. 2.5, which depicts on one hand the number of jets that have a certain amount of subjets at different values of y_{cut} and on the other hand, the mean subjet multiplicity as a function of y_{cut} for inclusive jet production; for comparison, NLO QCD calculations are also shown. The data sample of these studies consists of jets reconstructed in the laboratory frame with $E_T^{jet} > 15$ GeV and $-1 < \eta^{jet} < 2$ in a NC DIS sample with $Q^2 > 125$ GeV^2.

In the analyses presented here, distributions in the subjet variables are investigated and the topology of subjets is studied by means of normalised differential cross sections as functions of these subjet variables. The next chapter presents an outline of the measurements performed.

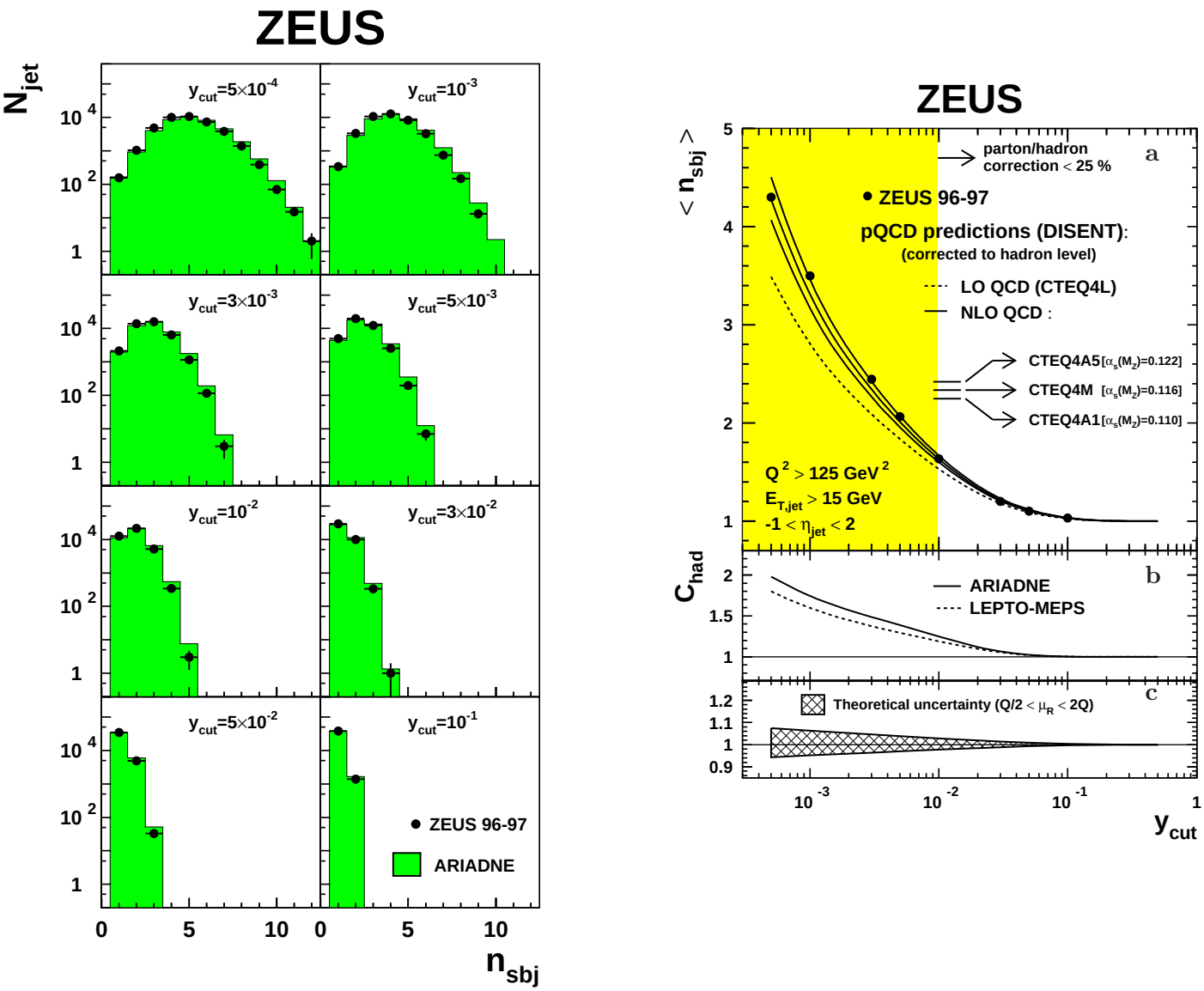

Figure 2.5: **Left**: Distribution of the number of subjets within a jet at different values of y_{cut} for an inclusive jet sample. **Right**: a) The mean subjet multiplicity corrected to the hadron level $\langle n_{sbj} \rangle$, as a function of y_{cut} for inclusive jet production in NC DIS with $Q^2 > 125$ GeV^2, $-1 < \eta_{jet} < 2$ and $E_T^{jet} > 15$ GeV (dots). The NLO QCD calculations, corrected for hadronization effects and using $\mu_R = \mu_F = Q$, are shown for several sets of proton PDFs (solid lines). The LO QCD calculations are also shown (dashed line). b) The parton-to-hadron correction, C_{had}, used to correct the QCD predictions (ARIADNE, solid line; LEPTO-MEPS, dashed line). c) The relative uncertainty on the NLO QCD calculation due to the variation of the renormalisation scale.

Chapter 3

Description of the analyses

In this section, a short introduction to the analyses is presented. In both of them the topology of jets is studied by means of subjets, which were introduced in section 2.3. In the past, subjet physics has allowed the performance of several stringent tests of the validity of pQCD.

In the previous chapter, the basics of jet physics were covered. In particular, it was stated that jet studies constitute a testing ground for the predictions of pQCD since many of the characteristics of jets are derived from the details of parton physics. Measurements of jet production, determinations of α_s as well studies of the jet substructure have been performed confirming the predictive power of pQCD in a variety of contexts at HERA [16, 26, 28–46].

In the work presented here, the validity of pQCD to adequately describe the physics of jets is further put into test by studing the topology of high-E_T jets by means of subjets. This work goes beyond previous studies [26, 27], which focused on the average subjet multiplicity, by studying normalised differential cross sections with respect to subjet variables. In the first analysis presented here, jets with exacly two subjets are considered [47] and in the second one, those that have three subjets constitute the sample [48]. The aim is to investigate the extent up to which the substructure of jets is dictated by the pattern of parton radiation and whether specific features that characterise pQCD such as the color flow manifest themselves through correlations in the energy flow within a jet. For that purpose, subjets are considered and regions of phase space identified in which the subjets are closely related to the underlying emitted partons.

In both analyses, it is required that $Q^2 > 125$ GeV^2. Jets are reconstructed in the laboratory frame with the k_T-cluster algorithm. The jets are then required to satisfy $E_T^{jet} > 14$ GeV and $-1 < \eta^{jet} < 2.5$.

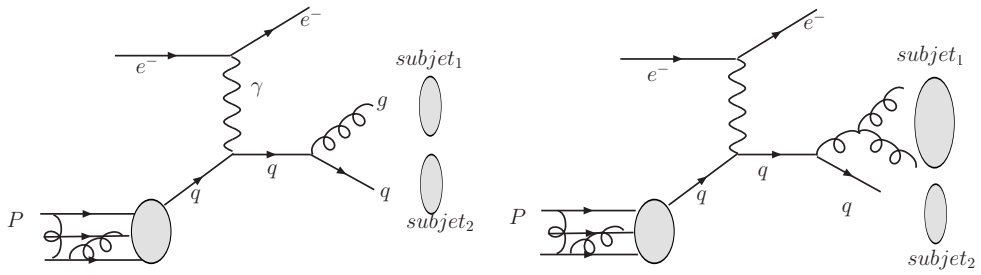

Figure 3.1: Feynman diagrams contributing to the production of jets with two subjets $\mathcal{O}(\alpha_s)$ (left) and $\mathcal{O}(\alpha_s^2)$ (right).

3.1 Two-subjet analysis

In this first analysis, the jets are required to have exactly two subjets at a value of $y_{cut} = 0.05$. A schematic representation of two of the contributing diagrams is shown in figure 3.1. There is no 'a priori' reason to choose this specific value of y_{cut}. The chosen value of y_{cut} is a compromise between several effects that go in opposite directions concerning their dependence with y_{cut}. Statistics and resolution increase as y_{cut} decreases, since one is able to resolve more subjets. However, when a jet is examined at very low y_{cut} values, the transition from the partonic state to the hadronic one may undergo significant changes which would yield sizeable hadronization corrections and would difficult the comparison of the corrected pQCD calculations with the data. After all, the hadronization correction is validated by the fact that the distributions look similar at both partonic and hadronic levels.

The variables used in this analysis are listed below:

- The fraction of the transverse energy of the jet carried by each subjet, E_T^{sbj}/E_T^{jet}.
- The difference between the pseudorapidity of each subjet and that of the jet, $\eta^{sbj} - \eta^{jet}$.
- The difference between the azimuthal angle of each subjet and that of the jet, $|\phi^{sbj} - \phi^{jet}|$.
- α^{sbj} is an angular variable defined in the $\eta - \phi$ plane as follows. It is the angle between the highest-E_T subjet and the proton beam direction, which is represented as a line of constant ϕ in the $\eta - \phi$ plane, as seen from the jet center's point of view. This is depicted in figure 3.2. This variable allows to test whether the phenomenon of color-coherence between initial and final states is present.

The variation of the subjet distributions with respect to the transverse energy of the jet, the jet's pseudorapidity, Q^2 and Bjorken x is also studied. One expects a

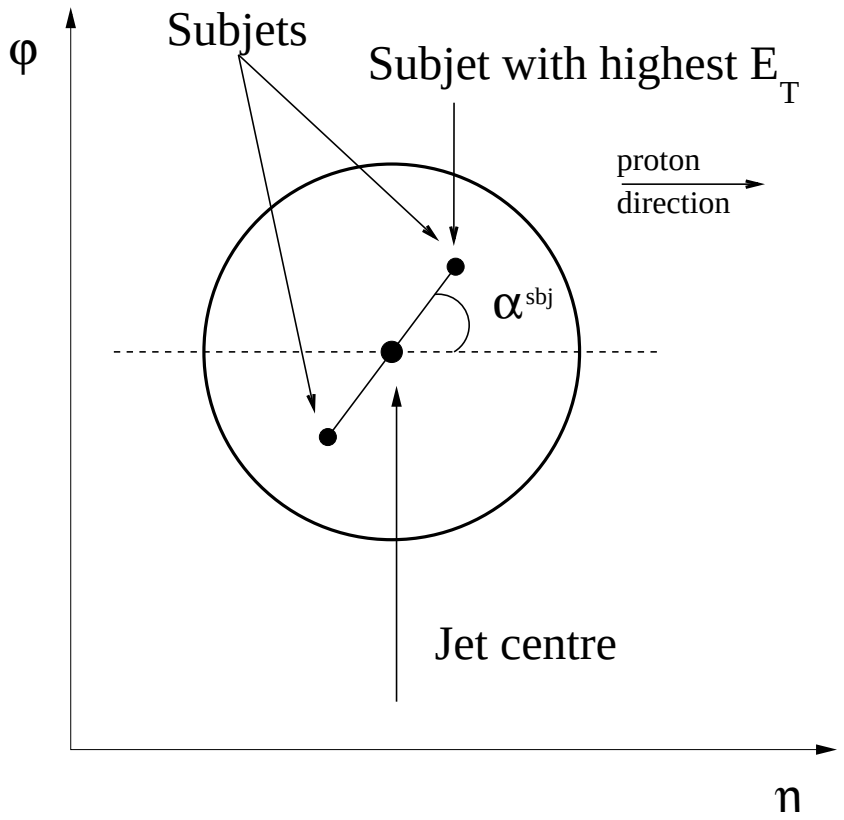

Figure 3.2: Schematic representation of α^{sbj}, the angle in the $\eta - \phi$ plane between the highest-E_T subjet and the proton beam direction as seen from the jet center.

small dependence with the energy scale since the splitting functions, which govern the evolution of the parton radiation, depend logarithmically on it.

The normalised differential cross sections are compared to the predictions of pQCD at next-to-leading order calculated with the program DISENT [49].

3.2 Three-subjet analysis

Jets with exactly three subjets are required for this second analysis. The value of y_{cut} chosen for this analysis is $y_{cut} = 0.01$. In order to resolve three subjets with sufficient statistics the value of y_{cut} had to be lowered to gain the necessary resolution. In this analysis, the four variables previously presented are also used and three more have been designed to study the pattern of QCD radiation. The entire set of variables considered is listed below:

- The fraction of the transverse energy of the jet carried by each subjet, E_T^{sbj}/E_T^{jet}.
- The difference between the pseudorapidity of each subjet and that of the jet, $\eta^{sbj} - \eta^{jet}$.

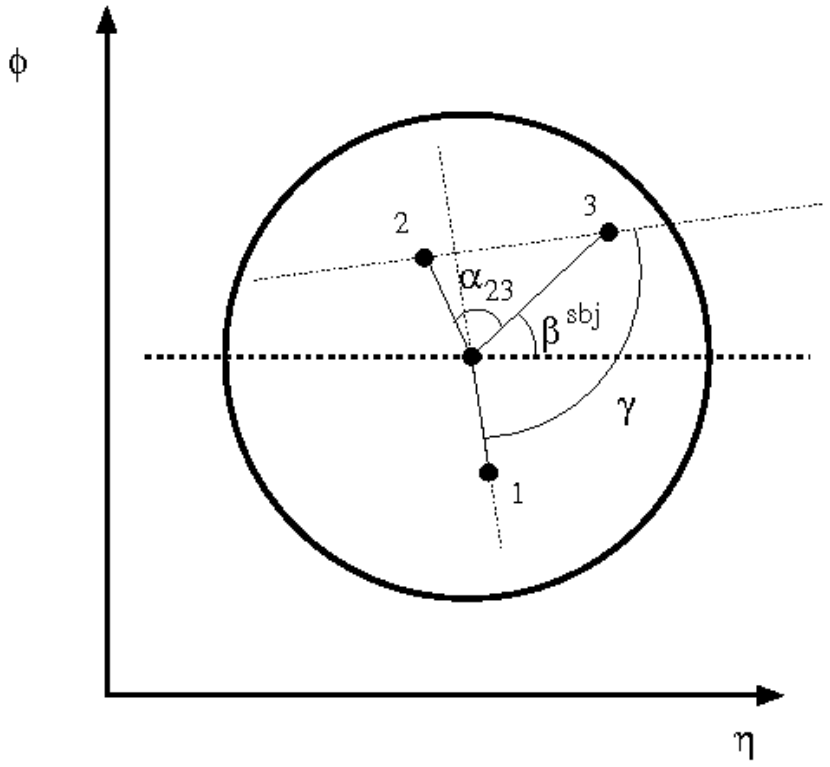

Figure 3.3: Schematic representation of the variables β^{sbj}, α_{23} and γ^{sbj}.

- The difference between the azimuthal angle of each subjet and that of the jet, $|\phi^{sbj} - \phi^{jet}|$.

- β^{sbj} is the angle in the $\eta-\phi$ plane between the lowest-E_T subjet and the proton beam direction as seen from the jet center (see figure 3.3).

- α_{23} is the angle in the $\eta - \phi$ plane between the two lowest-E_T subjets (see figure 3.3).

- γ^{sbj} is the angle in the $\eta - \phi$ plane between the highest-E_T subjet and the vector difference of the lowest-E_T subjets (see figure 3.3).

- The difference between the pseudorapidity of the lowest-E_T subjet and that of the jet, $\eta^{sbj}_{low} - \eta^{jet}$.

It should be noted that all the variables considered are invariant under longitudinal boosts along the beam axis.

The normalised differential cross sections are also compared to the predictions of pQCD at NLO, which have been performed in this case with the program NLOJET++ [50].

3.3 Color factors: LEP and HERA

In QCD, the color factors C_F, C_A and T_F (see section 1.5) represent the relative strengths of the processes $q \to qg$, $g \to gg$ and $g \to q\bar{q}$ and are a physical manifestation of the underlying group structure. The non-abelian character of the group $SU(3)$ induces the self-coupling of the gluons leading, in particular, to the appearance of the triple-gluon vertex (TGV).

Investigations of the color factors have been carried out at LEP (see, for example [51–61]) using angular correlations in four-jet events from Z° hadronic decays. Examples of Feynman diagrams contributing to four-jet production in Z° decays are shown in Fig. 3.4. The contributions of the diagrams shown in that figure are proportional to (a) $C_F C_A$, (b) $C_F C_F$ and (c) $C_F T_F$, respectively, independently of the underlying gauge symmetry making the four-jet cross section sensitive to the color factors. The best way to extract experimental information on the color factors is to study the angular correlations dictated by the helicity structure of the vertexes. The results of a direct extraction of the color factors at LEP [62] are shown in figure 3.5 and found to be consistent with the predictions of $SU(3)$.

At HERA, the effects of the different color configurations arising from the underlying gauge structure have been studied in three-jet production in NC DIS and photoproduction [15, 37]. These measurements provide complementary information to that already obtained in e^+e^- annihilation since they probe the gauge structure in a different environment, a hadron-induced reaction, and are sensitive to new color configurations. The results show that the data are best described by the admixture of color configurations predicted by $SU(3)$. The measured normalised differential cross sections as functions of several angular variables for three-jet production in the Breit frame of NC DIS are shown in figure 3.6 and are compared with lowest-order calculations based on different gauge-symmetry groups.

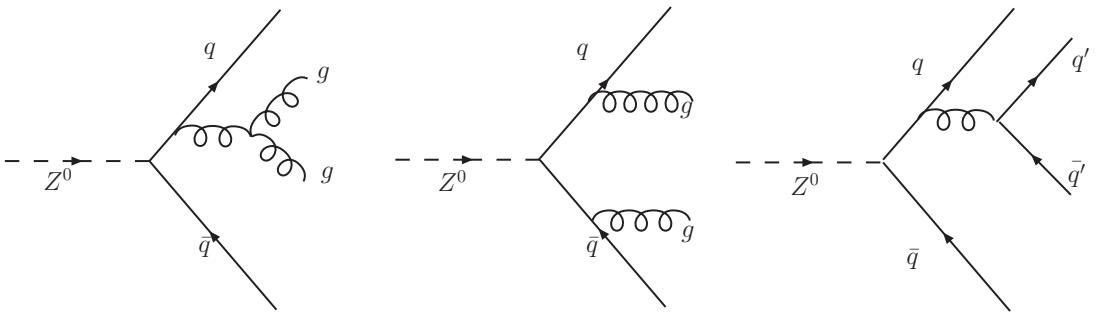

Figure 3.4: Examples of Feynman diagrams contributing to four-jet production in Z° decays.

The cross section for the production of jets with three subjets in NC DIS is also

sensitive to the color factors C_F, C_A and T_F. Therefore, angular correlations between the subjets are expected to be sensitive to the different color configurations. The cross section for the production of jets with three subjets at $\mathcal{O}(\alpha_s^2)$ can be written as follows

$$\sigma_{ep\to 3 \text{ subjets}} = C_F C_F \cdot \sigma_A + C_F C_A \cdot \sigma_B + C_F T_F \cdot \sigma_C + T_F C_A \cdot \sigma_D, \tag{3.1}$$

where σ_A, ..., σ_D are the partonic cross sections for the different color configurations. Examples of Feynman diagrams contributing to the four color configurations are shown in figure 3.7: (A) double-gluon bremsstrahlung from a quark line, (B) the splitting of a virtual gluon into a pair of final-state gluons, (C) the production of a $q\bar{q}$ pair through the exchange of a virtual gluon emitted by an incoming quark, and (D) the production of a $q\bar{q}$ pair through the exchange of a virtual gluon arising from the splitting of an incoming gluon. Other possible diagrams and interferences correspond to one of the four configurations. It is worth noticing that both σ_B and σ_D contain contributions from the triple-gluon vertex, characteristic of QCD. It should also be noted that the $T_F C_A$ contribution, which arises from gluon-induced processes, is not present in e^+e^- annihilation.

In the program DISENT (see chapter 5), it is possible to calculate the predictions for each color configuration (σ_A, ..., σ_D) separately, so that predictions based on different groups can be obtained. The normalised differential cross sections as functions of the subjet variables for each color configuration also provide valuable information: different color configurations leading to significant differences in shape for the differential cross sections ensures good sensitivity to the color flow and that the choice of jet algorithm does not impose a significant bias.

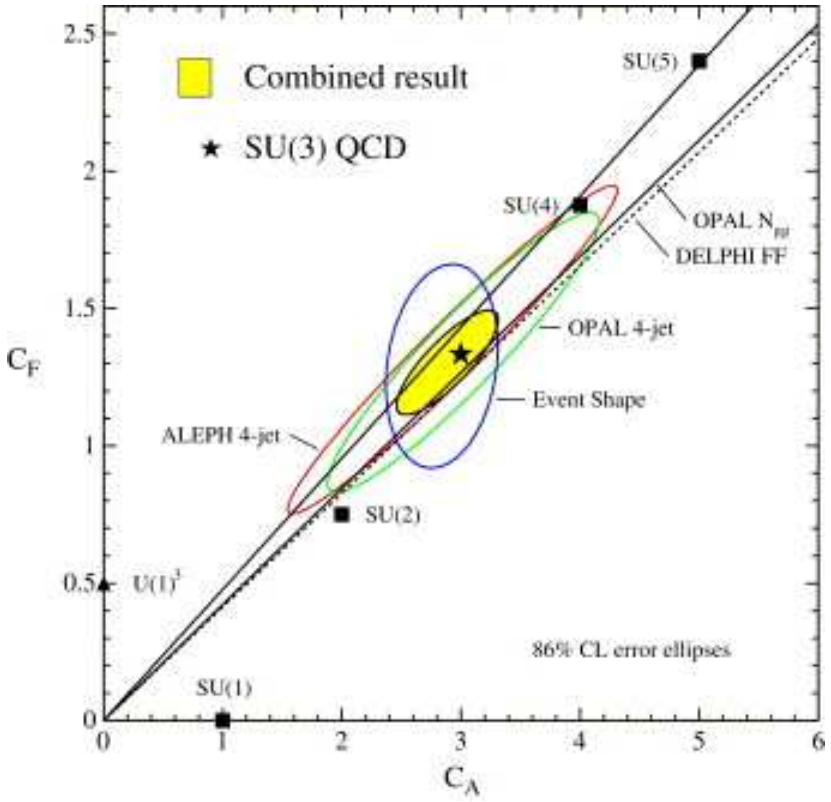

Figure 3.5: Combined result for the direct determination of the underlying symmetry of the strong interactions in e^+e^- annihilation at LEP using angular correlations in four-jet final states.

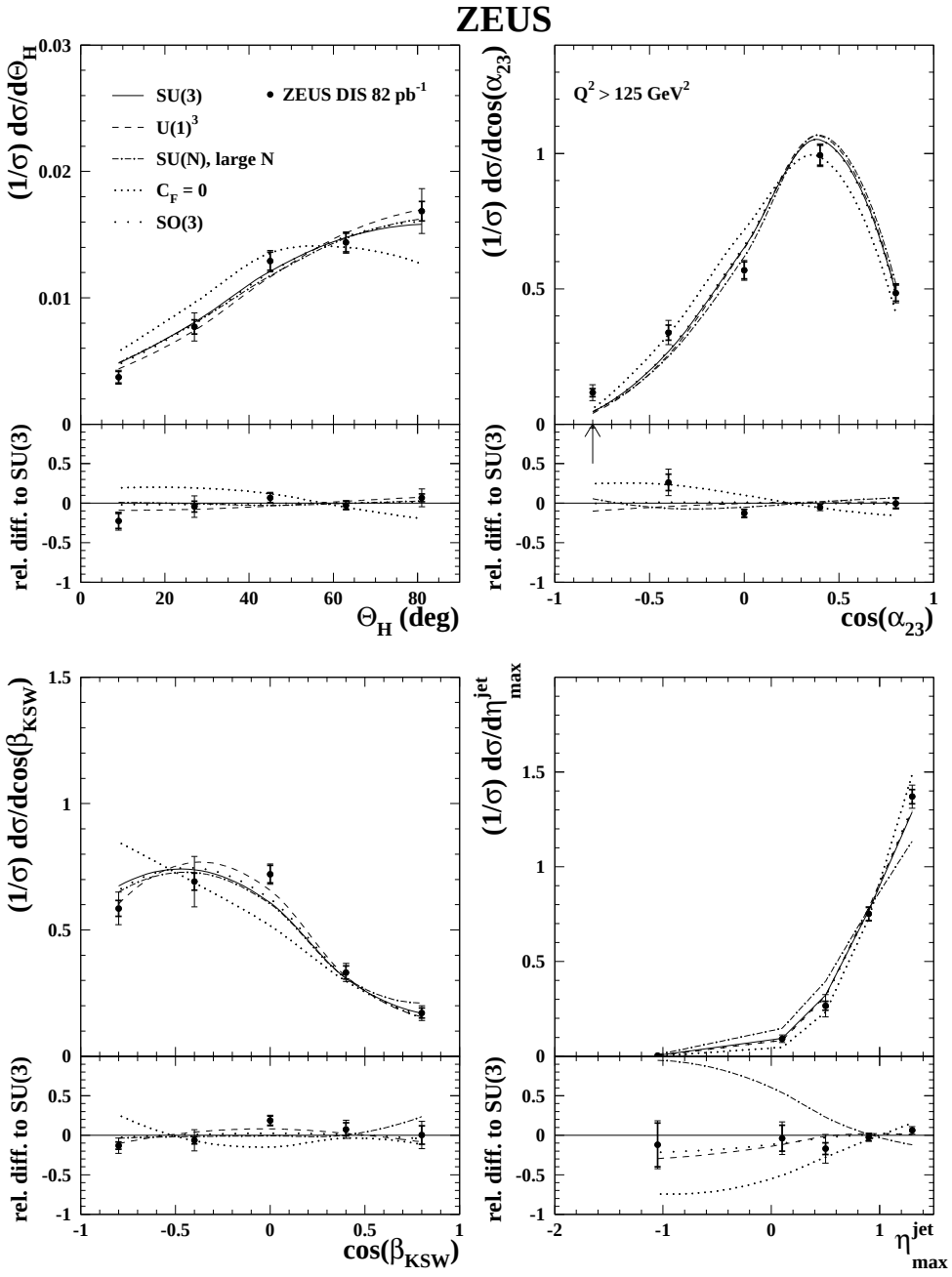

Figure 3.6: Measured normalized differential cross sections for three-jet production in NC DIS ep scattering at ZEUS (dots) integrated over $E_{T,B}^{jet1}$ GeV, $E_{T,B}^{jet2,3} > 5$ GeV and $-2 < \eta_{\mathrm{B}}^{\mathrm{jet}} < 1.5$ in the kinematic region given by $Q^2 > 125$ GeV^2 and $|\cos\gamma_h| < 0.65$ as functions of Θ_H, $\cos\alpha_{23}$, $\cos\beta_{ksw}$ and η_{max}^{jet}. The data points are plotted at the bin centers. For comparison, the $O(\alpha_s^2)$ calculations are shown for different symmetry groups. The lower part of the figures displays the relative difference to the calculations based on SU(3).

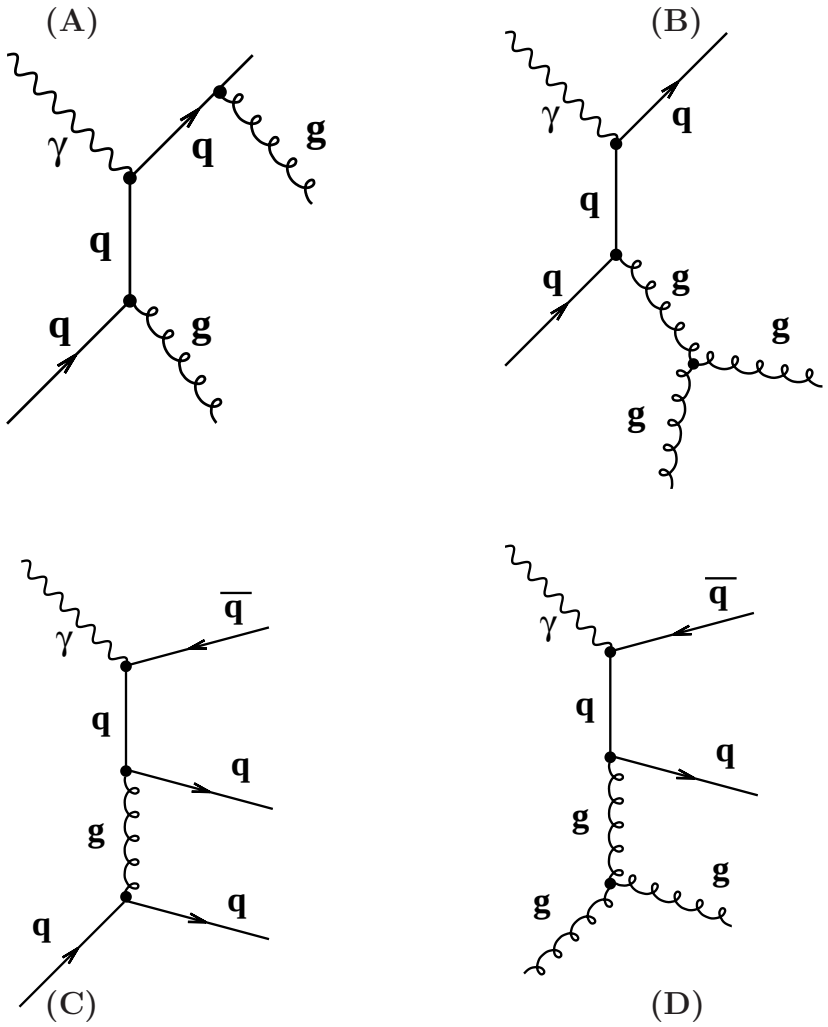

Figure 3.7: Examples of Feynman diagrams contributing to the production of jets with three subjets in NC DIS for each color configuration: (a) $C_F C_F$, (b) $C_F C_A$, (c) $C_F T_F$ and (d) $T_F C_A$.

Chapter 4

The HERA collider and the ZEUS detector

4.1 The Hadron Electron Ring Accelerator

Figure 4.1: Aerial view of DESY.

The HERA (Hadron Elektron Ring Anlage) collider is located at DESY in Ham-

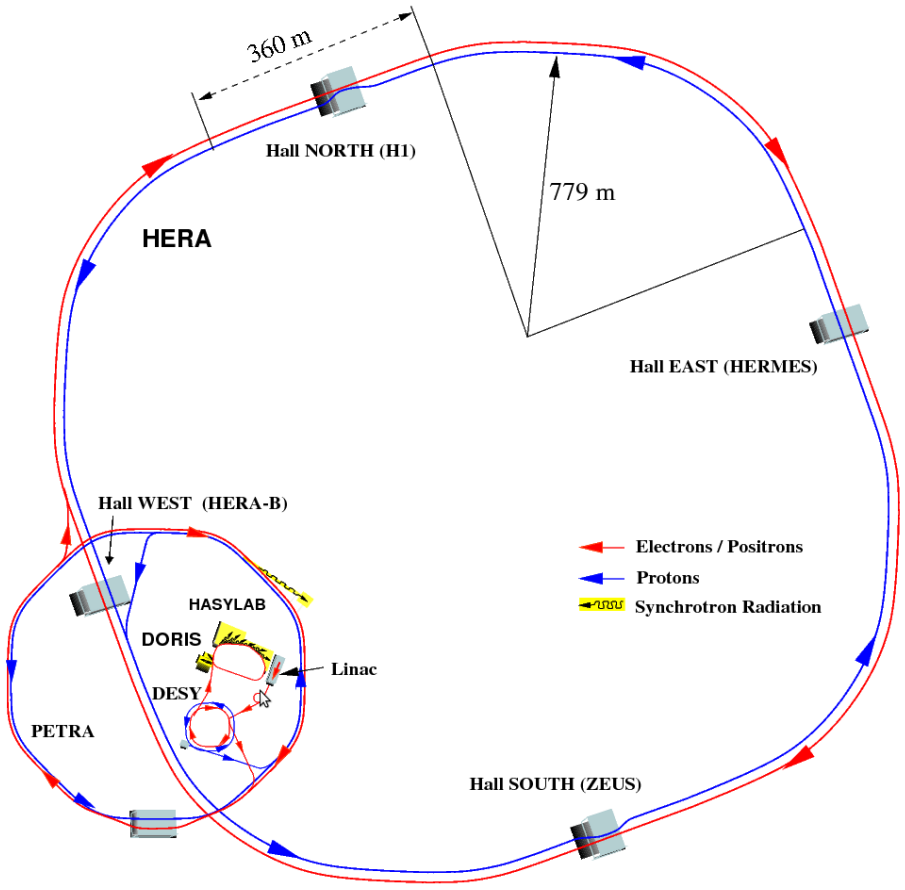

Figure 4.2: The HERA accelerator complex. Four experiments are located in the experimental halls: South (ZEUS), West (HERA-B), North (H1), and East (HERMES).

burg, Germany. It offers unique opportunities to explore the structure of the proton as it is the first *ep* collider in the world. Figure 4.1 shows an aerial view of DESY and the surrounding area including the location of the two largest accelerators HERA and PETRA.

HERA was approved in 1984 and first collisions were observed in 1991. Operations for physics started in 1992 and ended in 2007. HERA consists of one storage ring for protons and one for electrons. The design energy was 30 GeV for electrons and 820 GeV for protons. Each storage ring consists of four 90° arcs connected by 360 m long straight sections and is located (10–25) m below ground. Superconducting magnets are used for the proton storage ring. Four experimental halls (North, South, East, West) are situated in the middle of the straight sections. The two collider experiments, H1 and ZEUS, are located in the northern and southern experimental halls, respectively. In both interaction regions electrons and protons collided head-on at zero crossing angle. Two fixed-target experiments, HERMES

and HERA-B, have been installed in the eastern and western experimental halls, respectively. They made use of only the HERA electron (HERMES) and proton (HERA-B) beams, respectively. HERMES [63] is investigating the spin structure of the nucleon and HERA-B [64] aimed to study the $\mathcal{CP}$-violation in the $B^0\overline{B^0}$-system. Figure 4.2 shows the layout of the HERA collider, the four experimental halls and the system of pre-accelerators used at DESY. In a first step, electrons and protons were accelerated using linear accelerators. A small storage ring PIA (Positron-Intensity-Accumulator) was used in between the linear accelerator and DESY II to accumulate electrons until sufficient intensity was reached. In a next step, the particles were injected into DESY II (electrons) and DESY III (protons). After injection into PETRA and further acceleration, electrons and protons were injected into HERA. From 1995 to 1997 positrons were used instead of electrons because severe lifetime problems of the electron beam were observed. The reason was most likely the capturing of positively-charged dust which originated from ion getter pumps from the HERA electron vacuum system by the electron beam [65]. With the installation of new pumps in the winter shutdown 1997/1998 the problem was significantly reduced and HERA switched back to electrons in 1998.

The data used in the analysis of jets with two subjets presented here were collected during the running period 1998-2000, when HERA operated with protons of energy $E_p = 920$ GeV and electrons or positrons of energy $E_e = 27.5$ GeV, and correspond to an integrated luminosity of 81.7 ± 1.9 pb^{-1}, of which 16.7 pb^{-1} (65.0 pb^{-1}) was for e^-p (e^+p) collisions. In Fig 4.3 the integrated luminosity delivered by HERA and that collected by ZEUS as a function of time can be seen.

4.1.1 HERA II

Between 2000 and 2002, HERA underwent a luminosity upgrade, which was primarily achieved by installing focusing magnets which diminished the interaction area of the two beams in order to increase the luminosity. The periods before and after the upgrade are commonly referred to as HERA I and HERA II, respectively.

Since the upgrade, HERA was able to provide longitudinally-polarized electron/positron beams to the *ep* collision process. Polarisation at HERA is measured by two independent detectors, the Longitudinal Polarimeter (LPOL) and the Transverse Polarimeter (TPOL). The polarisation of the beam is basically obtained by measuring the asymmetry in the cross sections of a Compton scattering process between the lepton beam and a photon beam. This asymmetry is found to be proportional to the transverse polarisation P_Y and longitudinal polarisation P_Z of the lepton beam.

The lepton beam in the HERA storage ring can be transversely polarised though

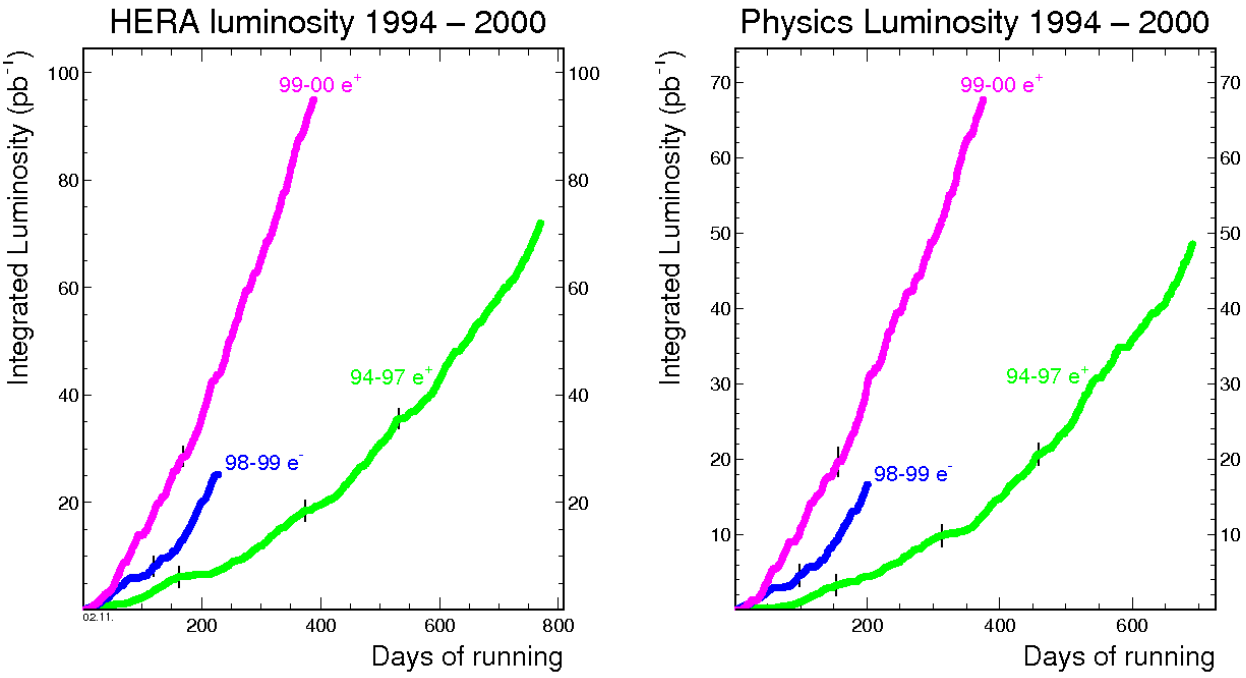

Figure 4.3: Integrated luminosity delivered by HERA in the different running periods (left plot) and the one taken with the ZEUS detector (right plot). The latter is used for physics analysis.

the Sokolov-Ternov effect: the leptons spins are naturally polarised transversely to the direction of motion due to the magnetic field that makes the leptons bend. Furthermore, the probabilities of spin flipping from up to down and from down to up are not equal, the probability of flipping from up to down is higher and, therefore, transverse polarisation grows with time until it reaches its maximum value. The spin rotators can change the lepton beam's spin from transverse to longitudinal and the longitudinal polarised lepton beam then collides with a proton beam at the ZEUS and H1 detectors (see Fig. 4.4). The polarisation of the lepton beam increases in time gradually according to the following formula:

$$P(t) = P_{max}(1 - e^{-t/\tau}), \tag{4.1}$$

where P_{max} is the asymptotic polarisation, τ is the build-up time and $P(0)$ is assumed to be 0. If the magnetic field is uniform in the storage ring, the asymptotic polarisation is:

$$P_{max} = P_{ST} = 92.4\%, \tag{4.2}$$

where P_{ST} stands for Sokolov-Ternov polarisation.

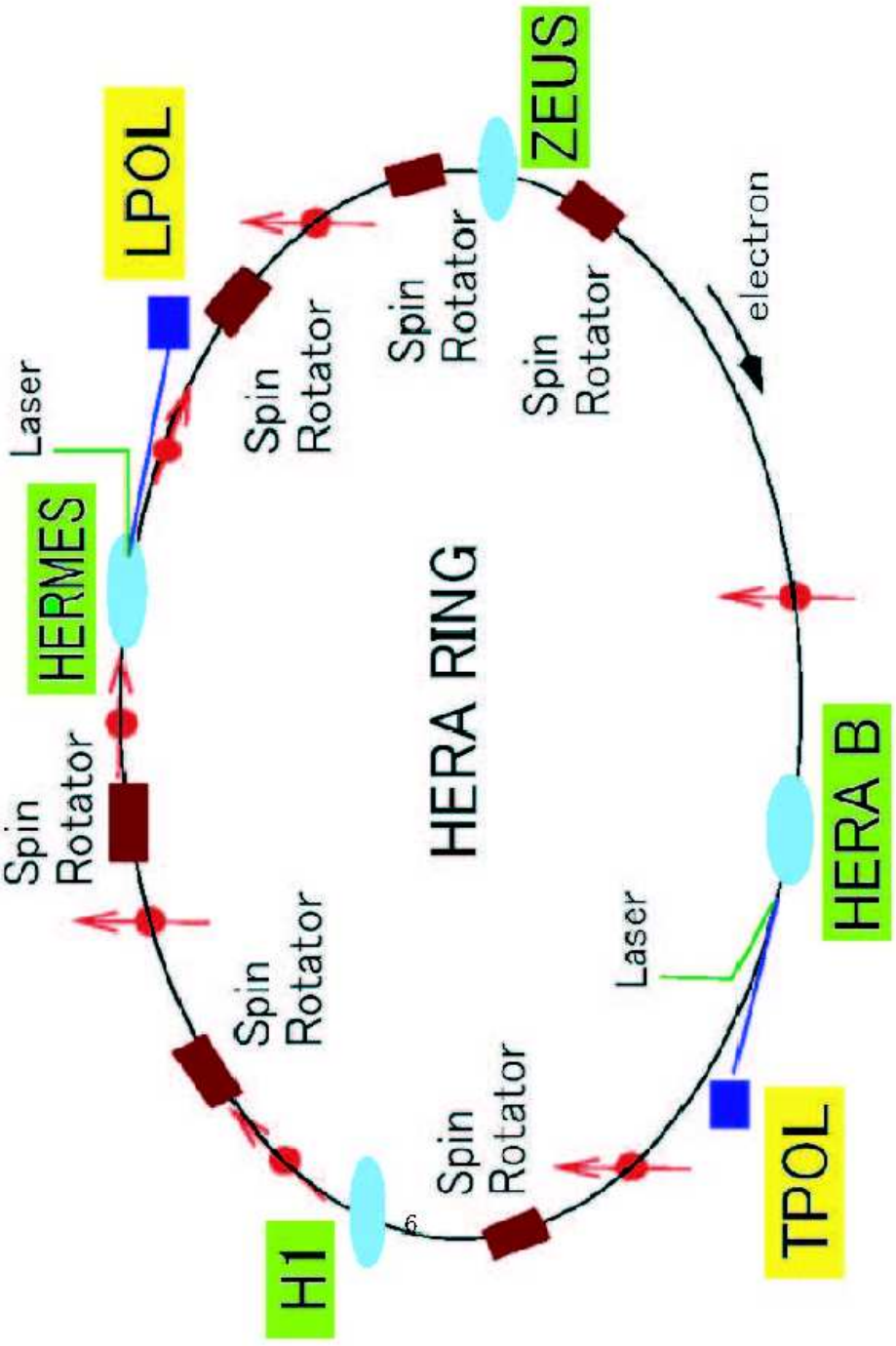

Figure 4.4: HERA Ring and polarisation instrumentation.

Parameter [Unit]	Electrons	Protons
Beam Energy [GeV]	27.5	920 (460)
Particles per bunch [10^{10}]	≤ 3.68	≤ 8.75
Number of bunches	184	180
Horiz./vert. Emittance[nm]	20/3	3.8/3.8
Bunch length [cm]	0.9	12
Vert./Hor. β at IP[cm]	26/62	18/245(36/490)
Beam Lifetime in collision	10-15	200
Longitudinal Polarisation [%]	30-45	-
Peak Luminosity	$5(1.5) \cdot 10^{31}$ cm^{-2} s^{-1}	
Average Luminosity	$1(0.25) \cdot$ pb^{-1}d^{-1}	

Table 4.1: HERA parameters in 2007.

However, this value can never be achieved due to some depolarisation effects, like magnet misalignments or non-uniform magnetic field. If these depolarisation effects are depicted as a constant τ_D, the asymptotic polarisation P_{max} deviates from P_{max} according to the expression:

$$P_{max} \;=\; P_{ST}\frac{\tau_D}{\tau_{ST}+\tau_D}, \tag{4.3}$$

where τ_{ST} is the Sokolo-Ternov build-up time needed to achieve P_{max}.

In addition, the build-up time τ can be written as:

$$\tau = \tau_{ST}\frac{\tau_D}{\tau_{ST}+\tau_D}, \tag{4.4}$$

At HERA, τ_{ST} is 37 minutes for the 27.5 GeV lepton beam.

The data used in the analysis of jets with three subjets presented here were collected during the HERA II running period and correspond to an integrated luminosity of 299.2 ± 7.8 pb^{-1}.

The HERA parameters from the 2007 runing period are given in Table 4.1.

4.2 The ZEUS Detector

The ZEUS detector [66, 67] is a general purpose magnetic detector designed to study various aspects of electron-proton scattering. It has been in operation since 1992 until 2007 and consists of various sub-components to measure the hadrons and leptons in the final-state and, therefore, to characterize the final-state in terms of energy, direction, and type of the produced particles.

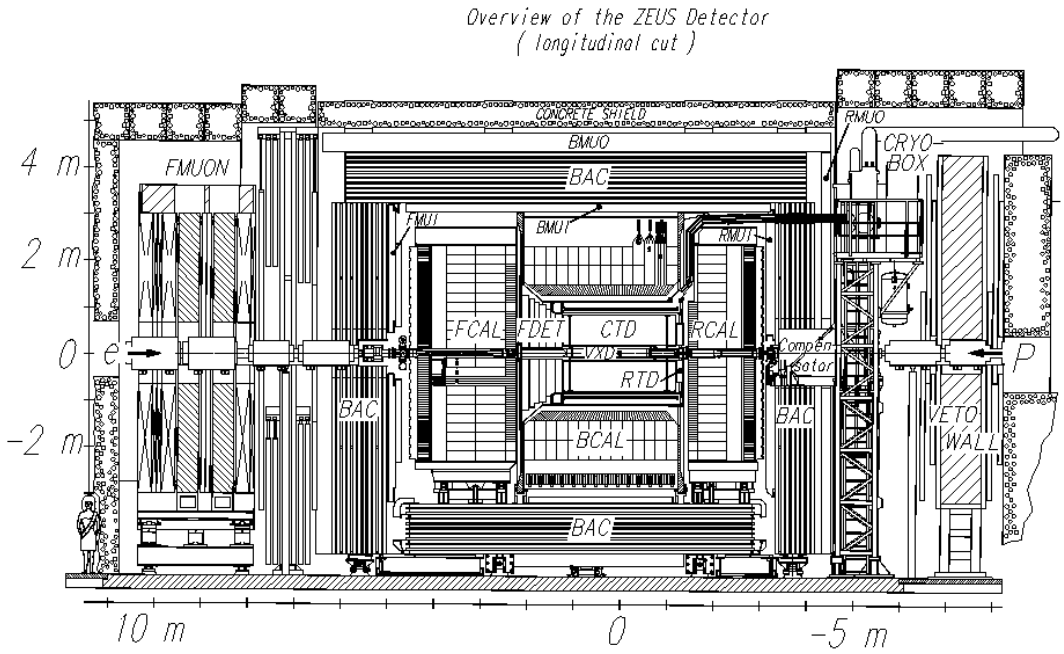

Figure 4.5: View of the ZEUS detector along the beam direction.

The coordinate system of the ZEUS detector is a Cartesian right-handed coordinate system. The origin ($(X, Y, Z) = (0, 0, 0)$) is located at the nominal interaction point. The Z-axis points in the proton beam direction, the Y-axis upwards, and the X-axis horizontally towards the center of HERA. The polar (azimuthal) angle θ (ϕ) is determined relative to the positive Z-axis (X-axis). With this definition the polar angle of the incoming electron beam is 180° and that of the incoming proton beam is 0°. The +Z-direction is referred as the *forward*, and the –Z-direction as the *backward* direction.

The ZEUS detector consists of the main detector located around the nominal interaction point and several small detectors positioned along the beam line in both positive and negative Z-directions. The main detector is shown in Figs. 4.5 and 4.6 along and perpendicular to the beam direction, respectively. The design is asymmetric with respect to the Z-axis because of the large forward-backward asymmetry of the final-state system. The difference in the energy of the electron beam (27.5 GeV) and proton beam (920 GeV) results in a center-of-mass system which is moving in the direction of the proton beam relative to the laboratory frame.

The inner part of the main detector consists of the tracking system enclosed by a superconducting solenoid which produces an axial magnetic field of 1.43 T. The CTD, a cylindrical drift chamber, surrounds the beam pipe at the interaction

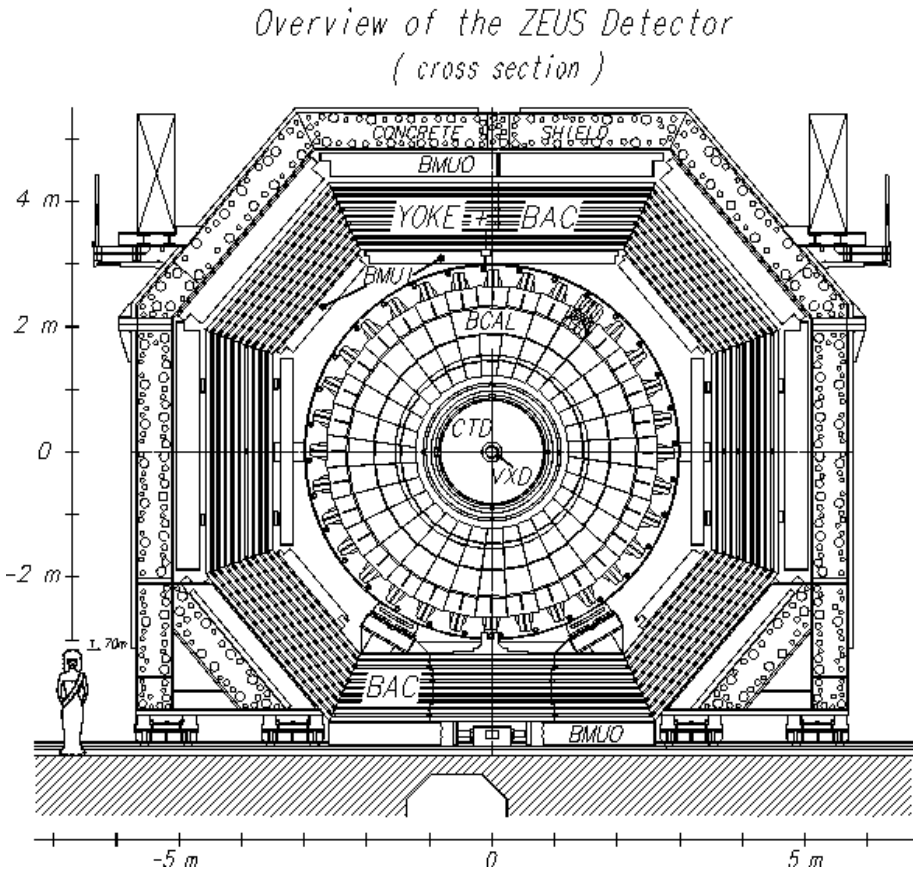

Figure 4.6: View of the ZEUS detector perpendicular to the beam direction. See text for a description of the components.

point. In order to provide additional means of track reconstruction in the forward (backward) direction, the CTD was supplemented by the FTD (RTD). The FTD consists of three sets of planar drift chambers with transition radiation detectors (TRD) in between. The RTD is one planar drift chamber with three layers. The vertex detector VXD measures the event vertex and possibly secondary vertices and improves the momentum and angular resolution of charged particles as determined with the CTD alone. In 1994 high voltage problems and damage due to synchrotron radiation caused part of the VXD to be off and it was removed. In 2001 a silicon microvertex detector (MVD) [68] was installed between the beampipe and the inner radius of the CTD. The MVD is organised into a barrel with three cylindrical layers and a forward section with four planar layers perpendicular to the HERA beam direction. The barrel contains 600 single-sided silicon strip sensors each having 512 strips of width 120 μm; the forward section contains 112 sensors each of which has 480 strips of width 120 μm.

The high resolution uranium calorimeter (UCAL) encloses the tracking detectors. It is subdivided into the forward (FCAL), barrel (BCAL), and rear (RCAL) parts.

The UCAL in turn is surrounded by an iron yoke made of 7.3 cm thick iron plates. The yoke serves two purposes: it provides a return path for the solenoid magnetic field flux and, in addition, is instrumented with proportional chambers. The latter design feature makes it possible to measure energy leakage out of the UCAL. The yoke is therefore referred to as the backing calorimeter (BAC). As the yoke is magnetized to 1.6 T by copper coils, it is used to deflect muons. In order to detect and measure the momentum of muons, limited streamer tubes are mounted surrounding the iron yoke in the barrel (BMUI, BMUO) and the rear (RMUI, RMUO) regions. As the particle density and the muon momentum in the forward direction is higher than in the barrel and rear directions due to the energy difference of the electron and proton beams, the muon chambers in the forward direction are designed differently. Limited streamer tubes mounted on the inside of the iron yoke (FMUI) and drift chambers and limited streamer tubes mounted outside the iron yoke (FMUO) are used for this purpose. Two iron toroids provide a toroidal magnetic field of 1.7 T. In the backward direction at $Z = -7.3\,\mathrm{m}$, a veto wall outside the detector composed of iron and scintillation counters is used to reject background events dominated by proton-beam-gas reactions.

4.2.1 The Central Tracking Detector

The tracking system of the ZEUS detector consists of the forward, central and rear tracking devices, which operate under a high magnetic field of 1.43 T to achieve a high resolution for high momentum tracks. All the tracking quantities used in this analysis are provided by the Central-Tracking Detector (CTD) [69–71]. The CTD is a cylindrical drift chamber which provides a high-precision measurement of the direction and transverse momentum of charged particles and of the event vertex. The position resolution in $r - \phi$ is about $230\,\mu$m and the transverse momentum resolution is

$$\frac{\sigma(p_t)}{p_t} = 0.0058 \cdot p_t(\mathrm{GeV}) \oplus 0.0065 \oplus \frac{0.0014}{p_t}\,, \tag{4.5}$$

where the first term corresponds to the resolution of the hit positions, the second term to smearing from multiple scattering within the CTD and the last term to multiple scattering before the CTD. The position of the interaction point in X and Y is measured with a resolution of 0.1 cm and in Z with a resolution of 0.4 cm.

The CTD is filled with a mixture of argon, CO_2 and ethane. Particle identification is possible by measurements of the mean energy loss dE/dx of charged particles within the tracking detector. The CTD covers a polar angle of $15° < \theta < 164°$ and the full range of the azimuthal angle ϕ. Its active volume has a length of 205 cm, an inner radius of 18.2 cm, and an outer radius of 79.4 cm.

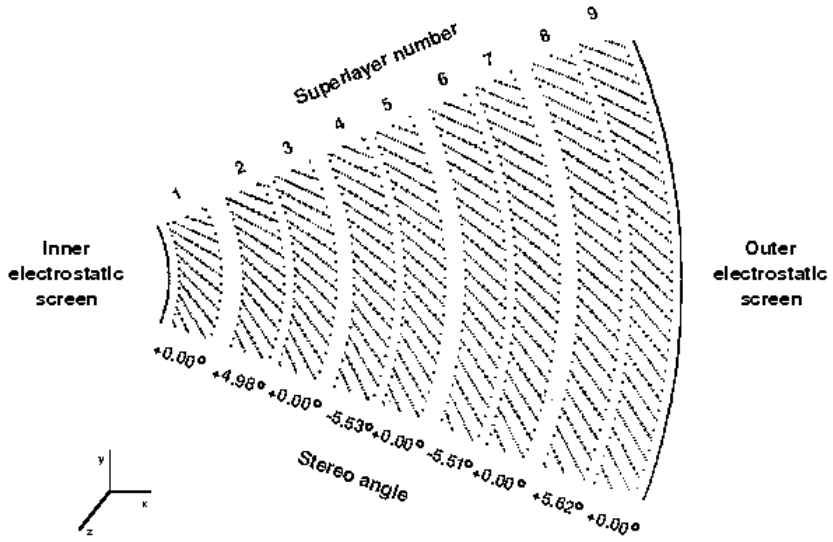

Figure 4.7: Layout of a CTD octant. Each octant has nine superlayers with the even numbered ones declined with respect to the beam axis ('Stereo angle').

The CTD is designed as a multi-cell superlayer chamber and subdivided into eight sections and nine superlayers. One octant is shown in Fig. 4.7. The CTD consists of 576 cells with each cell being equipped with eight sense wires. The number of cells increases from 32 in the innermost superlayer to 96 cells for the outermost superlayer. Every other superlayer has its sense wires rotated by a certain angle with respect to the beam axis. The angles for each superlayer are given in Fig. 4.7. With this configuration, the Z position of a track can be reconstructed with an accuracy of aproximately 2 mm.

4.2.2 The Uranium-Scintillator Calorimeter (UCAL)

Calorimeters in particle physics measure the energy of particles by their absorption in a medium that becomes ionized or excited through shower processes. The ZEUS calorimeter (UCAL) has been designed as a sampling calorimeter, where absorber layers alternate with scintillator layers, which are the optical readout. The calorimeter is required to be hermetic with a nearly full solid-angle coverage and to have a good hadronic energy resolution by achieving an equal response to electromagnetic and hadronic particles.

The UCAL is divided into three parts, which cover different polar angles [72–75]. All parts of the calorimeter, FCAL ($2.2° < \theta < 39.9°$), BCAL ($36.7° < \theta < 128.1°$), and RCAL ($128.1° < \theta < 176.5°$) are built of alternating layers of 3.3 mm thick depleted uranium and 2.6 mm thick plastic scintillator plates (SCSN38). The natural

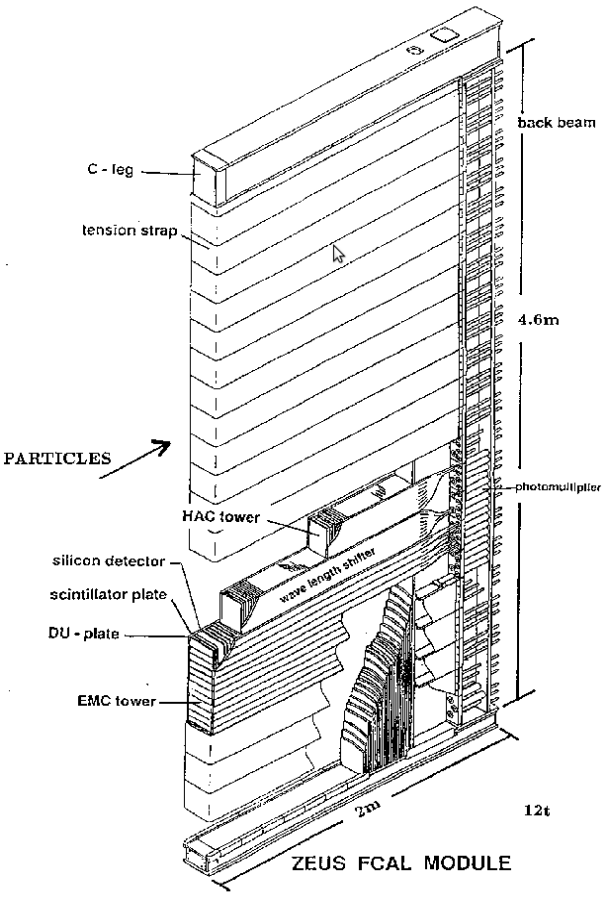

Figure 4.8: Layout of a FCAL module. The UCAL modules are subdivided into one electromagnetic (EMC) and two hadronic (HAC1, HAC2) sections, which in turn are divided into cells. A cell is read out on two opposite sides by one wavelength shifter each.

radioactivity of ^{238}U is used as a reference signal to calibrate the readout channels to a precision of $< 0.2\%$.

Uranium is an advantageous absorber for hadron calorimetry, since it provides a high yield of spallation neutrons which impart the energy to the hydrogen nuclei of the scintillator. Together with an additional contribution of photons from neutron capture of the uranium, this helps to compensate the signal loss of hadrons arising from the loss of binding energy, nuclear fission fragments and from undetected decay products. Electrons and photons do not suffer such losses as they interact predominantly with the atomic electrons and not with the nuclei. The ratio between the pulse heights of electrons and hadrons, e/h, which has been achieved is

$$e/h \;=\; 1.00 \;\pm 0.03 \tag{4.6}$$

The three calorimeter parts are subdivided into modules. The modules are

transversally separated into towers, and the towers in turn longitudinally into electromagnetic (EMC) and hadronic sections (HAC). The design of an FCAL module is shown in Fig. 4.8. The FCAL and RCAL modules are planar and perpendicular with respect to the beam axis (see Fig. 4.5), while the BCAL modules are wedge-shaped and projective in the polar angle. The calorimeter modules are further segmented into cells. The cell dimensions are 20cm×20cm for hadronic cells and 5cm×20cm (10cm×20cm) for electromagnetic cells in the FCAL and BCAL (RCAL). The design of the three calorimeter parts takes into account the different particle densities and energies due to the asymmetric electron and proton beam energies. Each EMC section is segmented transversally into four cells (two in RCAL), while a HAC tower is not divided transversally. They are instead longitudinally subdivided into two (one in RCAL) hadronic cells (HAC1, HAC2). Each cell is read out on two opposite sides. This is done on each side by a wavelength shifter coupled to one photomultiplier tube. The information of both photomultiplier tubes is used to provide a limited reconstruction of the position of the measured particle and to check the uniformity of the readout.

The single particle energy resolution for electrons and hadrons was determined in test-beam experiments to be $\sigma_E/E = 0.18/\sqrt{E}$ and $\sigma_E/E = 0.35/\sqrt{E}$ respectively, where E is measured in GeV.

4.3 The luminosity measurement

The luminosity, $\mathcal{L} \equiv N/\sigma$, relates the number of events N with the cross section σ. A precise determination of the luminosity is essential for any cross section measurement in a high-energy physics experiment. The luminosity of ep-collisions at HERA is measured by observing the rate of hard bremsstrahlung photons from the Bethe-Heitler process $ep \to e\gamma p$ [76]. As the theoretical cross section is known to an accuracy of 0.5% from QED calculations, a precise measurement of the photon rate permits a precise determination of the ep-luminosity at HERA.

Figure 4.9 shows the layout of the HERA magnet system and the ZEUS luminosity detectors in the backward (–Z)-direction. In the case of ZEUS, this is done by two lead/scintillator electromagnetic calorimeters at Z = −34 m (LUMIE) and Z = −107 m (LUMIG). Photons with $\theta_\gamma < 0.5$ mrad originating from the Bethe-Heitler process $ep \to e\gamma p$ are detected by the LUMIG detector [77–79]. The energy resolution of the LUMIG detector was measured under test-beam conditions to be $18\%/\sqrt{E}$. It was also determined that the carbon/lead filter placed in front of the detector to shield it against synchrotron radiation degrades the resolution to $23\%/\sqrt{E}$. The impact position of incoming photons can be determined with a resolution of

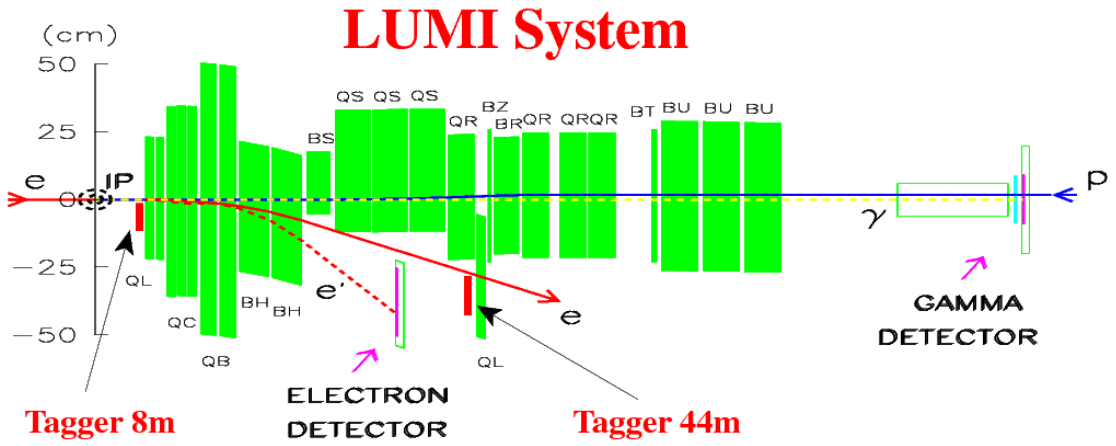

Figure 4.9: Location of ZEUS detectors in negative Z-direction. Shown are the gamma (LUMIG) and electron detectors (LUMIE) used for the luminosity measurement.

0.2 cm in X and Y, because at a depth of $7X_0$ 1 cm wide scintillator strips are installed within the LUMIG detector. The LUMIG detector is also used to determine the electron-beam tilt and to measure photons from initial-state radiation.

The LUMIE calorimeter [77–79] at Z = −35 m detects electrons in the limited energy range from 7 to 20 GeV which are produced under polar angles of less than 5 mrad with respect to the electron-beam direction. These electrons are deflected by the HERA magnet system and leave the beam pipe at Z = −27 m through an exit window similar to the one in front of the LUMIG detector. The LUMIE detector has an energy resolution of $18\%/\sqrt{E}$ under test-beam conditions. It was initially designed to measure the electrons of the Bethe-Heitler process $ep \to e\gamma p$ at the same time as the photons of this process are measured in the LUMIG detector. It was found that this was not necessary to have a precise measurement of the luminosity.

The system described above was modified by the addition of active filters in order to suppress the increased synchrotron radiation background of the upgraded HERA collider. Furthermore, a second system was added: a magnetic spectrometer arrangement [80]. A small fraction ($\sim$ 9%) of the small-angle energetic photons from the Bethe-Heitler process convert in the exit window of the vacuum chamber. Electron-positron pairs from the converted photons were bent vertically by a dipole magnet and detected in tungsten-scintillator calorimeters located above and below the photon beam at $Z = -104$ m. The advantage of the spectrometer system is that it does not suffer from pile-up (multiple interactions at high luminosity) and is not sensitive to direct synchrotron radiation, whereas the calorimeter system has higher acceptance. Figure 4.10 shows the integrated luminosity delivered by HERA (left) and collected by ZEUS (right) as a function of time for the HERA II period.

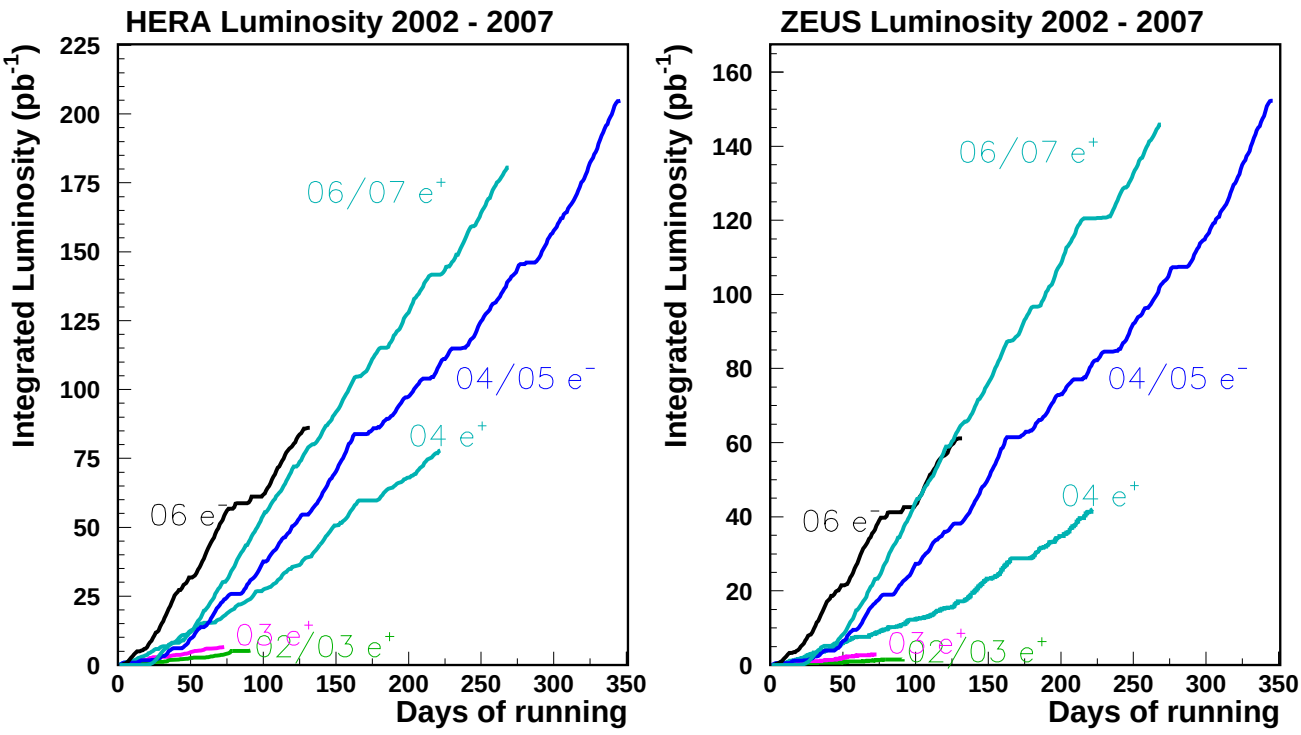

Figure 4.10: Integrated luminosity delivered by HERA in the different running periods (left plot) after the upgrade and the one taken with the ZEUS detector (right plot). The latter is used for physics analysis.

4.4 The ZEUS trigger and data acquisition systems

The short bunch crossing time at HERA of 96 ns, equivalent to a rate of about 10^7 crossings per second, is a technical challenge and puts stringent requirements on the ZEUS trigger and data acquisition systems. The total interaction rate, which is dominated by background from upstream interactions of the proton beam with residual gas in the beampipe, is of the order 10 - 100 kilo-events per second (10 - 100 kHz) while the rate of ep physics events in the ZEUS detector is of the order of a few Hz [81, 82]. Other background sources are electron-beam gas collisions, beam halo and cosmic events.

ZEUS employs a sophisticated three-level trigger system [67, 83] in order to select ep physics events efficiently while reducing the rate to a few Hz. A schematic diagram of the ZEUS trigger system is shown in Fig. 4.11.

The First Level trigger (FLT) is a hardware trigger, designed to reduce the input rate below 1 kHz. Each detector component has its own FLT, which stores the data in a pipeline, and makes a trigger decision within 2 μs after the bunch crossing. The decision from the local FLTs are passed to the Global First Level Trigger (GFLT), which decides whether to accept or reject the event, and returns this

decision readout within 4.4 μs. The typical information available at FLT are CAL activity (total transverse energy, missing transverse momentum,...), CTD tracks (number of tracks,...), hits in the muon chambers, etc.

If the event is accepted, the data is fully digitalized and transferred to the Second Level Trigger (SLT). The trigger signals at the SLT have a better resolution than those at the FLT. Moreover, some information is first available at the SLT like CAL timings, which are useful in rejecting non-*ep* background events. The SLT is designed to reduce the rates to the order of 50-100Hz. Each detector component has its own SLT, which passes a trigger decision to the Global Second trigger (GSLT) [84].

If the event is accepted by the GSLT, all detector components send their data to the Event Builder (EVB), which combines all the data of an event into a single record of ADAMO [85] database tables. This is the data structure on which the Third Level Trigger (TLT) code runs. The TLT is software based and runs part of the offline reconstruction code. It is designed to reduce the rate to a few Hz.

4.5 Event reconstruction and analysis

The scheme of the ZEUS offline and Monte Carlo (MC) simulation programs is shown in Fig. 4.12. Events from the real detector or simulated events are reconstructed by the program ZEPHYR, where the signals of the different components are calibrated and highly complex tasks, like tracking reconstruction, are performed. After processing the raw data, the user has access to the raw and reconstructed quantities via the program EAZE. In the framework of EAZE, the user writes his own analysis program in either Fortran or C. It is used to reconstruct relevant quantities and perform selection cuts. Subsets of the data or MC simulated events can be saved for further analysis. The program LAZE is an event-display program which allows graphical viewing of various aspects of an event including the tracks of charged particles in the CTD, energy depositions in the CAL, and other component-related quantities. To allow fast access to specific types of events during reconstruction, it is checked whether each event meets one of the conditions designed by the ZEUS analysis groups. If a specific condition is met, a flag called a DSTBIT is set. Before analyzing detailed component information in the user's EAZE program, the events can be preselected by requiring certain DSTBITS. This allows a faster loop over the whole data sets since only those events are processed further.

Simulated MC events are generated using the program AMADEUS (named ZDIS in previous versions) which contains a shell environment to steer a number of MC generator programs. The output data is stored in the same (ADAMO) format as the data from the real detector and passed to the ZEUS detector simulation program

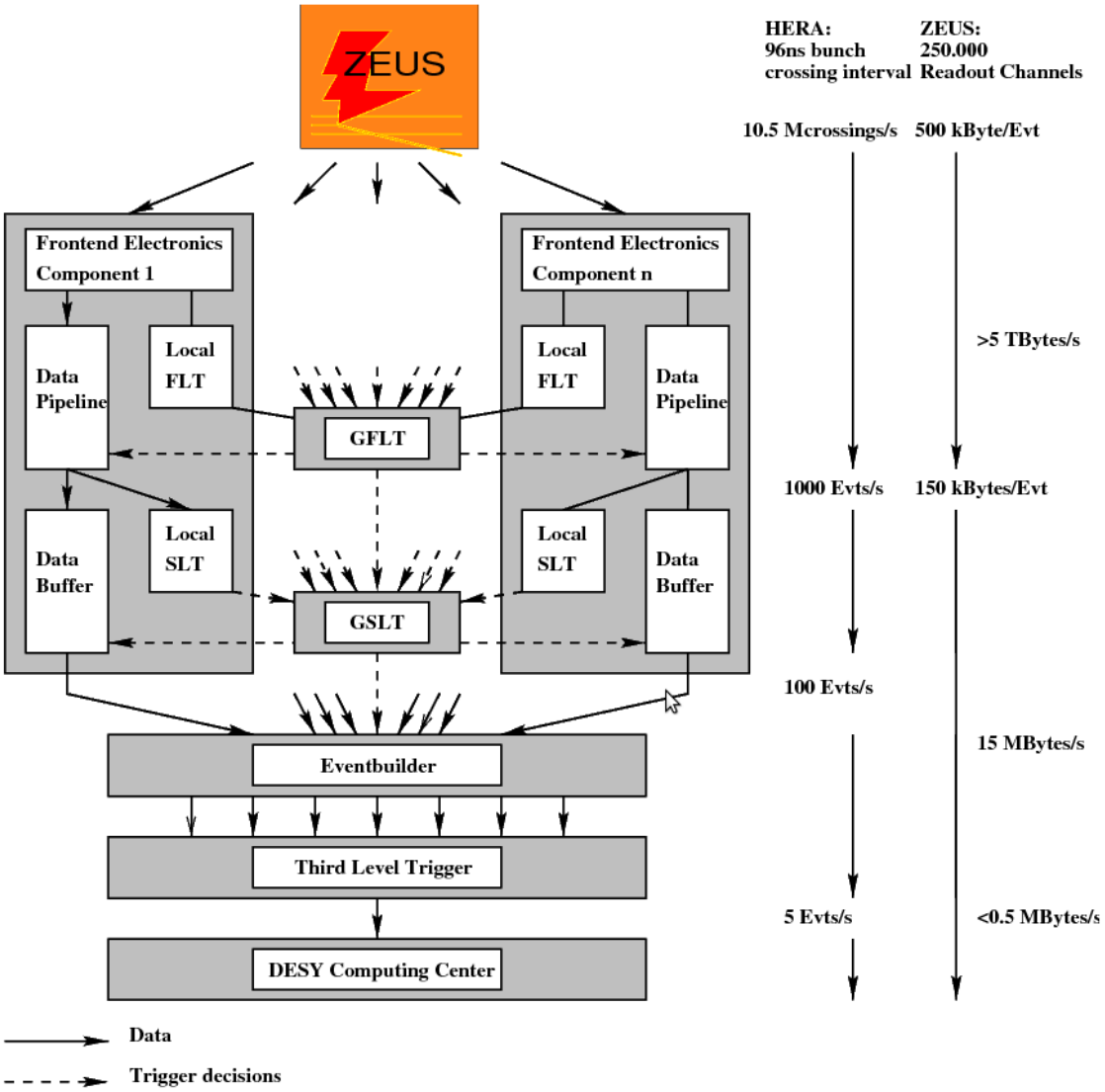

Figure 4.11: Schematic diagram of the ZEUS trigger and data acquisition systems.

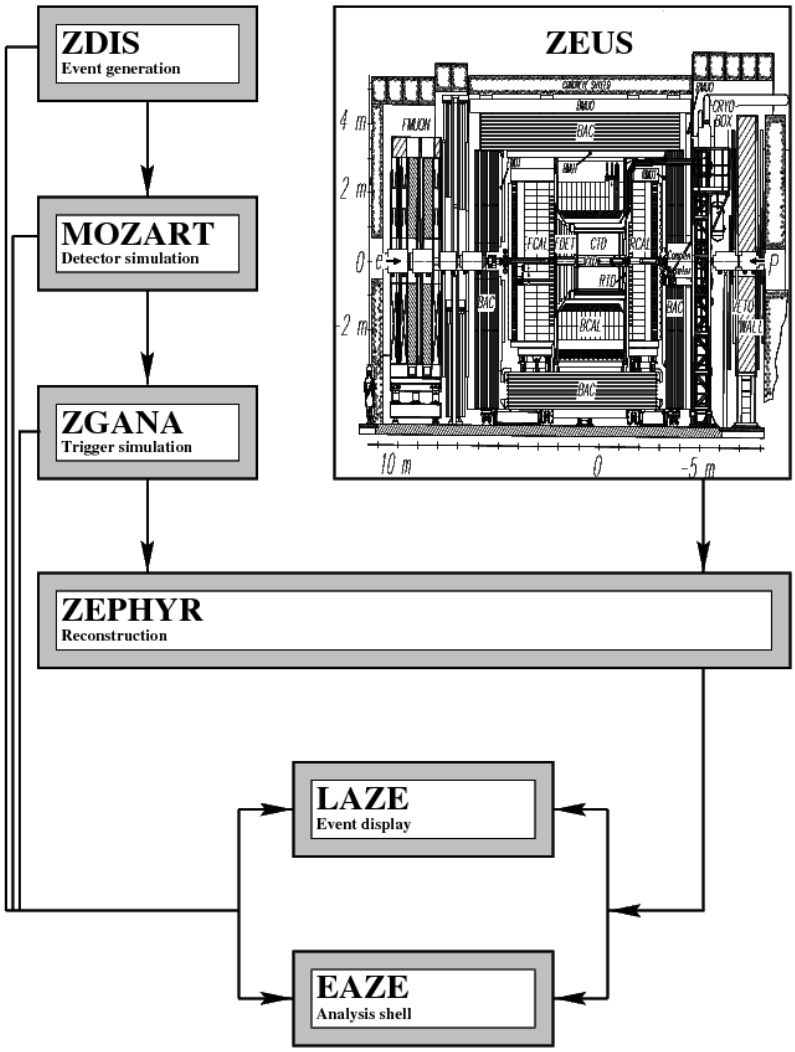

Figure 4.12: Interrelationship of the ZEUS offline and Monte Carlo (MC) simulation programs.

MOZART, based on the CERN GEANT program [86]. A simulation of the ZEUS trigger chain is done by the program ZGANA. Interfaces between the programs used for MC generation and the programs EAZE and LAZE provide specific MC information such as generated kinematic quantities, vertices and particles to the user. An overview of the physics analysis environment of the ZEUS experiment can be found in [87].

4.6 Event and detector simulation

In order to correct the data for trigger and detector effects, a full Monte Carlo simulation is required. This can be split in two pieces. First, an event generator, which calculates the scattering processes at hadron level from given matrix elements. Using hadronisation models, the final-state particles are obtained as a list of 4-vectors. This is what we mean by *generator-level*. In the second step, these particles are passed to a full simulation of the trigger and detector, yielding output in the form of ADAMO tables, which can be treated in the same way as the data. This is called *detector-level*.

Events from the event generator are processed by the MOZART package. This is a GEANT-based program which simulates the response of each detector component, based on the current knowledge of the ZEUS detector from both physics studies and test-beam results. Each particle interaction with dead material and detector component is simulated, including effects of digitization of the signals and known sources of noise. The ZGANA package simulates the trigger response to the event, based on the component signals, and the ZEus PHYsics Reconstruction (ZEPHYR) package performs the full offline reconstruction using all calibration constants. The Monte Carlo events simulated are then written in an identical format as the data taken with the ZEUS detector.

Chapter 5

Fixed-order pQCD calculations

5.1 Introduction

Theoretical predictions of QCD in its perturbative regime are compared with the measurements presented. The order in the expansion at which complete calculations are available is $\mathcal{O}(\alpha_s^3)$ for subjet analyses in ep scattering. For the two-subjet analysis, a calculation at $\mathcal{O}(\alpha_s)$, where one can have up to two partons in the final state, corresponds to the leading-order contribution to the process. The next order in the perturbative expansion, $\mathcal{O}(\alpha_s^2)$, includes virtual and real corrections to the two-parton final state and thus constitutes the next-to-leading order (NLO) contribution to the two-subjet analysis. All the diagrams involved in such calculations are available in the program DISENT [49].

For the three-subjet analysis, however, three partons in the final state such that they are reconstructed in a single jet with three subjets, can only occur at $\mathcal{O}(\alpha_s^2)$ and higher orders. Therefore, $\mathcal{O}(\alpha_s^2)$ constitutes the leading-order contribution to three-subjet production. The virtual and real corrections (i.e. up to four partons in a jet) to the LO process are available in the program NLOJET++ [50] and, thus, it was used to evaluate the pQCD calculations at NLO for the three-subjet analysis. A schematic representation of the preceeding discussion is shown in figure 5.1.

It is worth noting that, as indicated in section 2.1, the laboratory frame is the frame where one can have up to four partons in the same jet at order $\mathcal{O}(\alpha_s^3)$. In the Breit frame, one always has at least two jets back-to-back, which means that it cannot happen that in a four-parton final state all four partons are in the same jet, hence making it impossible to obtain predictions for the jet substructure at NLO in a three-parton final state.

The calculation of subjet cross sections involves the convolution of the partonic cross section and the proton PDFs, separated from one another by the factorization

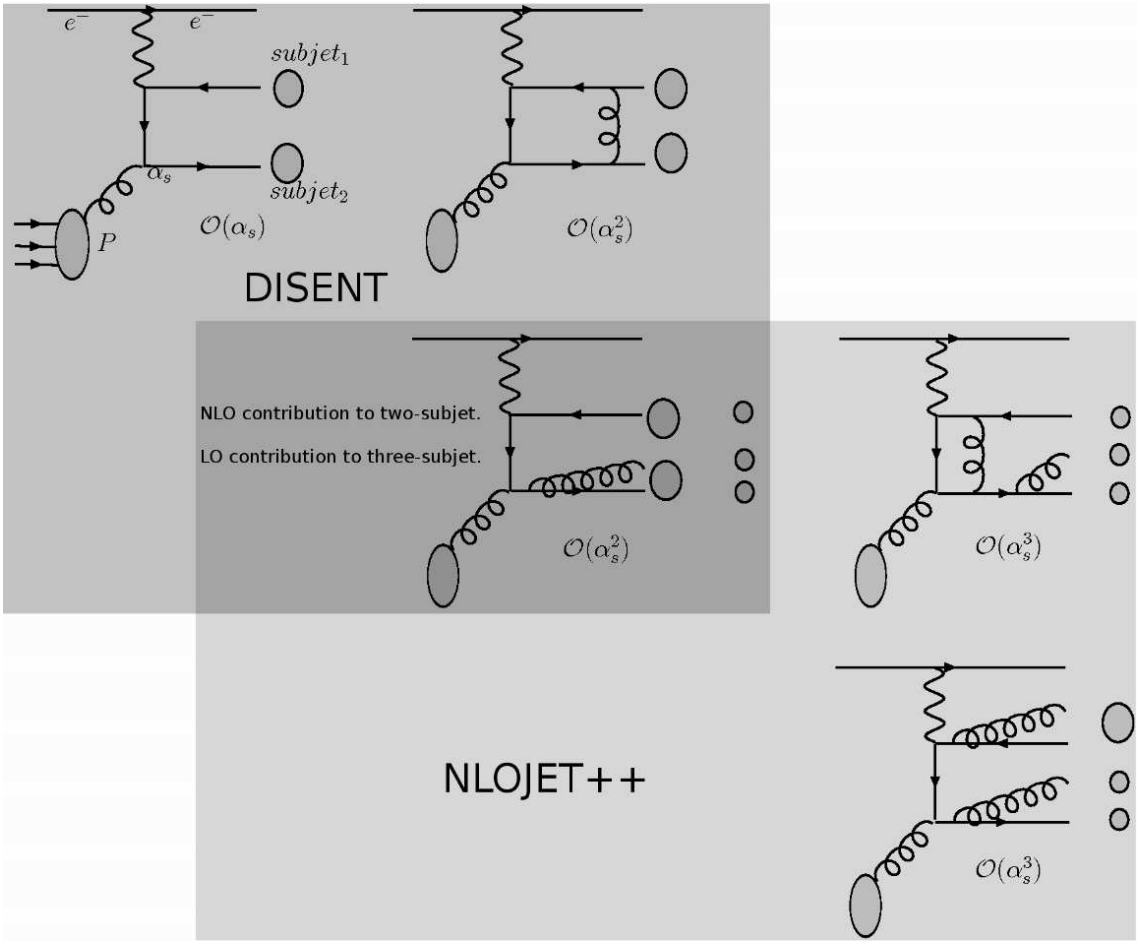

Figure 5.1: A schematic representation of the diagrams involved in the fixed-order pQCD calculations and the programs needed for each contribution. Diagrams with the same number of final-state partons are shown in the same row. Diagrams belonging to the same order in the perturbative expansion are drawn in the same column.

scale μ_F. The matrix elements are evaluated at the renormalization and factorization scales, μ_R and μ_F, which have to be set by hand by the user, who also has to provide the set of PDFs. In the present case the ZEUS-S PDFs [1] set was used. The choices of these inputs are not completely free, they carry an uncertainty due to the particular choices made.

The final stage of a fixed-order QCD jet-production calculation is a set of partons in the final state. Unlike non-strong-interacting particles, partons are expected to undergo a process of parton radiation and hadronization before they reach the detector and the modelling of this process is of tantamount importance to eventually perform a comparison between the data and the predictions, since this may give rise to a large correction to the topology of the event. This is accomplished by first complementing the fixed-order calculations with a simulation of the higher-orders

contribution to the jet production, leading to the 'parton cascade' picture mentioned in section 1.6.1. In these analyses, two different parton-cascade models have been used, the Color Dipole Model [88–91], as implemented in ARIADNE 4.08 [92, 93], and the matrix elements plus parton shower model of LEPTO 6.5 [94]. After the parton cascade is completed, the hadronization of the partons must be simulated. This is the process by which colored partons are transformed into colorless hadrons. The difficulty of this process lies on the non-perturbative effects involved, which are not fully understood. Only phenomenological models are available to generate the hadronic final state from the final-state partons. The hadronization does not change significantly the overall properties of the jet, such as the energy or the angular direction, since it is a process that happens at a soft energy of ~ 300 MeV, whereas in these analyses the transverse energy of the jets is at least 14000 MeV. The Lund String Model [95] and the Cluster Model [96] are the most important hadronization models available.

Understanding the effects and biases that arise as a consequence of the interaction with the detection device is also a key point to provide reliable measurements of physical quantities. A simulation of the detector has been developed for this purpose and it is interfaced with the event generators in such a way that the output of the simulation undergoes the same processing as the data. This is presented in chapter 6.

5.2 Theoretical predictions in pQCD

A program like DISENT does not solve equation 1.37 exactly. Instead, it generates pseudorandom events in the phase space and calculates various terms in the perturbative expansion, each with a specific weight. After convoluting each configuration with the PDFs, the total contribution to the cross section is obtained:

$$\sigma \sim \frac{1}{N} \sum_{\text{event}}^{N} \sum_{\text{j parton i}} f_i(\xi_j, \mu_{Fj}) \cdot \hat{\sigma}(\xi_j, Q_j^2, \alpha_s(\mu_{Rj}), \mu_{Rj}, \mu_{Fj}), \tag{5.1}$$

which approximates the exact solution in the limit $N \to \infty$. With DISENT, $5 \cdot 10^{10}$ events were enough to obtain a satisfactory statistical accuracy, while with NLOJET++, 10^{12} events were generated in order to get the same level of accuracy.

The k_T-cluster algorithm was applied to the partons in the final state in the same way as in the data and simulated events, and calculations for subjet observables were obtained.

The calculation of the matrix elements for each configuration is made internally in DISENT. The user, on the other hand, has to provide:

- The choice of factorization scale; for the analyses presented here, it was chosen

to be $\mu_F = \sqrt{Q^2}$.

- The choice of renormalization scale; it was also chosen to be $\mu_R = \sqrt{Q^2}$.
- The number of active flavors, which was set to five.
- The PDF set; the ZEUS-S parameterizations of the proton PDFs were used as default.
- The strong coupling constant, calculated at two loops, was set equal to that assumed in the determination of the proton PDFs, namely, $\alpha_s(M_Z) = 0.118$.

5.3 Two-subjet analysis

In Fig. 5.2 the next-to-leading order ($\mathcal{O}(\alpha_s^2)$) calculations of the normalised differential cross sections as functions of the variables described in section 3.1 are shown for the two-subjet analysis. These are the partonic predictions and cannot be directly compared with the data. As already mentioned, the jets in the calculations are jets of partons. Figure 5.3 shows the prediction for quark-induced ($eq \to eqg$) and gluon-induced ($eg \to eq\bar{q}$) subprocesses separately. It is observed that the shapes of the distributions for quark- and gluon-induced subprocesses are different, which means that the distributions are sensitive to the details of the pattern of parton radiation.

5.4 Three-subjet analysis

In Figs. 5.4 and 5.5 the corresponding distributions are shown for the three-subjet analysis. In section 3.3 it was shown that the cross section for the production of jets with three subjets can be expressed, at leading order, as a combination of four color configurations (see equation 3.1). In figures 5.6 and 5.7 the normalised differential cross section for each of these configurations is shown. The fact that different color contributions exhibit significantly different shapes shows that there is a good sensitivity to the underlying color dynamics and hence to the specific details of the parton radiation. This is indeed observed in the aforementioned figures. For example, in Fig. 5.6(a), the distribution of the color configuration B grows very signficantly from the first bin to the second, while that of D exhibits a monotonic decrease. In figure 5.6(d) the shapes of the distributions for the configurations B and D are very different. One of the most dramatic examples is shown in Fig. 5.7(c), in which the distribution of configuration B peaks at $\eta_{low}^{sbj} - \eta^{jet} \approx -0.7$ while that for D peaks at $\eta_{low}^{sbj} - \eta^{jet} \approx 0.5$.

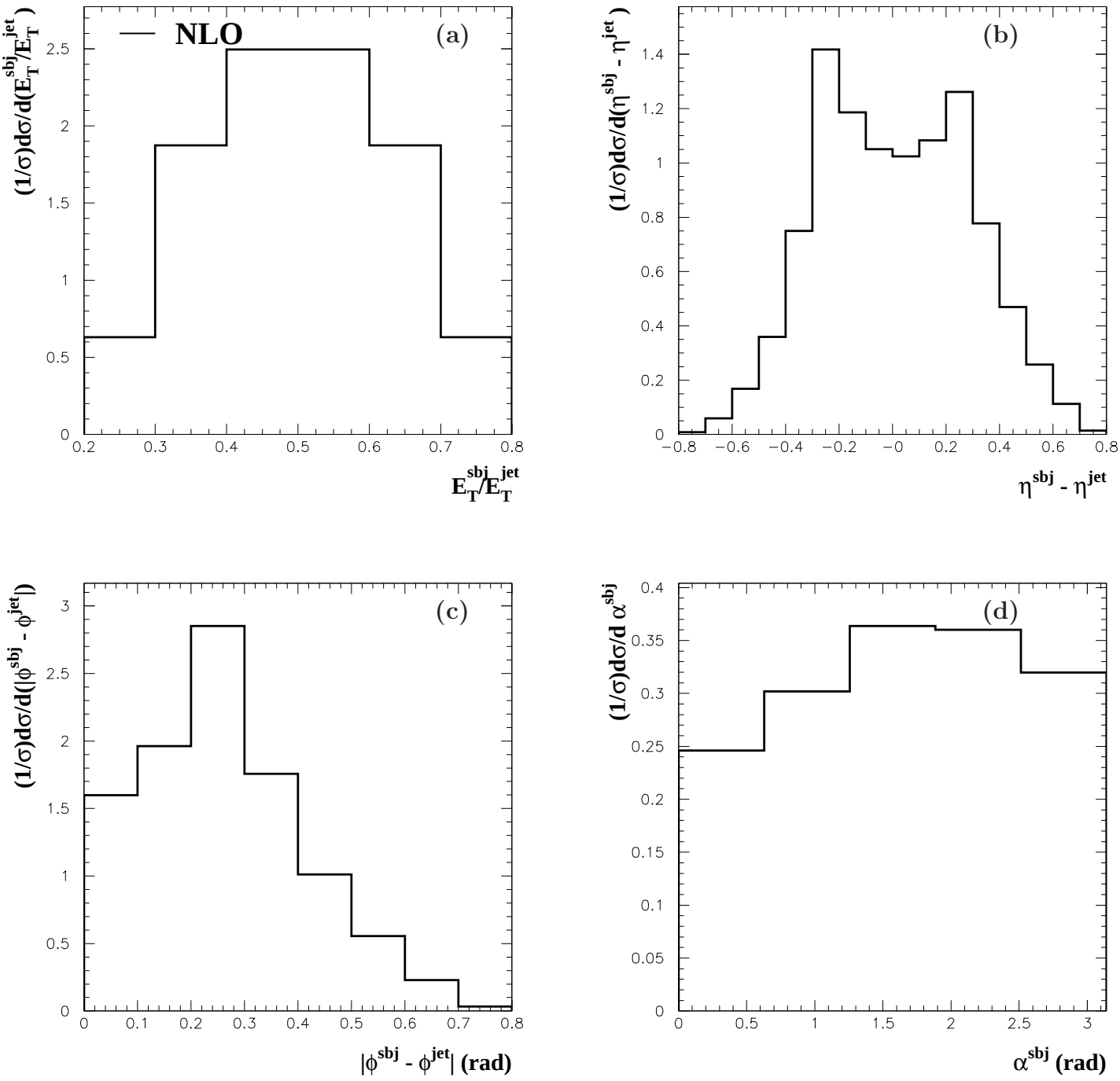

Figure 5.2: Predictions at NLO ($\mathcal{O}(\alpha_s^2)$) of the normalised differential cross sections for the inclusive production of jets with exactly two subjets at $y_{cut} = 0.05$ (histograms) as functions of **a)** E_T^{sbj}/E_T^{jet}, **b)** $\eta^{sbj} - \eta^{jet}$, **c)** $|\phi^{sbj} - \phi^{jet}|$ and **d)** α^{sbj}.

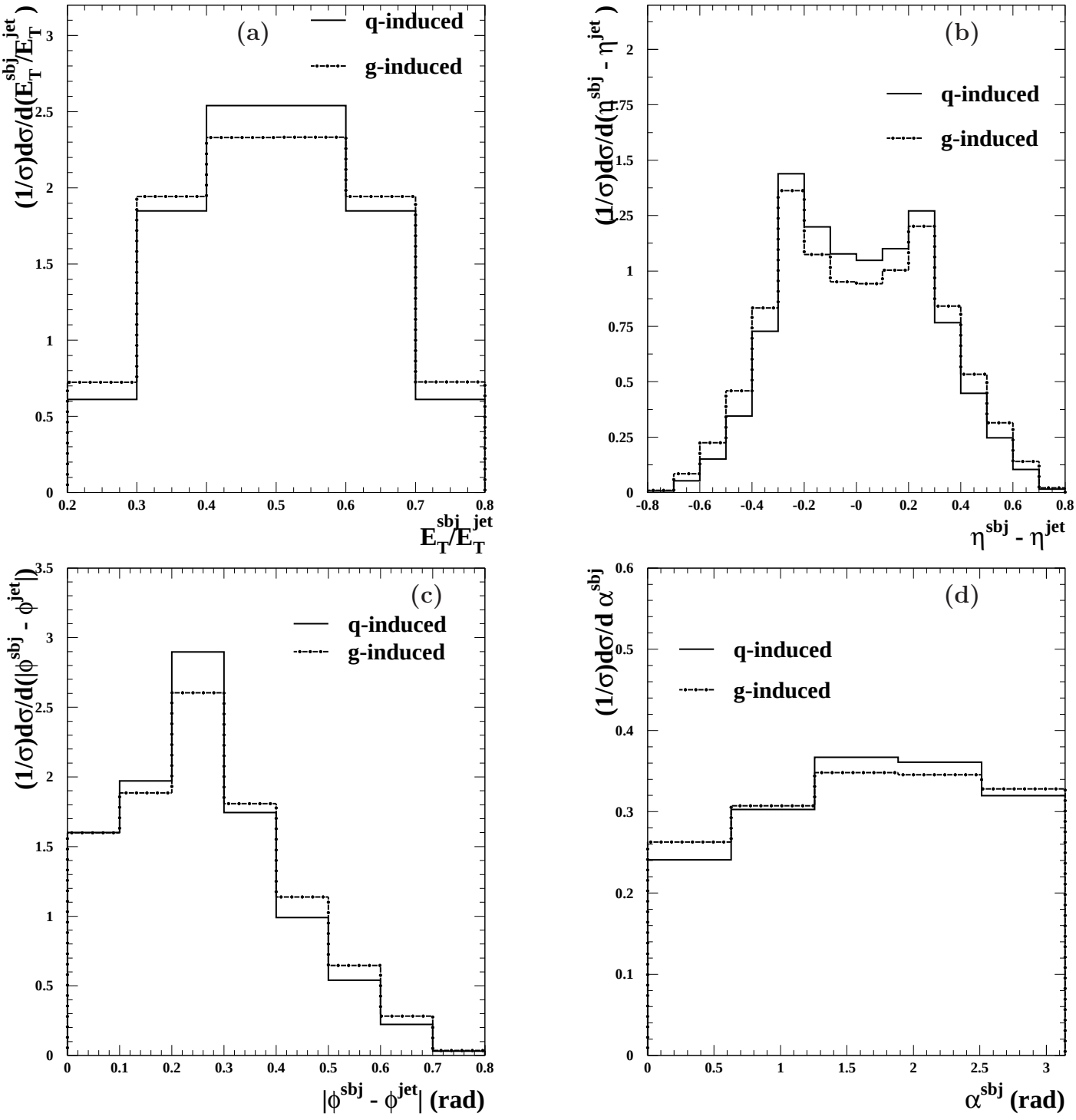

Figure 5.3: Predictions at NLO ($\mathcal{O}(\alpha_s^2)$) of the normalised differential cross sections separately for quark- and gluon-induced processes for the inclusive production of jets with exactly two subjets at $y_{cut} = 0.05$ (histograms) as functions of **a)** E_T^{sbj}/E_T^{jet}, **b)** $\eta^{sbj} - \eta^{jet}$, **c)** $|\phi^{sbj} - \phi^{jet}|$, and **d)** α^{sbj}.

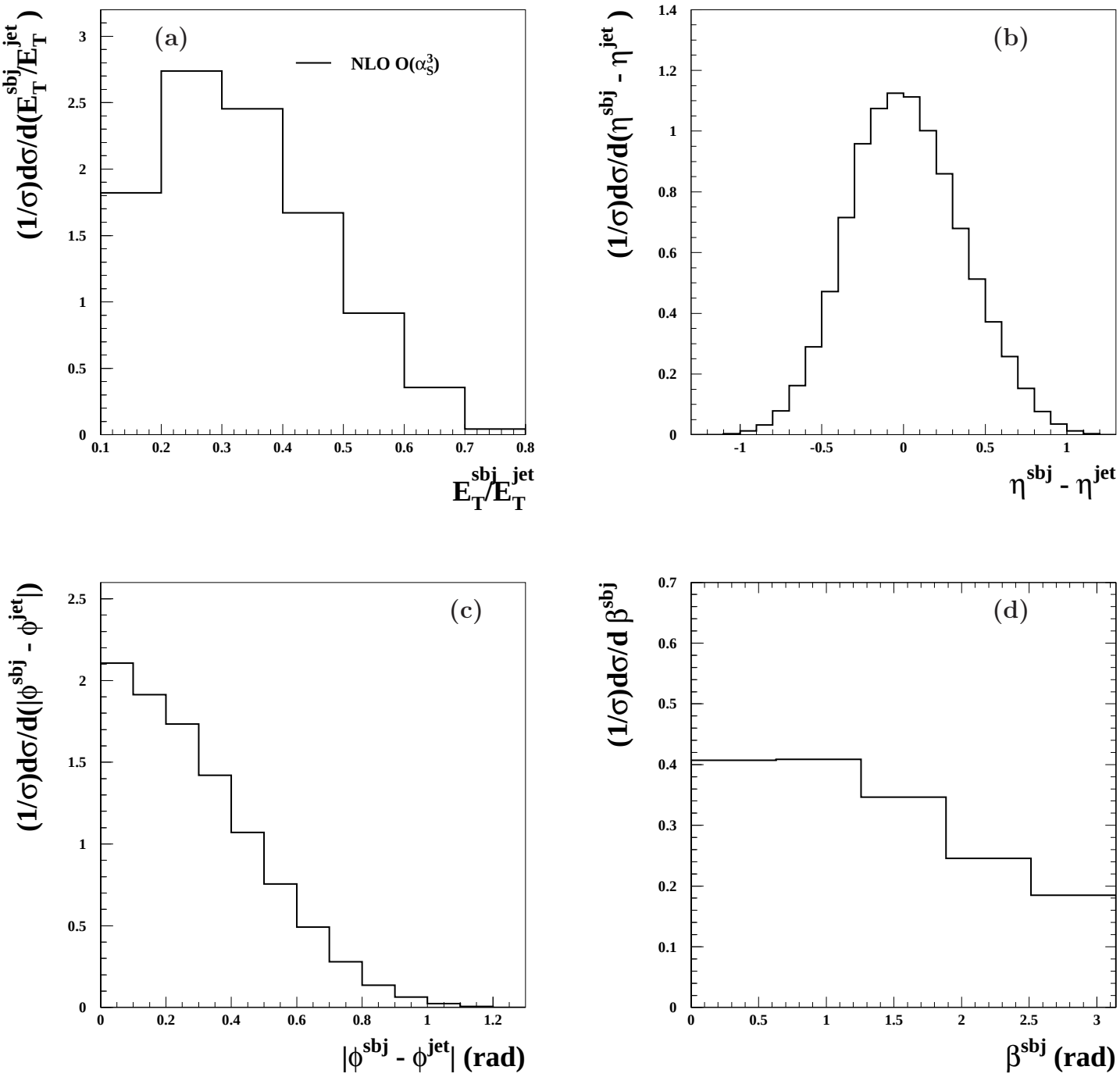

Figure 5.4: Predictions at NLO ($\mathcal{O}(\alpha_s^3)$) of the normalised differential cross sections for the inclusive production of jets with exactly three subjets at $y_{cut} = 0.01$ (histograms) as functions of a) E_T^{sbj}/E_T^{jet}, b) $\eta^{sbj} - \eta^{jet}$, c) $|\phi^{sbj} - \phi^{jet}|$ and d) β^{sbj}.

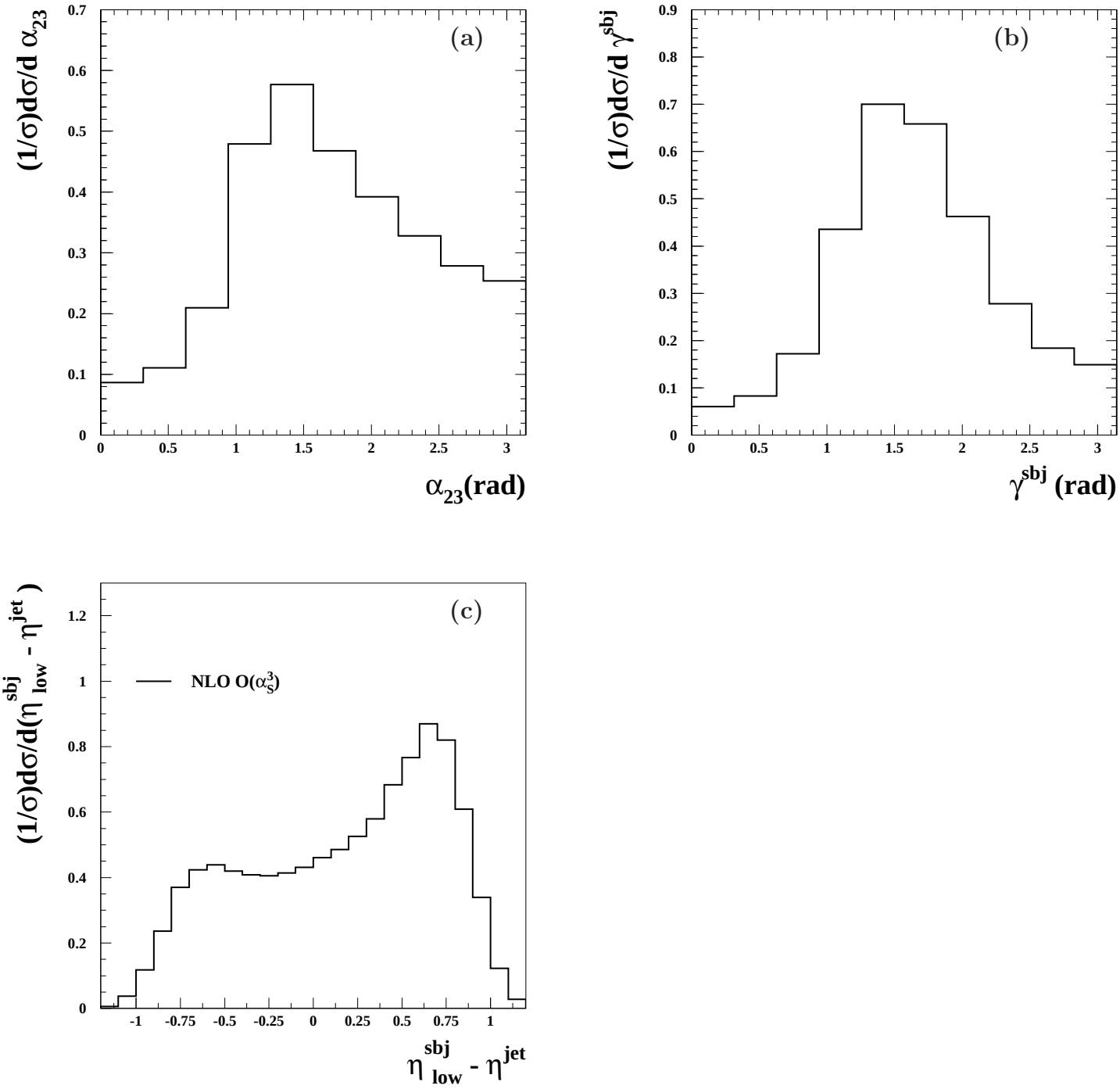

Figure 5.5: Predictions at NLO ($\mathcal{O}(\alpha_s^3)$) of the normalised differential cross sections for the inclusive production of jets with exactly three subjets at $y_{cut} = 0.01$ (histograms) as functions of a) α_{23}, b) γ^{sbj} and c) $\eta_{low}^{sbj} - \eta^{jet}$.

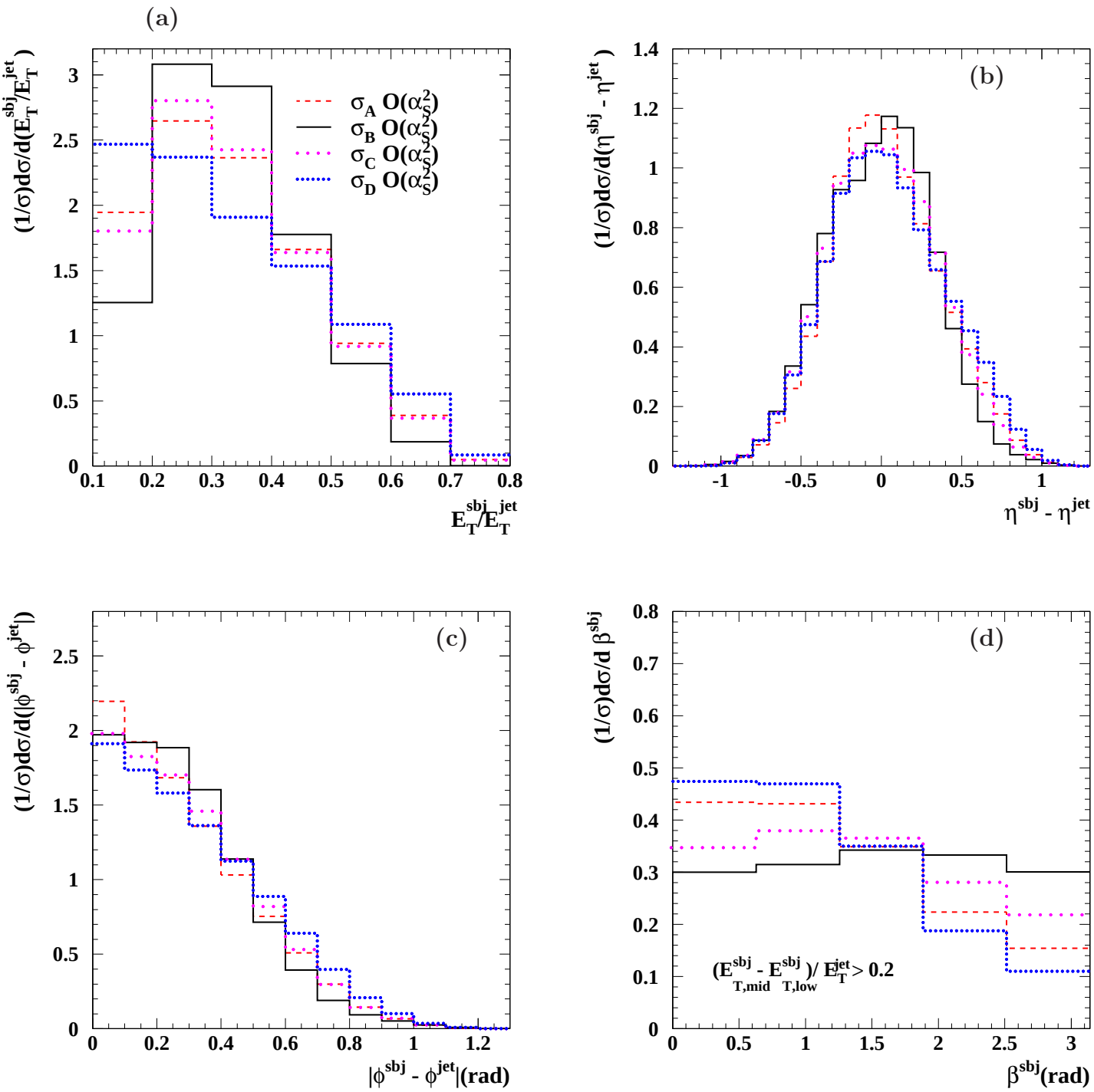

Figure 5.6: Predictions at LO ($\mathcal{O}(\alpha_s^2)$) of the normalised differential cross sections for the inclusive production of jets with exactly three subjets at $y_{cut} = 0.01$ separately for each color configuration (histograms) as functions of a) E_T^{sbj}/E_T^{jet}, b) $\eta^{sbj} - \eta^{jet}$, c) $|\phi^{sbj} - \phi^{jet}|$ and d) β^{sbj}.

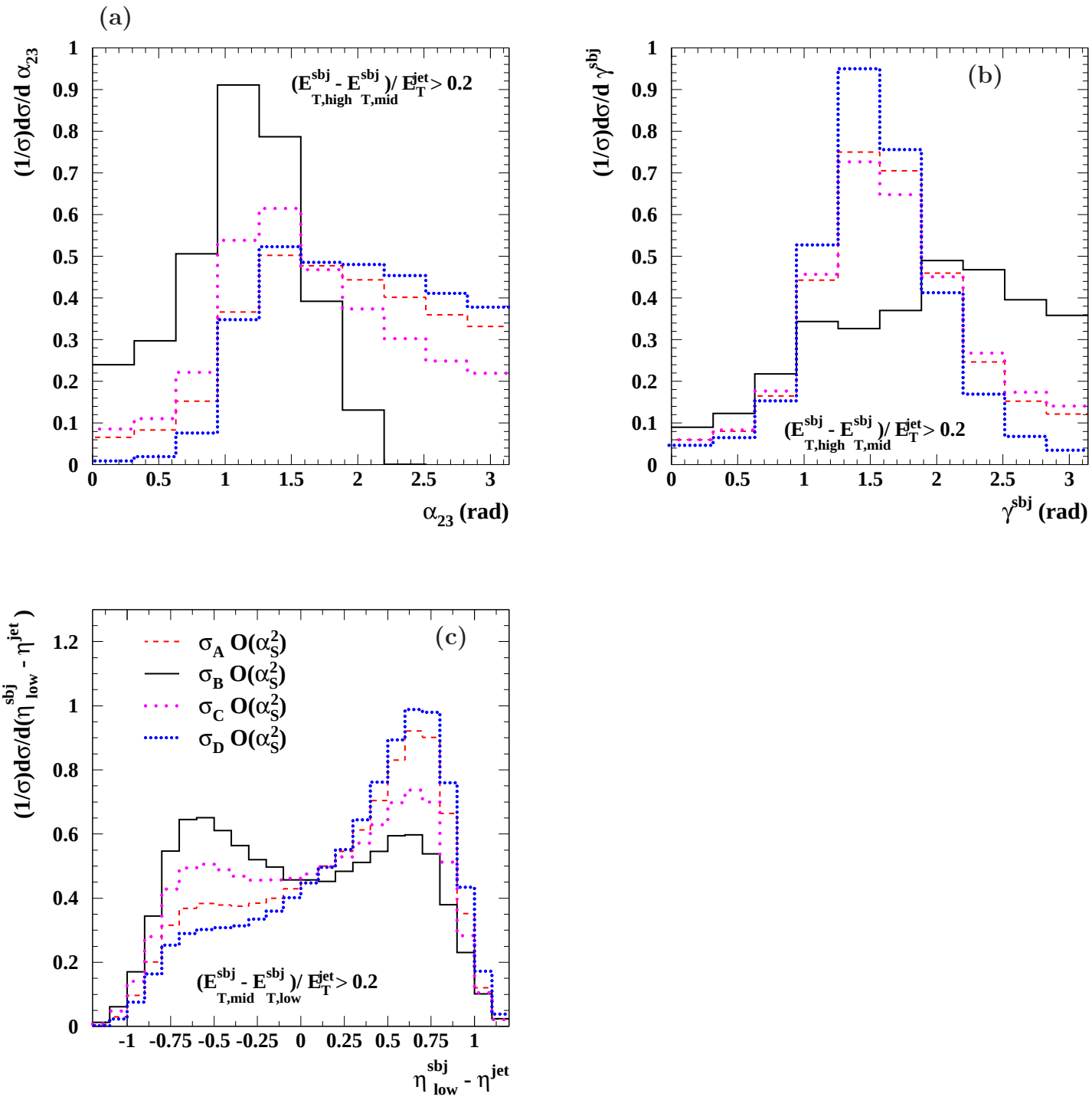

Figure 5.7: Predictions at LO ($\mathcal{O}(\alpha_s^2)$) of the normalised differential cross sections for the inclusive production of jets with exactly three subjets at $y_{cut} = 0.01$ separately for each color configuration (histograms) as functions of a) α_{23}, b) γ^{sbj} and c) $\eta^{sbj}_{low} - \eta^{jet}$.

5.5 Estimation of the theoretical uncertainties

It was previously stated that the particular choices of certain quantities in the calculation imply an associated uncertainty. The scales μ_R and μ_F are arbitrary, in the sense that their values are not fixed by any theoretical principle and their effect should disappear if all the orders in the expansion were included. Naturally, the uncertainties in experimentally-determined quantities like α_s and the proton PDFs, which play a role in the calculations, also constitute additional sources of theoretical uncertainty. Here is a list of the sources that contribute to the theoretical uncertainty of the calculations.

Contribution from higher orders

Since the perturbative expansion is truncated at some order (the second for the two-subjet analysis, the third for the three-subjet one), an uncertainty arises from the absence of the rest of the terms. The contribution from these terms can be estimated by studying the dependence of the predictions on the renormalization scale. The argument behind this is that, since the full calculation should not depend on μ_R, the terms not present on the calculation must compensate for any change induced when changing μ_R. The standard procedure is to change the value of μ_R by factors 2 and 1/2 and to take the differences with respect to the default calculation as the estimated uncertainty. As shown in figure 5.8 (and figure 11.16, which is shown in the appendix), this source of uncertainty is rather small for the two-subjet analysis. That is also the case for the three-subjet analysis, as shown in figures 5.9 and 5.10. It should be noted that the smallness of this sources of uncertainty comes from the fact that the differential cross sections are normalised.

The effects of uncalculated higher-order terms that contribute to the evolution of the proton PDFs is estimated by varying the factorization scale μ_F by factors 2 and 1/2 and taking the differences with respect to the default calculation. This source of uncertainty is also found to be relatively small.

Uncertainties in the proton PDFs

The parton densities are obtained from fits to experimental data, which means that there is some experimental uncertainty associated to them. However, to propagate these uncertainties directly to the results is not trivial. The way the estimation is actually done is by performing calculations with additional parameterizations of the PDFs which account for the experimental uncertainties. The additional parameterizations are obtained by means of the Hessian method [97]. The calculations are repeated using these additional sets of PDFs which account for the variation of the

parameters used to fit the proton PDFs. The uncertainty of an observable V is taken to be:

$$(\delta V)^2 = \frac{1}{4}\sum_{i=1}^{n}[V(a_i^+) - V(a_i^-)]^2, \tag{5.2}$$

where the sum runs over the additional sets of PDFs. $V(a_i^+)$ and $V(a_i^-)$ correspond to the value of the observable V evaluated using sets of PDFs with positive and negative variations of the i-th parameter, respectively. Given that the differential cross sections are normalised and restricted to large values of Q^2, the effect of this type of uncertainty is very small.

Uncertainties in Hadronization corrections

Since this correction is estimated by using a phenomenological model, its uncertainty is estimated by using an alternative model and taking the observed difference as an estimation of the uncertainty. This source turns out to be by far the dominant source of theoretical uncertainty, as it is shown in figures 5.8 to 5.10.

Uncertainty in $\alpha_s(M_Z)$

The value of the strong coupling constant is an experimentally-determined quantity and, therefore, it carries an associated uncertainty. The world average for $\alpha_s(M_Z)$ has an uncertainty of $\sim 1\%$ [98]. To estimate the effect of this uncertainty, calculations were performed using additional sets of proton PDFs for which different values of $\alpha_s(M_Z)$ were assumed in the fits. First, calculations are repeated with two additional sets of PDFs in which $\alpha_s(M_Z) = 0.117$ and $\alpha_s(M_Z) = 0.119$, respectively, were assumed in the fits. Then, the difference in the cross section due to a variation of 1% on the value of $\alpha_s(M_Z)$ is linearly interpolated from the differences obtained by using the two aforementioned values of $\alpha_s(M_Z)$. The resulting uncertainty turns out to be very small.

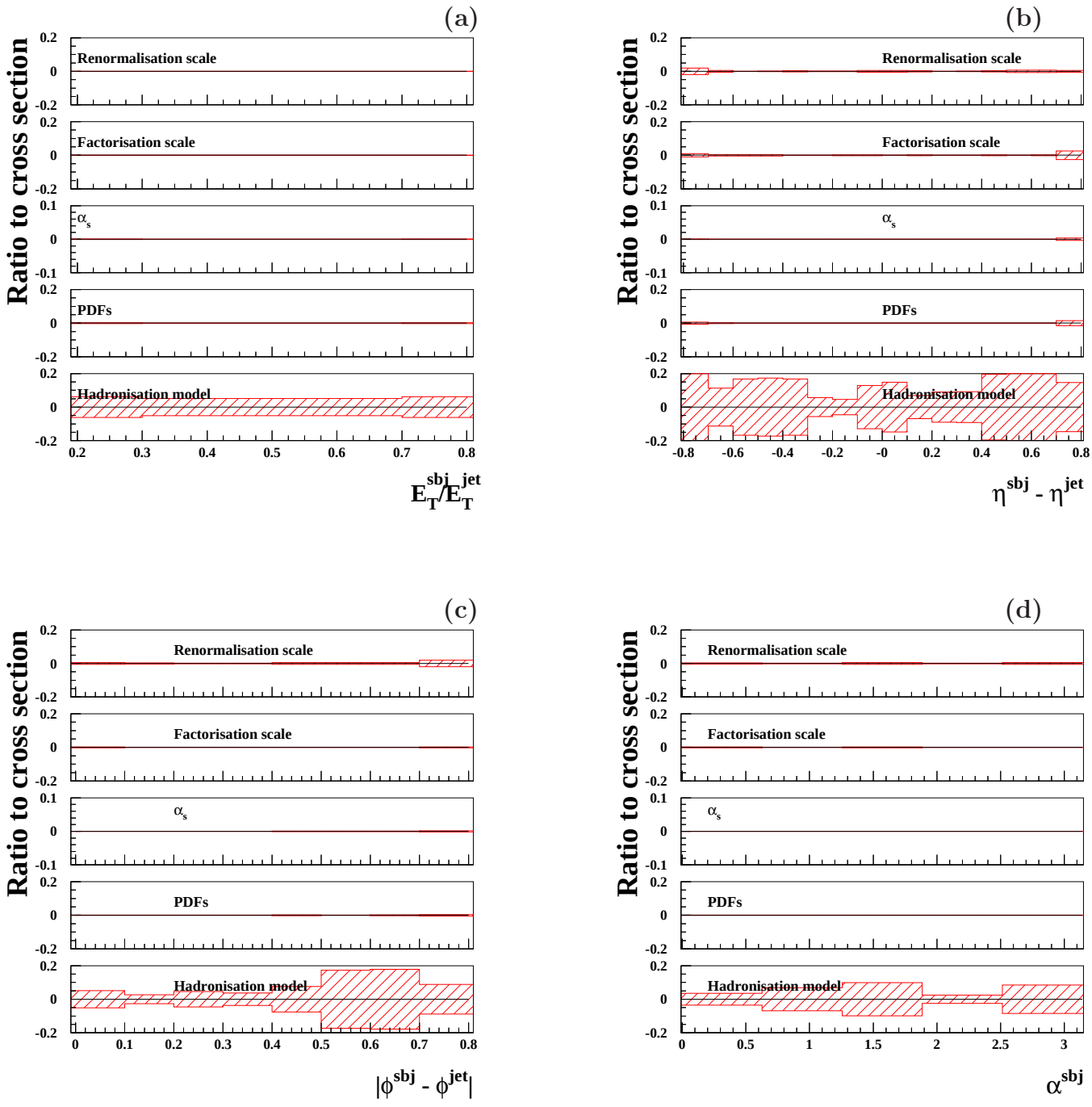

Figure 5.8: Relative theoretical uncertainties of the normalised differential cross-section calculations for the inclusive production of jets with exactly two subjets at $y_{cut} = 0.05$ as functions of (a) E_T^{sbj}/E_T^{jet}, (b) $\eta^{sbj} - \eta^{jet}$, (c) $|\phi^{sbj} - \phi^{jet}|$ and (d) α^{sbj}.

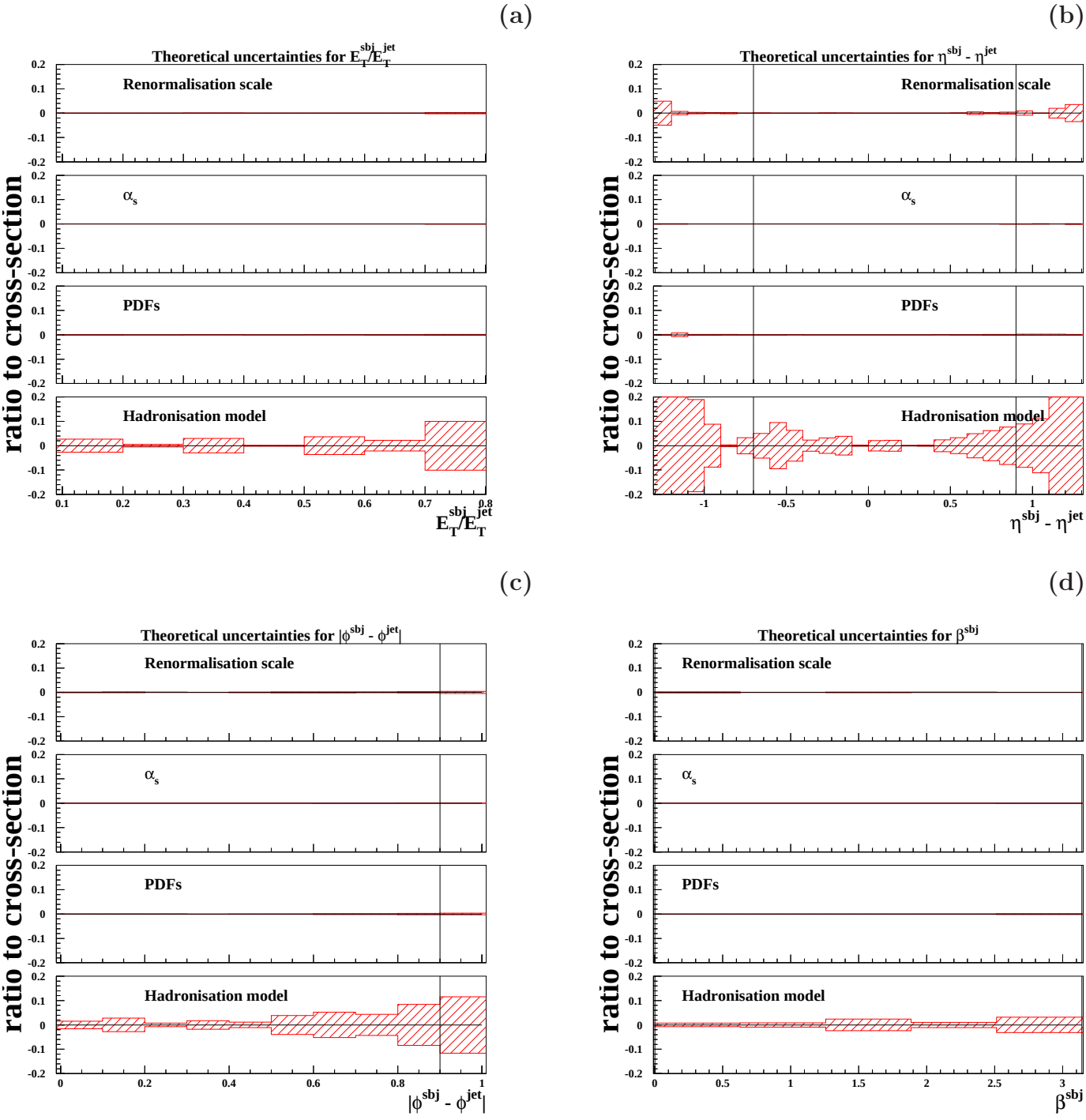

Figure 5.9: Relative theoretical uncertainties of the normalised differential cross-section calculations for the inclusive production of jets with exactly three subjets at $y_{cut} = 0.01$ as functions of (a) E_T^{sbj}/E_T^{jet}, (b) $\eta^{sbj} - \eta^{jet}$, (c) $|\phi^{sbj} - \phi^{jet}|$ and (d) β^{sbj}.

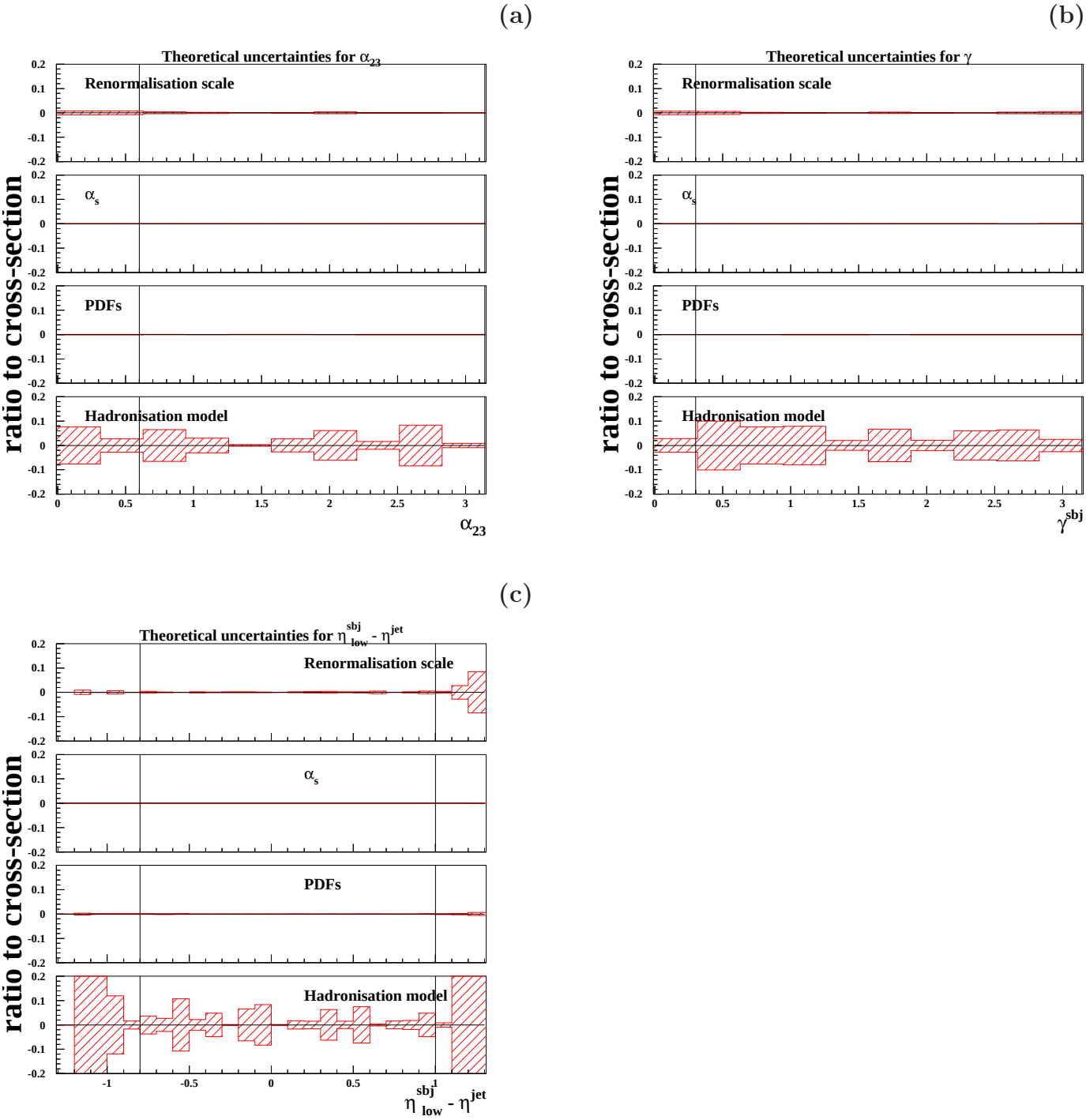

Figure 5.10: Relative theoretical uncertainties of the normalised differential cross-section calculations for the inclusive production of jets with exactly three subjets at $y_{cut} = 0.01$ as functions of (a) α_{23}, (b) γ^{sbj} and c) $\eta^{sbj}_{low} - \eta^{jet}$.

Chapter 6

Monte Carlo event generators

There are several steps intrinsic to the method of measuring that need to be modelled in order to be able to compare the measured data with the predictions of any theory. These steps are very different in nature and yet they are combined together in a single tool, the Monte Carlo event generator. The two basic phenomena that require modelling are the detector effects and the transmutation of partons into jets of colorless hadrons.

In this chapter, a description of the most important aspects of Monte Carlo event generation is presented, in particular for the models and generators which were used in the analyses. In the context of these analyses, the uses of event generators are listed below:

- Studies of the reconstruction and resolution of the jet observables, by which it is possible to quantify the effects that the detector induce in the quality of reconstruction and resolution of the jet variables to be used.
- Studies of purity and efficiency (the definitions are presented in chapter 8).
- To obtain correction factors to be applied to the raw measurement in order to compare the data with theory.
- To obtain correction factors to be applied to the pQCD calculations in order to compare data and theory at the same level.
- To estimate the systematic uncertainties in the measurements (see chapter 8).

The basic elements of a MC event generator are outlined below and graphically represented in Fig 6.1.

- **Hard subprocess:** The starting point of the simulation is the generation of an event according to the partonic distributions for the variables and processes

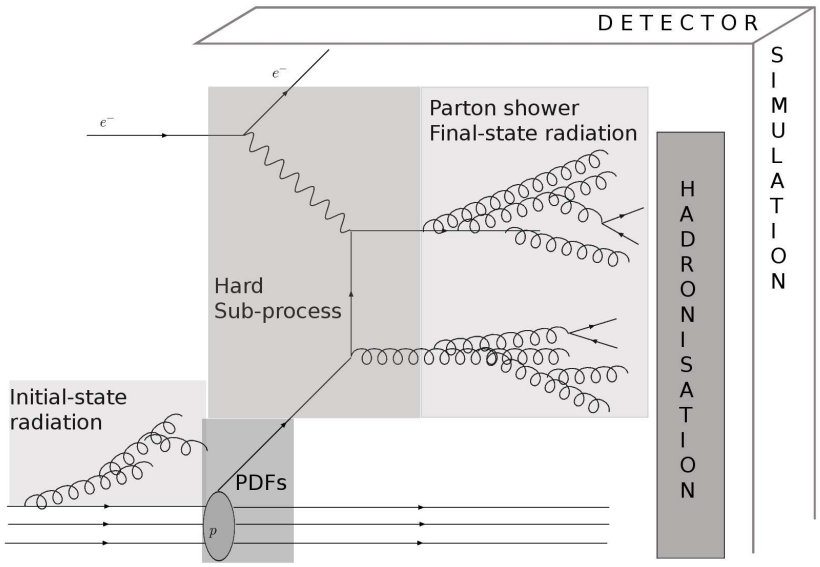

Figure 6.1: Schematic representation of a Monte Carlo event generator. The matrix elements are supplemented by an initial- and final-state parton-shower before hadronization. The final-state particles can then be interfaced with a detector simulation.

of interest. This is done through a pQCD calculation at $\mathcal{O}(\alpha_s)$, which proceeds via the processes Quark-parton model, Boson-gluon (BGF) fusion and QCD-Compton (QCDC), a schematic representation of which is shown in Fig. 6.2.

- **Initial- and final-state radiation:** The scattered colored partons branch into more partons. As discussed in section 1.6.1, the logarithmic enhancements due to collinear parton-emission can be summed at all orders in α_s. This is simulated by generating an arbitrary number of branchings which follow the DGLAP evolution equations. QED processes are also included in the simulation and can have interesting effects in the final state. The state of the simulation at the end of the parton cascade is known as 'MC at parton level'.

- **Hadronization:** The colored partons are transformed into colorless hadrons via a non-perturbative process. Only phenomenological models are available to generate the hadronic final state starting from the partons. The state of the simulation after the hadronization process is known as 'Monte Carlo at hadron level'.

- **Proton remnant:** A DIS event contains a 'proton remnant' in the forward region composed of the 'spectator partons' that have not taken part in the hard interaction. The color connection between the scattered parton and the remnant has to be simulated as well and can have a detectable effect on the

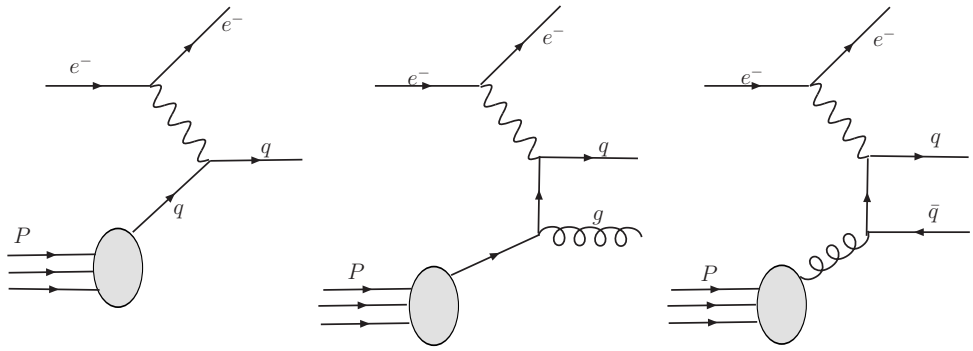

Figure 6.2: Examples of the Feynman diagrams contributing to the processes Quark-parton model, QCD-Compton and Boson-gluon fusion, respectively.

hadronic final state.

- **Detector simulation:** Once the hadron level is reached, the final-state particles are subjected to simulations of the detector; a simulation of the trigger set-up is also performed. This process provides events in the same output format as the data and, therefore, data and MC can be directly compared. This stage is known as 'Monte Carlo at calorimeter or detector level'.

6.1 Multipartonic production

A description of the hadronic final state in high-energy processes must incorporate a simulation of the logarithmic enhancements due to collinear emission at higher orders. Two of the models available for the implementation of this multipartonic production are discussed below.

6.1.1 The Matrix Element plus Parton Shower (MEPS) approach

The parton shower mimics the dynamics of the evolution of the PDFs with the fundamental difference that each branching parton moves towards decreasing virtuality when the branching is initiated by a final-state parton. Analogously, a parton in the initial state can initiate a branching process in which partons are emitted with increasing virtuality until one of them scatters off the initial electron, as shown in Fig. 1.9 in section 1.6.1. The general behaviour of initial- and final-state showers are similar since they are both based on the DGLAP evolution equations. In section 1.6.1 the Sudakov form factor was introduced, which is more convenient for Monte Carlo simulation techniques. It expresses the probability that a parton does not branch between some initial maximum virtuality and some minimum virtuality,

and from this one can find the mass of the decaying parton, the energy fraction in the branching and the flavour of the daugther partons. The process is iterated with decreasing virtuality until all parton virtualities are below some cut-off m_0^2 which is around 1 GeV^2. The angular ordering prescription (see section 2.2.1) is also included to account for soft-gluon coherence.

One of the limitations of the parton shower approach is that the emission of partons at large angles is not well simulated. To improve the simulation of multijet events, an approach was developed in which the first emission is generated according to the matrix elements and then additional softer emissions are added by using the parton shower. This approach, known as matrix elements plus parton shower (MEPS), is available in LEPTO [94] and is one of the two models that has been utilized for the generation of the Monte Carlo samples used in the analyses presented here.

6.1.2 The Color Dipole Model

In the color-dipole model (CDM) [88–91], as implemented in the ARIADNE 4.08 [92, 93] program, the cascade is not separated into initial- and final-state emissions. The outgoing quark is viewed as part of a color dipole system together with the proton remnant. The emission of a gluon can then be treated as radiation from this color dipole and to a good approximation the emission of a second, softer gluon can be treated as radiation from two independent dipoles, one between the quark and the gluon and the other between the gluon and the proton remnant. This approach can be generalised and the emission of a third gluon is given by three independent dipoles. In this model, the subsequent gluon emissions are strongly ordered in transverse momentum, which induces the angular ordering of the emitted gluons and thus reproduces the effects of soft-gluon coherence.

In CDM there is no division between initial- and final-state radiation. It is assumed that radiation can be described by the color dipole formed between the struck quark and the proton remnant. The model was originally implemented for e^+e^-, where there are two point-like antennae formed by the two outgoing quarks. In DIS, the proton remnant is treated as an extended object with a transverse size, so that, due to the destructive interference in the remnant, only a fraction

$$a = (\mu/p_T)^\alpha$$

of it takes part in the emission of a gluon with transverse momentum p_T, where μ describes the size and α the dimension of the proton remnant.

When implementing this procedure in the ARIADNE program there is the question of how to treat the recoils. Since only a part of the remnant takes part in the

radiation, only that part should take the recoil. This would mean an extra 'kink' on the string which in the Lund string picture is equivalent to an extra gluon. In ARIADNE, the remnant is therefore divided into a collinear gluon which takes part in the radiation and receives a recoil.

Although gluon emission in the CDM is close to the form of the exact matrix element, the processes initiated by gluons, the so-called Boson-Gluon Fusion, are not included at all in the model. This is corrected by introducing a matching procedure for the first emission in a DIS event. The initial dipole between the struck quark and the proton remnant can emit an anti-quark (the anti-partner of the struck quark), in which case the process is matched to the BGF matrix element.

6.2 Hadronization models

Once the parton shower is finished, the non-perturbative physics of hadronization comes into play. We are forced to rely on phenomenological models to complete the hadronization of the final-state partons. The general approach to hadronization is based on the hypothesis of local parton-hadron duality (see section 2.2), in which it is assumed that the flow of momentum and quantum numbers at the hadron level is already established at the parton level, so that the effect of hadronization is to smear the energy configuration of the parton level.

The are several phenomenological models to simulate this process, of which the Lund string model is discussed.

6.2.1 The Lund String Model

It has been suggested that the confined color field behaves like a vortex line, similar to the magnetic field in a type II super conductor. The field of such a vortex line is the same as the field of a chain of dipoles lined up along the vortex line. Given this picture, the color dipole approximation of the QCD cascade seems a natural formulation.

The Lund string model [95] is based on the observation that when a gluon is emitted from, for example, a $q\bar{q}$ pair produced in e^+e^- annihilation, it can be described as radiation from the color dipole between the two quarks and that subsequent emission of a softer gluon can be described as radiation from two independent dipoles; one stretched from the quark to the gluon and one from the gluon to the anti-quark. Thus, the color interaction between two partons at the end of the parton shower is represented as a one-dimensional massless relativistic string, so that when a q and a $\bar{q}$ move apart, the string acts as a confinement potential which is roughly linear with its length. As the q and $\bar{q}$ move away from each other the potential increases

and the string may be broken by the production of another pair $q'\bar{q}'$. This leads to two color singlet sistems, $q\bar{q}'$ and $q'\bar{q}$, each of them with a string evolving in an independent way, so that further breakings may occur. The string is fragmented iteratively according to:

$$f(z) \sim \frac{1}{z}(1-z)^a exp(-b\frac{m_T^2}{z}), \tag{6.1}$$

where z is the fraction of the quantity $E + p_L$ of the parent string taken by the daugther and $m_T = \sqrt{p_T^2 + m^2}$, where p_T and p_L refer to the transverse and longitudinal momentum relative to the string axis. The transverse momentum to the string axis, p_T, follows a Gaussian spectrum. The string break-up processes continues until only on-shell hadrons remain, each hadron corresponding to a small piece of the string.

Gluons act as transverse excitations (kinks) on the string-like field. The breaking of a dipole into two dipoles corresponds to one more kink on the string.

6.3 Detector Simulation

As previously discussed, a model of the effects and biases that the detector induces is very important. The final state of the MC-generated events is processed through a simulation of the ZEUS detector which is based on GEANT 3.13 [86]. This simulation program includes, amongst other things, the response of the detector components as well as the interaction of the particles with dead material. Once the effects are simulated, the generated events undergo a simulation of the same trigger requirements as the data and are processed by the same reconstruction and offline programs. The final state of the MC-generated events is in the same format as the ZEUS data.

6.4 Event generators for NC DIS

In the analyses presented, the LEPTO program was used using two different approaches for the parton shower.

6.4.1 The LEPTO Monte Carlo generator

The first step of the simulation is the hard-scattering process. LEPTO [94] is based on the leading-order electroweak cross section of the underlying parton-lepton scattering and also includes QCD corrections using exact first-order matrix elements. The PDFs are provided using the standard library PDFLIB [99], which contains the

information for most parametrizations of the proton's parton distributions. For the samples used in the analyses presented here, the CTEQ5D [100] proton PDFs were used.

LEPTO does not provide radiative corrections, this is done by HERACLES 4.6.1 [101, 102], which is then interfaced with LEPTO via a program called DJANGOH 1.1 [103, 104].

After the hard-scattering process has been calculated, the parton shower starts. In section 6.1, two different approaches were discussed. With LEPTO, one can select either the MEPS or the CDM approach. The comparison between the corrections obtained with CDM and MEPS is usually used to make an estimation of the systematic uncertainty arising from the modelling of the parton shower.

Once the parton radiation is completed, the hadronization is performed with the Lund string model, as implemented in JETSET [105–108]. After the fragmentation process, the final-state hadrons are provided and the event is fed to the simulation of the detector.

In the next two chapters, after the data sample selection is explained, a comparison of data and the Monte Carlo event generators is shown for several distributions, so that the quality of the detector simulation as well as the corrections applied to the data can be quantified.

Chapter 7

Event selection and variable reconstruction

7.1 Introduction

In this chapter, a description of the selection and variable reconstruction of the NC data samples is given. The analyses presented were performed with data taken by the ZEUS detector in the 1998-2000 running period for the two-subjet analysis and in the 2004-2007 running period for the three-subjet one.

Since the aim is to make measurements for neutral current events, there are three main features that have to be looked for when selecting the sample in which to perform the analysis:

- The presence of a scattered electron.
- The presence of at least one high-energy jet.
- Balanced transverse momentum.

The main ZEUS detector component used in the analyses is the UCAL. The jet-finding algorithm was applied on the four-momenta of the energy deposits in the UCAL as initial input to reconstruct jets. SINISTRA [109, 110], the electron-finder neural network, also uses the information in the UCAL to reconstruct the scattered electron candidate. The CTD also plays an important role since some of the cleaning cuts involve tracks and an interaction vertex needs to be reconstructed.

Cleaning cuts are applied on the data and Monte Carlo samples to remove the different backgrounds. There are multiple sources of background such as photoproduction events (PHP), which is the process with highest cross section at HERA, charged-current events (CC) as well as non-physics events such as beam-gas interactions or cosmic rays.

In order to perform a proper jet reconstruction, one needs to pay attention to several points:

- The detector resolution of the jet variables E_T^{jet}, η^{jet} and ϕ^{jet} has to be known. Any alteration of these variables arising from detector effects needs to be corrected and indeed the transverse energy of the jets was corrected in both analyses.
- The absolute energy scale of the jets has to be known and needs to be well simulated in the MC.
- The regions of the UCAL where the reconstruction of the jets is not sufficiently good have to be identified and excluded in the selection.

All these points need the use of MC simulations. The legitimacy of using the MC simulations rests on their ability to properly reproduce the distributions in the data for all the observables used in the analyses. The MC samples are generated with minimal bias and then subjected to exactly the same selection criteria as the data. The 'control plots' for the distributions in the data and MC, as well as their comparison, are presented at the end of this chapter.

7.2 Data samples for the two-subjet analysis

The data sample selected for this analysis consists of:

- NC DIS events with $Q^2 > 125$ GeV^2 and at least one jet with $E_T^{jet} > 14$ GeV and $-1 < \eta^{jet} < 2.5$ in the laboratory frame. An integrated luminosity of 81.7 ± 1.9 pb^{-1} was used.

There were 128986 events in the sample that satisfy these criteria plus the cleaning cuts described later. The final sample contained 132818 jets, of which 21162 had exactly two subjets at $y_{cut} = 0.05$.

7.3 Data samples for the three-subjet analysis

The data sample selected for this analysis consists of:

- NC DIS events with $Q^2 > 125$ GeV^2 and at least one jet with $E_T^{jet} > 14$ GeV and $-1 < \eta^{jet} < 2.5$ in the laboratory frame. An integrated luminosity of 299.2 ± 7.8 pb^{-1} was used.

  The final sample contained 429133 jets, of which, 80002 had exactly three subjets at $y_{cut} = 0.01$.

For some of the subjet variables, the ordering in transverse energy of the subjets is relevant and, thus, further requirements are introduced to ensure a correct reconstruction. In the case of β^{sbj} and $\eta^{sbj}_{low} - \eta^{jet}$, where one needs to know which is the lowest-E_T subjet, it was required that:

$$\frac{E_T^{mid}}{E_T^{jet}} - \frac{E_T^{low}}{E_T^{jet}} > 0.2,$$

where E_T^{mid} corresponds to the subjet with the next-to-lowest transverse energy and E_T^{low} is the lowest-E_T subjet. This requirement ensures that the lowest-E_T subjet is well separated in tranverse energy from the other two so that migrations due to detector effects or other fluctuations are mimized. With this extra requirement 10939 jets are found and normalised cross sections as functions of β^{sbj} and $\eta^{sbj}_{low} - \eta^{jet}$ are obtained.

Likewise, in the case of α_{23} one needs to be sure which are the lowest- and next-to-lowest E_T subjets, though the order is irrelevant. This is thus equivalent to knowing which is the highest-E_T subjet and, therefore, the following requirement is applied:

$$\frac{E_T^{high}}{E_T^{jet}} - \frac{E_T^{mid}}{E_T^{jet}} > 0.2,$$

where E_T^{high} corresponds to the subjet with the highest transverse energy. In the case of γ^{sbj} the same reasoning applies: the important issue is to distinguish the highest-E_T subjet from the other two and thus the same cut is applied. Given this requirement, 27606 jets are found, and normalised cross sections as functions of α_{23} and γ^{sbj} are obtained.

Studies of the underlying color dynamics using the variables β^{sbj}, α_{23}, $\eta^{sbj}_{low} - \eta^{jet}$ and γ^{sbj} are performed with these additional requirements included.

7.4 Event selection

In the beginning of the chapter it was stated that the main properties of a NC DIS event are: balanced transverse momentum, the presence of a scattered electron and the presence of jets in the final state. These properties are looked for in the process of data taking via the use of the trigger chains. The following sections contain an outline of the specific trigger chain and the selection cuts used in the analyses. These criteria are divided into two categories:

- **Online selection**: these are the triggers used during the online data taking. It consists of a three-level trigger chain which aims to minimize CPU time

during data taking. They implement reasonably-inclusive cuts to prevent the loss of interesting physics data.

- **Offline selection**: this selection includes full jet and scattered electron reconstruction as well as all the cleaning cuts for background removal.

7.4.1 Online selection

As previously stated, the online selection proceeds through a three-level trigger chain. The computations involved in the selection become more refined and CPU-demanding as one goes up in the trigger chain. In what follows, the criteria used during the 1998-2000 running period are described. The criteria used during the 2004-2007 running period are very similar.

First Level Trigger

At the FLT level, minimum overall UCAL energy deposits were required. The conditions imposed were:

- $E^{FLT}_{EMC} > 10$ GeV or
- $E^{FLT} > 15$ GeV or
- $E^{FLT}_{BEMC} > 3.4$ GeV or
- $E^{FLT}_{REMC} > 2.0$ GeV or
- $E^{FLT}_{T} > 11.6$ GeV

Additionally, it was demanded that the event has at least one CTD track associated with the nominal vertex.

Second Level Trigger

At the SLT, the following conditions were imposed:

- A reconstructed vertex with -60 cm $< z_{vtx} < 60$ cm. This cut removed events which occurred far from the interaction region, since the detector response could be very different for such events. This cut also removed beam-gas related events.
- $E - p_Z > 8.0$ GeV, where E and p_Z are the energy and the longitudinal momentum of the event, determined from energy deposits in the UCAL. For a NC interaction of massless particles, $E - p_Z = E_e + E_p - p_{Z,e} - p_{Z,p} = 2E_e =$

2×27.5 GeV, so that events with $E - p_Z << 55$ GeV are associated with PHP or CC interactions.

- $E_T^{cone} > 8.0$ GeV, where E_T^{cone} is the sum of transverse energy of all UCAL cells outside a cone of 10° around the proton beam direction.

- $E - p_Z > 12$ GeV or $p_Z/E < 0.95$ to further reduce the contamination from beam-gas interactions.

Third Level Trigger

The following conditions were imposed at the TLT:

- The number of 'bad tracks' had to be smaller than 6. A 'bad track' was defined as a track which is long enough for a good reconstruction (i.e. it has more than 5 hits in axial superlayers and more than 5 hits in stereo superlayers, and more than 20 hits in total) and points to a very backward vertex ($z_{vtx} < -75$cm). The cut on the number of 'bad tracks' suppressed proton beam-gas background events, which usually contain forward-going tracks coming from the backward region.

- A reconstructed vertex with -60 cm $< z_{vtx} < 60$ cm.

- $E - p_Z < 75$ GeV.

An event was required to fulfill at least one of the following conditions at the TLT:

- $E_T^{cone} > 25$ GeV.

- The time available at the TLT level permitted the application of a jet-finding algorithm. Events with at least one jet of $E_T^{jet} > 10$ GeV and $\eta^{jet} < 2.5$ were retained. The jet algorithm was applied over all the cells in the UCAL, including those that would be associated with the electron candidate, so that the electron candidate was usually identified as a jet at this point.

- $p_Z/E < 1.0$ and two or more jets with $E_T^{jet} > 6$ GeV and $\eta^{jet} < 2.5$.

As described in the experimental setup, during the offline reconstruction of the events some additional requirements were imposed and stored in a bit structure (DST bits). However, no further requirements were applied at this level for the jet analyses.

7.4.2 Offline selection

At this stage, the samples contain events from several sources and here is where selection criteria and further requirements come into play.

Identification of the scattered electron. The SINISTRA electron finder.

A neural network approach was developed based on the showering properties of the electron in the segmented UCAL. This neural network estimates the probability that a given energy deposit in the UCAL corresponds to an electron, therefore distinguishing from the single hadrons or jets of particles for which the pattern of energy deposits in the UCAL can look quite similar at low energies. Electrons and background populate different regions in a multidimensional configuration space parametrized by the variables that characterize the shower. The neural network was trained using Monte Carlo samples for both electrons and hadrons. A high efficiency was found for electron identification.

The electron-identification algorithm used in these analysis is called SINISTRA [109, 110]. The algorithm proceeds by merging together groups of cells according to predefined criteria. Each cell is merged with the adjacent cell of highest energy. This clustering procedure associates cells which most likely come from a single particle shower. A cluster is defined to be composed of no more than 3×3 cells. A candidate cluster for an electron is called an island. The input variables are the energies registered in the corresponding island and the neural network projects the information into one output variable P, which is interpreted as the probability that the island originates from the scattered electron ($P \sim 1$) or has a hadronic origin ($P \sim 0$).

It is possible to define the electron four-momentum using the constituent cells and weighting their respective positions with their energies. Using the energy and position of the constituent cells, the four-momentum of the island is reconstructed. Each island was associated a probability. The one with the largest probability was taken as the scattered electron.

Efficiency and purity studies of the electron candidates have shown that an optimal selection required an associated probability of at least $P > 0.9$ and that the probability given by SINISTRA was reliable if the island had an energy larger than 10 GeV. These were the requirements imposed on the identified scattered electron for the events in the NC DIS samples.

To further improve the purity and efficiency of the electron candidate, additional requirements were imposed:

- $y_e < 0.95$, where $y_e = 1 - E'_e(1 - \cos\theta_e)/(2E_e)$ and E'_e and θ_e are the energy and polar angle of the electron candidate. With this condition, fake electron

candidates in the FCAL were removed.

- the total energy not associated with the electron candidate within a cone of radius 0.7 units in the $(\eta - \phi)$ plane around the electron direction should be less than 10% of the electron energy. This condition removed photoproduction and DIS events in which part of a jet was falsely identified as the scattered electron.

- for $20^\circ < \theta_e < 140^\circ$, the fraction of the electron energy within a cone of radius 0.3 units in the $\eta - \phi$ plane around the electron direction should be larger than 0.9; for $\theta_e < 20^\circ$, the cut was raised to 0.98. This condition removed events in which a jet was falsely identified as the scattered electron.

7.4.3 Signal selection

The cuts previously explained are not enough to select a clean sample of NC DIS events. There are sources of background which can give substantial contributions and therefore contaminate the data sample. The sources are several: photons, jets or isolated particles can potentially be mis-identified as the scattered electron. One of the backgrounds is photoproduction, defined as the NC process with low values of the transferred momentum, $Q^2 \leq 1$ GeV^2. Another known background is the so-called 'beam-gas events', which comes from molecules leaking into the vacuum and colliding with the proton beam upstream of the interaction point. This kind of collisions leaves a large number of 'bad tracks' in the CTD which do not come from the primary vertex. Charged-current events are a source of background as well. Their characteristic signal is the presence of missing transverse momentum arising from the final-state neutrino escaping undetected. The cleaning cuts applied to remove the background coming from these sources are:

- Using the definition of a bad track already given, the number of bad tracks is required to be less than 5. The presence of many bad tracks in the detector is typical of an event produced by a beam-gas interaction.

- $38 < (E - p_Z) < 65$ GeV, where E is the total energy as measured in the UCAL, $E = \sum_i E_i$ and p_Z is the z-component of the vector $\vec{p} = \sum_i E_i \vec{r_i}$. In both cases the sum runs over all UCAL cells, E_i is the energy of the UCAL cell i and $\vec{r_i}$ is a unit vector along the line joining the reconstructed vertex and the geometric centre of cell i. This cut removed events with large initial-state radiation and further reduced the background from photoproduction.

- $p_T/\sqrt{E_T} < 3$ GeV$^{1/2}$, where p_T is the total transverse momentum as measured with the UCAL ($p_T \equiv \sqrt{p_X^2 + p_Y^2}$) and E_T is the total transverse energy in

the UCAL. This cut removed charged-current DIS events, cosmic rays and beam-related background.

- A cut in -34 cm $< z_{vtx} <$ 34 cm (35 cm) for the two-subjet (three-subjet) analysis. This cut removed events whose vertex is far from the nominal interaction region. These events were removed because the detector response to events far from the nominal interaction region can be significantly different.

- There can be background from elastic Compton processes ($ep \to ep\gamma$), since the photon or the electron could be falsely identified as a jet. In these events two electromagnetic clusters are expected in the UCAL and, thus, two SINISTRA electron candidates were requested. Cuts on energy and isolation were applied as for the first candidate. If there was a second candidate that passes these cuts and the energy on the whole UCAL excluding that belonging to the two candidates was found to be less than 4 GeV, the event was rejected.

Phase-space region and jet selection

The phase-space of the analyses was defined in terms of Q^2. The double-angle method [111] was used to reconstruct Q^2:

$$Q^2_{DA} = 4 \cdot E_e^2 \frac{\sin\gamma_h(1+\cos\theta_e)}{\sin\gamma_h + \sin\theta_e - \sin(\theta_e+\gamma_h)}, \tag{7.1}$$

where γ_h is defined by the relation

$$\cos\gamma_h = \frac{(1-y)xE_p - yE_e}{(1-y)xE_p + yE_e}, \tag{7.2}$$

and corresponds to the scattering angle of the struck quark in quark-parton-model events. This angle is reconstructed using the UCAL according to

$$cos\gamma_h = \frac{(\sum_h p_{xh})^2 + (\sum_h p_{yh})^2 - (\sum_h (E-p_Z)_h)^2}{(\sum_h p_{xh})^2 + (\sum_h p_{yh})^2 + (\sum_h (E-p_Z)_h)^2}, \tag{7.3}$$

where the sums run over all the UCAL cells not associated to the scattered electron candidate.

This method does not involve the final-state electron or jet energies, which have a poorer detection resolution than angles; therefore, this method exhibits better reconstruction properties than others in the kinematic region considered here.

A cut of $Q^2 > 125$ GeV^2 was used to select a region that is well into the DIS regime. Additional selection cuts designed to improve the reconstruction of the jets were applied:

- Only jets with transverse energies larger than 14 GeV have been included.
- Only jets within the pseudorapidity range $-1 < \eta^{jet} < 2.5$ have been considered.

7.5 Jet reconstruction using the UCAL

The UCAL is the main component used to perform the reconstruction of jets. In this analysis, jets are reconstructed using the k_T clustering algorithm in the laboratory frame using the UCAL cells four-momenta as the initial set of objects. The jet algorithm was applied after excluding those cells associated with the scattered electron candidate. A four-momentum, p^μ, was associated to each cell, where p^0 corresponds to the energy deposit in the cell and $\vec{p}$ was determined by treating the cell as a massless particle and its position to be at the center of the cell.

It is important to quantify the effect of the resolution of the detector in the jet variables and any bias that the dead material in front of the UCAL may introduce in their measurement. It is also necessary that the energy scale of the jets be the same in the data and MC samples. To ensure that this is the case, studies of the energy-scale in the UCAL for the data and MC simulations were carried out for each of the analyses. This section describes both of these studies.

7.5.1 Jet energy scale corrections

The energy scale uncertainty of the UCAL coupled with differences in the hadronic final state between the data and MC simulations has traditionally been the dominant systematic uncertainty in jet measurements. Energy-scale uncertainties of $\pm(3-5)\%$ lead to uncertainties of $\sim \pm(10-20)\%$ in the cross-section measurements.

QPM-type of events, in which the final state consists of the scattered electron and one jet were used to calibrate the UCAL. Since the total P_T should be ≈ 0 the electron's E_T, which is estimated using the double-angle methond ($p_{T,DA}$) must compensate the jet's E_T. The key idea is that the ratio $R = \frac{E_T^{jet}}{p_{T,DA}}$ should be the same in the MC and in the data, which should indeed be the case if the usage of MC for acceptance corrections is to be legitimate. Therefore, the double ratio $R' = \frac{R^{DATA}}{R^{MC}}$ was used as an energy-scale correction factor to match the energy scale in the data and MC The values of the double ratio R' are expected to be different in different regions of the detector and thus the correction factors were obtained[1] as

[1]The corrections were obtained using the inclusive sample of jets before the requirements on the number of subjets were applied.

η^{jet} region	Energy-scale corrections
[-1.0,-0.25]	0.999
[-0.25,0.75]	1.006
[0.75,1.25]	1.013
[1.25,1.75]	0.987
[1.75,2.5]	0.982

Table 7.1: Energy-scale correction factors applied to the E_T^{jet} of the jets in the data for the two-subjet analysis.

η^{jet} region	I	II	III	IV	V	VI	VII	VIII	IX	X
[-1.0,-0.25]	0.990	0.974	0.987	0.979	0.981	0.974	0.980	0.990	0.997	0.976
[-0.25,0.75]	0.994	0.995	0.991	0.987	0.979	0.988	0.987	0.984	0.985	0.982
[0.75,1.25]	1.013	1.013	1.019	1.011	1.015	1.009	1.010	1.008	1.012	1.010
[1.25,1.75]	0.995	1.001	1.003	0.996	0.994	0.995	0.995	0.997	0.995	0.990
[1.75,2.5]	0.991	0.994	0.994	0.990	0.990	0.987	0.989	0.988	0.990	0.992

Table 7.2: Energy-scale correction factors applied to the E_T^{jet} of the jets in the data for the three-subjet analysis. Each column corresponds to a different data-taking period.

a function of η^{jet}. Table 7.1 shows the $\frac{1}{R'}$ factors applied to correct the E_T^{jet} of the jets in the data for the two-subjet analysis.

For the three-subjet analysis, the corrections were calculated separately for each data-taking period corresponding to a change in polarization and/or lepton beam (e^+/e^-). Thus, different corrections are applied depending on the data-taking period. The results can be seen in table 7.2.

7.5.2 Detector bias and resolution

To study the effects and bias that the detector could introduce in the measurements, comparisons of the hadronic system before and after the simulation were made. The correlations between the hadron level and detector level were studied for the variables E_T^{jet}, η^{jet} and ϕ^{jet}. Jets at hadron level were matched to jets at detector level by requiring the distance between them in the $\eta - \phi$ plane to be smaller than unity. It should be noted that the studies have been done with the inclusive jet samples without any requirement on the number of subjets.

The correlation between the hadron- and detector-level jets of the MC simulation is a measure of the resolution and bias on the jet variables introduced by the detector. Any bias that may have been present was identified as a deviation from a perfect

correlation. On the other hand, the spread of the correlation reflects the detector resolution. Figure 7.1 shows the correlation between the hadron and detector levels for the jet variables E_T^{jet}, η^{jet} and ϕ^{jet} as obtained with ARIADNE in the two-subjet analysis; figure 7.2 shows the corresponding distributions for the three-subjet analysis. The distributions of $(E_T^{jet}(\mathrm{CAL}) - E_T^{jet}(\mathrm{HAD}))/E_T^{jet}(\mathrm{HAD})$, $\eta^{jet}(\mathrm{CAL}) - \eta^{jet}(\mathrm{HAD})$, and $\phi^{jet}(\mathrm{CAL}) - \phi^{jet}(\mathrm{HAD})$ for the two-subjet (three-subjet) analysis are shown in Fig. 7.3 (7.4).

As can be seen in these figures, the detector does not alter the angular direction of the jets but the jets lose energy as they go through the dead material in front of the UCAL. This loss of energy can be quantified by means of a gaussian fit to the relative difference between the hadronic level and the detector level. The correction factors are obtained as follows:

- The standard cuts were applied at the hadron level to select the jets in the MC sample. At the detector level, the cuts in the transverse energy are relaxed since the uncorrected energy is usually smaller than the corrected one.
- For each event, the jets at hadron and detector level were matched. The distance in the $\eta - \phi$ plane between the jets at hadron and detector level is calculated:

$$\Delta[hd] = \sqrt{(\eta^{jet}(CAL) - \eta^{jet}(HAD))^2 + (\phi^{jet}(CAL) - \phi^{jet}(HAD))^2}. \quad (7.4)$$

  If the smallest distance found between two jets is smaller than unity, the jets are matched. This procedure is repeated until all the jets were matched or no pair of jets is left for which the distance is less than unity.
- The mean value $< E_T^{jet}(CAL) >$ as a function of $E_T^{jet}(HAD)$ was parametrized by a straight line or set of straight lines if necessary. The fitted function has the form

$$E_T^{jet}(CAL) = m \cdot E_T^{jet}(HAD) + n. \quad (7.5)$$

  For a given jet at detector level the corrected energy is then obtained by inverting this function:

$$E_T^{jet}(COR) = \frac{E_T^{jet}(CAL) - n}{m}. \quad (7.6)$$

- The energy loss is not the same in all the detector regions, yielding a dependence in the jet pseudorapidity. Thus, the jet parameterization was done in fourteen different η^{jet} regions. For the three-subjet analsysis Fig. 7.5 shows the correlation between hadron level and detector level E_T^{jet} before any correction was applied. The improvements due to the corrections can be seen in figure 7.6.

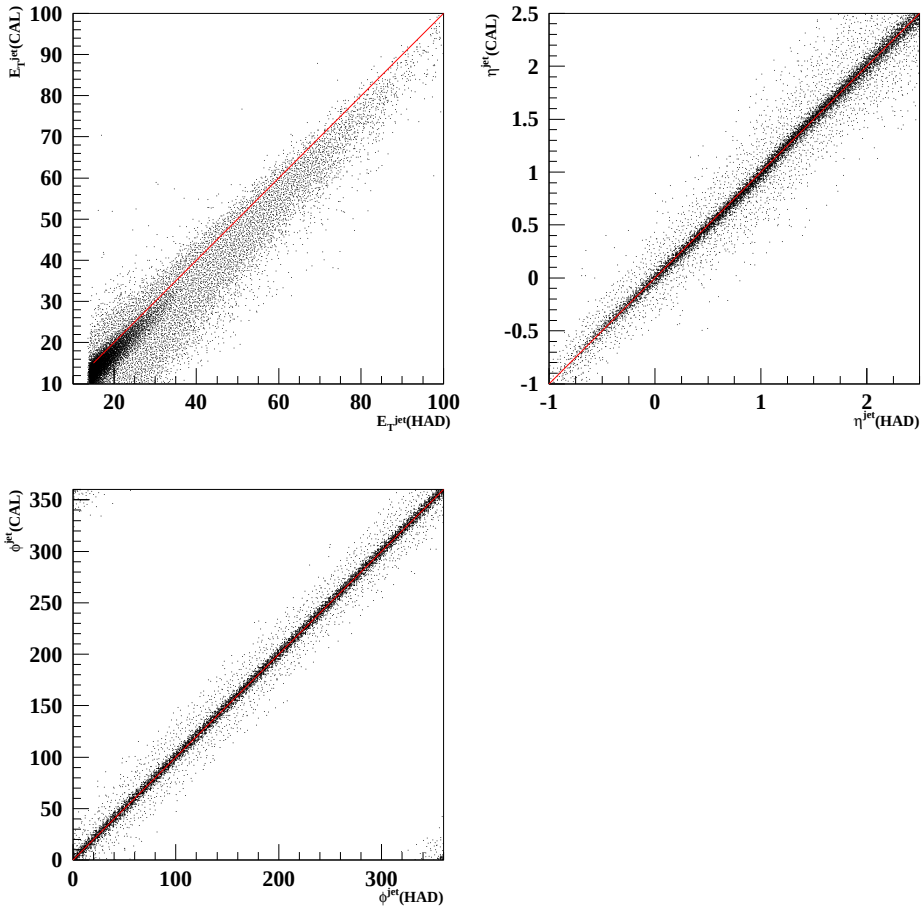

Figure 7.1: Correlations between detector and hadron levels for the jet variables E_T^{jet}, η^{jet} and ϕ^{jet} for the inclusive-jet sample of the two-subjet analysis using the CDM MC.

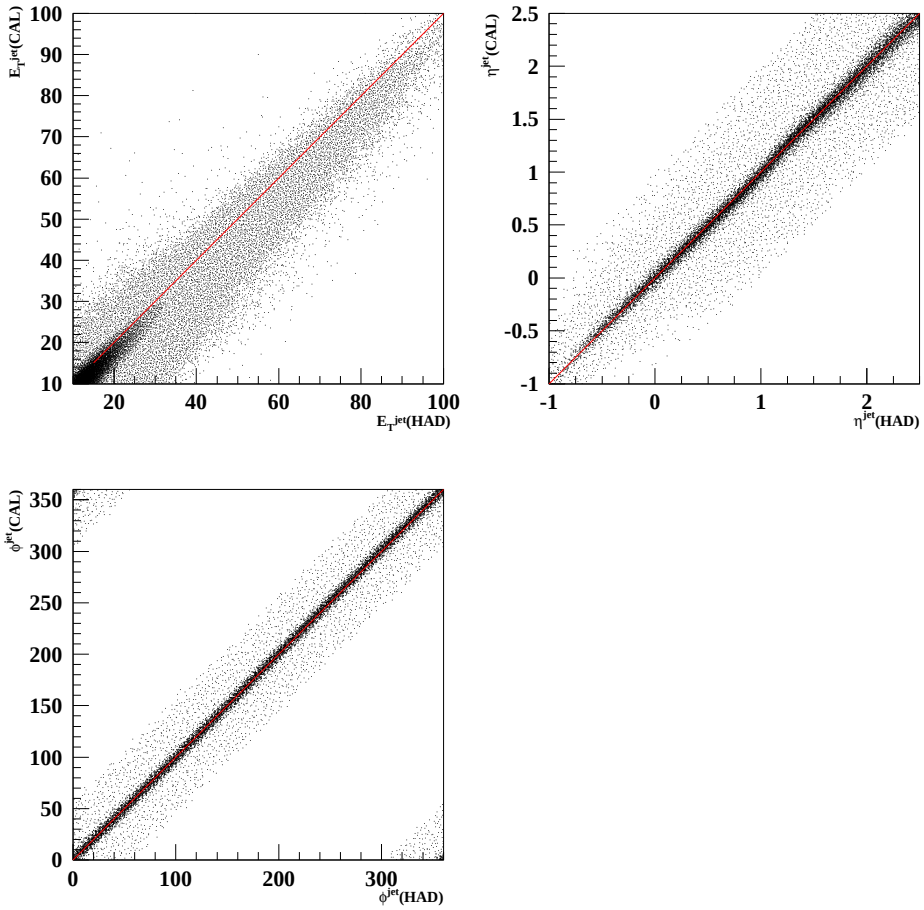

Figure 7.2: Correlations between detector and hadron levels for the jet variables E_T^{jet}, η^{jet} and ϕ^{jet} for the inclusive-jet sample of the three-subjet analysis using the CDM MC.

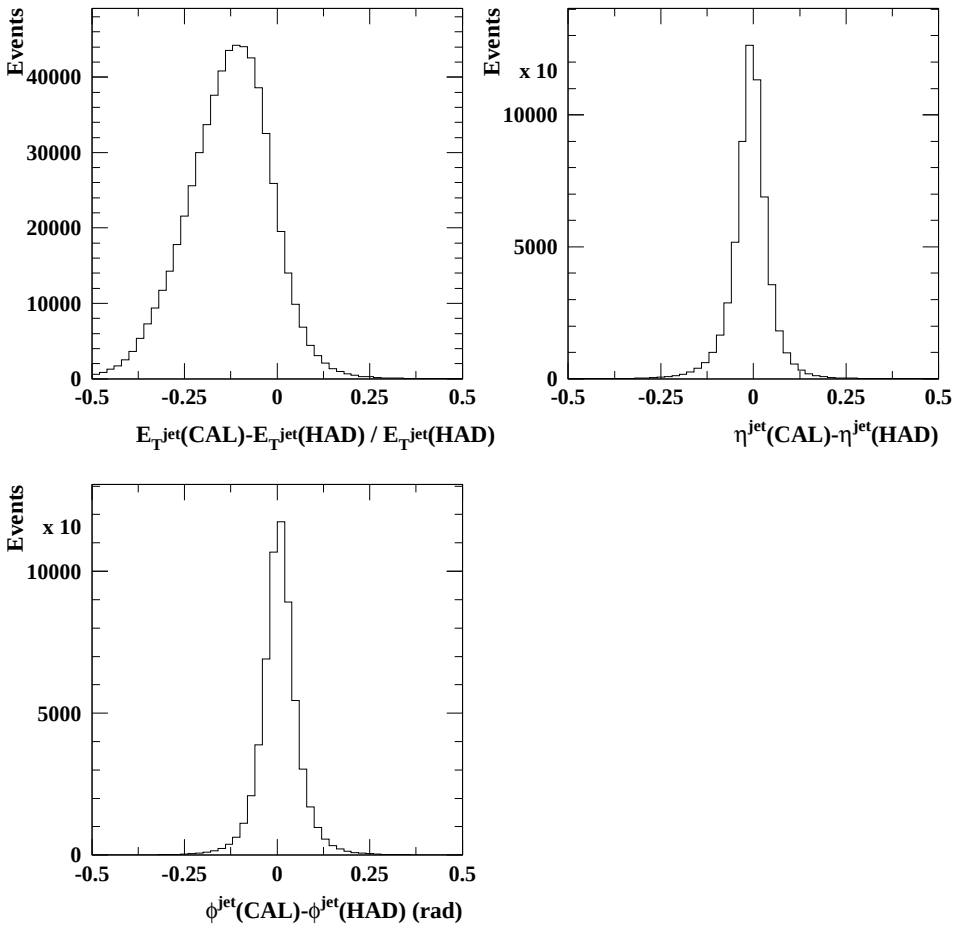

Figure 7.3: Differences between detector and hadron levels for the jet variables E_T^{jet}, η^{jet} and ϕ^{jet} for the inclusive-jet sample of the two-subjet analysis using the CDM MC.

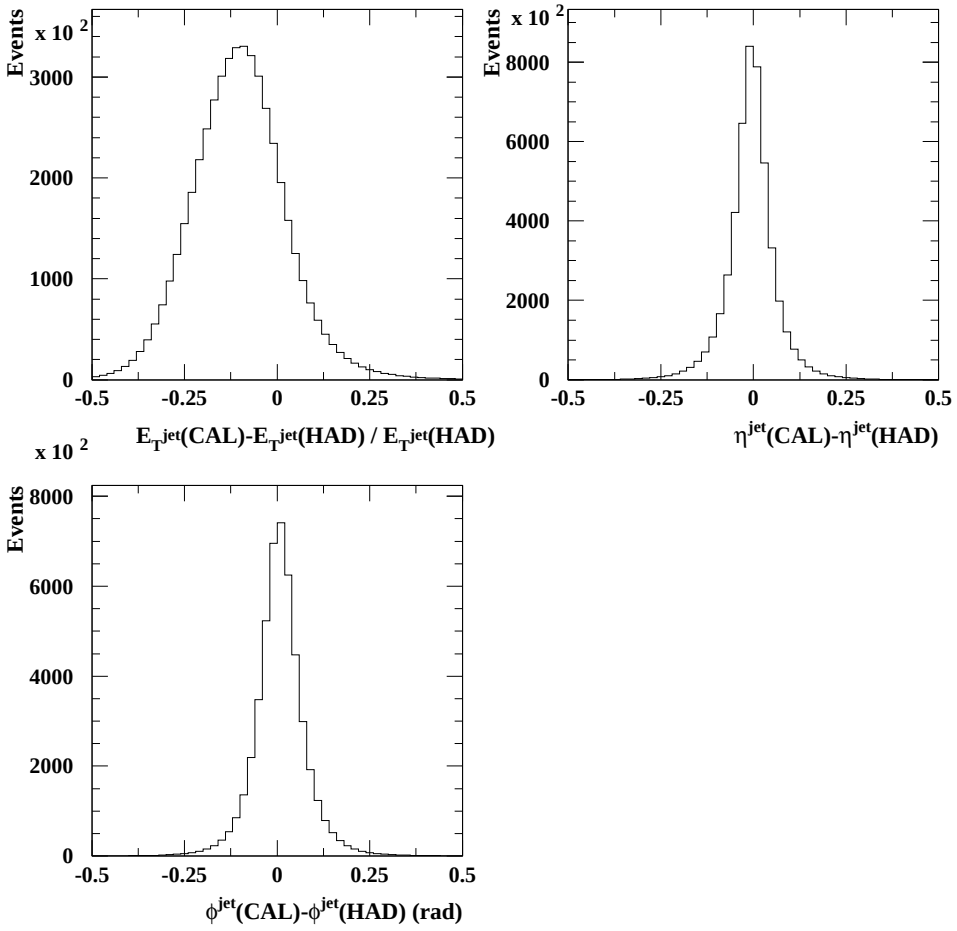

Figure 7.4: Differences between detector and hadron levels for the jet variables E_T^{jet}, η^{jet} and ϕ^{jet} for the inclusive-jet sample of the three-subjet analysis using the CDM MC.

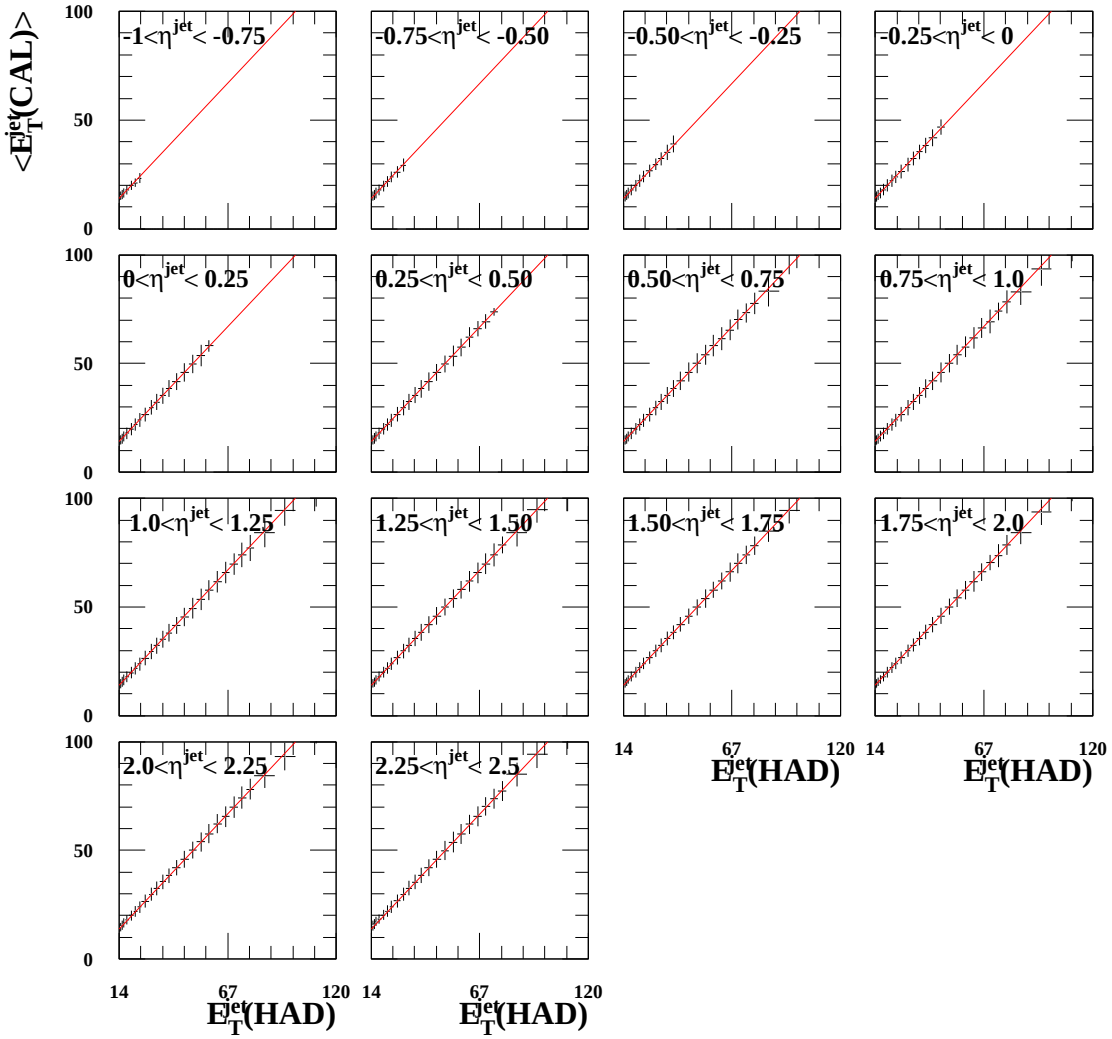

Figure 7.5: $< E_T^{jet}(CAL) >$ as a function of $E_T^{jet}(HAD)$ in each region of η^{jet} using the MC simulations based on CDM for the three-subjet analysis.

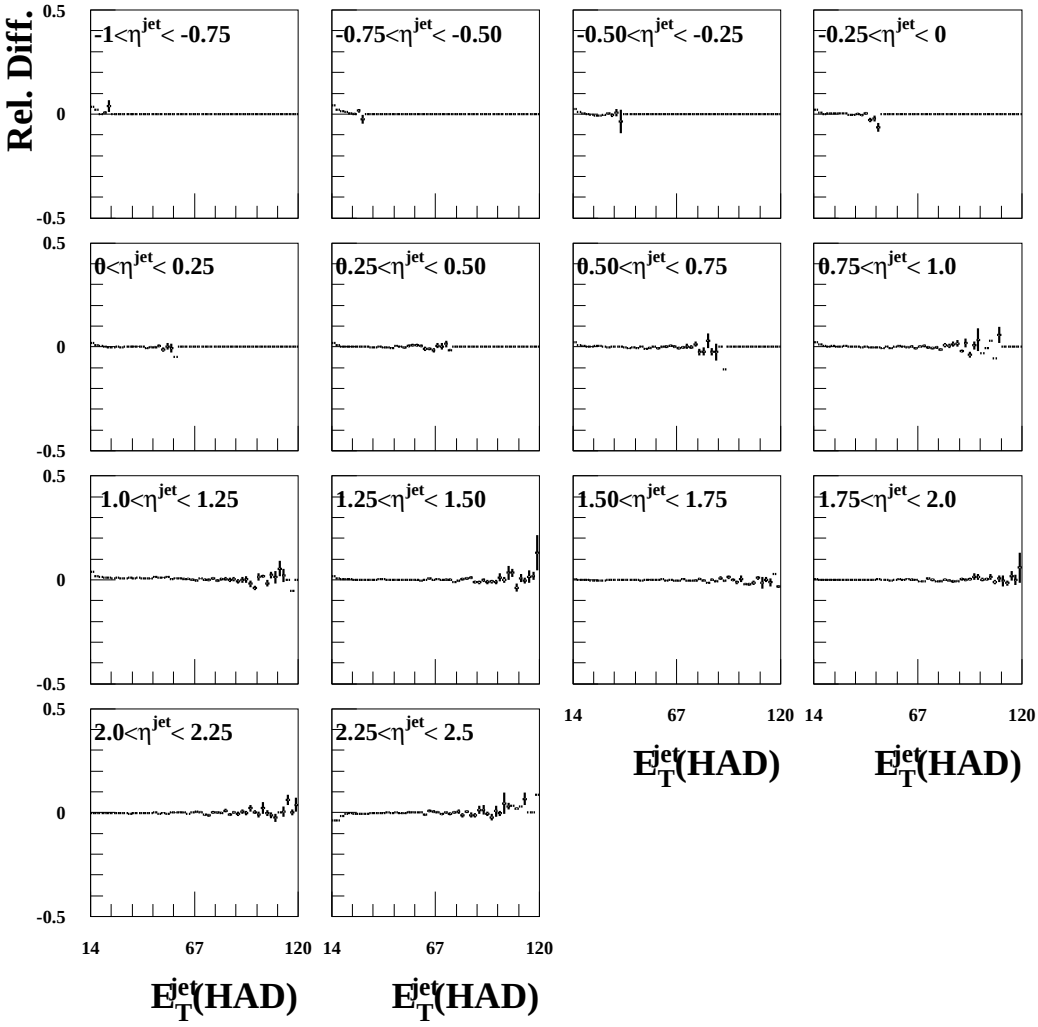

Figure 7.6: The average relative difference $< (E_T^{jet}(CORR) - E_T^{jet}(HAD))/E_T^{jet}(HAD) >$ as a function of $E_T^{jet}(HAD)$ in each region of $\eta^{jet}(HAD)$ using the MC simulations based on CDM for the three-subjet analysis.

7.6 Data and Monte Carlo distributions

The legitimacy of using the MC simulations to perform corrections and reconstruction studies relies on the fact that these simulations describe the distributions in the data sample for all the variables used. This section includes all the comparisons of the data distributions to those of the MC simulation. It should be noted that the studies have been done with the inclusive jet samples without any requirement on the number of subjets.

7.6.1 Comparisons of data and MC for the two-subjet analysis

In figs. 7.7 to 7.10 the comparisons between data and the Monte Carlo simulations based on MEPS and CDM are shown. Fig. 7.7 shows a comparison of the total energy in the calorimeter, as well as the total energy in the forward, barrel and real regions of the calorimeter. In the RCAL distribution, the peak due to the scattered electron is clearly visible.

Fig. 7.8 shows the comparisons of the distributions for the total transverse energy, the vertex position along the beam direction, Q^2_{DA} and $log_{10}(x_{DA})$, where x_{DA} is reconstructed using the double-angle method:

$$x_{DA} = \frac{E_e}{E_p} \cdot \frac{\sin\gamma_h + \sin\theta_e + \sin(\theta_e + \gamma_h)}{\sin\gamma_h + \sin\theta_e - \sin(\theta_e + \gamma_h)}. \tag{7.7}$$

Fig. 7.9 shows the comparison for the scattered electron energy, its polar angle, the p_T of the hadronic system and the number of good[2] tracks. It can be seen that the electron energy peaks at the value of the electron beam energy, 27.5 GeV, and that the electron tends to be at large angles with respect to the proton direction, as expected.

Finally, fig. 7.10 shows the distributions of the number of bad tracks, $p_T/\sqrt{E_T}$, the transverse energy of the jets and their pseudorapidity. Both MC simulations are able to describe well the distribution of the jet variables, which validates their use to provide corrections.

[2]Tracks which are associated to the vertex and fulfill the conditions $15^\circ < \theta < 164^\circ$, $0.2 < p_T < 150$ GeV and the number of degrees of freedom larger than 9.

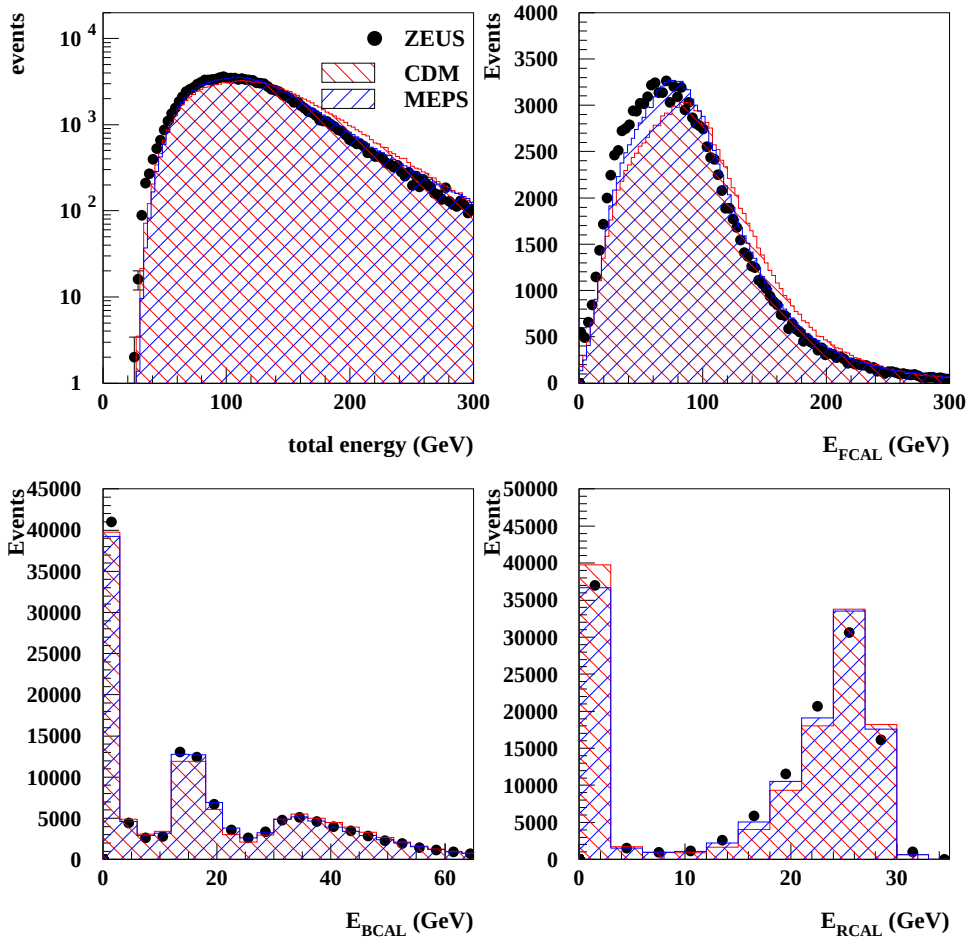

Figure 7.7: Comparison between data and the Monte Carlo simulations based on CDM and MEPS for the total energy in the calorimeter, energy in the FCAL, energy in the BCAL and energy in the RCAL. The MC distributions are normalised to the total number of events in the data.

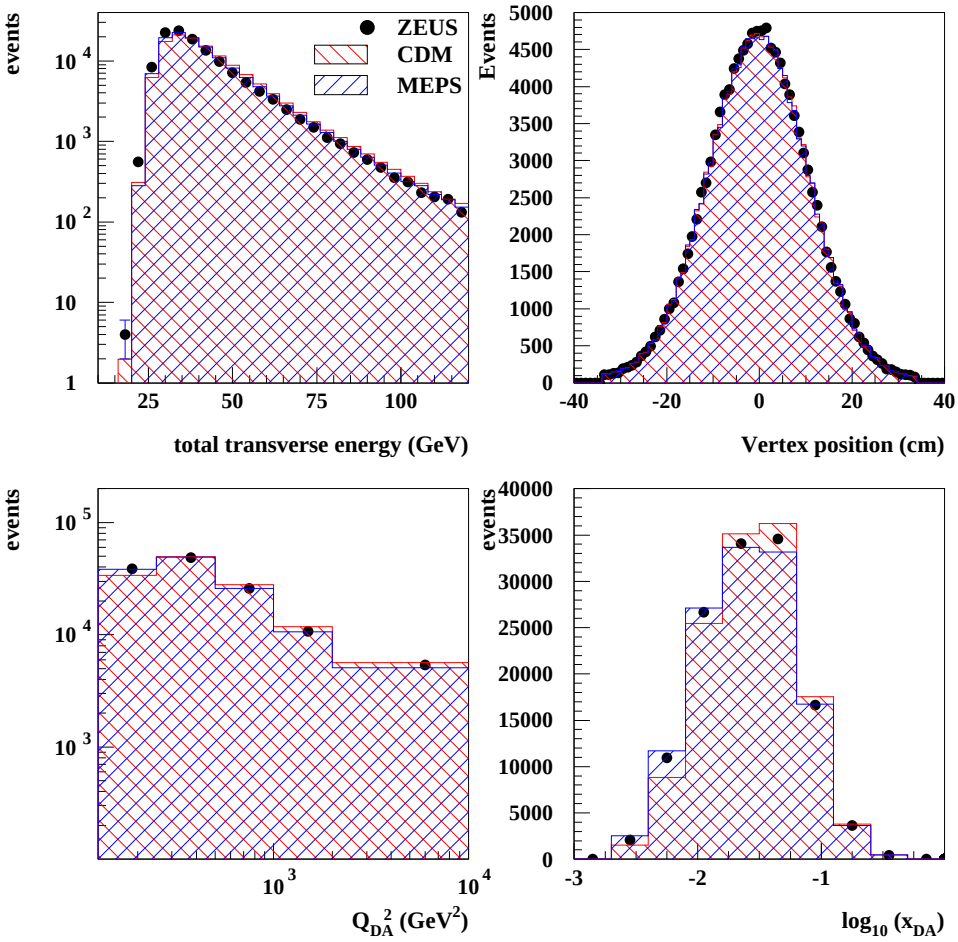

Figure 7.8: Comparison between data and the Monte Carlo simulations based on CDM and MEPS for the total transverse energy, the z-vertex, Q^2_{DA} and $log_{10}(x_{DA})$. The MC distributions are normalised to the total number of events in the data.

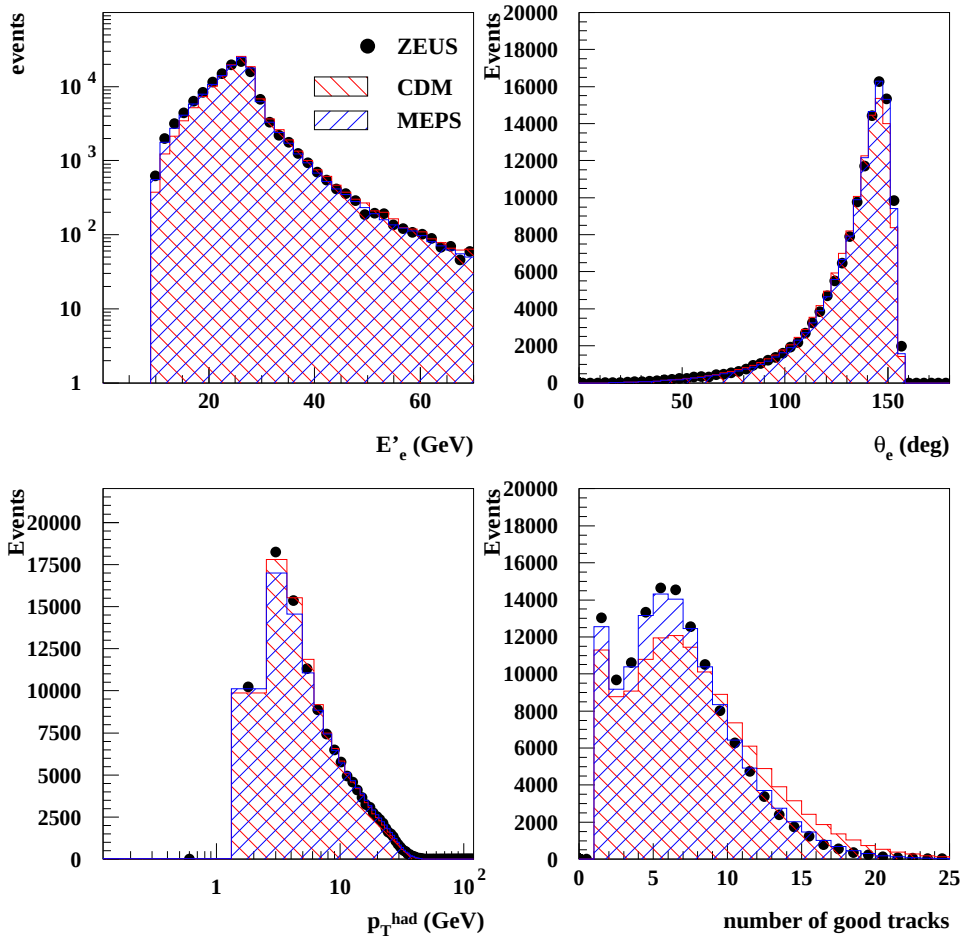

Figure 7.9: Comparison between data and the Monte Carlo simulations based on CDM and MEPS for the electron's energy, its polar angle, p_T^{HAD} and the number of good tracks. The MC distributions are normalised to the total number of events in the data.

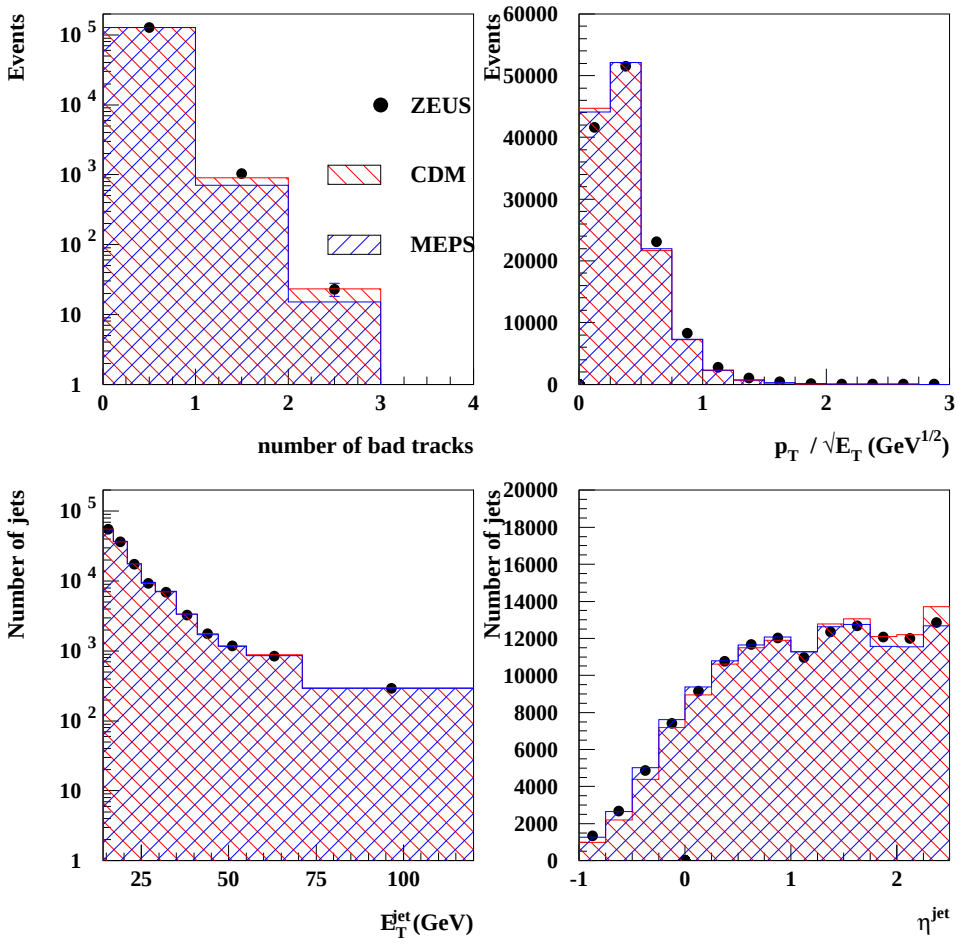

Figure 7.10: Comparison between data and the Monte Carlo simulations based on CDM and MEPS for the number of bad tracks, $p_T/\sqrt{E_T}$, E_T^{jet} and η^{jet}. The MC distributions are normalised to the total number of events (for the distributions in the number of bad tracks and $p_T/\sqrt{E_T}$) or to the total number of jets (for the distributions in E_T^{jet} and η^{jet}) in the data.

7.6.2 Data and Monte Carlo distributions for the three-subjet analysis

Comparisons between data and MC distributions for the same variables shown in the previous section but for the three-subjet analysis are shown in figures 7.11 to 7.14.

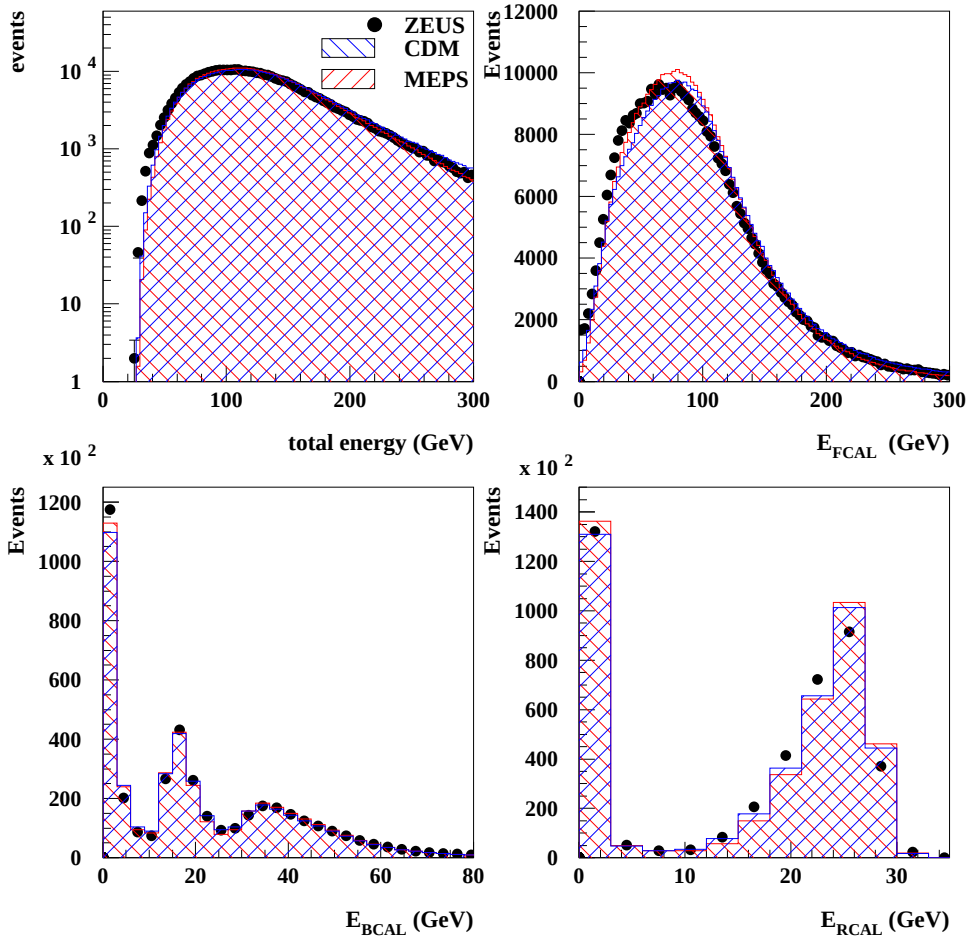

Figure 7.11: Comparison between data and the Monte Carlo simulations based on CDM and MEPS for the total energy in the calorimeter, energy in the FCAL, energy in the BCAL and energy in the RCAL. The MC distributions are normalised to the total number of events in the data.

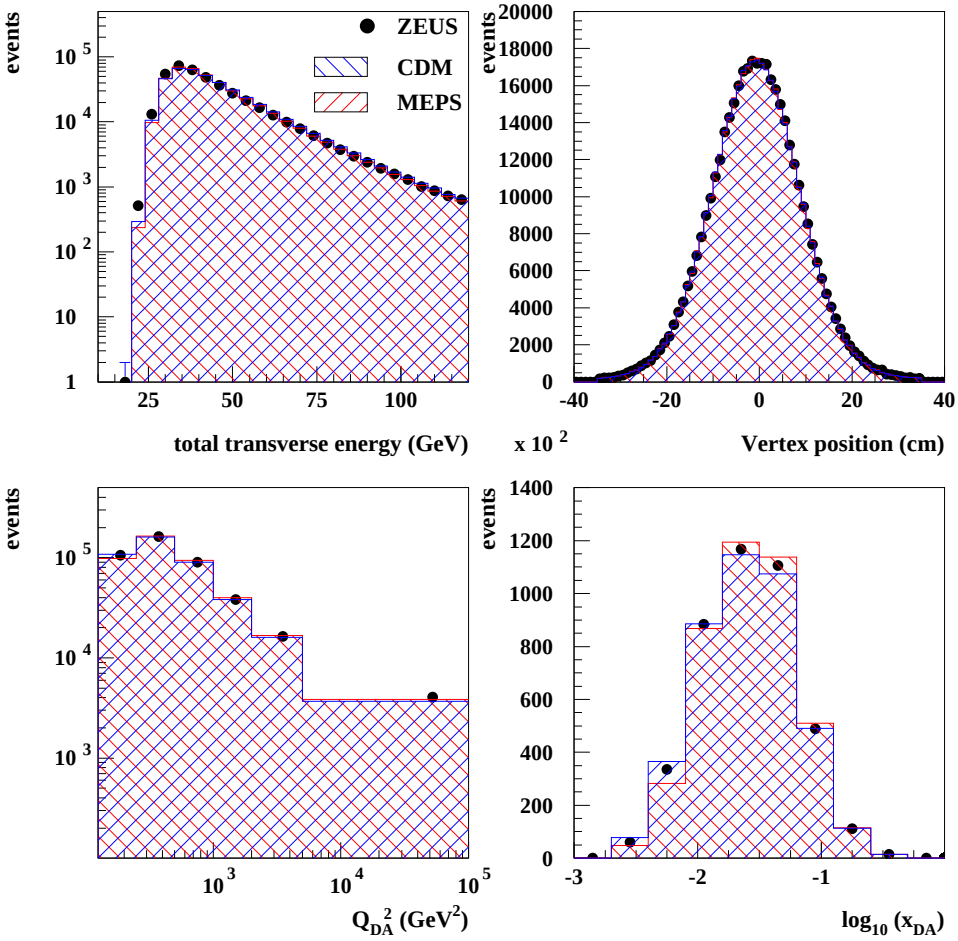

Figure 7.12: Comparison between data and the Monte Carlo simulations based on CDM and MEPS for the total transverse energy, the z-vertex, Q^2_{DA} and $log_{10}(x_{DA})$. The MC distributions are normalised to the total number of events in the data.

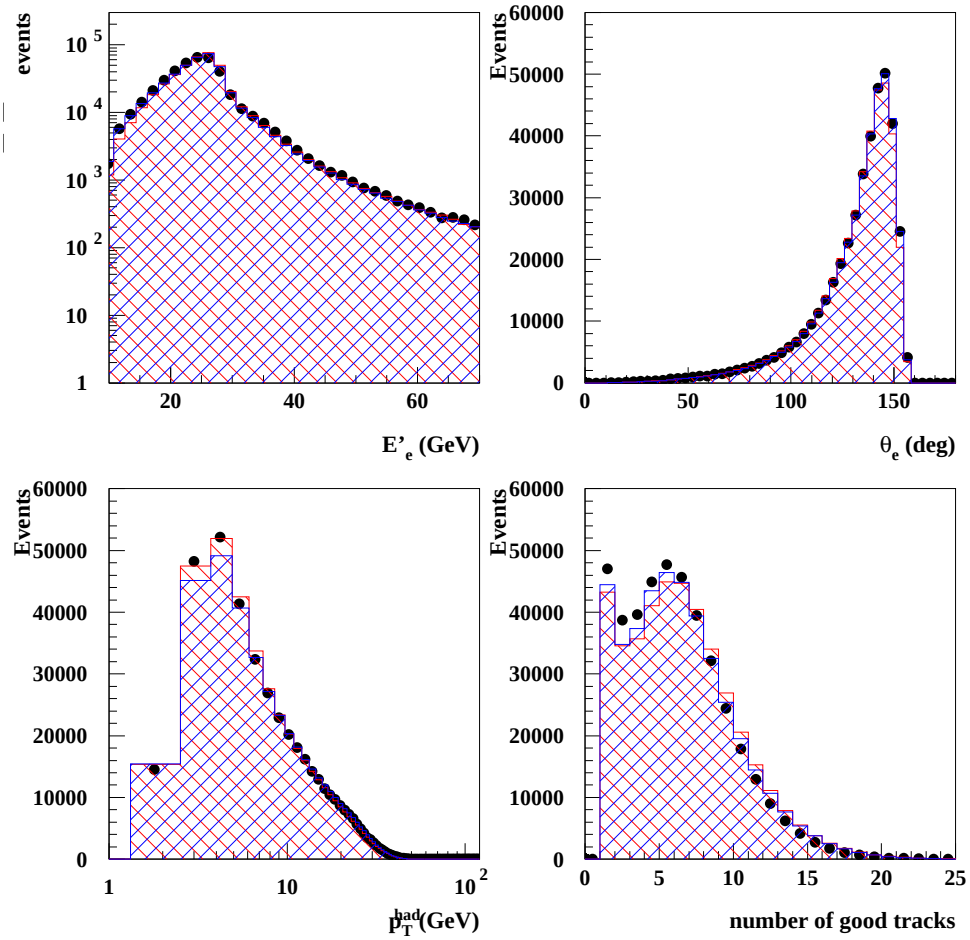

Figure 7.13: Comparison between data and the Monte Carlo simulations based on CDM and MEPS for the electron's energy, its polar angle, p_T^{HAD} and the number of good tracks. The MC distributions are normalised to the total number of events in the data.

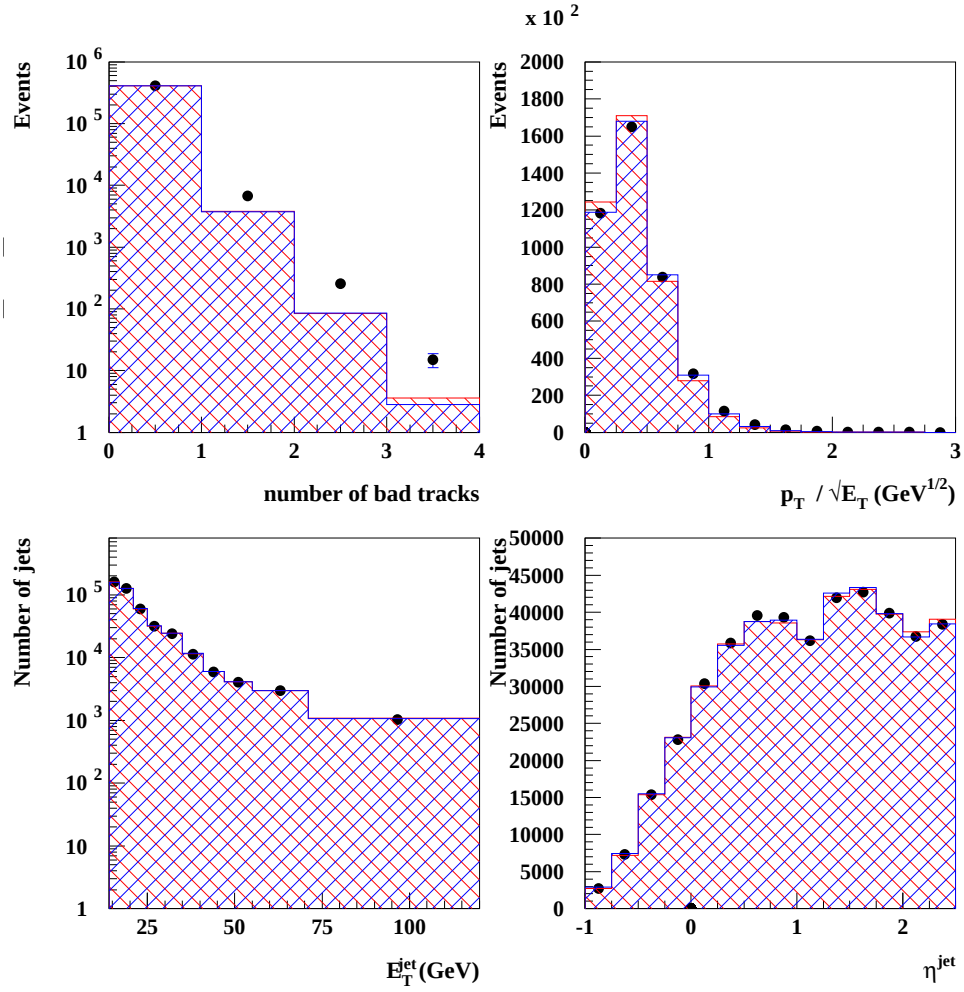

Figure 7.14: Comparison between data and the Monte Carlo simulations based on CDM and MEPS for the number of bad tracks, $p_T/\sqrt{E_T}$, E_T^{jet} and η^{jet}. The MC distributions are normalised to the total number of events (for the distributions in the number of bad tracks and $p_T/\sqrt{E_T}$) or to the total number of jets (for the distributions in E_T^{jet} and η^{jet}) in the data.

7.6.3 Comparisons between data and MC for subjet distributions in the two-subjet analysis

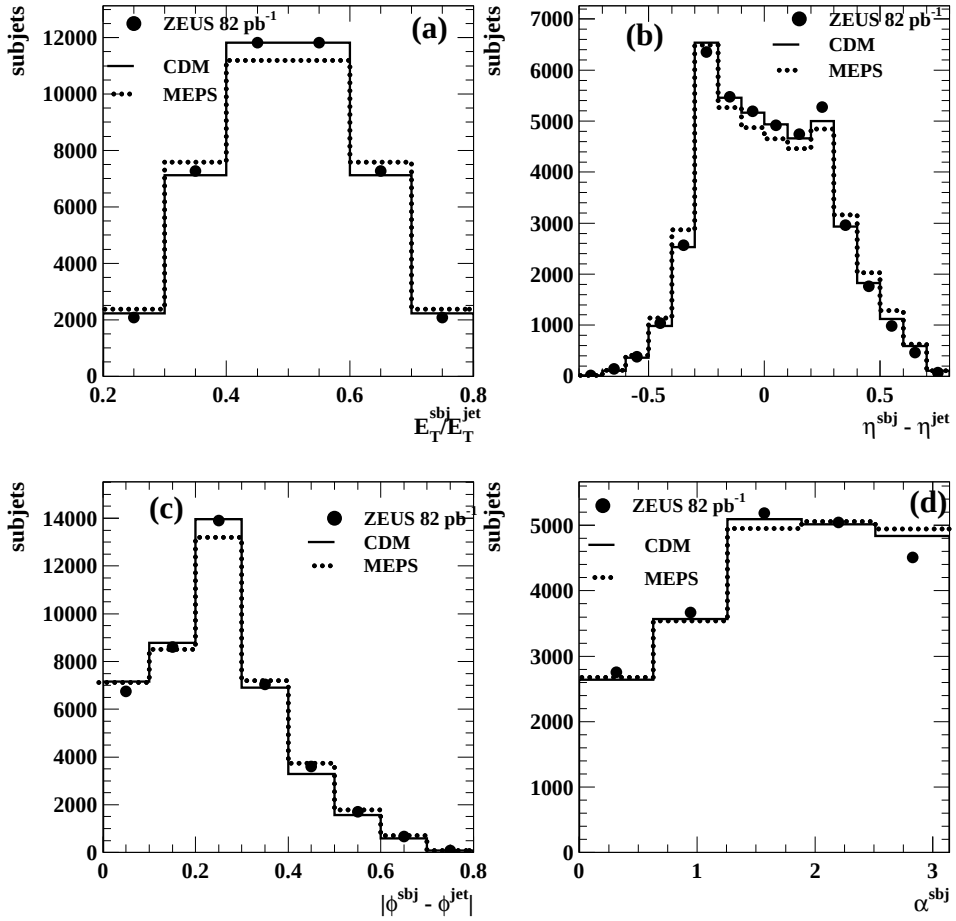

Figure 7.15: Comparison between data and the Monte Carlo simulations based on CDM and MEPS for (a) E_T^{sbj}/E_T^{jet}, (b) $\eta^{sbj} - \eta^{jet}$, (c) $|\phi^{sbj} - \phi^{jet}|$ and (d) α^{sbj}. The MC distributions are normalised to the total number of subjets in the data.

In this section, a comparison between the data and MC is shown for the variables used to study the substructure of jets. This comparison can be seen in figure 7.15, where it can be appreciated that both MC models describe the data reasonably well although it is found that the description provided by MEPS is somewhat poorer. The fact that both MC models provide a good description of the data at detector level is a fundamental feature since it shows that the effects and biases introduced by the detector are well understood and therefore validates the usage of the models to correct the data for those effects. Both models describe adequately the data

and therefore an average will be used to estimate these corrections. The difference between them will then be taken as the systematic uncertainty associated to the modelling of the parton shower, as will be explained in chapter 9.

7.6.4 Comparisons between data and MC for subjet distributions in the three-subjet analysis

The correlations between the hadron and detector levels for the subjet variables are shown in figures 7.16 and 7.17. In figures 7.18 and 7.19 the comparison for the variables used in the three-subjet analysis can be seen. The Monte Carlo distributions are normalised to the data and a good description is achieved. The distribution of $\eta_{low}^{sbj} - \eta^{jet}$ is the one that exhibits some discrepancies; the lowest-transverse-energy subjet in the data populates the region of $\eta_{low}^{sbj} - \eta^{jet} < 0$ with a slightly larger frequency than what the models account for.

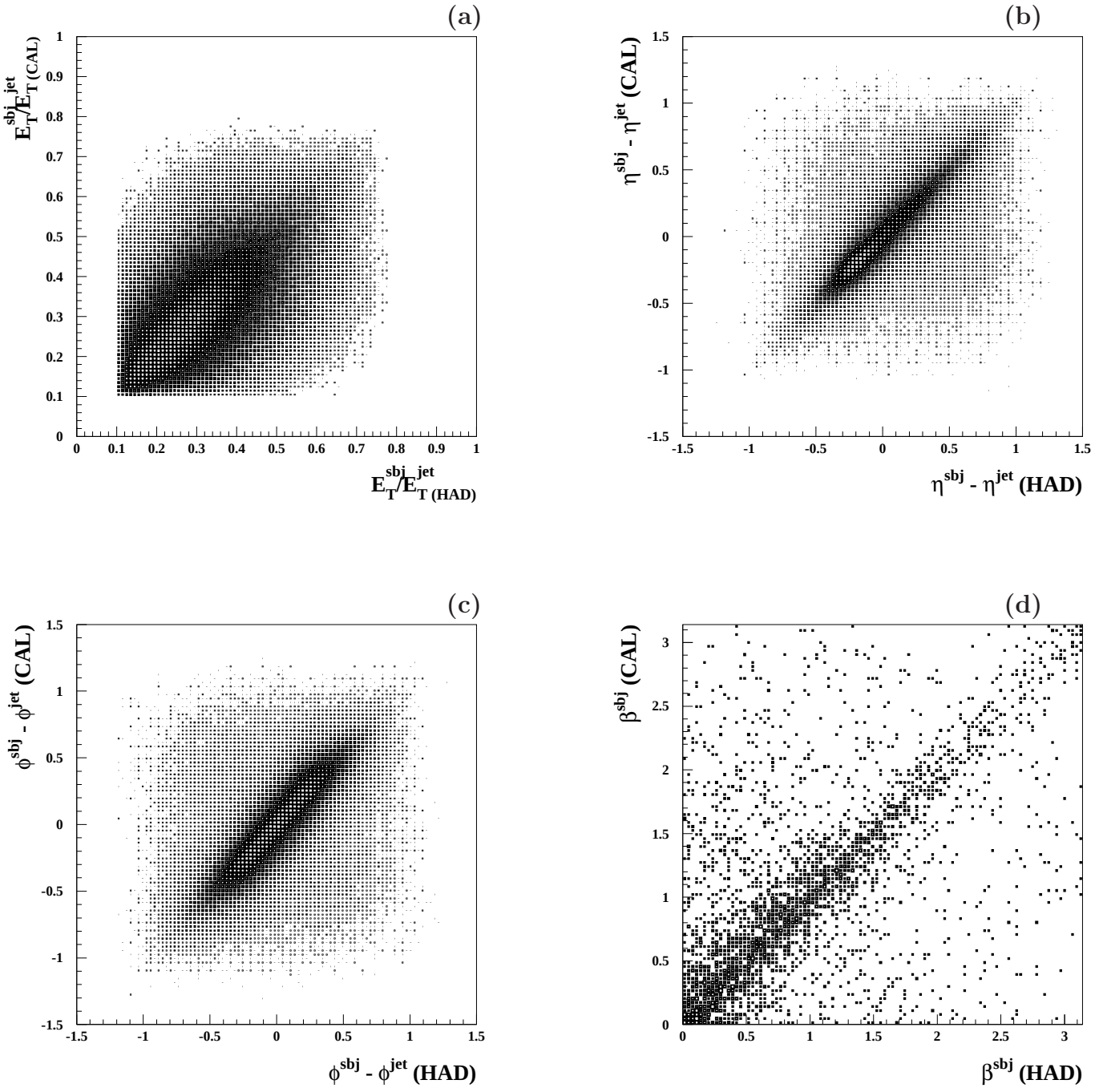

Figure 7.16: Correlations between the hadron and detector levels for the subjet variables (a) E_T^{sbj}/E_T^{jet}, (b) $\eta^{sbj} - \eta^{jet}$, (c) $\phi^{sbj} - \phi^{jet}$ and (d) β^{sbj} using the MEPS MC.

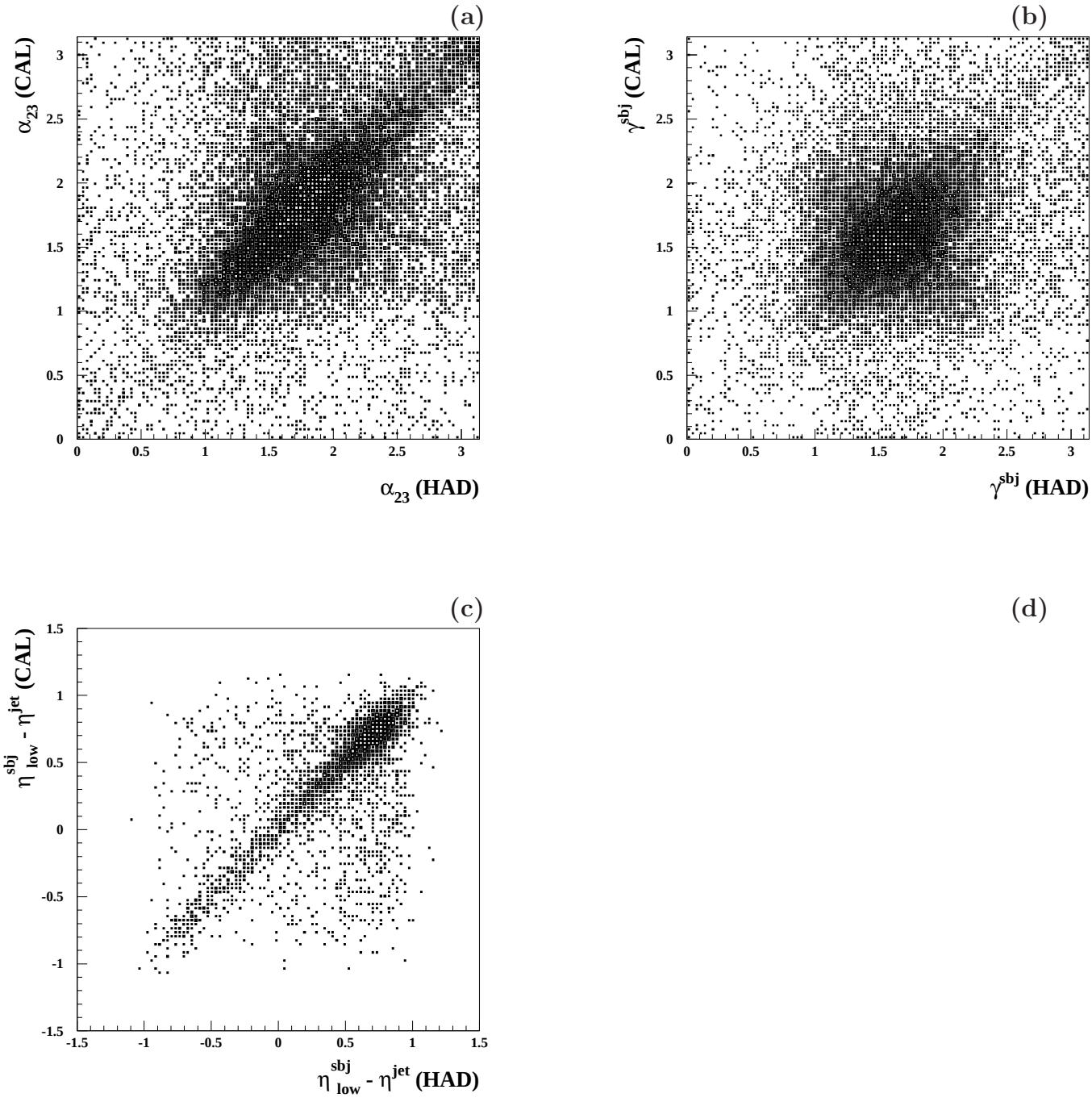

Figure 7.17: Correlations between the hadron and detector levels for the subjet variables (a) α_{23}, (b) γ^{sbj} and (c) $\eta^{sbj}_{low} - \eta^{jet}$ using the MEPS MC.

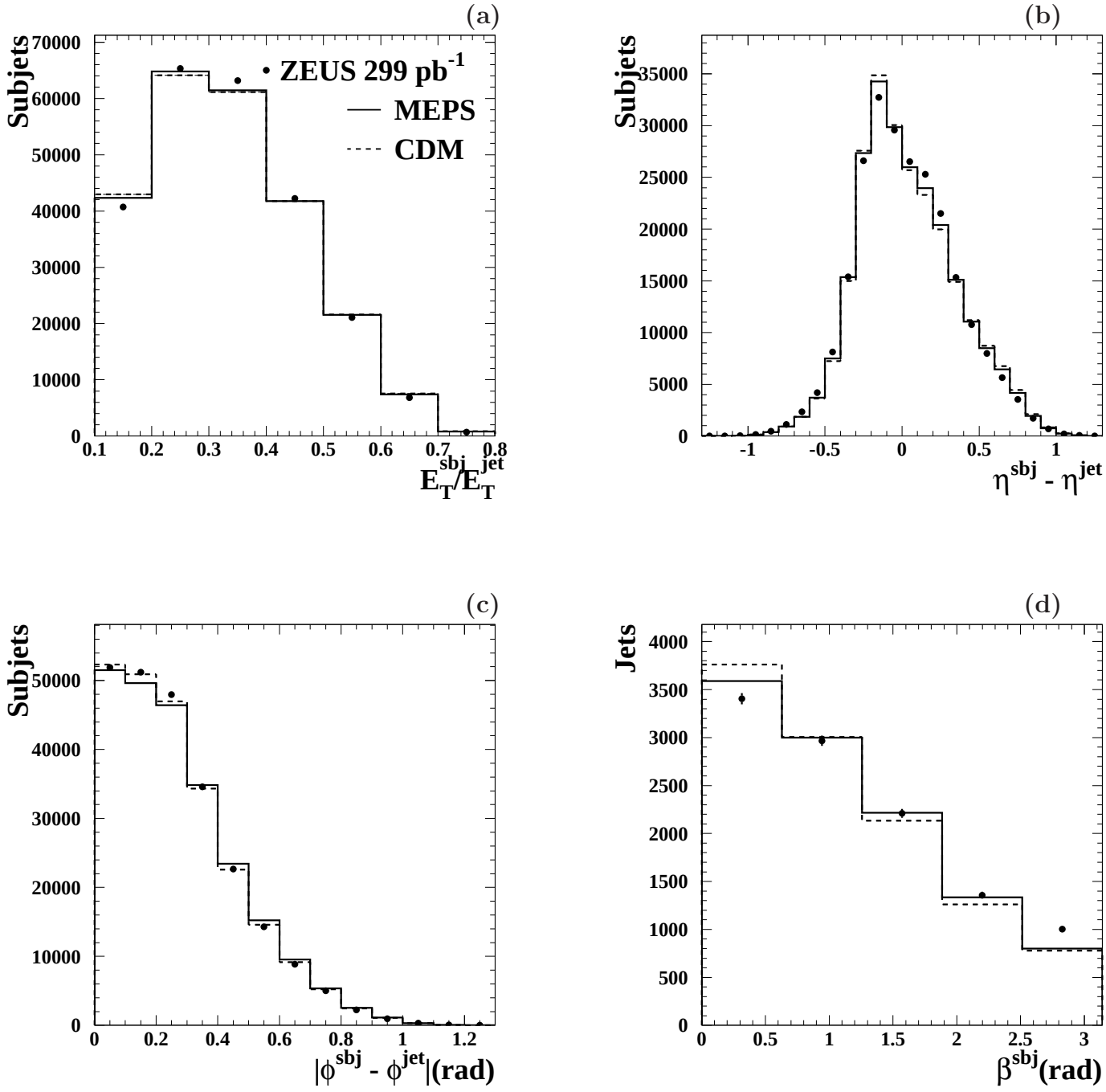

Figure 7.18: Comparisons between data and the Monte Carlo simulations based on CDM and MEPS for (a) E_T^{sbj}/E_T^{jet}, (b) $\eta^{sbj} - \eta^{jet}$, (c) $|\phi^{sbj} - \phi^{jet}|$ and (d) β^{sbj}. The MC distributions are normalised to the total number of subjets in the data.

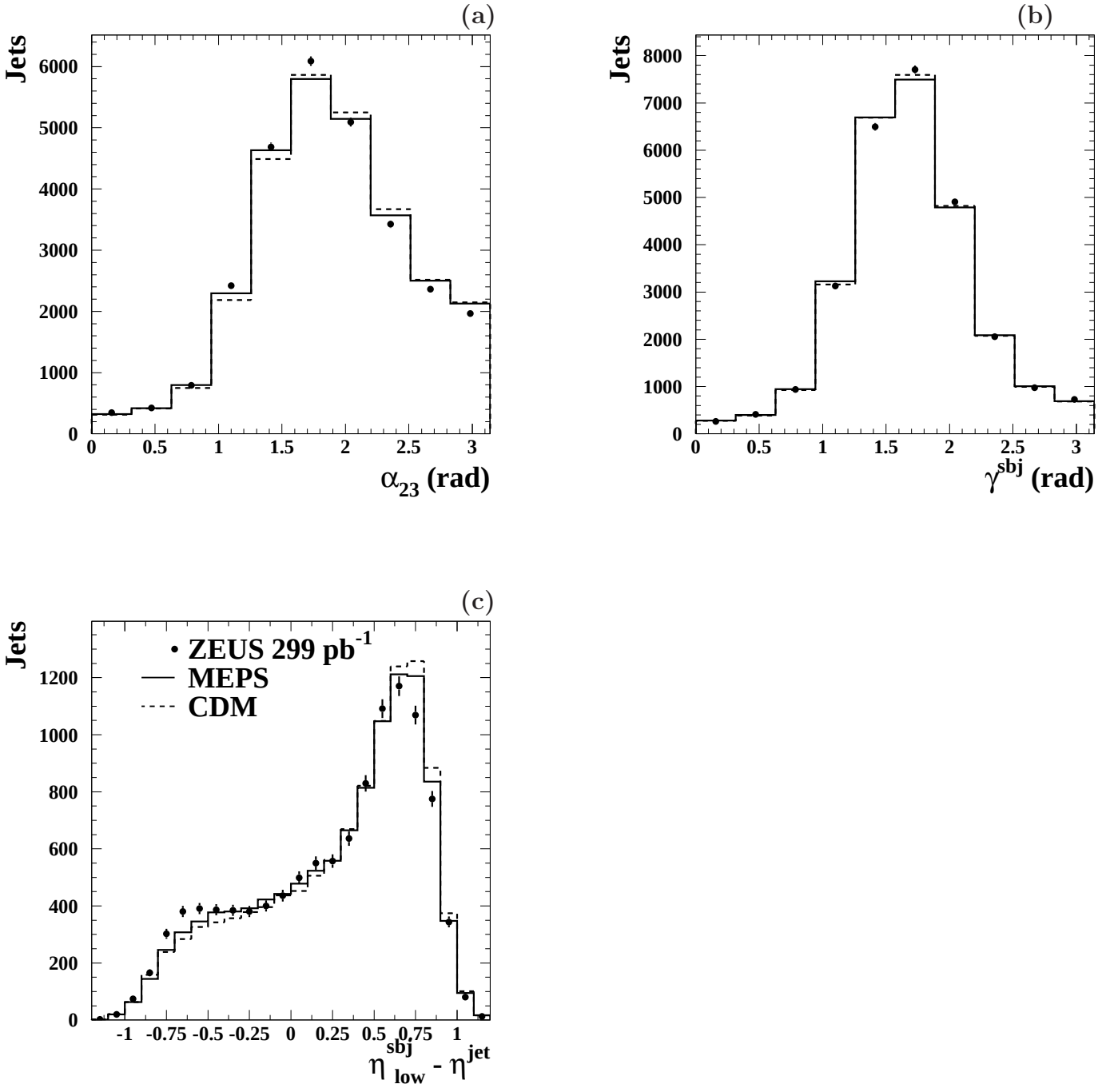

Figure 7.19: Comparisons between data and the Monte Carlo simulations based on CDM and MEPS for (a) α_{23}, (b) γ^{sbj} and (c) $\eta^{sbj}_{low} - \eta^{jet}$. The MC distributions are normalised to the total number of subjets in the data.

Chapter 8

Correction factors and systematic uncertainties

8.1 Correction factors

As already mentioned in the previous chapter, the legitimacy of using the Monte Carlo simulations to obtain corrections rests on how well the simulations describe the distributions that are to be corrected. We have now seen how this is indeed the case for both Monte Carlo models. In this chapter, the correction factors as well as the sources of systematic uncertainties are presented.

The data distributions were corrected for detector effects to compute the measured differential cross sections. These corrections took into account the efficiency of the trigger, the selection criteria and the purity and efficiency of the jet and subjet reconstruction. The correction factors were applied using the bin-by-bin method and were obtained from the simulations after the E_T^{jet} corrections were applied to the jets.

The conventional approach of quantifying possible systematic uncertainties is to vary the assumptions by reasonable amounts, such as their known or estimated uncertainty, and calculate the impact of such variations on the final results by taking the difference induced by these variations as an estimation of the uncertainty. Ideally, the analysis should have little sensitivity to small variations in quantities the exact values of which are not fully known, such as the background subtraction cuts, the choice of a certain parton-cascade model or the energy scale of the jets. The analysis is carried through with independent variations and the induced changes in the final results are added in quadrature and taken as the overall systematic uncertainty.

8.1.1 Acceptance correction factors for the two-subjets analysis

The subjet distributions were corrected for detector effects using the bin-by-bin method. Since both MC simulations were able to describe adequately the data, an average of the acceptance correction factors evaluated with each of the two models was used. The difference between the average and either CDM or MEPS was then taken as the systematic uncertainty due to the modelling of the parton cascade.

The acceptance correction factors (C_{ACC}) are defined as $C_{ACC} = \frac{purity}{efficiency}$, where efficiency is the fraction of generated events in a given bin that are reconstructed in that same bin, whereas purity is defined as the fraction of reconstructed events in a given bin that are generated in that same bin, where 'generated' refers to the hadronic level and 'reconstructed' to the detector level. Thus, the correction factor is given by:

$$C_{ACC} = \frac{P}{E} = \frac{(N_{HAD} \bigcap N_{DET})/N_{DET}}{(N_{HAD} \bigcap N_{DET})/N_{HAD}} = \frac{N_{HAD}}{N_{DET}}. \tag{8.1}$$

Thus, if N_i^{DAT} is the number of jets (or subjets) reconstructed in a given bin x_i, with a width of Δx_i, the corrected differential cross section is given by

$$\frac{d\sigma_i^{corr}}{dx} = \frac{N_i^{DAT}}{(\Delta x_i)\mathcal{L}} \cdot \frac{N_{HAD,i}^{MC}}{N_{DET,i}^{MC}}, \tag{8.2}$$

where $\mathcal{L}$ is the integrated luminosity and $N_{HAD,i}^{MC}$ ($N_{DET,i}^{MC}$) is the number of jets or subjets in the MC at hadron (detector) level in the given bin i.

Since the differential cross sections are normalised, the only effect the corrections have is to change the shape of the data distributions. In order to visualize the change in shape induced by the corrections, figure 8.1 shows the ratio of the normalised distributions at hadron level over those at detector level. It is shown that the effect of the corrections is to modify the shape of the data distributions by typically less than 20%.

The corresponding figures for the evolution of the distributions with E_T^{jet}, η^{jet}, Q^2 and Bjorken's x, are shown in the appendix.

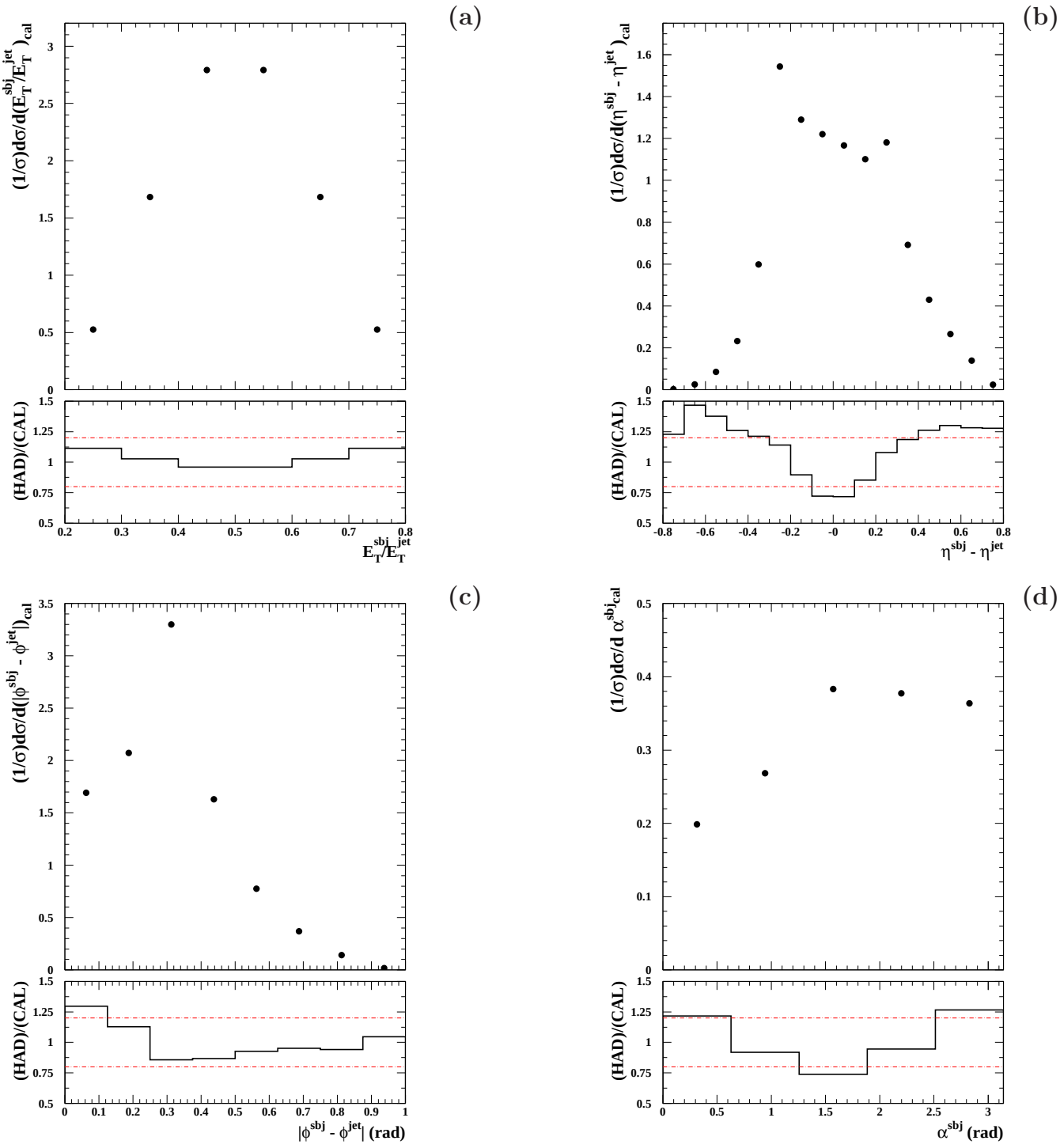

Figure 8.1: The normalised distributions in the Monte Carlo at detector level for the two-subjet analysis (dots) as functions of a) E_T^{sbj}/E_T^{jet}, b) $\eta^{sbj} - \eta^{jet}$, c) $|\phi^{sbj} - \phi^{jet}|$ and d) α^{sbj}. The lower plots show the ratio of the normalised distributions at hadron level over those at detector level. The horizontal dot-dashed lines represent changes of 20%.

8.1.2 Acceptance correction factors for the three-subjets analysis

In this case, although both Monte Carlo models were able to adequately reproduce the data at detector level, it was observed that MEPS was generally able to give a better description of the data than CDM. The data were therefore corrected with MEPS as default and the correction with CDM was taken as an alternative to estimate the systematic uncertainty due to the modelling of the parton shower. Figures 8.2 and 8.3 show the normalised distributions at detector level together with the ratios of the normalised distributions at hadronic level over those at detector level, which quantify the change in shape induced by the corrections. The vertical lines in the plot show the regions where there is sizeable statistics in the data. The horizontal dot-dashed lines in the lower plots indicate modifications of $\pm 20\%$. As can be seen in these figures, it is generally the case that the corrections applied do not modify the shape by more than 20%.

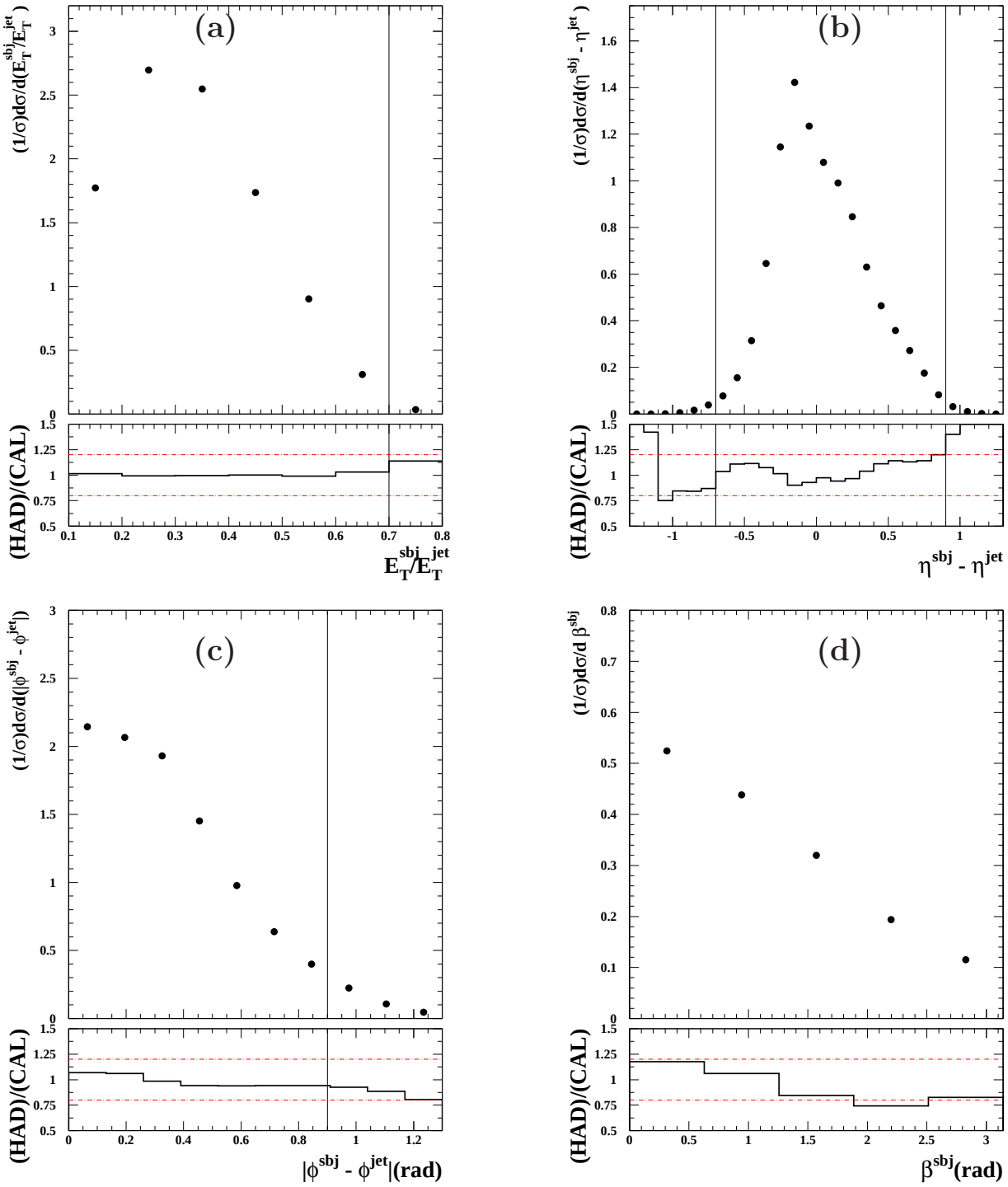

Figure 8.2: The normalised distributions in the Monte Carlo at detector level for the three-subjet analysis (dots) as functions of a) E_T^{sbj}/E_T^{jet}, b) $\eta^{sbj} - \eta^{jet}$, c) $|\phi^{sbj} - \phi^{jet}|$ and d) β^{sbj}. The lower plots show the ratio of the normalised distributions at hadron level over those at detector level. The horizontal dot-dashed lines represent changes of 20%.

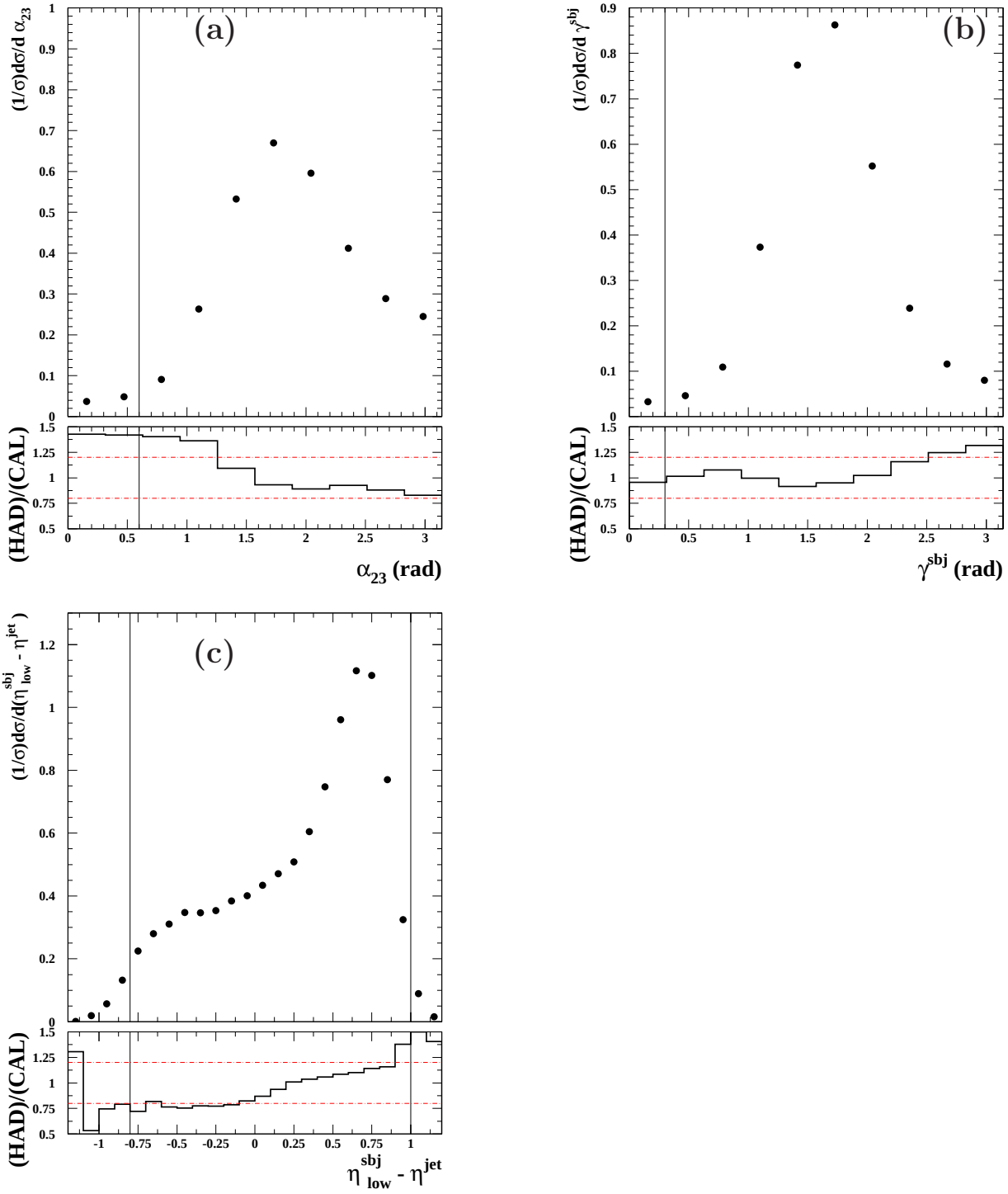

Figure 8.3: The normalised distributions in the Monte Carlo at detector level for the three-subjet analysis (dots) as functions of a) α_{23}, b) γ^{sbj} and c) $\eta^{sbj}_{low} - \eta^{jet}$. The lower plots show the ratio of the normalised distributions at hadron level over those at detector level. The horizontal dot-dashed lines represent changes of 20%.

8.1.3 Parton-to-hadron corrections. Two-subjet analysis

The final state in a fixed-order pQCD calculation is a set of partons. To compare the data and theory at the same level, parton-to-hadron correction factors were obtained and applied to the DISENT predictions. In an analogous manner as in the data, the correction factors C_{PH} are defined to be:

$$C_{PH,i} = \frac{N^{MC}_{HAD,i}}{N^{MC}_{PAR,i}}, \tag{8.3}$$

where $N^{MC}_{PAR,i}$ stands for the number of jets or subjets of partons in the Monte Carlo. As previously stated, the description of the fixed-order calculation by the partonic level of the Monte Carlo was improved by performing a reweighting of the contributing processes at parton level. The reweighting is then also applied to the hadronic level for correction purposes only. Fig. 8.4 shows a comparison between the predictions of pQCD at NLO with the distributions in the MC after they have been reweighted.

As for the acceptance correction factors, the effect that these corrections induce on the pQCD calculations is to modify the shape of the distributions. Figure 8.5 shows the ratios of the normalised distributions at hadron level over those at parton level, which quantify the changes in shape. It is shown that the changes in shape induced by the hadronization corrections are generally below 20%.

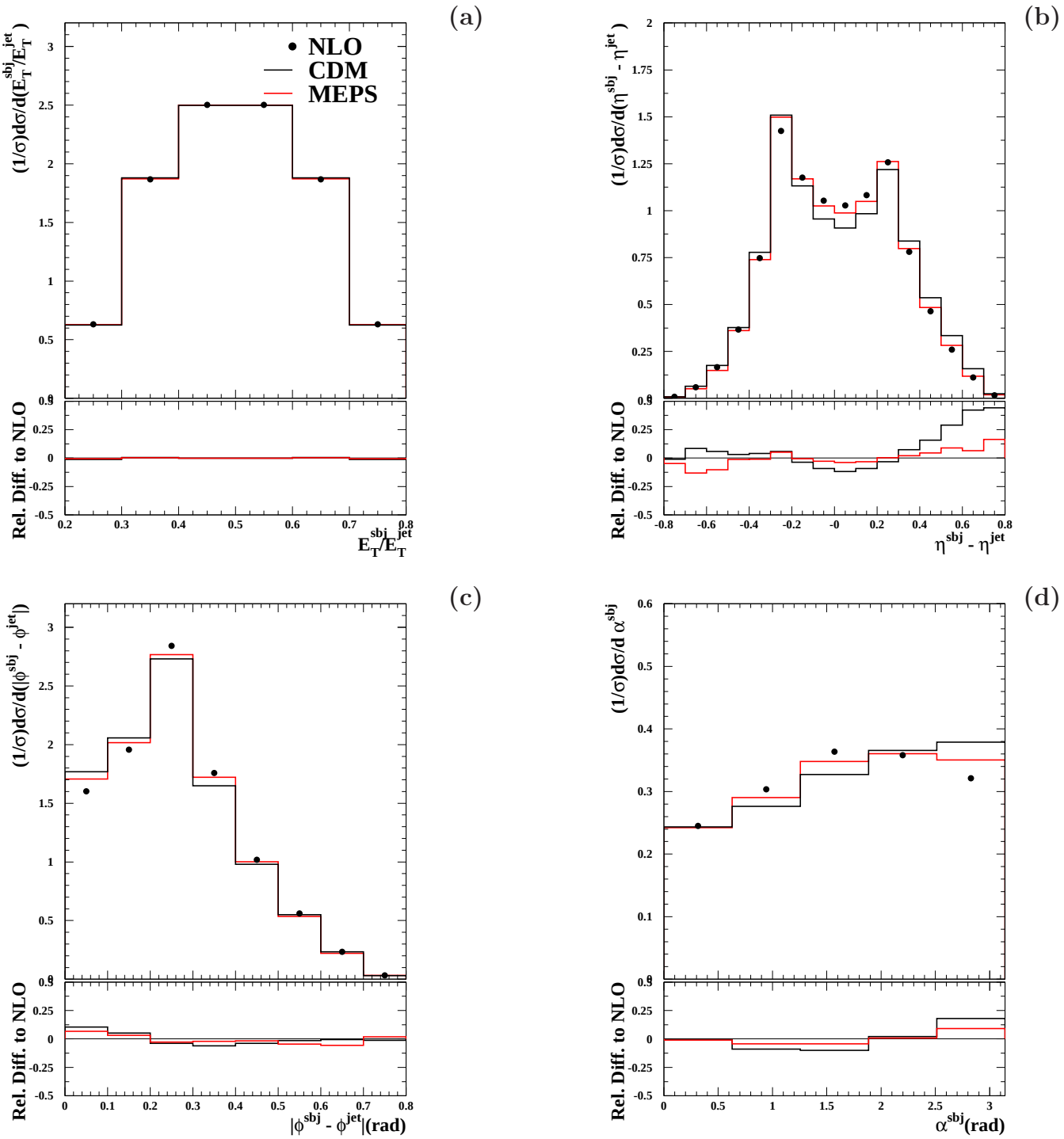

Figure 8.4: The predictions for the normalised differential cross sections at NLO in the two-subjet analysis (dots) compared with the distributions at the parton level in the Monte Carlo simulations based on CDM (black lines) and MEPS (red lines). The distributions shown are: a) E_T^{sbj}/E_T^{jet}, b) $\eta^{sbj} - \eta^{jet}$, c) $|\phi^{sbj} - \phi^{jet}|$ and d) α^{sbj}. The lower plots show the relative differences of the distributions in the MC with respect to the NLO predictions.

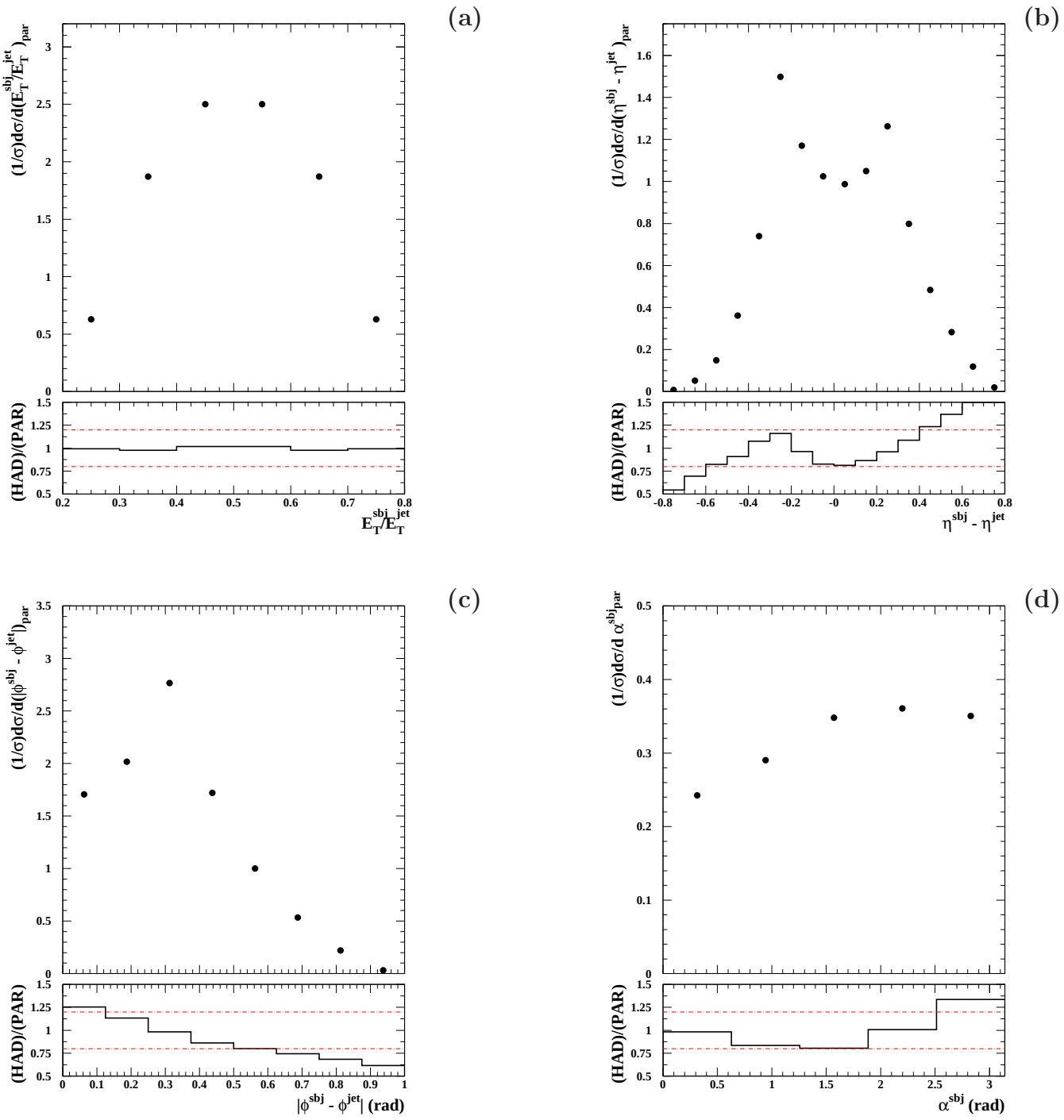

Figure 8.5: The normalised distributions in the Monte Carlo at parton level for the two-subjet analysis (dots) as functions of a) E_T^{sbj}/E_T^{jet}, b) $\eta^{sbj} - \eta^{jet}$, c) $|\phi^{sbj} - \phi^{jet}|$ and d) α^{sbj}. The lower plots show the ratio of the normalised distributions at hadron level over those at parton level. The horizontal dot-dashed lines represent changes of 20%.

8.1.4 Parton-to-hadron corrections. Three-subjet analysis

Let's now turn to the corresponding correction factors for the three-subjet analysis. In this case, a reweighting of the parton level was not needed since both Monte Carlo models were able to provide a good description of the calculations at both LO ($\mathcal{O}(\alpha_s^2)$) and NLO ($\mathcal{O}(\alpha_s^3)$). Fig. 8.6 and 8.7 show the comparison between the NLO calculations and the partonic-level distributions in the MC models. It is also observed that MEPS generally provides a slightly better description of the fixed-order calculations and, thus, the corrections are obtained with MEPS. The correction with CDM was taken as an alternative to estimate the theoretical uncertainty due to the modelling of the parton shower.

Figures 8.8 and 8.9 show the ratios of the normalised distributions at hadron level over those at parton level, which accounts for the changes in shape induced in the fixed-order calculations by the corrections. The conclusion drawn in the previous section also holds; the corrections change the shape of the fixed-order calculations by a factor which is typically smaller than 20%.

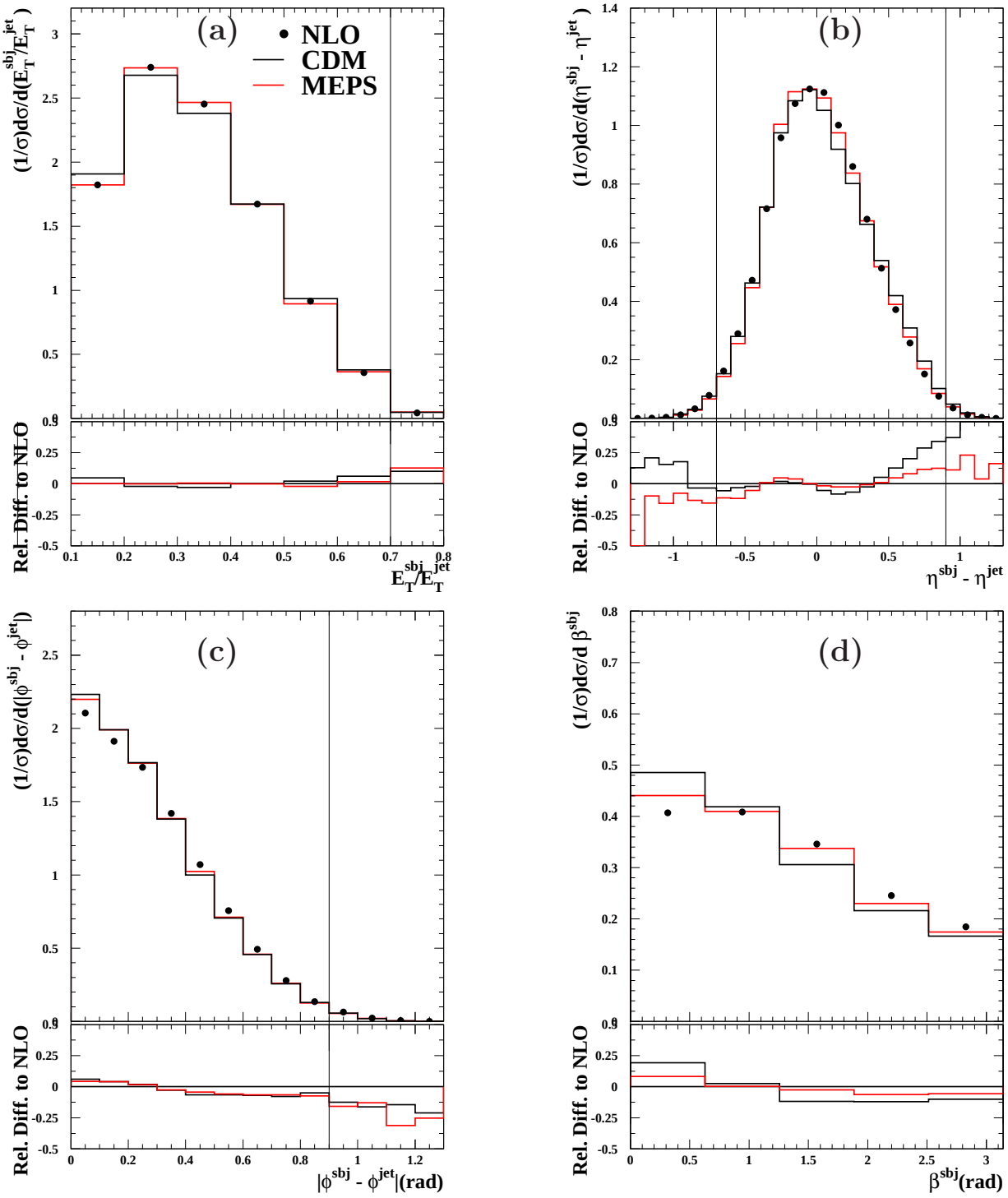

Figure 8.6: The predictions for the normalised differential cross sections at NLO in the three-subjet analysis (dots) compared with the distributions at the parton level in the Monte Carlo simulations based on CDM (black lines) and MEPS (red lines). The distributions shown are: a) E_T^{sbj}/E_T^{jet}, b) $\eta^{sbj} - \eta^{jet}$, c) $|\phi^{sbj} - \phi^{jet}|$ and d) β^{sbj}. The vertical lines represent the region of the distribution where there are sizeable statistics. The lower plots show the relative differences of the distributions in the MC with respect to the NLO predictions.

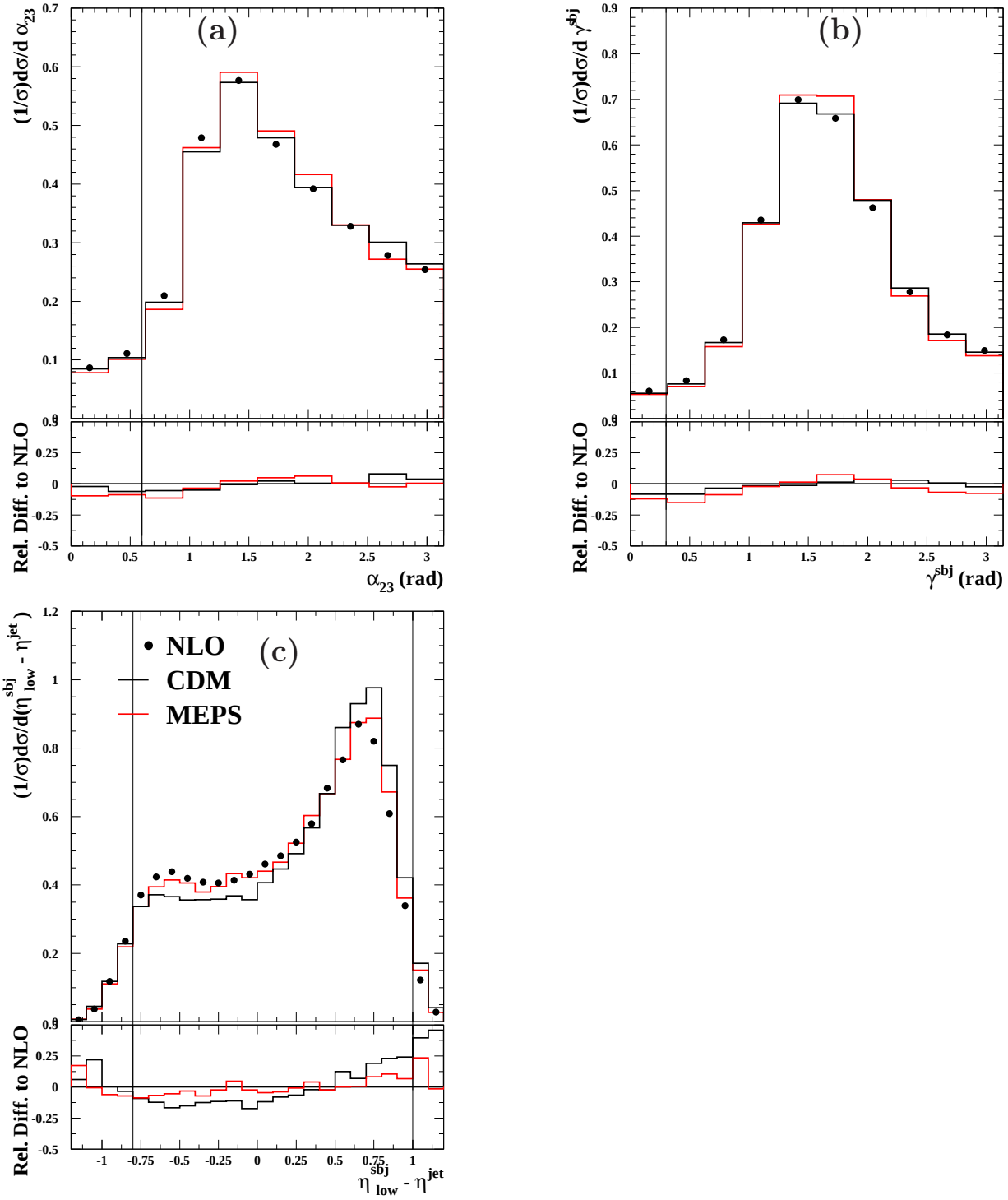

Figure 8.7: The predictions for the normalised differential cross sections at NLO in the three-subjet analysis (dots) compared with the distributions at the parton level in the Monte Carlo simulations based on CDM (black lines) and MEPS (red lines). The distributions shown are: a) α_{23}, b) γ^{sbj} and c) $\eta^{sbj}_{low} - \eta^{jet}$. The vertical lines represent the region of the distribution where there are sizeable statistics. The lower plots show the relative differences of the distributions in the MC with respect to the NLO predictions.

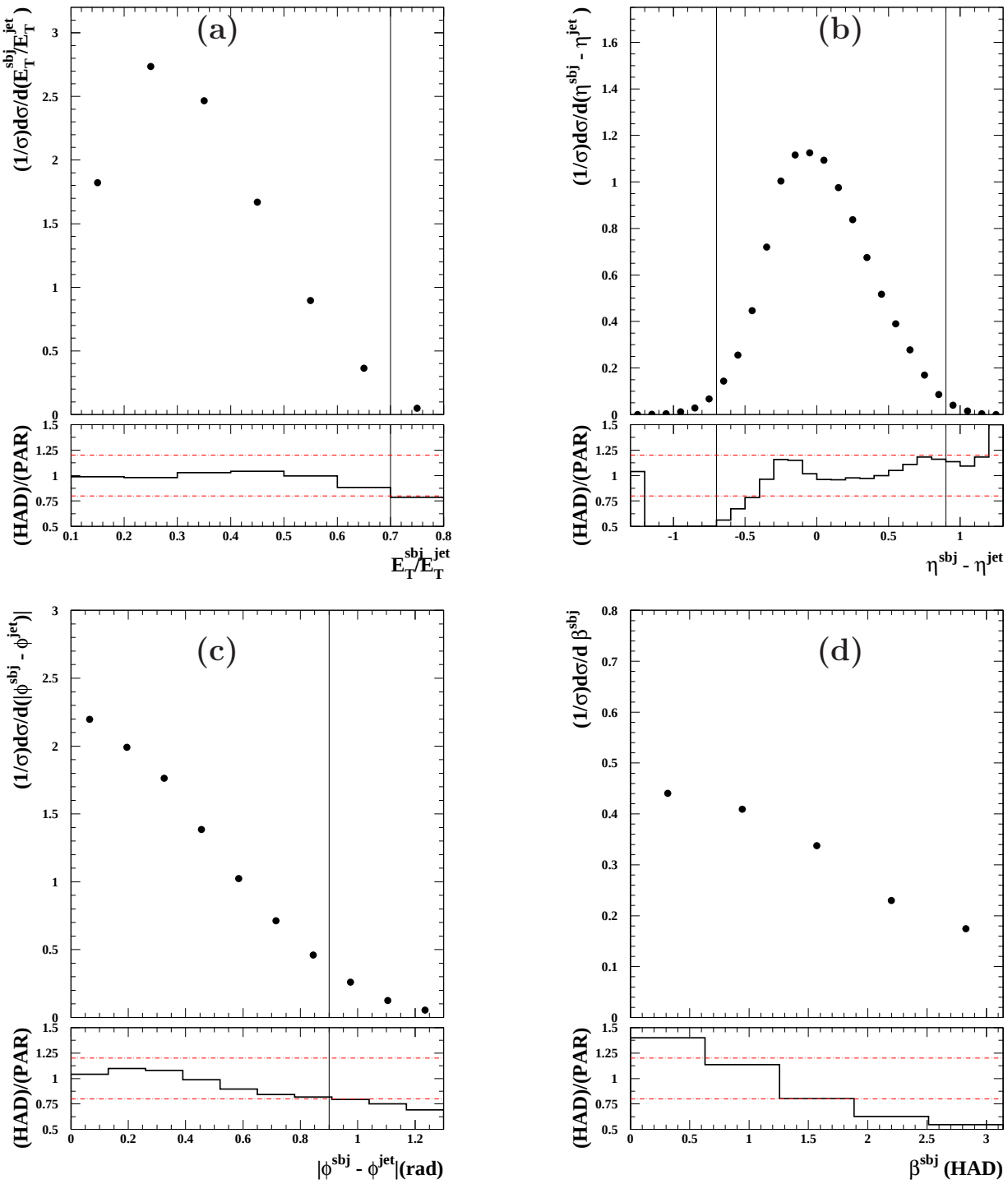

Figure 8.8: The normalised distributions in the Monte Carlo at parton level for the three-subjet analysis (dots) as functions of a) E_T^{sbj}/E_T^{jet}, b) $\eta^{sbj} - \eta^{jet}$, c) $|\phi^{sbj} - \phi^{jet}|$ and d) β^{sbj}. The vertical lines represent the region of the distribution where there are sizeable statistics in the data. The lower plots show the ratio of the normalised distributions at hadron level over those at parton level. The horizontal dot-dashed lines represent changes of 20%.

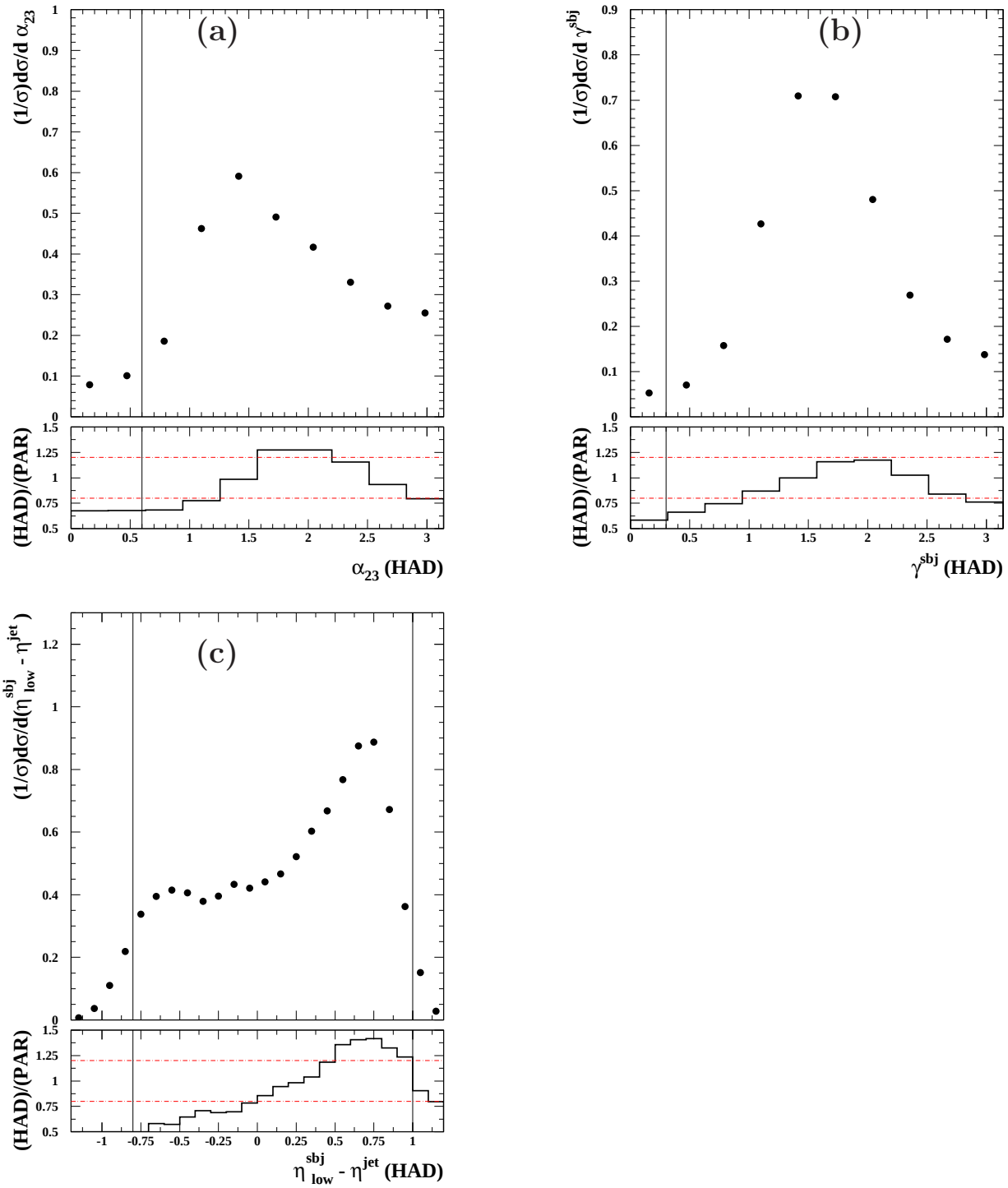

Figure 8.9: a)The normalised distributions in the Monte Carlo at parton level for the three-subjet analysis (dots) as functions of a) α_{23}, b) γ^{sbj} and c) $\eta^{sbj}_{low} - \eta^{jet}$. The vertical lines represent the region of the distribution where there are sizeable statistics. The lower plots show the ratio of the normalised distributions at hadron level over those at parton level. The horizontal dot-dashed lines represent changes of 20%.

8.2 Statistical and systematic uncertainties

Statistical uncertainties

As in most experiments where event counting is involved, the underlying probability distribution for the generation of events is taken to be a Poisson distribution. This is particularly useful since the variance is the number of events and thus the standard deviation is identified with the square root of the number of events. However, one has to keep in mind that 'events' in our context means events that contain jets, N_{ev}. More specifically, in our case N_{ev} is the number of events such that at least one jet satisfies all the requirements imposed. This is the quantity that follows a Poissonian distribution. However, since the events that contain several jets such that more than one jet satisfies the requirements on the number of subjets are rare, the number of events that contain jets is very similar to the total number of jets in the sample, $N_{jets} \sim N_{ev}$. Thus, the uncertainty on the number of jets is to a very good approximation given by $\sqrt{N_{jets}}$. Therefore, for those distributions in which there is one entry per jet, the total number of entries in each bin k also approximately follows a Poissonian distribution and the uncertainty is taken to be $\sigma_k = \sqrt{N_k}$. If the number of entries per jet is more than one, then the total number of entries no longer follows a Poisson distribution, since the entries are correlated and this needs to be taken into account to obtain an accurate estimation of the statistical uncertainty.

This is done by weigthing the contribution of a given jet to the statistical uncertainty in a given bin with the number of entries that the jet has in that given bin. That is:

$$\sigma_k = \sqrt{\sum_j N_{k,j}^2}, \tag{8.4}$$

where the sum runs over the number of jets and $N_{k,j}$ corresponds to the number of entries that the jet j provides to the bin k of a given distribution. In the case where there is one entry per jet, equation 8.4 reduces to $\sigma_k = \sqrt{N_k}$.

The distribution of the two-subjet analysis in which the correlation amongst entries has to be taken into account is that in $|\phi^{sbj} - \phi^{jet}|$. The differential cross sections as functions of E_T^{sbj}/E_T^{jet} and $\eta^{sbj} - \eta^{jet}$ also have two entries per jet, but it is always the case that the entries fall into different bins. In the first case the fractions of tranverse energy of the subjets ($f_{1,2}$) satisfy that $f_1 > 0.5 > f_2$ and in the second, it is always the case that $(\eta^{sbj1} - \eta^{jet}) \cdot (\eta^{sbj2} - \eta^{jet}) < 0$, and thus every jet contributes to $\eta^{sbj} - \eta^{jet} > 0$ and $\eta^{sbj} - \eta^{jet} < 0$, that is, always in different bins.

For the three-subjet analysis, these restrictions are not present and the correlations have to be taken into account according to equation 8.4 for E_T^{sbj}/E_T^{jet}, $\eta^{sbj} - \eta^{jet}$

and $|\phi^{sbj} - \phi^{jet}|$.

8.2.1 Systematic uncertainties: two-subjet analysis

The following sources of systematic uncertainty were considered in this analysis:

- The deviations in the results obtained by using either CDM or MEPS to correct the data with respect to their average were taken to represent the systematic uncertainties due to the modelling of the parton cascade.
- Variations on the simulation of the CAL response to low-energy particles. From a study of the CAL response to low-energy pions it was observed that the EMC response in the data is different for positive and negative pions by 10-15% (being higher for positive pions). These differences are not reproduced by the Monte Carlo simulation whereas the CAL-response to π° and π^{+} particles is well described. This comparison showed that the simulated CAL-response to π^{-} particles is overestimated by 10-15%. The effect of this discrepancy on the measurements has been studied and included as an additional systematic uncertainty. The response of the EMC cells in the simulation was modified in the following way: for EMC cells with energy below 200 MeV the energy was reduced by[1] 5%; for EMC cells with energy between 200 MeV and 1 GeV the energy was reduced by a linear function with the energy such that the reduction factor is 5% at 200 MeV and 0% at 1 GeV; for EMC cells with energy above 1 GeV no reduction factor is applied.
- The uncertainty in the absolute energy scale of the jets was estimated to be $\pm 1\%$ [28, 29, 112]. The variation of the distributions induced by the change of $\pm 1\%$ in the jet energy scale was taken to be the corresponding uncertainty.
- The uncertainty in the absolute energy scale of the electron candidate was estimated to be $\pm 1\%$ [113]. The variation of the distributions induced by the change of $\pm 1\%$ in the scattered-electron-candidate energy was taken to be the corresponding uncertainty.
- The uncertainty in the simulation of the trigger was studied and was found to be negligible.

The systematic uncertainties were added in quadrature to yield the total systematic uncertainty. The latter was added in quadrature with the statistical uncertainty to provide the total uncertainty, shown as error bars in the figures (see chapter 9).

[1] As a first approximation it is expected to have the same fraction of π°, π^{+} and π^{-} within a jet. For the sake of simplicity it was decided to apply a global 5% reduction factor.

Figure 8.10 shows the systematic uncertainties as well as the statistical uncertainties of the normalised differential cross sections. It can be seen that the uncertainty due to the modelling of the parton shower represents the dominant source of uncertainty and that it is comparable to the statistical uncertainty for all distributions. The uncertainty due to the modelling of the response to low-energy particles is also significant, while the uncertainties in the electron and jet energy scales are almost negligible. In the appendix the corresponding figures for the distributions in different regions of E_T^{jet}, η^{jet}, Q^2 and Bjorken's x are shown.

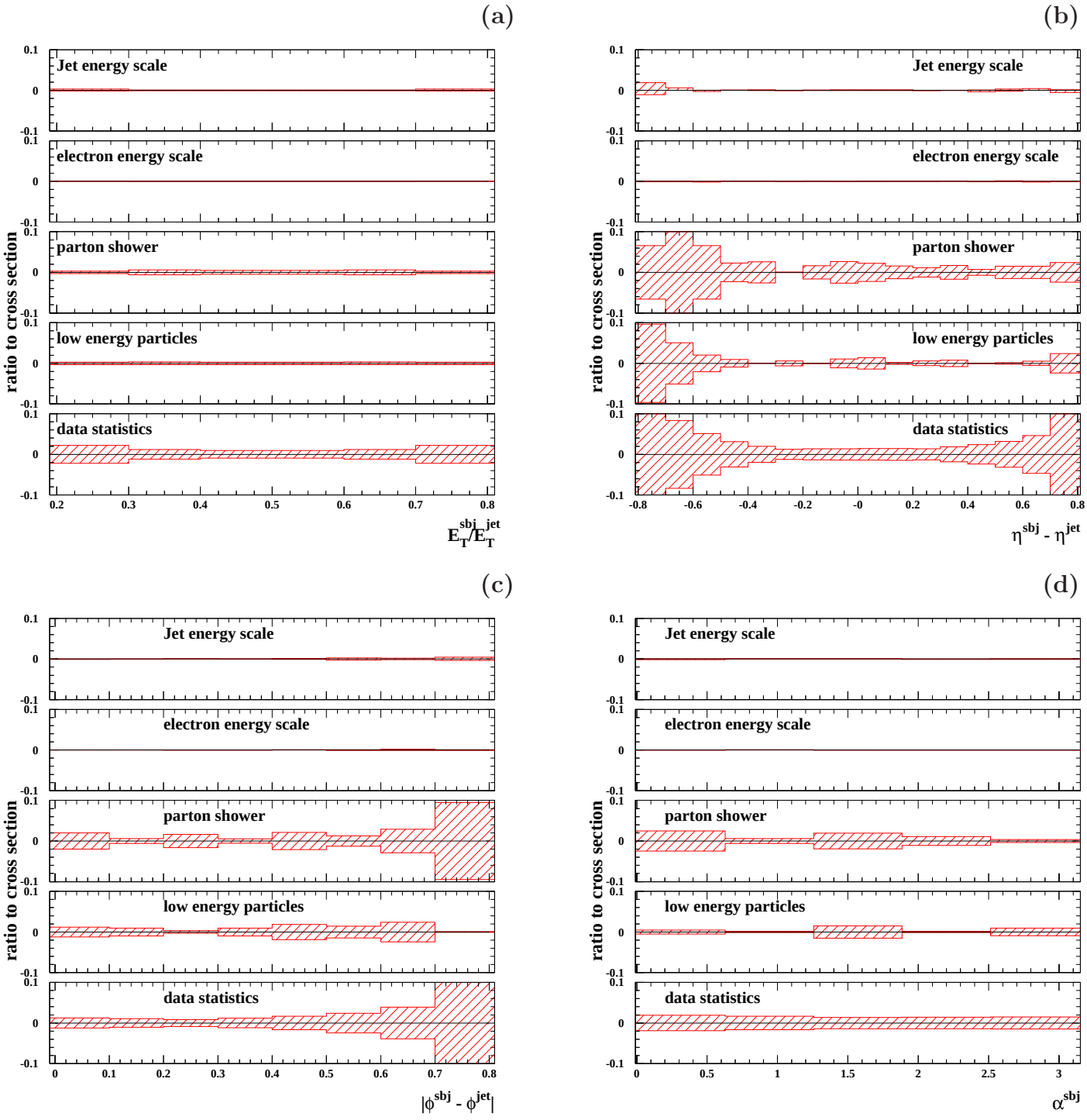

Figure 8.10: Relative systematic and statistical uncertainties of the normalised differential cross sections for the two-subjet analysis as functions of a) E_T^{sbj}/E_T^{jet} b) $\eta^{sbj} - \eta^{jet}$, c) $|\phi^{sbj} - \phi^{jet}|$ and d) α^{sbj}.

8.2.2 Systematic uncertainties: three-subjet analysis

In this analysis, the sources of systematic uncertainties considered were:

- The deviation in the results obtained by using CDM to correct the data was taken to represent the systematic uncertainty due to the modelling of the parton shower.
- Variations in the simulation of the CAL response to low-energy particles.
- The uncertainty in the absolute energy scale of the jets was estimated to be $\pm 3\%$. The variation of the distributions induced by the change of $\pm 3\%$ in the jet energy was taken to be the corresponding uncertainty.
- The uncertainty in the absolute energy scale of the electron candidate was estimated to be $\pm 3\%$. The variation of the distributions induced by the change of $\pm 3\%$ in the scattered-electron-candidate energy was taken to be the corresponding uncertainty.
- The uncertainty due to the heavy quark content in the MC simulations was estimated by varying the contribution of the heavy quarks to the jet sample by factors 2 and 1/2, which very likely constitutes an overestimation of this uncertainty.
- The uncertainty in the simulation of the trigger was found to be negligible.

Figures 8.11 and 8.12 show the relative systematic uncertainties as well as the statistical uncertainties in the data of the normalised differential cross sections considered. As in the case of the two-subjet analysis, the modelling of the parton shower gives the dominant contribution, which is comparable with the data statistics. The uncertainties on the response to low-energy particles and the heavy-quark content contribute as well.

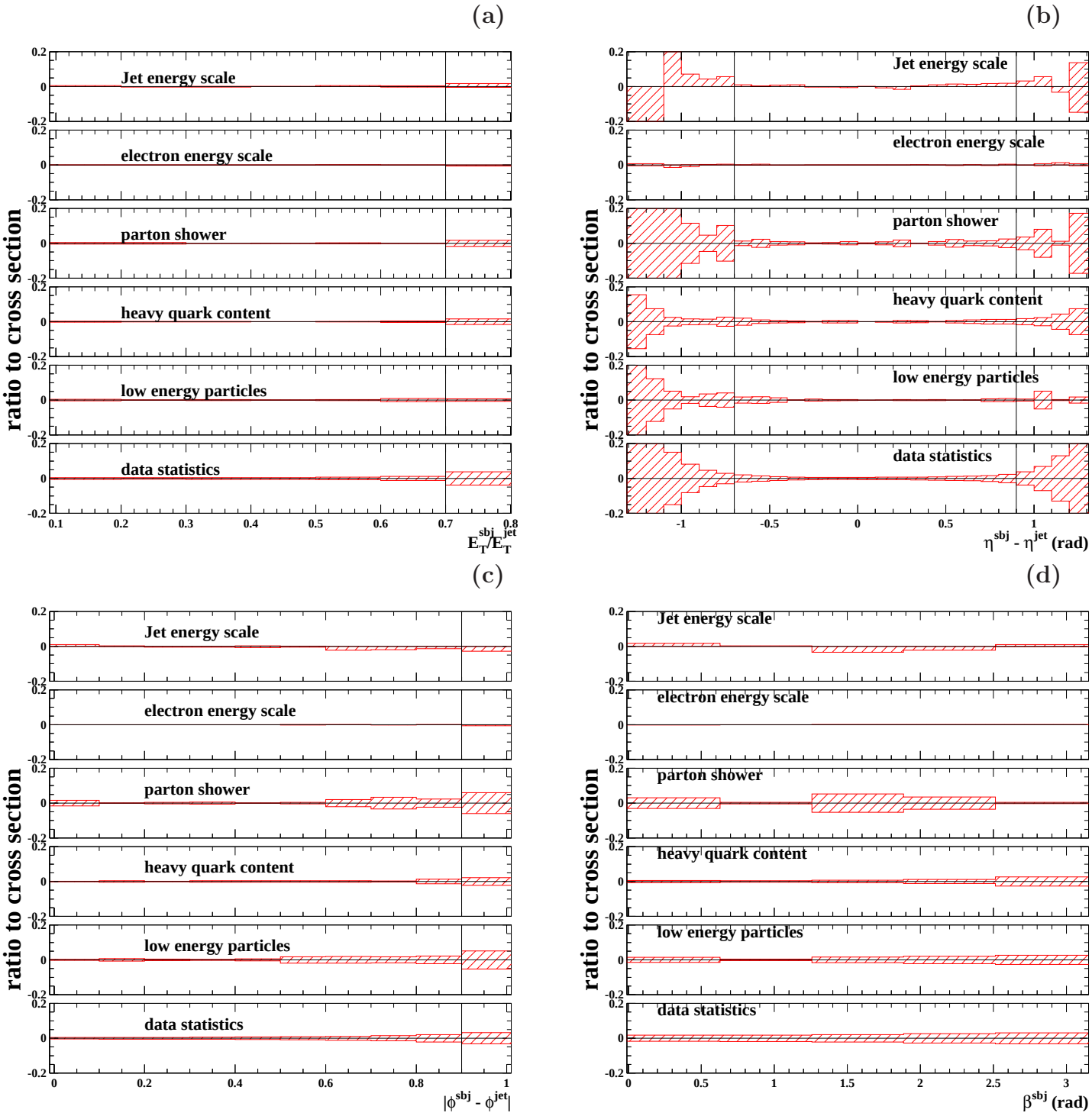

Figure 8.11: Relative systematic and statistical uncertainties of the normalised differential cross sections for the three-subjet analysis as functions of a) E_T^{sbj}/E_T^{jet}, b) $\eta^{sbj} - \eta^{jet}$, c) $|\phi^{sbj} - \phi^{jet}|$ and d) β^{sbj}.

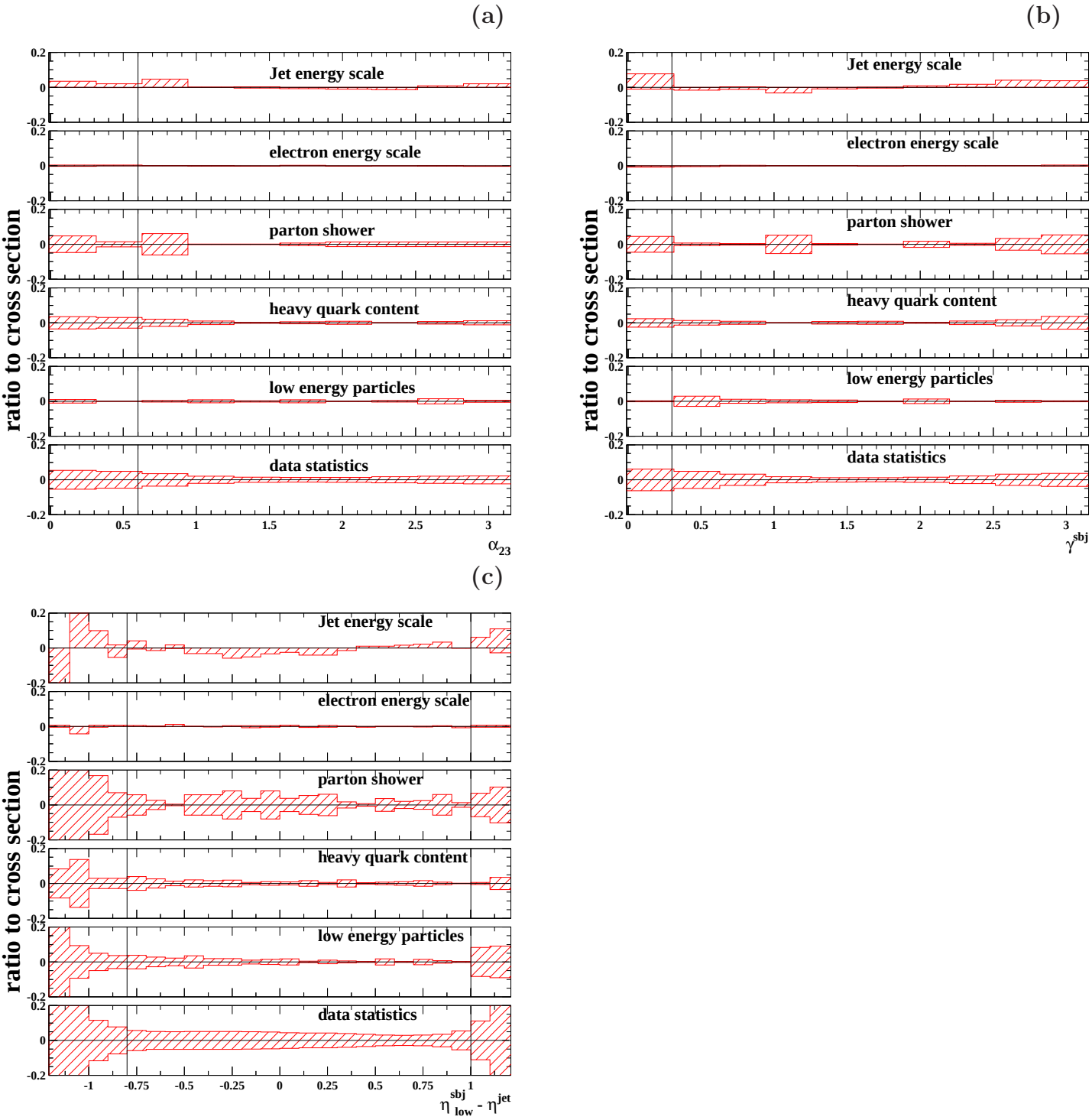

Figure 8.12: Relative systematic and statistical uncertainties of the normalised differential cross sections for the three-subjet analysis as functions of a) α_{23}, b) γ^{sbj} and c) $\eta^{sbj}_{low} - \eta^{jet}$.

Chapter 9

Results: subjet distributions in NC DIS

9.1 Introduction

In this chapter, the results of the two- and three-subjet analysis are presented. Normalised differential cross sections for the subjet variables are presented for jets with $E_T^{jet} > 14$ GeV, $-1 < \eta^{jet} < 2.5$ and such that they have exactly two (three) subjets at $y_{cut} = 0.05$ ($y_{cut} = 0.01$). Fixed-order pQCD calculations are compared to the data.

9.2 Two-subjet analysis

The results presented are:

- Normalised differential cross sections as functions of E_T^{sbj}/E_T^{jet}, $\eta^{sbj} - \eta^{jet}$, $|\phi^{sbj} - \phi^{jet}|$ and α^{sbj}, as well as comparisons with the predictions of fixed-order pQCD calculations.

- Normalised differential cross sections as functions of $\eta^{sbj}_{high} - \eta^{jet}$ and $\eta^{sbj}_{low} - \eta^{jet}$, where η^{sbj}_{high} (η^{sbj}_{low}) is the pseudorapidity of the subjet with the highest (lowest) E_T, $E^{sbj}_{T,high}$ ($E^{sbj}_{T,low}$), for jets in which $E^{sbj}_{T,low}/E_T^{jet} < 0.4$, as well as comparisons with the predictions of pQCD calculations.

- Measurements of the evolution of the normalised differential cross sections with E_T^{jet}, η^{jet}, Q^2 and Bjorken's x, compared to the predictions of pQCD calculations.

9.2.1 Normalised differential cross sections

The distribution of the fraction of the jet transverse energy carried by each subjet is presented in Fig. 9.1(a). It contains two entries per jet. Let f_1 and f_2 be the fractions for the subjets in a given jet. Then they are related by $f_2 = 1 - f_1$, so they can be written as $f_1 = f' + 0.5$ and $f_2 = -f' + 0.5$, respectively, with $f' = f_1 - 0.5$. It is evident that the distribution is symmetric around $E_T^{sbj}/E_T^{jet} = 0.5$ by construction. As already noted in section 8.2, this guarantees that the number of entries in each bin are not correlated and a Poissonian treatment of the statistical uncertainties is suitable.

It is observed that the cross section grows as the fractions get comparable, demonstrating that the two subjets tend to have similar transverse energies. The range of values that are allowed for E_T^{sbj}/E_T^{jet} are $0.22 < E_T^{sbj}/E_T^{jet} < 0.78$. These limits depend on the value of y_{cut}. Given that the algorithm requires that the last two clusters, in order to be resolvable into two subjets, satisfy

$$min(E_T^i, E_T^j)^2 D_{\eta\phi} \geq y_{cut}(E_T^{jet})^2,$$

where $D_{\eta\phi}$ is the distance in the $\eta - \phi$ plane, it is immediate to see that the minimum allowed fraction happens for $D_{\eta\phi} = 1$, which gives:

$$\frac{E_{T,low}^{sbj}}{E_T^{jet}} \geq \sqrt{y_{cut}}$$

and, thus, the maximum fraction, with two subjets, is

$$\frac{E_{T,high}^{sbj}}{E_T^{jet}} \leq 1 - \sqrt{y_{cut}}.$$

For $y_{cut} = 0.05$ one then obtains $E_{T,low}^{sbj} > 0.22$ and $E_{T,high}^{sbj} < 0.78$.

The distribution of $\eta^{sbj} - \eta^{jet}$ is show in Fig. 9.1(b). It also has two entries per jet. A two-peak structure can be seen, with a dip around $\eta^{sbj} - \eta^{jet} \sim 0$. The position of the center of the jet is determined as the transverse-energy-weighted position of the two subjets and since both subjets tend to have similar transverse energies, the two subjets tend to be at similar distances from the jet center in the $\eta - \phi$ plane; this means that $\eta^{sbj,1} - \eta^{jet} \sim -(\eta^{sbj,2} - \eta^{jet})$ and $\phi^{sbj,1} - \phi^{jet} \sim -(\phi^{sbj,2} - \phi^{jet})$. Therefore, if $\eta^{sbj} - \eta^{jet}$ is close to zero, it is needed that $|\phi^{sbj,1} - \phi^{sbj,2}|$ is close to unity for the algorithm not to cluster them together, which happens in few events and hence the dip in the distribution.

It can also be seen that the two peaks are asymmetric, the one occurring at negative values of $\eta^{sbj} - \eta^{jet}$ being clearly more pronounced. As previously said,

the jet center is reconstructed as the transverse-energy-weighted average of the two subjets and, therefore, the highest-E_T subjet will always be closer to the jet center than the other. If the highest-E_T subjet were populating the region of negative $\eta^{sbj} - \eta^{jet}$ more frequently than the region of positive values, the asymmetry of the peaks could be explained; we shall see that this is indeed the case. In Fig. 9.2 the distributions of $\eta^{sbj}_{high} - \eta^{jet}$ and $\eta^{sbj}_{low} - \eta^{jet}$ for $E^{sbj}_{T,low}/E^{jet}_T < 0.4$ are shown. The preference of the highest-E_T subjet to be in the rear part of the jet is here manifest and explains the asymmetry observed before. The reason for this behaviour is discussed later on. Apart from these features, the distribution in Fig. 9.1(b) shows that the cross section grows as $|\eta^{sbj} - \eta^{jet}|$ decreases, which means that the two subjets also tend to be close to each other, until they are so close that they stop being resolvable.

In Fig. 9.1(c) the distribution of $|\phi^{sbj} - \phi^{jet}|$ is shown. The reason behind the dip in the middle for the previous distribution is also valid for this distribution; a dip can indeed be seen at $|\phi^{sbj} - \phi^{jet}| \sim 0$. The distribution shows that the subjets also tend to have similar values of ϕ^{sbj} until they are so close in ϕ that only subjets with $|\eta^{sbj,1} - \eta^{sbj,2}| \sim 1$ are still resolvable.

In Fig. 9.1(d) the distribution of α^{sbj} is shown. It is observed that the cross section grows as α^{sbj} grows, meaning that the highest-E_T subjet tends to be away from the proton beam direction as seen from the jet's center point of view. This is compatible with the distributions in Figs. 9.1(b) and 9.2. The fact that the highest-E_T subjet tends to be in the rear part of the jet is understood as a manifestation of color-coherence effects between the initial and final states. As mentioned in section 2.2.1, the color-connected partners in the event, the jet and the proton remnant, define a region where soft emissions are enhanced. This region is the one between the two partners and, thus, soft emissions, which will constitute the lowest-E_T subjet, tend to be predominantly towards the proton beam direction, as observed in the measured distribution.

9.2.2 Comparison with NLO pQCD calculations

In the figures just discussed the NLO QCD predictions are also shown, where the hatched area represents the theoretical uncertainty. These calculations have been corrected to the hadron level with the aid of the Monte Carlo models. Since the calculations are normalized to unity, the uncertainties are correlated among the points; this correlation gives rise to the pulsating pattern exhibited by the theoretical uncertainties.

The QCD predictions give an adequate description of the data. In some distributions, however, it can be seen that the data points are situated at the upper (lower)

edge of the theoretical uncertainty, as it happens for $E_T^{sbj}/E_T^{jet} \sim 0.5$, $|\phi^{sbj} - \phi^{jet}| \sim 0$, $\alpha^{sbj} \sim 0$ or at the peaks in the $\eta^{sbj} - \eta^{jet}$ distribution ($E_T^{sbj}/E_T^{jet} \sim 0.25$, $|\phi^{sbj} - \phi^{jet}| > 0.3$ and $|\eta^{sbj} - \eta^{jet}| > 0.5$).

The calculation of the cross section as a function of E_T^{sbj}/E_T^{jet} exhibits a peak at $0.4 < E_T^{sbj}/E_T^{jet} < 0.6$, as seen in the data. The calculations for the $\eta^{sbj} - \eta^{jet}$ and α^{sbj} distributions predict that the subjet with higher transverse energy tends to be in the rear direction, in agreement with the data. It should be noted that the shapes of the distributions are very similar for the LO and NLO calculations. In the LO calculations two subprocesses contribute to the production of jets with two subjets: the quark-induced subprocess $eq \to eqg$ and the gluon induced subprocess $eg \to eq\bar{q}$. In the former a jet consists of a quark-gluon pair while in the latter it consists of a quark-antiquark pair. The agreement between data and calculations shows that the mechanism driving the subjet topology in the data is the $eq \to eqg$ and $eg \to eq\bar{q}$ subprocesses as implemented in the pQCD calculations.

To gain further insight into the pattern of parton radiation, the predictions for quark- and gluon-induced processes are compared separately with the data in figure 9.3. The NLO calculations predict that the two-subjet rate is dominated by quark-induced subprocesses; the relative contribution of quark-(gluon-)induced subprocesses is 81% (19%). The shape of the predictions for these two type of subprocesses are different; in quark-induced subprocesses, the two subjets have more similar transverse energies and are closer to each other than in gluon-induced subprocesses (see figure 9.3). The comparison with the measurements shows that the data are better described by the calculations for jets arising from a quark-gluon pair than those coming from a quark-antiquark pair, in agreement with the predicted dominance of quark-induced subprocesses.

9.2.3 Evolution of the pattern of parton radiation with E_T^{jet}, Q^2, η^{jet} and Bjorken's x

Figure 9.4 shows the normalised differential cross sections as functions of all the subjet variables in different regions of E_T^{jet}. Despite the fact that the mean subjet multiplicity decreases with increasing E_T^{jet}, the measured cross sections have very similar shapes across all regions in E_T^{jet}. This is better illustrated in Fig. 9.5, where the data for all E_T^{jet} regions have been plotted together. In particular, it is observed that the maximum of each measured normalised cross sections in every region of E_T^{jet} occurs in the same bin of the distribution. To quantify this dependence more precisely, the value of the cross section at a given bin in all regions of E_T^{jet} is plotted in Fig. 9.6, where the bin chosen has been the one that contains the maximum of the distribution in order to minimize the statistical error. The spread of the measured

maximum values is $\pm(4-6)\%$. For each of the four observables, the scaling behaviour of the subjet cross section is observed and in agreement with the expectation that the splitting functions evolve slowly (logarithmically) with the energy scale. The NLO QCD calculations are in agreement with the data and support this observation.

Figure 9.7 shows the normalised differential subjet cross sections in different regions of η^{jet}. The most relevant feature than can be learnt from these distributions is that the preference of the highest-E_T subjet to be in the rear part of the jet persists in the regions of negative pseudorapidity, as expected if color-coherence effects are indeed present. If they were not, the highest-E_T subjet would then be most of the time the one with the angle closest to 90°, which in the region of negative pseudorapidity is the one in the forward part of the jet. Figure 9.8 shows the data for all η^{jet} regions plotted together and in Fig. 9.9 the evolution of the maximum value of the distribution with η^{jet} can be seen.

Figure 9.10 shows the normalised differential subjet cross sections in different regions of Q^2. In this case, it is observed that the E_T^{sbj}/E_T^{jet} distribution does not change significantly with Q^2, but the other observables do show some variation. For instance, in Fig. 9.11 it can be seen that the dip in the $\eta^{sbj} - \eta^{jet}$ distribution is shallower for the region $125 < Q^2 < 250$ GeV^2 than at higher Q^2 and that the shape of the α^{sbj} distribution for that same region has a different shape than for the other regions. These features of the data are reasonably reproduced by the NLO calculations and understood as a combination of two effects: the fraction of gluon-induced events is predicted to be 32% for the region $125 < Q^2 < 250 GeV^2$ and below 14% for higher Q^2; the shape of the normalised cross section as functions of $\eta^{sbj} - \eta^{jet}$ and α_{sbj} changes from the region $125 < Q^2 < 250$ GeV^2 to $250 < Q^2 < 500$ GeV^2 for quark- and gluon-induced processes (see figure 9.12.)

Figure 9.13 shows the subjet cross sections at the bin that contains the maximum for each observable as a function of Q^2 together with the NLO predictions. It is observed that the maximum value of each measured normalised cross section in every region of Q^2 occurs in the same bin of the distribution, except for $|\phi^{sbj} - \phi^{jet}|$ in the highest-Q^2 region[1]. The spread of the measured maximum values in the E_T^{sbj}/E_T^{jet} and $|\phi^{sbj} - \phi^{jet}|$ distributions is $\pm(3-4)\%$. On the other hand, the measured and predicted values as functions of $\eta^{sbj} - \eta^{jet}$ and α^{sbj} exhibits a step-like behaviour between the lowest-Q^2 region and the rest.

Figure 9.14 shows the normalised differential subjet cross sections in different regions of x. Figure 9.15 shows the data for all x regions plotted together. It is observed that the maximum of each measured normalised cross section in every region of x occurs in the same bin of the distribution, except for $|\phi^{sbj} - \phi^{jet}|$

[1]For the $|\phi^{sbj} - \phi^{jet}|$ distribution, the same bin has been used for consistency.

in the highest x region. Figure 9.16 shows the maximum[1] value of the measured normalised cross section for each observable as a function of x. The shape of the E_T^{sbj}/E_T^{jet} measured distribution does not change significantly with x, whereas some dependence is expected (see Fig. 9.16a). The dependence of the $\eta^{sbj} - \eta^{jet}$ and α^{sbj} distributions with x exhibits features similar to those observed in the study of the Q^2 dependence; in particular, the maximum values (see Figs. 9.16b and 9.16d) exhibit a monotonic increase as x increases, which is reasonably reproduced by the calculations. As discussed previously, these features are understood as a combination of two effects: a decrease of the predicted fraction of gluon-induced events from 44% for $0.004 < x < 0.009$ to 6% for $x > 0.093$ and the change in shape of the normalised cross sections for quark- and gluon-induced processes as x increases (see Fig. 9.17.)

To investigate the origin of the change in shape of the normalised differential cross sections between the lowest and higher Q^2 and x regions, LO and NLO calculations were compared. The most dramatic change is observed when restricting the kinematic region to $125 < Q^2 < 250$ GeV^2 or $0.004 < x < 0.009$ (see Fig 9.18); the LO calculation of the $\eta^{sbj} - \eta^{jet}$ distribution does not exhibit a two-peak structure as seen in the NLO prediction and in the data. In addition, the LO calculation of the α^{sbj} distribution peaks at $\alpha^{sbj} \sim \pi/2$ in contrast with the NLO prediction and the data. This proves that the NLO QCD radiative corrections are responsible for these variations in shape and necessary for describing the data.

In summary, while the shapes of the normalised differential cross sections show only a weak dependence of E_T^{jet}, their dependence on Q^2 and x have some prominent features at low Q^2 or x. The weak dependence on E_T^{jet} is consistent with the expected scaling behaviour of the splitting functions; however, the restriction to low Q^2 or x values demonstrates that the NLO QCD radiative corrections are important there. The NLO QCD calculations, which include the two competing processes $eq \to eqg$ and $eg \to eq\bar{q}$ and radiative corrections, adequately reproduce the measurements.

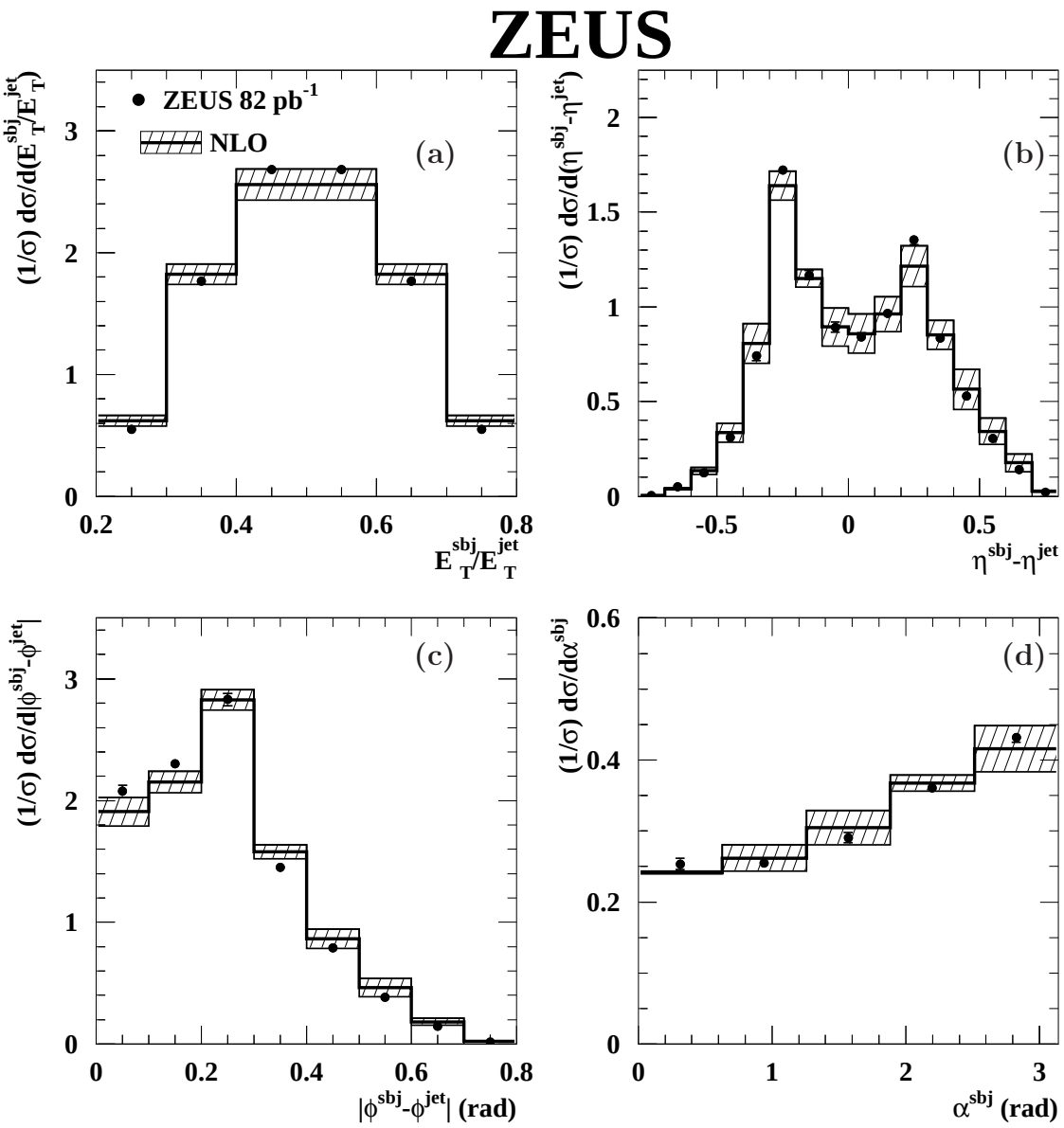

Figure 9.1: Measured normalised differential cross sections (dots) as functions of **a)** E_T^{sbj}/E_T^{jet}, **b)** $\eta^{sbj} - \eta^{jet}$, **c)** $|\phi^{sbj} - \phi^{jet}|$ and **d)** α^{sbj}. The inner error bars represent the statistical uncertainty and the outer ones represent the statistical and systematic uncertainties added in quadrature. The NLO pQCD predictions are shown as solid histograms with the hatched area representing the theoretical uncertainty.

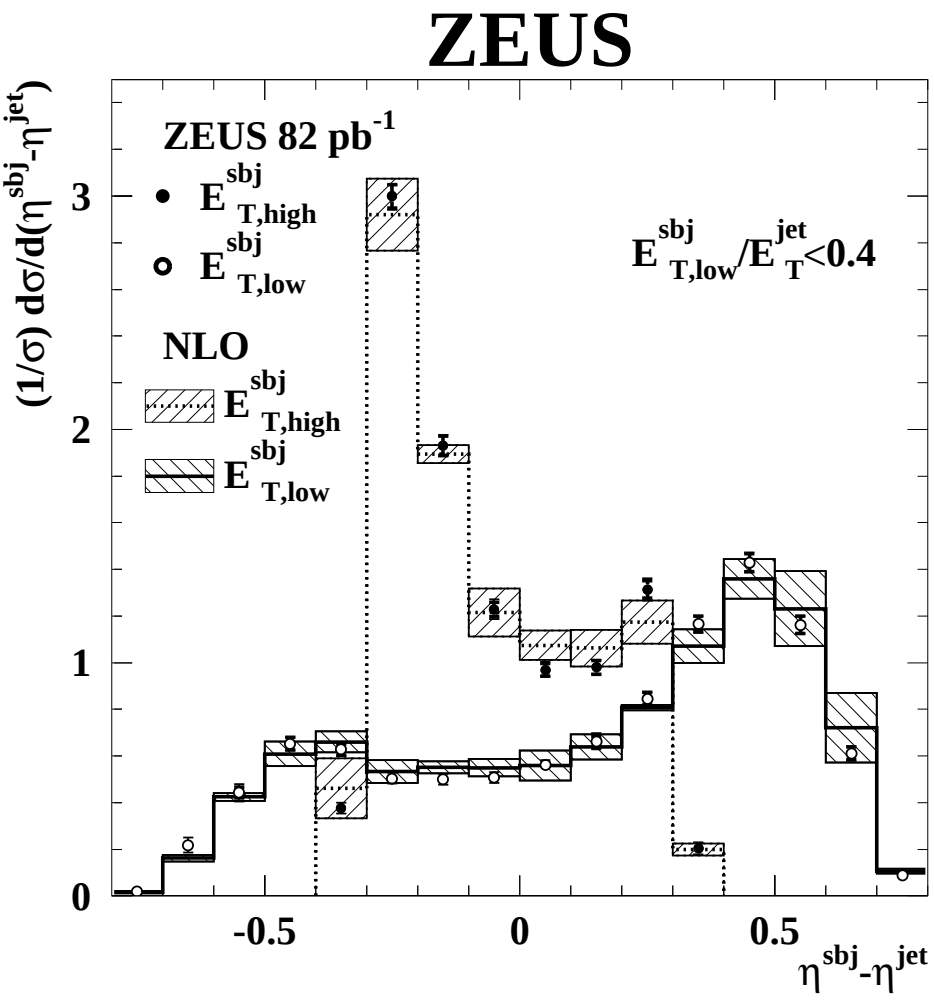

Figure 9.2: Measured normalised differential cross sections as functions of $\eta^{sbj} - \eta^{jet}$ separately for the higher (dots) and lower (open circles) E_T subjets with $E^{sbj}_{T,low}/E^{jet}_T < 0.4$. Other details are as in the caption to figure 9.1.

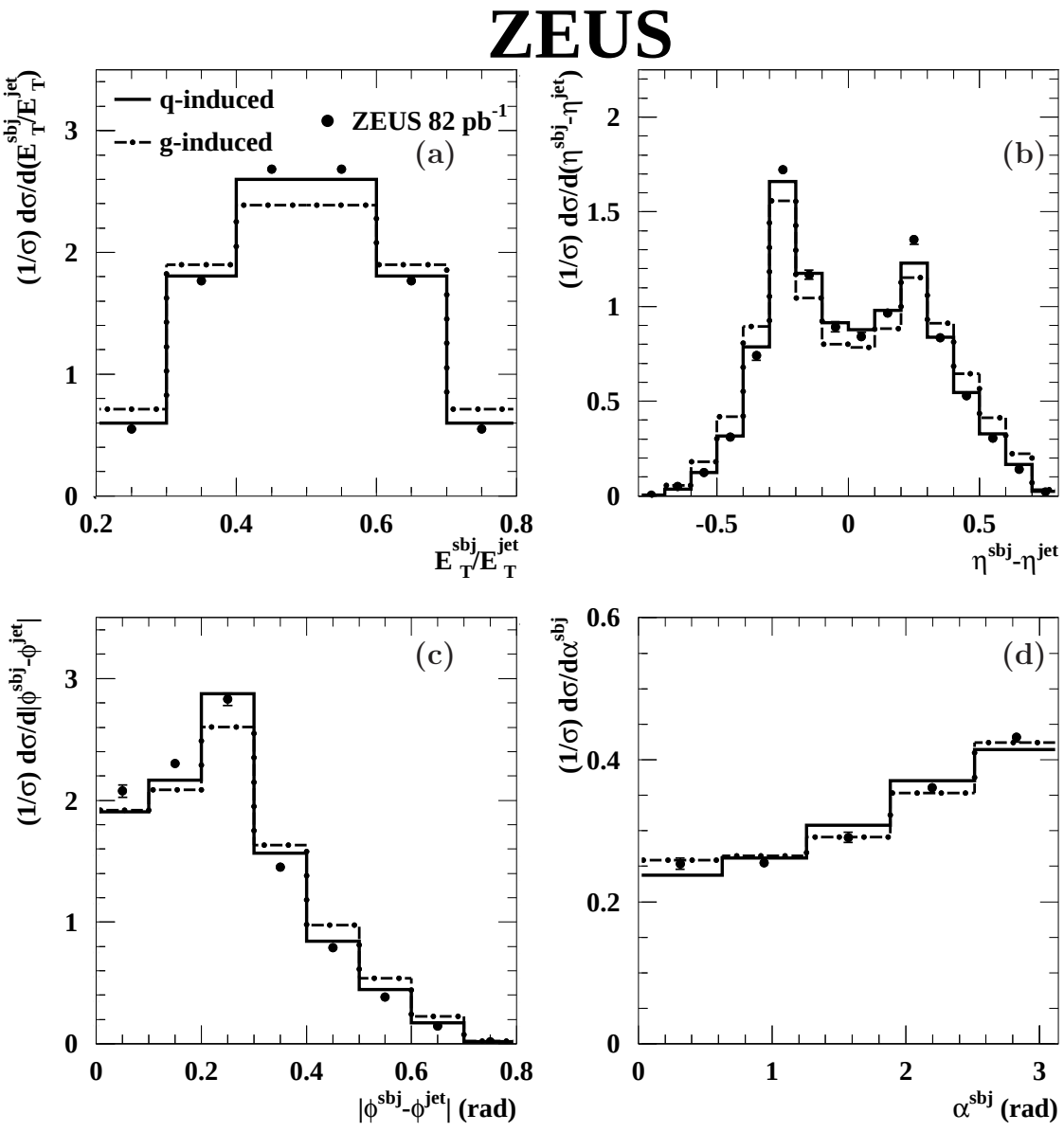

Figure 9.3: Measured normalised differential cross sections for the subjet variables (dots) compared to the NLO predictions for quark- (solid line) and gluon-induced (dot-dashed line) processes separately.

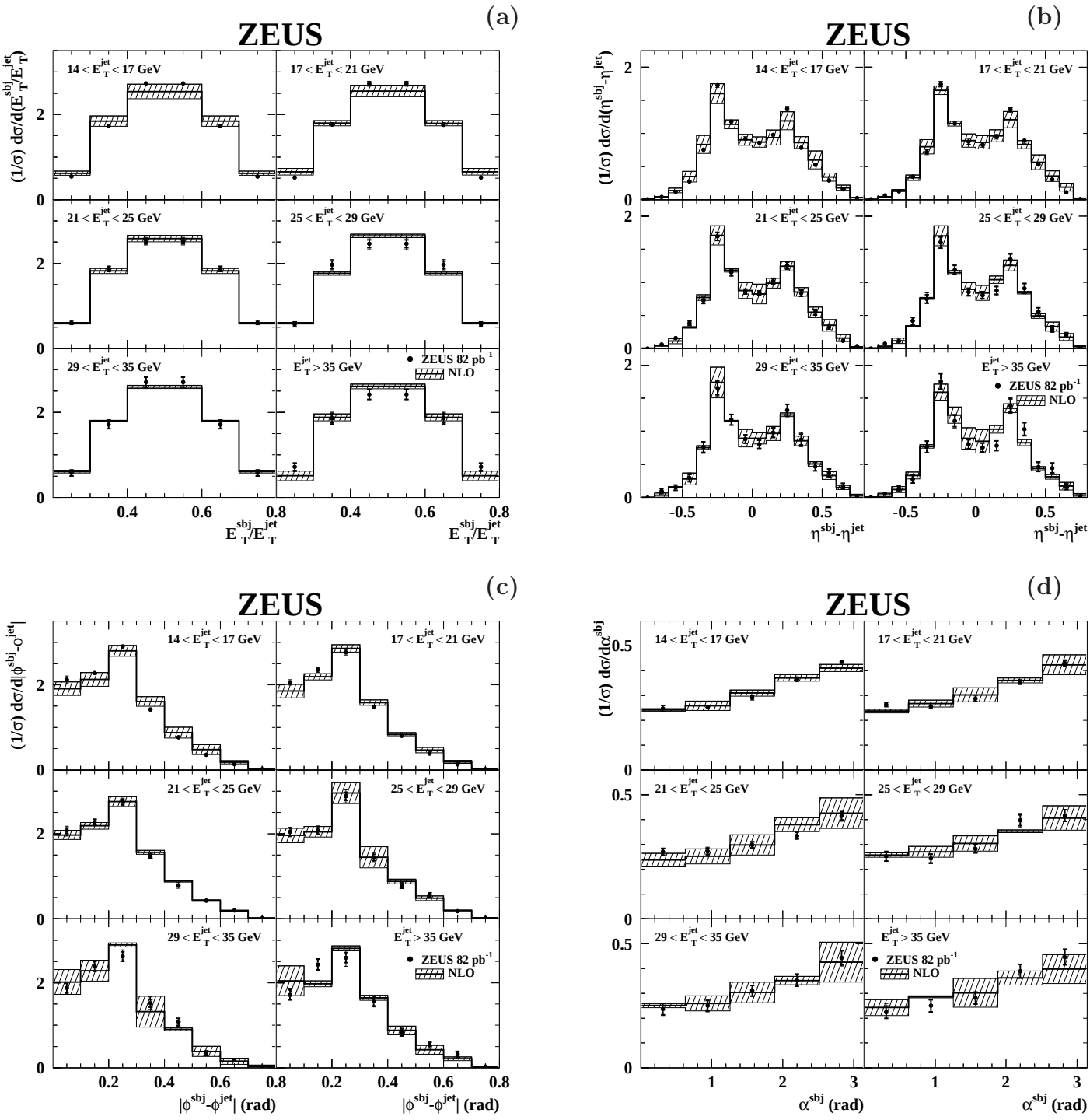

Figure 9.4: Measured normalised differential cross sections as functions of a) E_T^{sbj}/E_T^{jet}, b) $\eta^{sbj} - \eta^{jet}$, c) $|\phi^{sbj} - \phi^{jet}|$ and d) α^{sbj} in different regions of E_T^{jet}. Details concerning the error bars are as in the caption to Fig. 9.1.

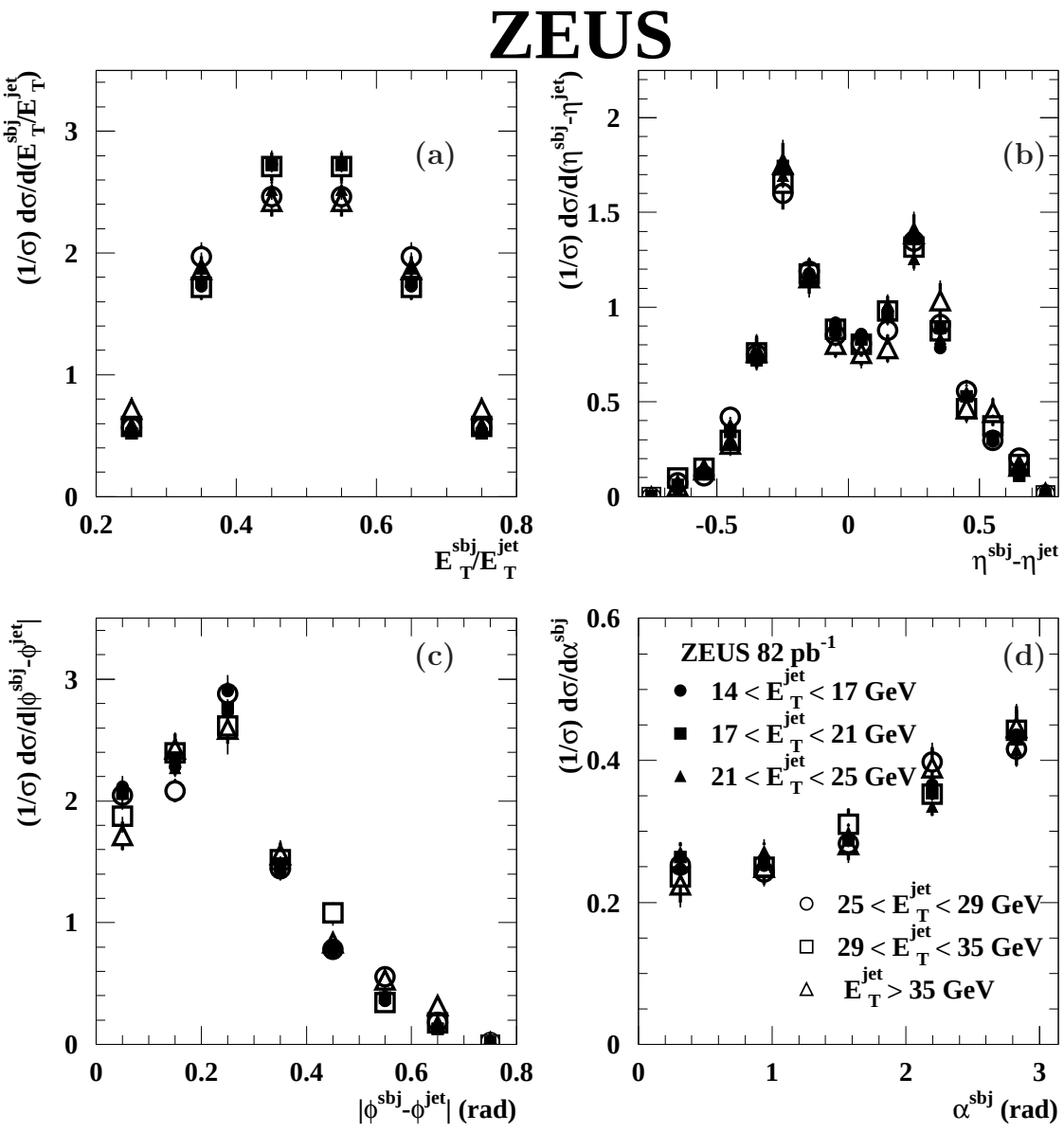

Figure 9.5: Measured normalised differential cross sections as functions of a) E_T^{sbj}/E_T^{jet}, b) $\eta^{sbj} - \eta^{jet}$, c) $|\phi^{sbj} - \phi^{jet}|$ and d) α^{sbj} in different regions of E_T^{jet}. Details concerning the error bars are as in the caption to Fig. 9.1.

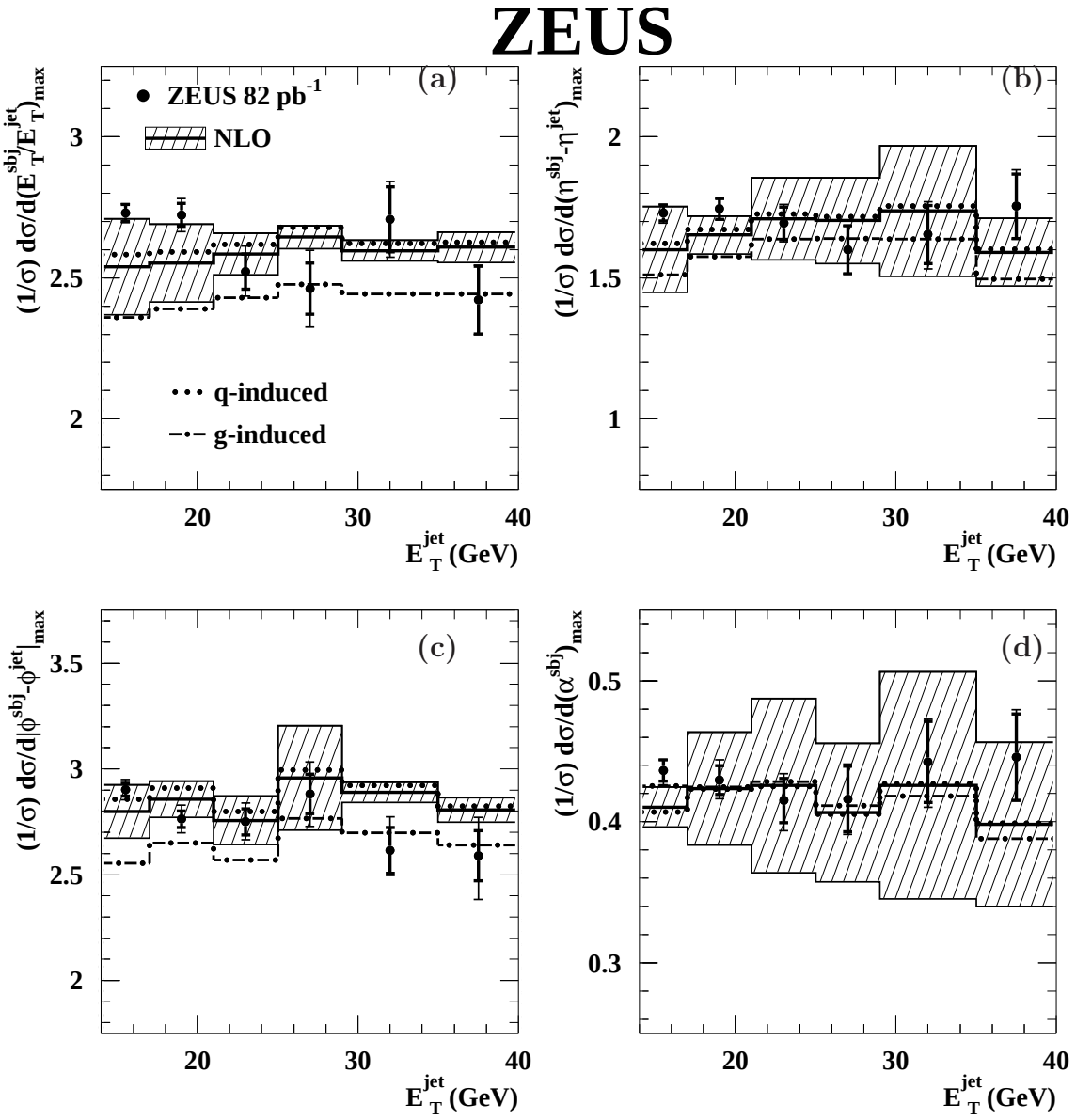

Figure 9.6: Maximum of the measured differential subjet cross sections in a) E_T^{sbj}/E_T^{jet}, b) $\eta^{sbj} - \eta^{jet}$, c) $|\phi^{sbj} - \phi^{jet}|$ and d) α^{sbj} as a function of E_T^{jet}. For comparison, the NLO predictions for quark- (dotted histograms) and gluon-induced (dot-dashed histograms) processes are also shown.

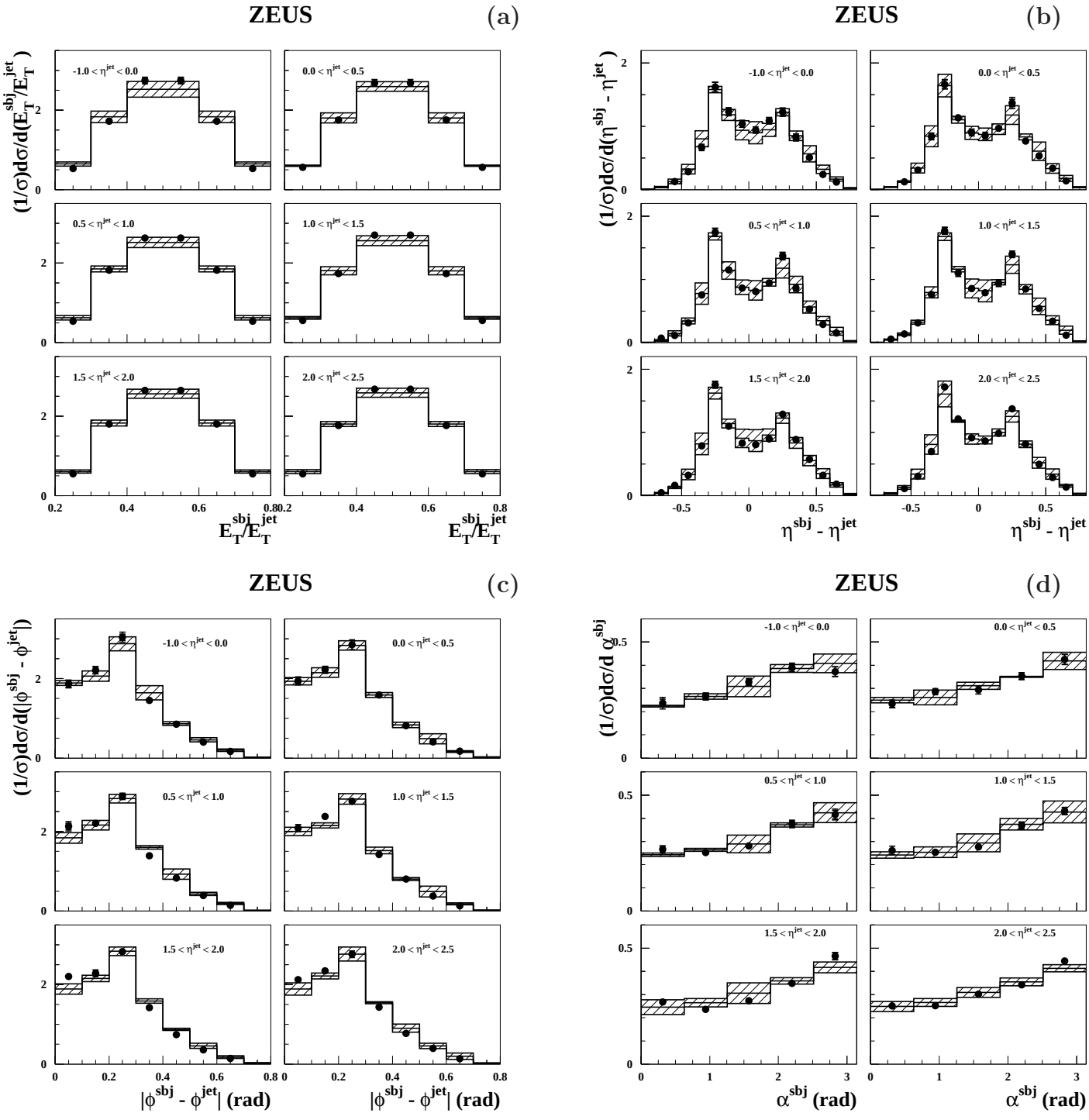

Figure 9.7: Measured normalised differential cross sections as functions of a) E_T^{sbj}/E_T^{jet}, b) $\eta^{sbj} - \eta^{jet}$, c) $|\phi^{sbj} - \phi^{jet}|$ and d) α^{sbj} in different regions of the pseudorapidity of the jet. Other details are as in the caption to Fig. 9.1.

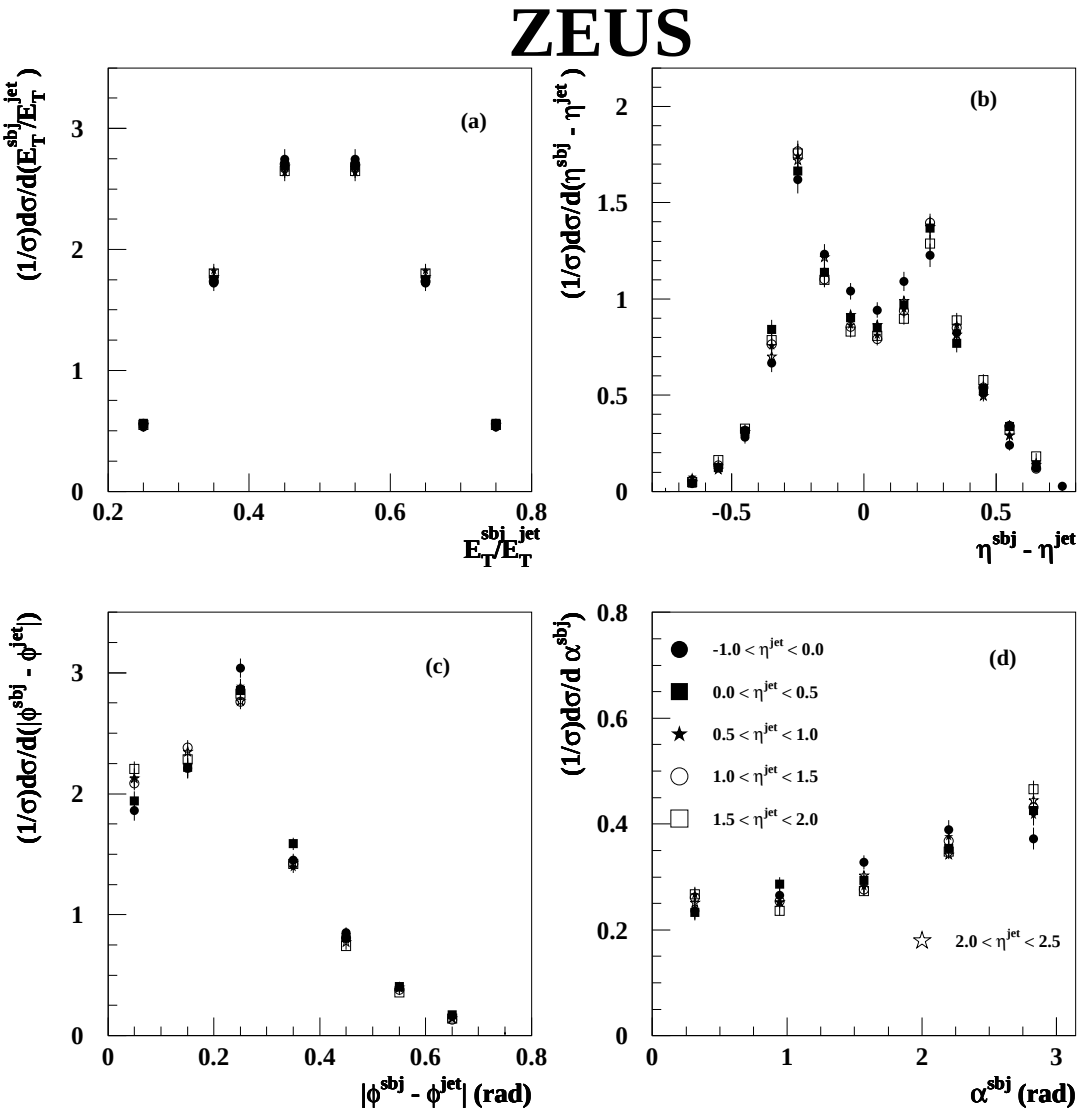

Figure 9.8: Measured normalised differential cross sections as functions of a) E_T^{sbj}/E_T^{jet}, b) $\eta^{sbj} - \eta^{jet}$, c) $|\phi^{sbj} - \phi^{jet}|$ and d) α^{sbj} in different regions of η^{jet}. Details concerning the error bars are as in the caption to Fig. 9.1.

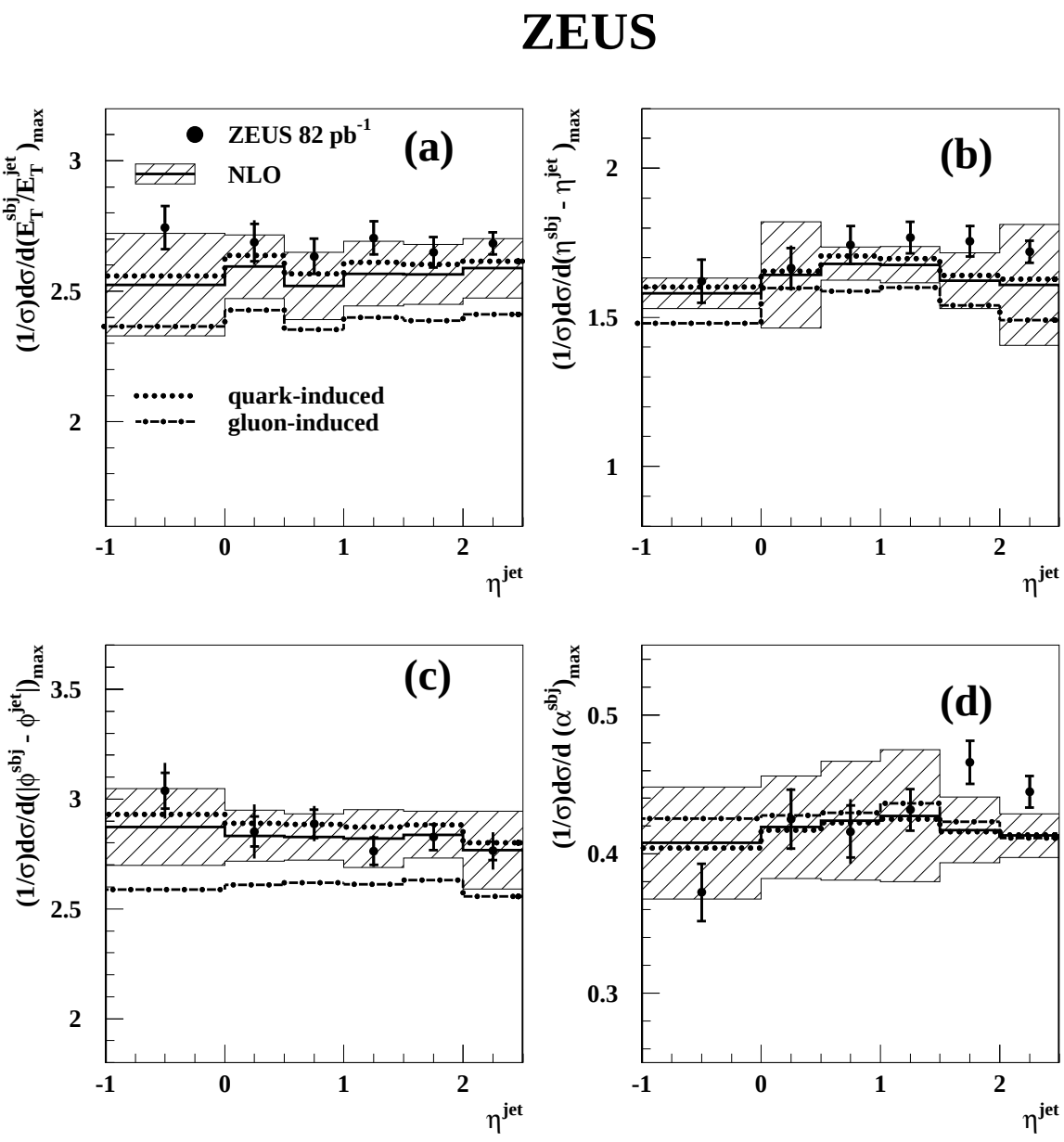

Figure 9.9: Maximum of the measured differential subjet cross sections in a) E_T^{sbj}/E_T^{jet}, b) $\eta^{sbj} - \eta^{jet}$, c) $|\phi^{sbj} - \phi^{jet}|$ and d) α^{sbj} as a function of η^{jet}. For comparison, the NLO predictions for quark- (dotted histograms) and gluon-induced (dot-dashed histograms) processes are also shown.

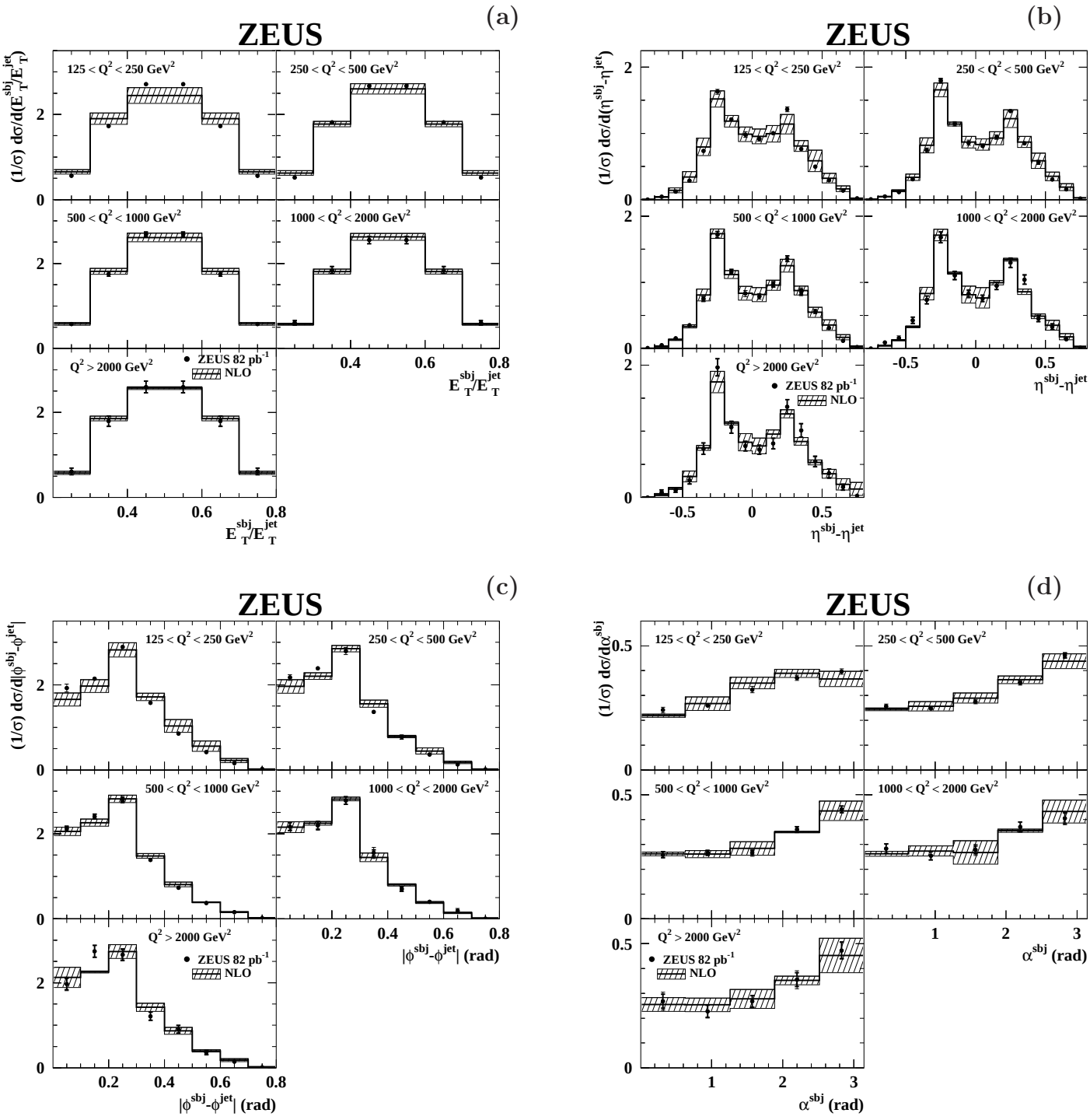

Figure 9.10: Measured normalised differential cross sections as functions of a) E_T^{sbj}/E_T^{jet}, b) $\eta^{sbj} - \eta^{jet}$, c) $|\phi^{sbj} - \phi^{jet}|$ and d) α^{sbj} in different regions of Q^2. Other details are as in the caption to figure 9.1.

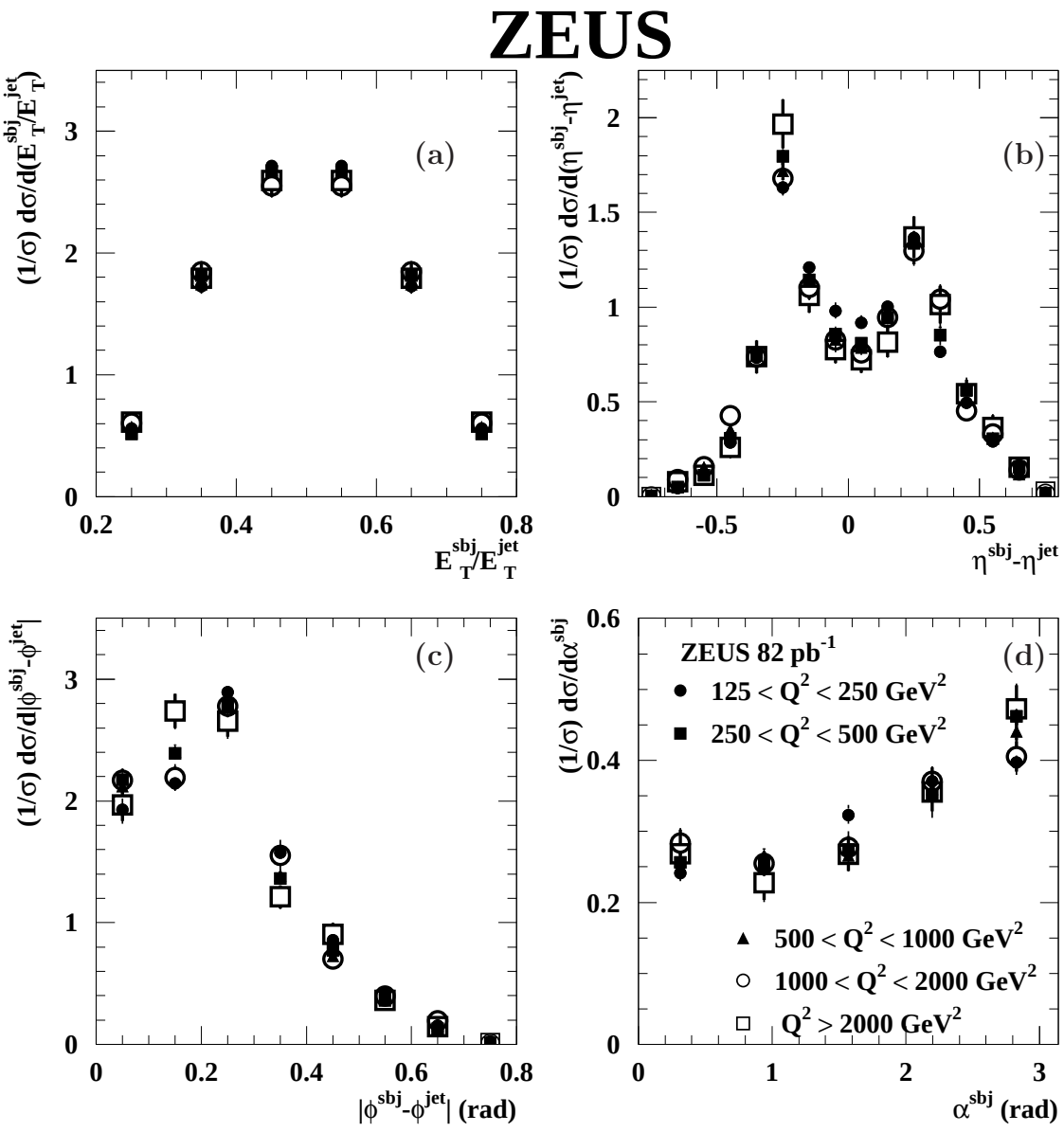

Figure 9.11: Measured normalised differential cross sections as functions of a) E_T^{sbj}/E_T^{jet}, b) $\eta^{sbj} - \eta^{jet}$, c) $|\phi^{sbj} - \phi^{jet}|$ and d) α^{sbj} in different regions of Q^2. Details concerning the error bars are as in the caption to Fig. 9.1.

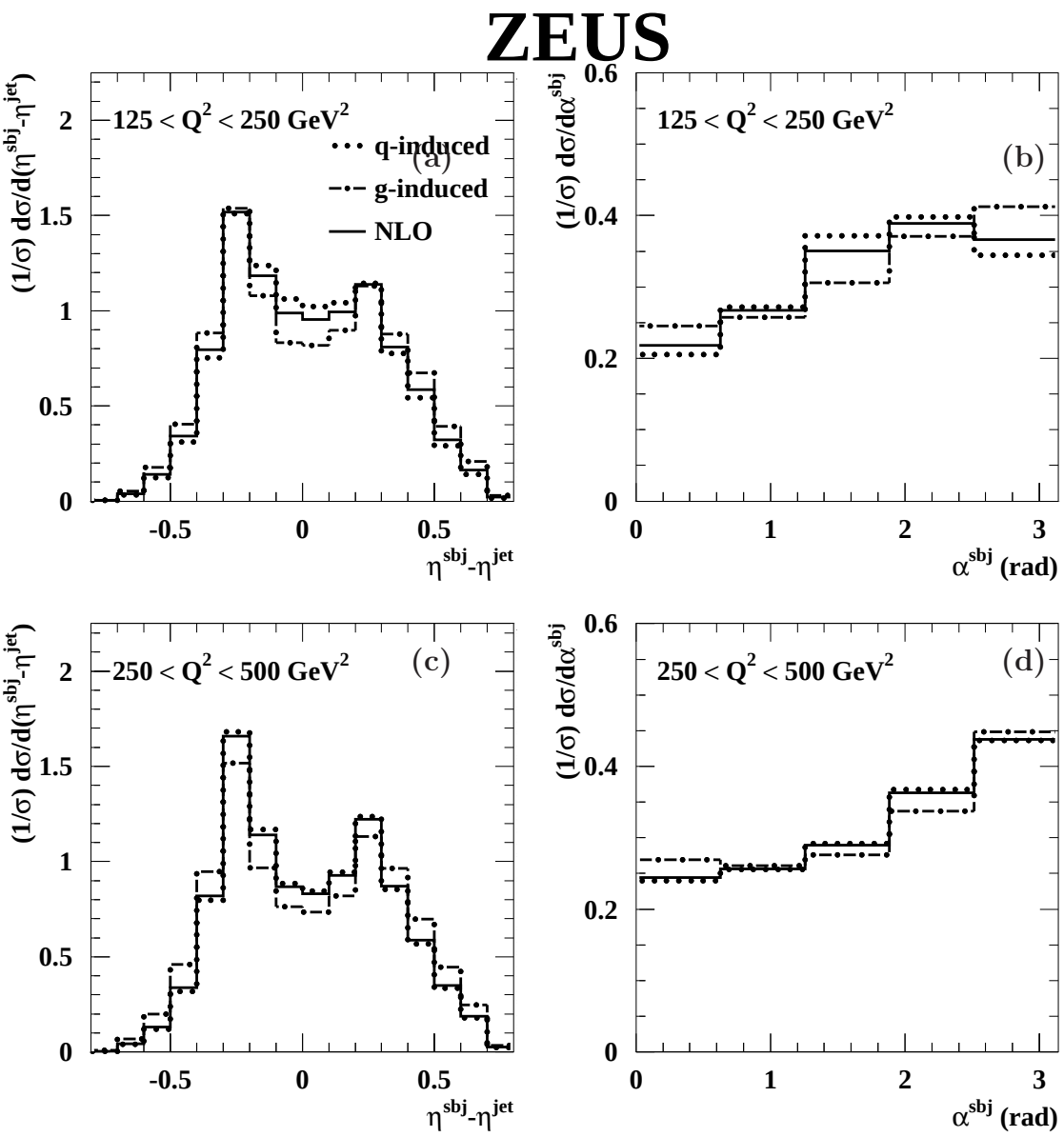

Figure 9.12: Predicted normalised differential subjet cross sections at NLO as functions of (a,c) $\eta^{sbj} - \eta^{jet}$ and (b,d) α^{sbj} in different regions of Q^2. The NLO predictions for quark- (dotted histograms) and gluon-induced (dot-dashed histograms) processes separately are also shown.

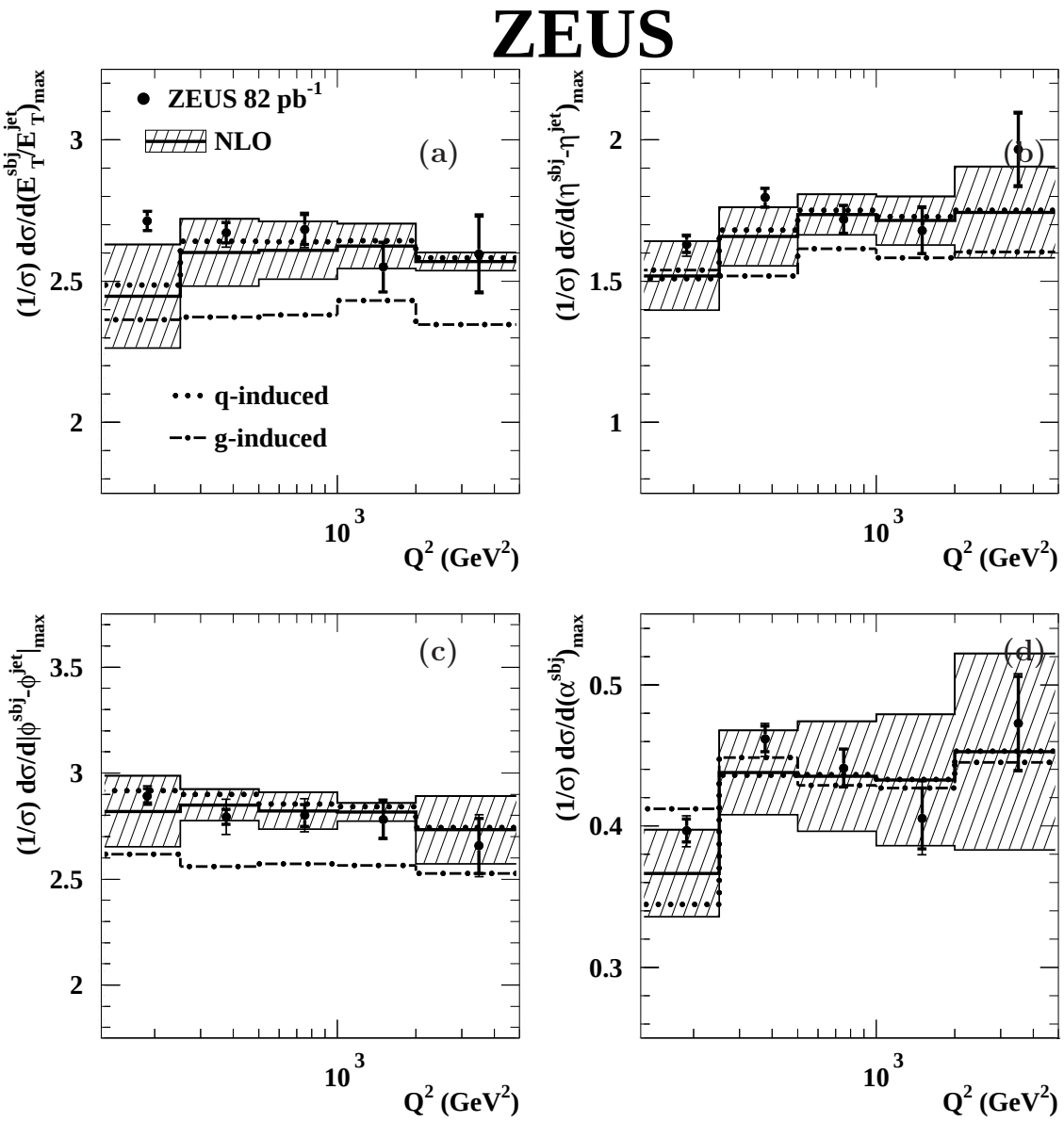

Figure 9.13: Maximum of the measured differential subjet cross sections in a) E_T^{sbj}/E_T^{jet}, b) $\eta^{sbj} - \eta^{jet}$, c) $|\phi^{sbj} - \phi^{jet}|$ and d) α^{sbj} as a function of Q^2. For comparison, the NLO predictions for quark- (dotted histograms) and gluon-induced (dot-dashed histograms) processes are also shown.

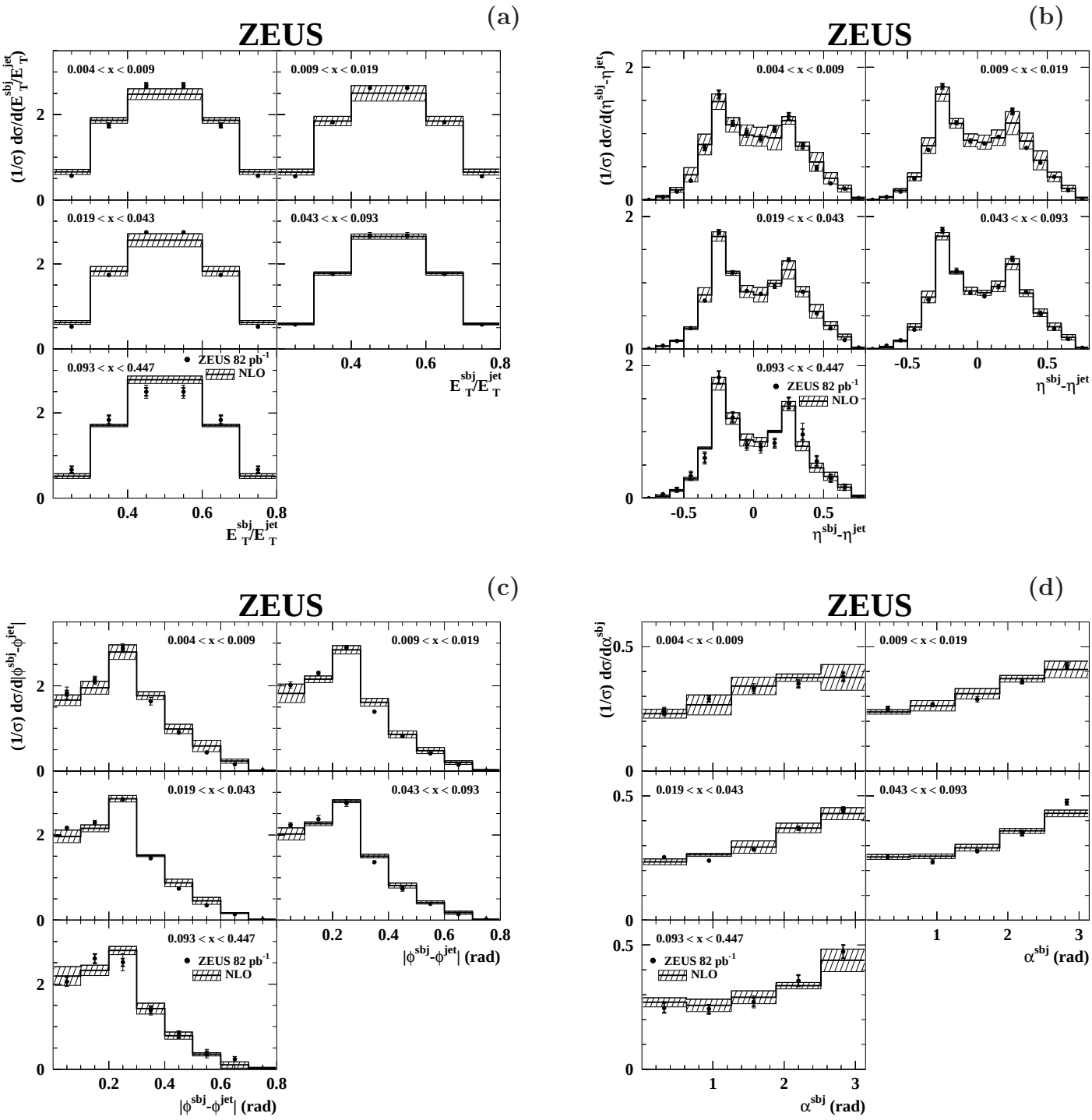

Figure 9.14: Measured normalised differential cross sections as functions of a) E_T^{sbj}/E_T^{jet}, b) $\eta^{sbj} - \eta^{jet}$, c) $|\phi^{sbj} - \phi^{jet}|$ and d) α^{sbj} in different regions of x. Other details are as in the caption to figure 9.1.

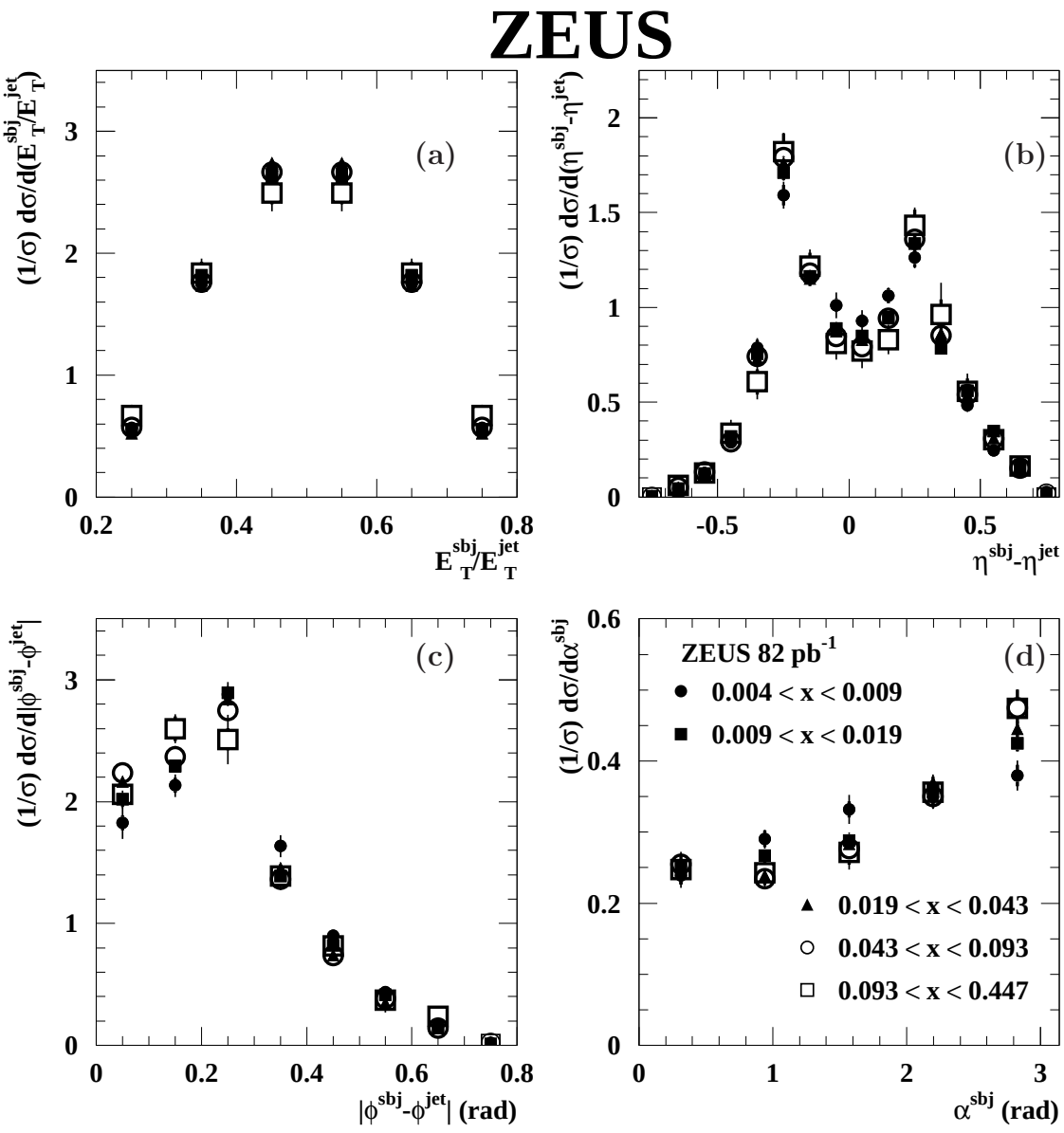

Figure 9.15: Measured normalised differential cross sections as functions of a) E_T^{sbj}/E_T^{jet}, b) $\eta^{sbj} - \eta^{jet}$, c) $|\phi^{sbj} - \phi^{jet}|$ and d) α^{sbj} in different regions of x. Details concerning the error bars are as in the caption to Fig. 9.1.

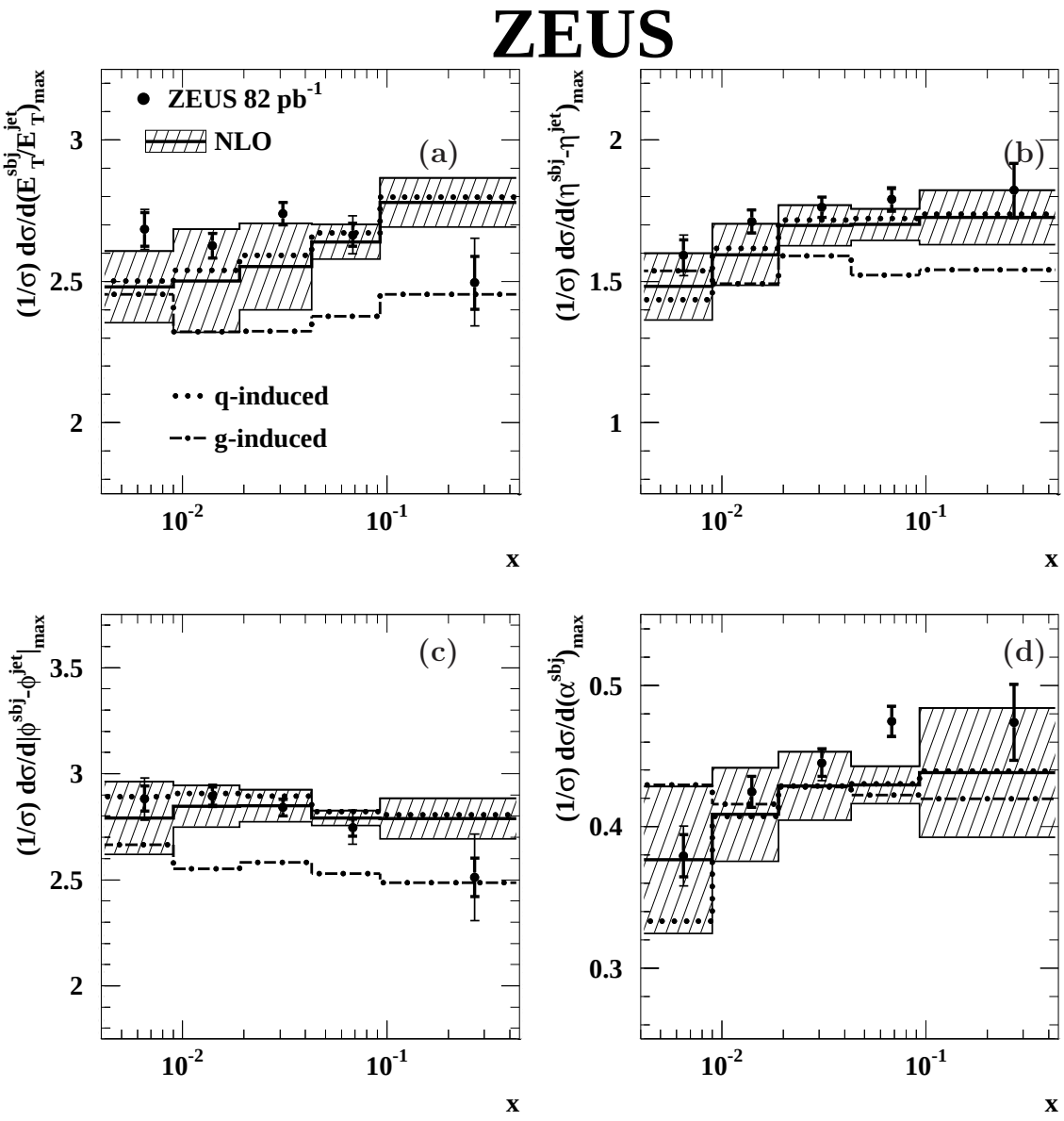

Figure 9.16: Maximum of the measured differential subjet cross sections in a) E_T^{sbj}/E_T^{jet}, b) $\eta^{sbj} - \eta^{jet}$, c) $|\phi^{sbj} - \phi^{jet}|$ and d) α^{sbj} as functions of x. For comparison, the NLO predictions for quark- (dotted histograms) and gluon-induced (dot-dashed histograms) processes are also shown.

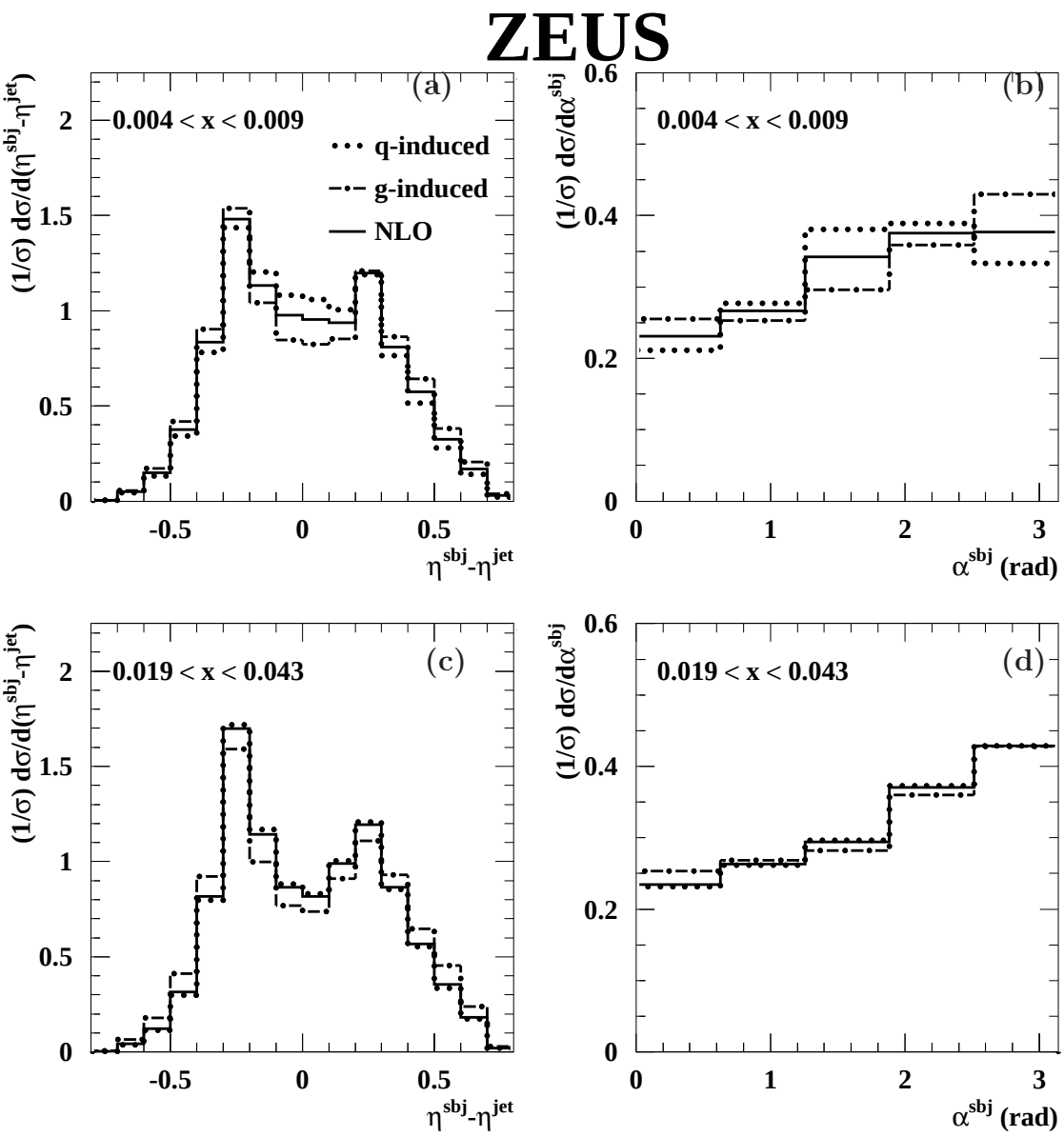

Figure 9.17: Predicted normalised differential subjet cross sections at NLO as functions of (a,c) $\eta^{sbj} - \eta^{jet}$ and (b,d) α^{sbj} in different regions of x. The NLO predictions for quark- (dotted histograms) and gluon-induced (dot-dashed histograms) processes separately are also shown.

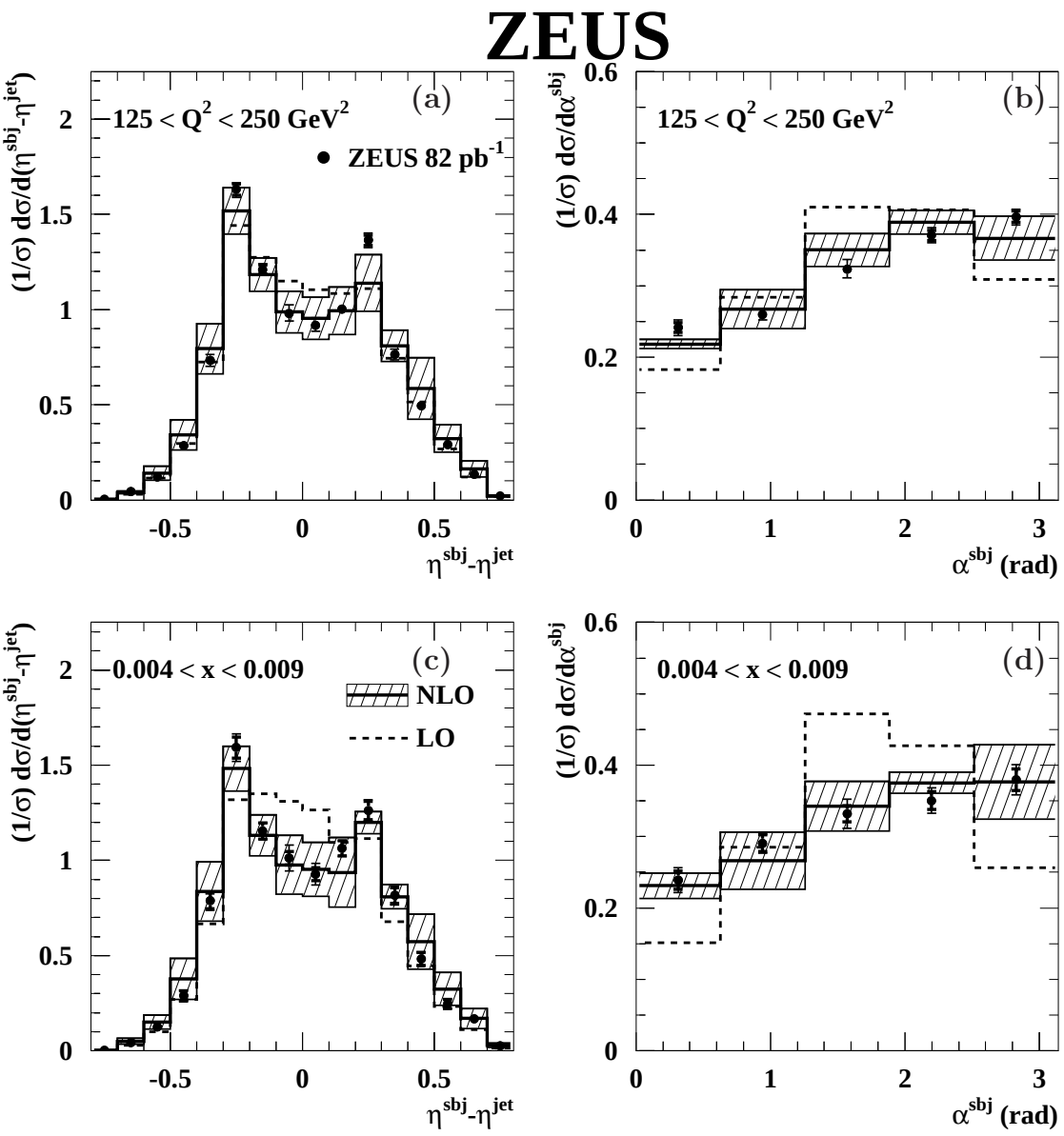

Figure 9.18: Measured normalised differential cross sections (dots) in restricted Q^2 and x regions as functions of (a,c) $\eta^{sbj} - \eta^{jet}$ and (b,d) α^{sbj}. The NLO (solid histograms) and LO (dashed histograms) calculations are also shown. The hatched bands represent the NLO theoretical uncertainty.

9.3 Three-subjet analysis

9.3.1 Normalised differential cross sections

In this section, subjet distributions for those jets that have exactly three subjets at a value of $y_{cut} = 0.01$ are presented. As mentioned before, the presence of the extra subjet allows for new variables to be constructed. The results presented are:

- Normalised differential cross sections as functions of E_T^{sbj}/E_T^{jet}, $\eta^{sbj} - \eta^{jet}$, $|\phi^{sbj} - \phi^{jet}|$, β^{sbj}, α_{23}, γ^{sbj} and $\eta_{low}^{sbj} - \eta^{jet}$ as well as comparisons with the predictions of fixed-order pQCD calculations.

- Comparison of the predictions of the normalised differential cross sections at leading order separately for each color configuration.

- Comparison of the measured normalised differential cross sections with the LO predictions based on the groups $SU(3)$ and $U(1)^3$ as well a scenario in which $C_F = 0$.

In figure 9.19(a) the distribution of E_T^{sbj}/E_T^{jet} is shown. It contains three entries per jet and it is thus no longer symmetric around 0.5 by construction. The minimum fraction of E_T that the subjets can have is $E_T^{sbj}/E_T^{jet} = \sqrt{y_{cut}} = 0.1$ and, therefore, the maximum fraction possible happens in the case that the lowest- and next-to-lowest-E_T subjets both have $E_T^{sbj}/E_T^{jet} = 0.1$ which implies that $E_{T,high}^{sbj}/E_T^{jet} = 0.8$. It is observed that the distribution peaks at values of $E_T^{sbj}/E_T^{jet} \sim 1/3$ showing that the three subjets tend to have similar transverse energy.

In Fig. 9.19(b) the distribution for $\eta^{sbj} - \eta^{jet}$ is shown. It also contains three entries per jet. The asymmetric two-peak structure observed in the two-subjet analysis is no longer present. In this case, it is allowed for one of the subjets to have values of $\eta^{sbj} - \eta^{jet}$ very close to zero since this does not imply that the others will be so close to it that they will not be resolvable. The structure of this distribution suggests that subjets tend to be close to each other in η.

Fig. 9.19(c) shows the normalised differential cross section as a function of $|\phi^{sbj} - \phi^{jet}|$. The dip in the middle that was observed in the two-subjet analysis is not present and it is also a consequence that values of $|\phi^{sbj} - \phi^{jet}| \sim 0$ do not imply that subjets are too close to each other. This distribution, together with the previous one, suggests that subjets tend to be near in the $\eta - \phi$ plane.

The distribution of β^{sbj} is shown in Fig. 9.19(d). It peaks at $\beta^{sbj} \sim 0$ and has a steeper fall-off than that of α^{sbj} in the two-subjet analysis. As previously mentioned, it is required that the fractions of E_T of the lowest- and next-to-lowest-E_T subjets

are such that $f_2 - f_3 > 0.2$, to ensure a better reconstruction of this variable. The observed distribution is compatible with the presence of color-coherence effects.

In Fig. 9.20(a) the normalised differential cross section as a function of α_{23} is shown. This is the angle between the two lowest-E_T subjets in the $\eta - \phi$ plane. Therefore, in order to ensure a good reconstruction of this variable, it is important to know which subjet is the highest-E_T one, and thus the cut $f_1 - f_2 > 0.2$ was applied. It can be seen that the distribution peaks at around $\alpha_{23} \sim \pi/2$ and that it is more often the case that the two lowest-E_T subjets are at angles bigger than $\pi/2$ than the opposite.

The distribution for γ^{sbj} is shown in Fig. 9.20(b). It peaks at $\gamma^{sbj} \sim \pi/2$ and is not symmetric around the peak; the region of $\gamma^{sbj} > \pi/2$ is more populated than that of $\gamma^{sbj} < \pi/2$.

The normalised differential cross section as a function of $\eta^{sbj}_{low} - \eta^{jet}$ is shown in Fig. 9.20(c). It shows very clearly that most of the time, the lowest-E_T subjet tends to be in the forward part of the jet, as expected from color-coherence effects. As in the two-subjet analysis, it has been studied whether this behaviour persists in different regions of η^{jet}. The corresponding plots can be seen in Fig. 9.21; it is observed that indeed the tendency for the lowest-E_T subjet to be in the forward part of the jet is mantained across all η^{jet} regions.

9.3.2 Comparison with LO and NLO QCD calculations

The comparison with the predictions of pQCD at both leading ($\mathcal{O}(\alpha_s^2)$) and next-to-leading ($\mathcal{O}(\alpha_s^3)$) order are also shown for each distribution together with the theoretical uncertainties in figures 9.19 and 9.20. The calculations provide a good description of the data for most of the distributions. The calculation of the cross section as a function of E_T^{sbj}/E_T^{jet} exhibits a peak at $0.2 < E_T^{sbj}/E_T^{jet} < 0.4$, as seen in the data. The calculations for the $\eta^{sbj}_{low} - \eta^{jet}$ and β^{sbj} distributions predict that the subjet with lowest E_T^{sbj} tends to be in the forward direction, in agreement with the data. The calculations for the α_{23} and γ^{sbj} distributions peak at $\pi/2$ and are asymmetric, as observed in the data. In figure 9.19(c) the largest discrepancy is observed: the subjets are somewhat closer to each other in ϕ in the data than in the fixed-order calculations. The distribution of α_{23} also shows a slight discrepancy: the peak at $\alpha_{23} \sim \pi/2$ is higher in the data than in the calculations. It should be noted that the shapes of the distributions are very similar for the LO and NLO calculations. In the LO calculations three subprocesses contribute to the production of jets with three subjets: $eq \to eqgg$, $eq \to eqq\bar{q}$ and $eg \to eq\bar{q}g$. The agreement between data and calculations shows that the mechanism driving the subjet topology in the data is the $eq \to eqgg$, $eq \to eqq\bar{q}$ and $eg \to eq\bar{q}g$ subprocesses as implemented in the

pQCD calculations.

9.3.3 Color dynamics through subjet correlations

The LO ($\mathcal{O}(\alpha_s^2)$) cross-section predictions for the production of jets with three subjets receive contributions from four different colour configurations:

$$\sigma_{ep\to 3 \text{ subjets}} = C_F C_F \cdot \sigma_A + C_F C_A \cdot \sigma_B + C_F T_F \cdot \sigma_C + T_F C_A \cdot \sigma_D \qquad (9.1)$$

Therefore, three subjet production provides a testing ground for the underlying colour dynamics.

Normalised differential three-subjet cross sections at LO of the individual colour configurations, σ_A, ..., σ_D, were calculated and are shown in figures 9.22 and 9.23. The four color configurations exhibit different behaviour in the distributions of the variables considered. In particular, the component which contains the contribution from the triple-gluon vertex in quark-induced processes ($eq \to eq(g \to gg)$), σ_B, has a very distinct shape with respect to the other components for all the variables considered: (a) the distribution is rather constant as a function of β^{sbj}; (b) the distribution in $\eta^{sbj}_{low} - \eta^{jet}$ has two peaks and a preference for the lowest-E_T^{sbj} subjet to be emitted backwards; (c) the distribution in α_{23} shows a preference for angles smaller than $\pi/2$; and (d) the distribution in γ^{sbj} shows a preference for large angles. Thus, it is demonstrated that correlations among the subjets show sensitivity to the different colour configurations.

The $SU(3)$-based predictions for the relative contribution of each colour component are: (A): 0.54-0.57, (B): 0.14-0.15, (C): 0.21-0.23 and (D): 0.08-0.09, depending on the requirements on the subjets. Therefore, the overall contribution from the diagrams that involve the triple-gluon vertex, configurations B and D, amounts to 22-23% in $SU(3)$. For the predictions based on $U(1)^3$ the relative contributions are: (A): 0.22-0.26 and (C): 0.74-0.78 whereas B and D do not contribute. In the scenario with $C_F = 0$, only σ_D survives.

The measured normalised differential three-subjet cross sections are compared to the LO predictions based on different symmetry groups in figures 9.24 and 9.25. In all distributions studied, the data disfavour the predictions based on $C_F = 0$. Some differences are observed between the data and the predictions of $U(1)^3$ in the distribution as a function of β^{sbj}. The measurements are best described by the calculations which include the admixture of colour configurations as predicted by $SU(3)$.

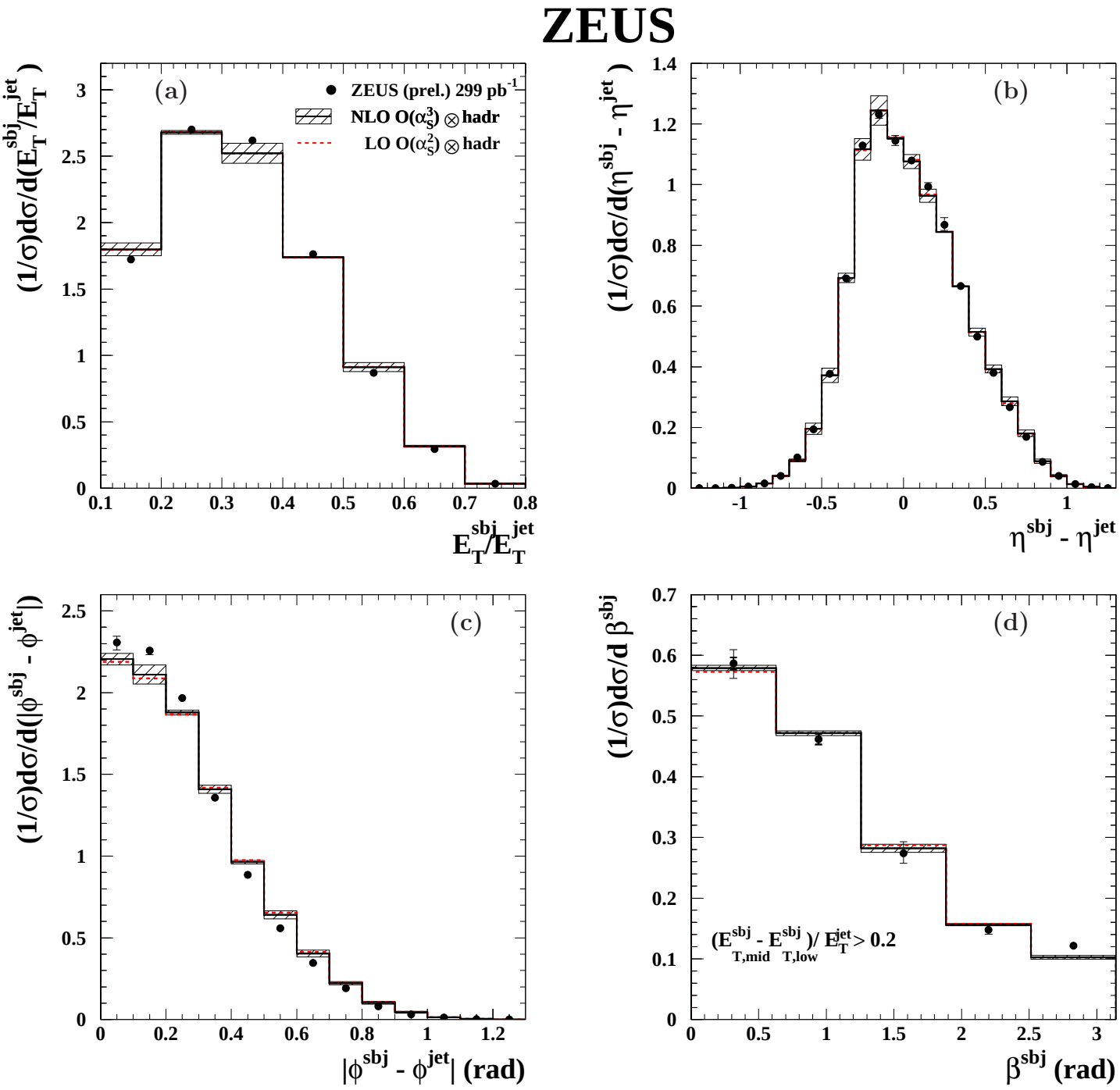

Figure 9.19: Measured normalised differential cross sections as functions of a) E_T^{sbj}/E_T^{jet}, b) $\eta^{sbj} - \eta^{jet}$, c) $|\phi^{sbj} - \phi^{jet}|$ and d) β^{sbj}. The inner error bar represent the statistical uncertainties of the data and the outer error bars show the statistical and systematic uncertainties added in quadrature. The data (dots) are compared to the predictions of pQCD calculations at leading order ($\mathcal{O}(\alpha_s^2)$, dashed lines) and next-to-leading order ($\mathcal{O}(\alpha_s^3)$, solid lines). The hatched bands represent the theoretical uncertainties of the NLO calculations.

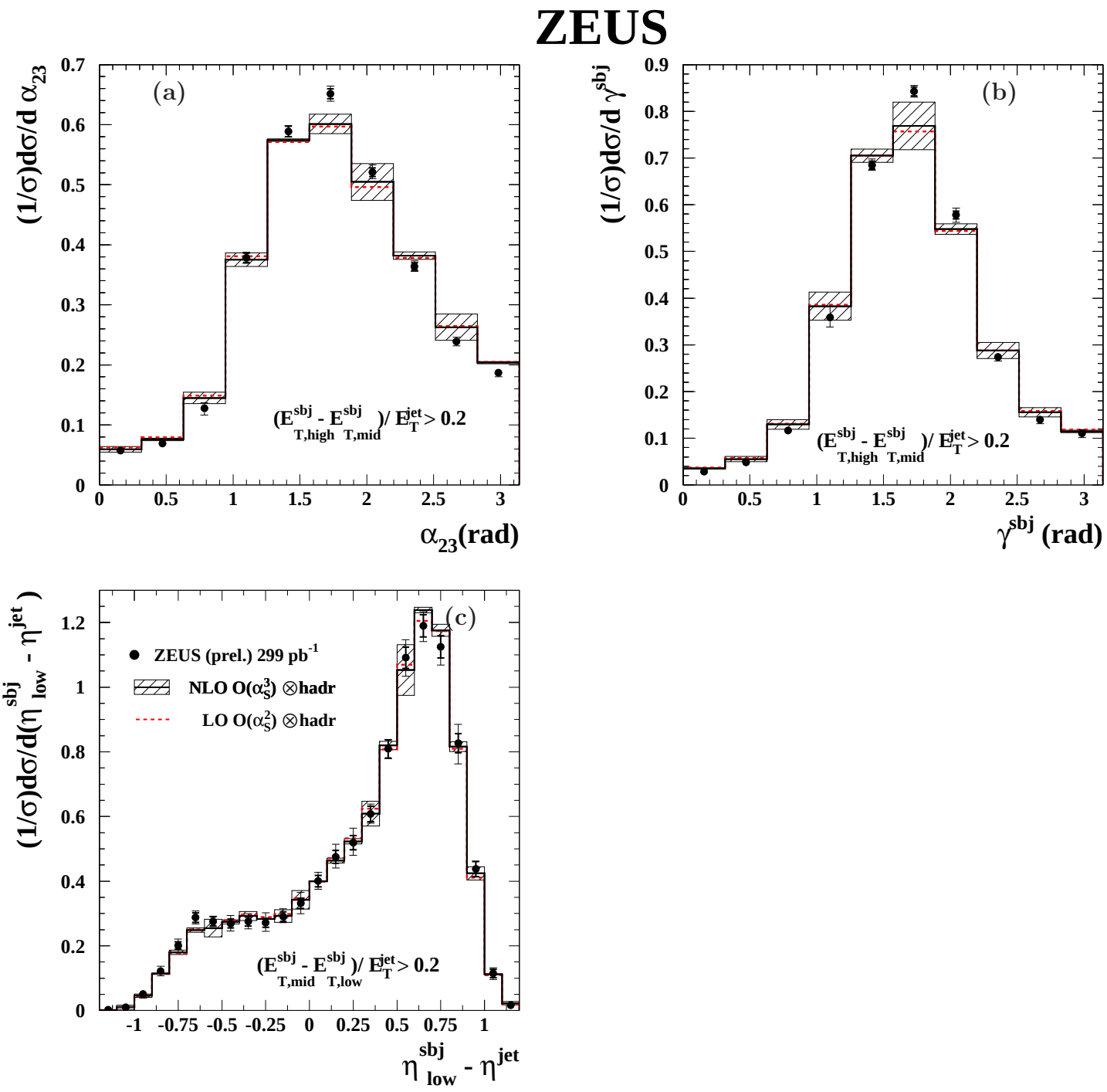

Figure 9.20: Measured normalised differential cross sections as functions of a) α_{23}, b) γ^{sbj} and c) $\eta^{sbj}_{low} - \eta^{jet}$. Other details are as in the caption to Fig. 9.19.

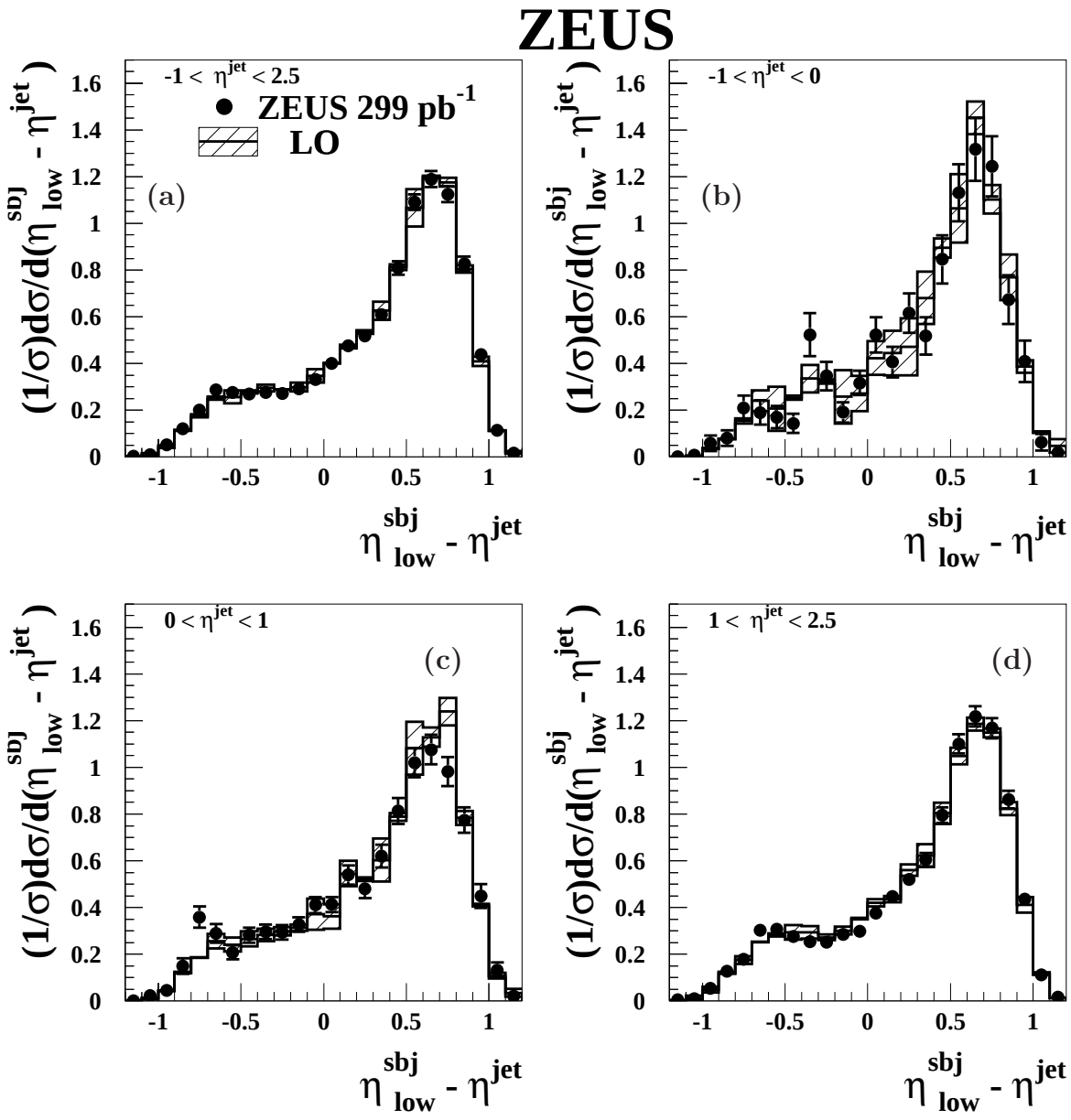

Figure 9.21: Measured normalised differential cross sections as functions of $\eta^{sbj}_{low} - \eta^{jet}$ in various regions of η^{jet}: a) $-1 < \eta^{jet} < 2.5$, b) $-1 < \eta^{jet} < 0$, c) $0 < \eta^{jet} < 1$ and d) $1 < \eta^{jet} < 2.5$. Other details are as in the caption to Fig. 9.19.

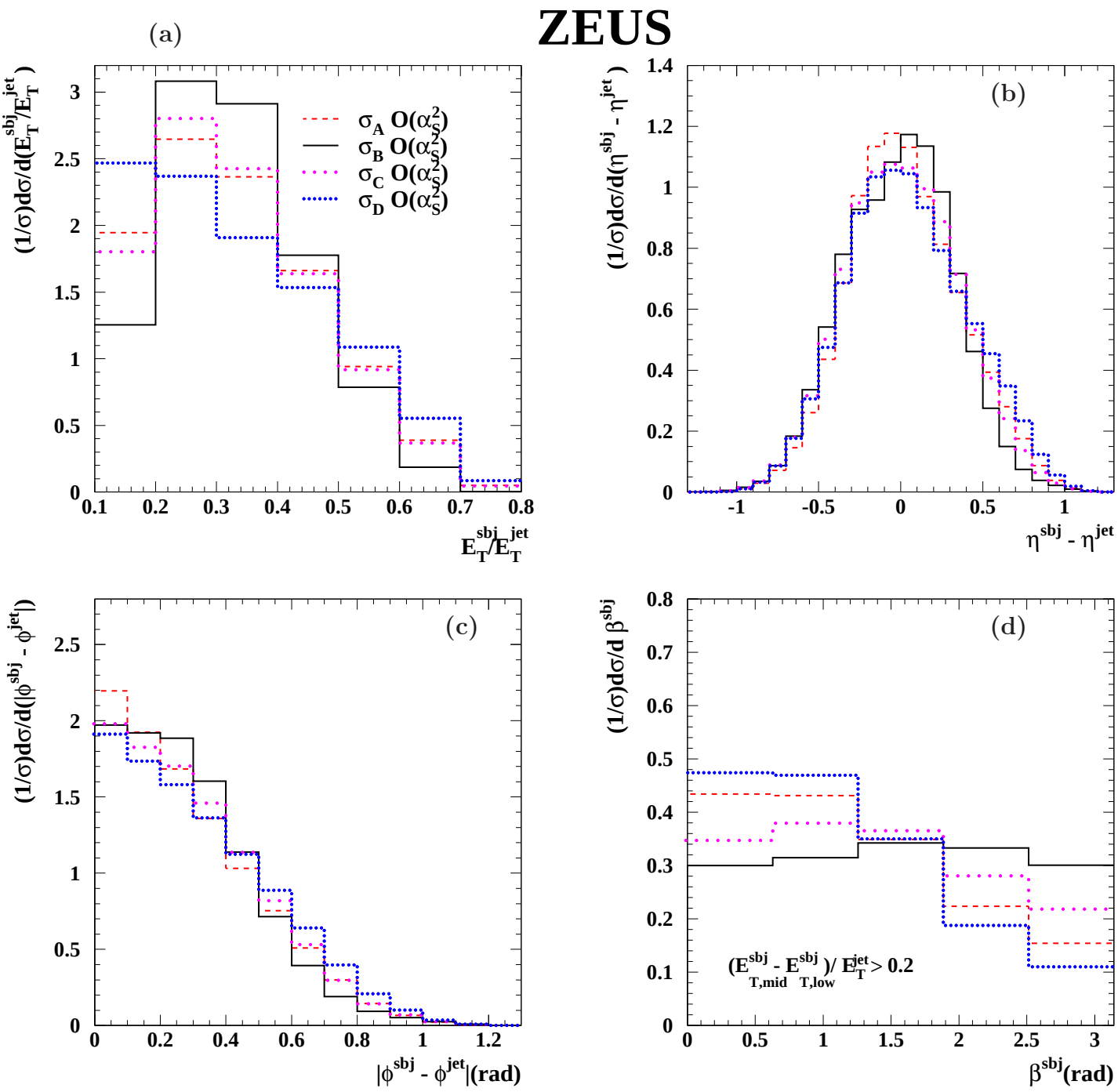

Figure 9.22: Predictions at LO ($\mathcal{O}(\alpha_s^2)$) of the normalised differential cross sections for the inclusive production of jets with exactly three subjets at $y_{cut} = 0.01$ separately for each color configuration (histograms) as functions of a) E_T^{sbj}/E_T^{jet}, b) $\eta^{sbj} - \eta^{jet}$, c) $|\phi^{sbj} - \phi^{jet}|$ and d) β^{sbj}.

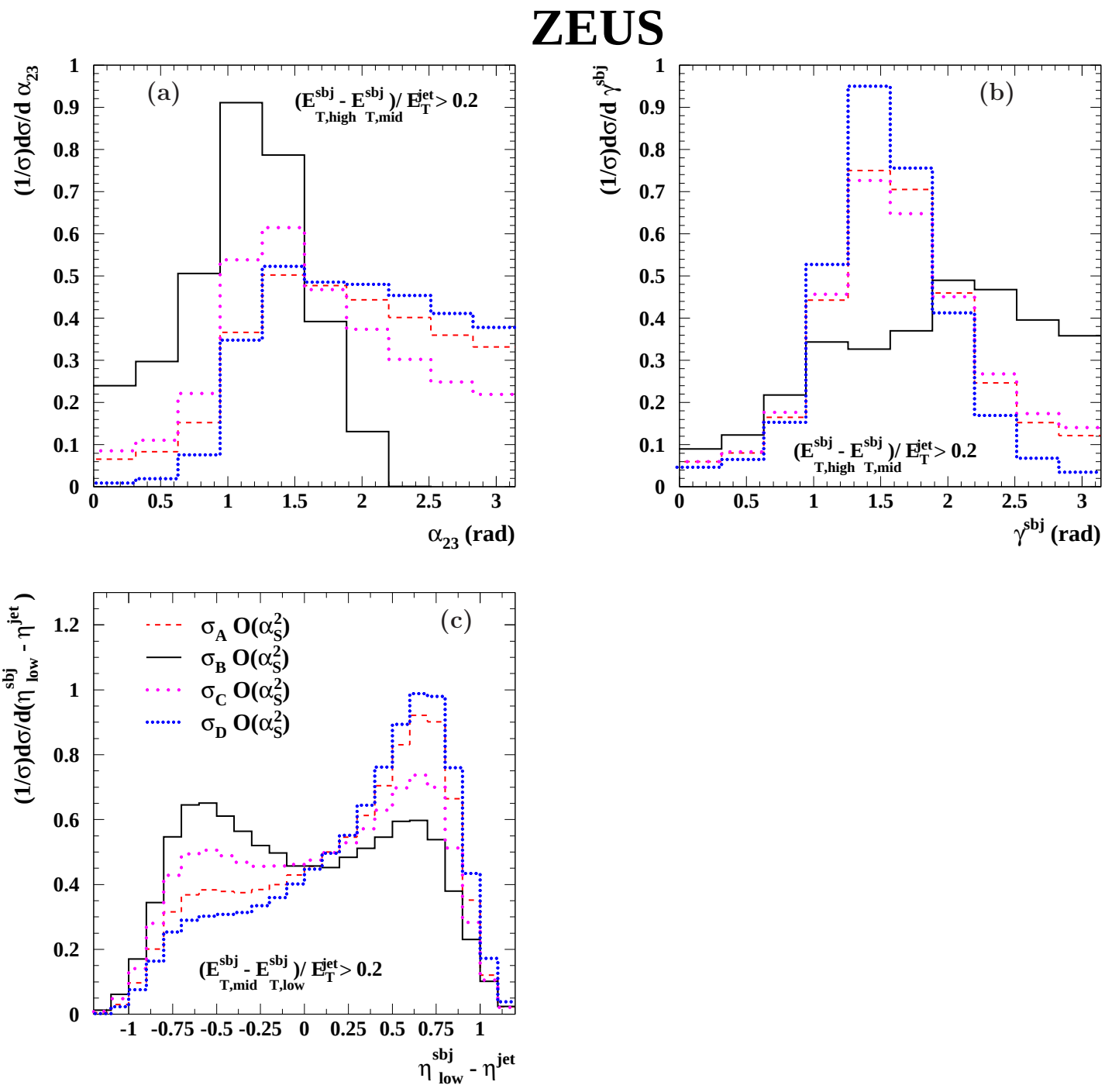

Figure 9.23: Predictions at LO ($\mathcal{O}(\alpha_s^2)$) of the normalised differential cross sections for the inclusive production of jets with exactly three subjets at $y_{cut} = 0.01$ separately for each color configuration (histograms) as functions of a) α_{23}, b) γ^{sbj} and c) $\eta^{sbj}_{low} - \eta^{jet}$.

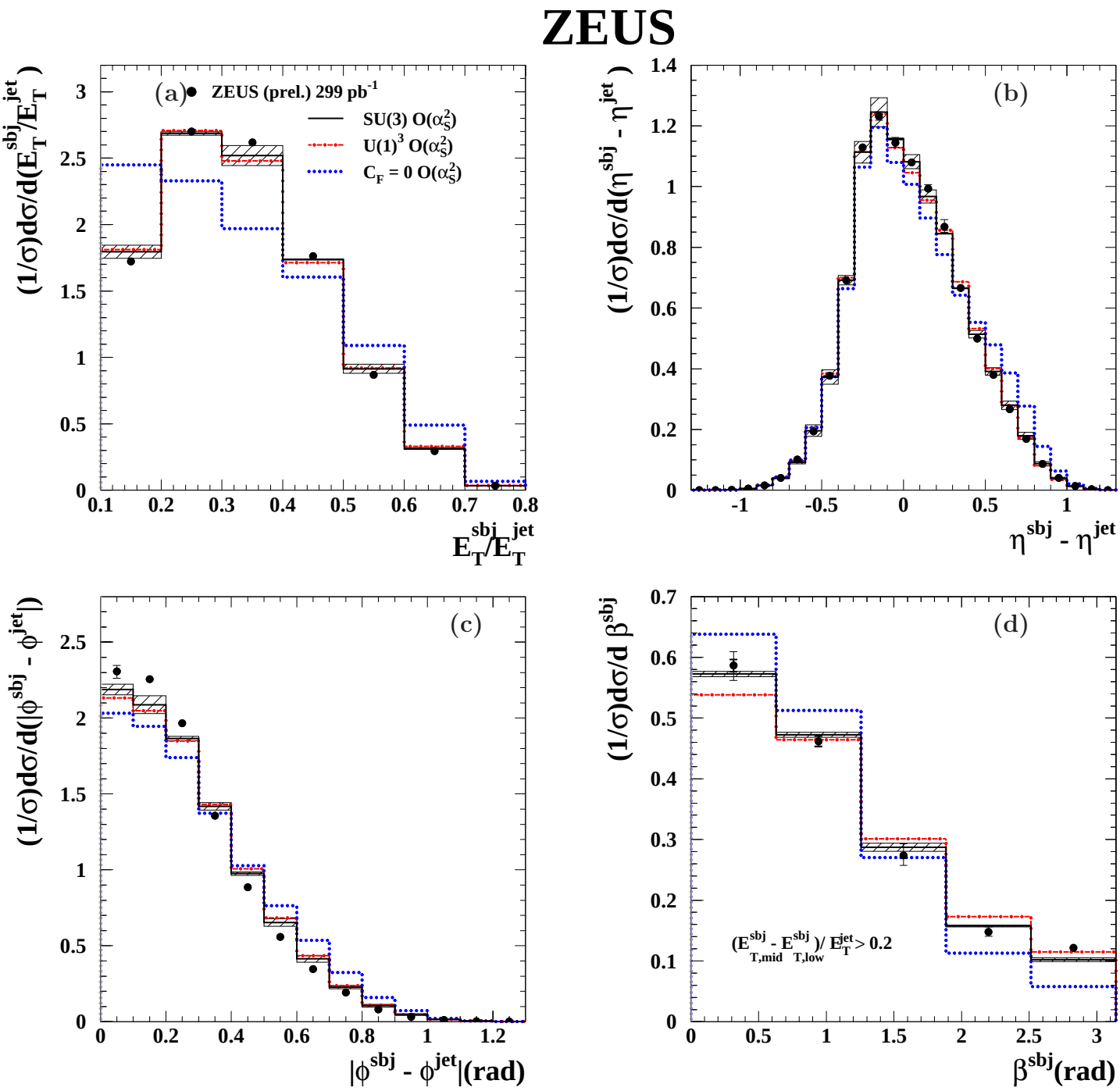

Figure 9.24: Measured normalised differential cross sections as functions of a) E_T^{sbj}/E_T^{jet}, b) $\eta^{sbj} - \eta^{jet}$, c) $|\phi^{sbj} - \phi^{jet}|$ and d) β^{sbj}. The data are compared to the LO predictions based on $SU(3)$ (solid line), $U(1)^3$ (dot-dashed line) and a scenario in which $C_F = 0$ (dotted line). Other details are as in the caption to Fig. 9.19.

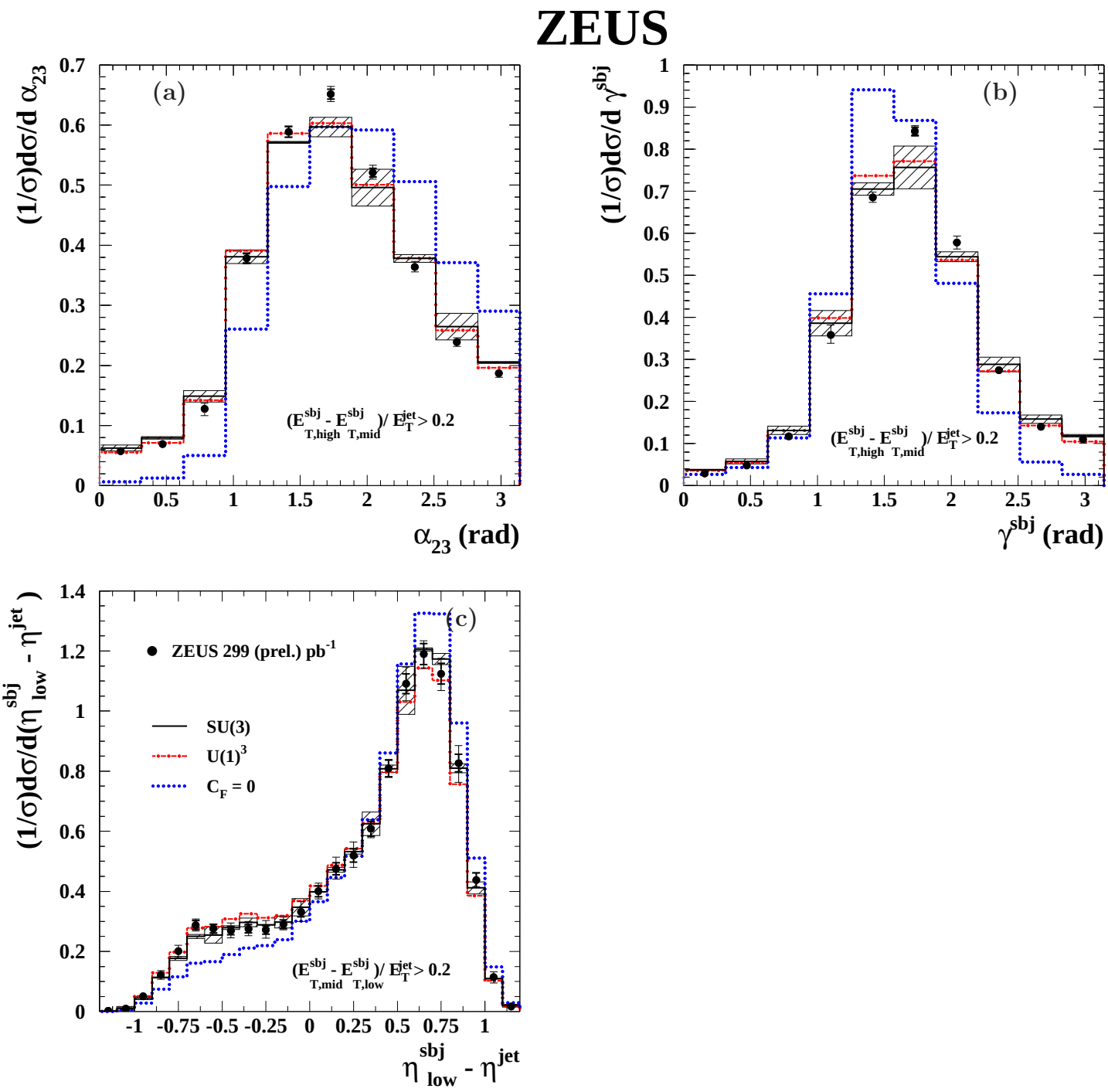

Figure 9.25: Measured normalised differential cross sections as functions of a) α_{23}, b) γ^{sbj} and c) $\eta^{sbj}_{low} - \eta^{jet}$. The data are compared to the LO predictions based on $SU(3)$ (solid line), $U(1)^3$ (dot-dashed line) and a scenario in which $C_F = 0$ (dotted line). Other details are as in the caption to Fig. 9.19.

Chapter 10

Summary and conclusions

In this chapter a brief summary of the results presented in this document is given.

Both analysis correspond to samples of inclusive-jet production in NC DIS with $Q^2 > 125$ GeV^2 in ep collisions at HERA collected by the ZEUS detector. The jet samples consist of those jets with a transverse energy $E_T^{jet} > 14$ GeV and pseudo-rapidity $-1 < \eta^{jet} < 2.5$ and were reconstructed in the laboratory frame with the k_T-cluster algorithm in its longitudinally-invariant inclusive mode. Subjets were reconstructed as the jet-like structures arising upon the re-application of the jet algorithm on those objects already belonging to a jet with given values of the resolution parameter y_{cut}.

10.1 Two-subjet analysis

In this analysis, those jets with two subjets at the resolution scale $y_{cut} = 0.05$ were considered. The data sample corresponds to 81.7 ± 1.9 pb^{-1} of integrated luminosity collected by the ZEUS detector during 1998-2000.

Normalised differential cross sections with respect to the subjet variables E_T^{sbj}/E_T^{jet}, $\eta^{sbj} - \eta^{jet}$, $|\phi^{sbj} - \phi^{jet}|$ and α^{sbj} were measured. Several features of parton radiation were observed: the subjets tend to have similar transverse energies and that the jet with the highest transverse energy tends to be in the rear part of the jet as a consequence of color-coherence effects, which induce the soft parton radiation to be emitted predominantly towards the proton beam direction. It was also observed that the subjets tend to be close to each other in the $\eta - \phi$ plane.

An adequate description of these features is given by NLO QCD calculations, which were performed with the program DISENT. This means that the pattern of parton radiation as predicted by QCD reproduces the subjet topology in the data. Furthermore, it was observed that the subjet distributions in the data are better

described by the calculations for jets arising from a quark-gluon pair ($q \to qg$) than by a quark-antiquark pair ($g \to q\bar{q}$), which is consistent with the NLO expectation that 82% of the jets arise from a quark-gluon pair.

The evolution of the normalised differential cross sections with the energy scale was also studied. A weak dependence with the E_T^{jet} was observed, which is consistent with the expectation that the dynamics of parton evolution depends logarithmically with the energy scale.

The normalised differential cross sections were studied in different regions of η^{jet} in order to confirm the prediction of color coherence by which the lowest transverse energy subjet would be predominantly emitted towards the proton beam even in the regions of negative η^{jet}, as was indeed observed.

The evolution of the subjet cross sections with Q^2 was also studied. It is observed that the distribution of E_T^{sbj}/E_T^{jet} does not change significantly, but some dependence can be seen in the other observables. These dependencies are reasonably reproduced by the NLO QCD calculations and understood as the combination of two effects: the fraction of gluon- and quark-induced events changes significantly from the lowest-Q^2 region to the higher-Q^2 regions. The second effect is that the shape of gluon- and quark-induced events also changes. Similar effects are seen in the evolution of the cross sections with x. To investigate further the changes in shape observed, LO and NLO calculations were compared. It is observed that there are significant differences between the two calculations, demonstrating that the NLO QCD radiative corrections are responsible for these variations in shape and necessary for describing the data.

10.2 Three-subjet analysis

In this analysis, those jets with three subjets at the resolution scale $y_{cut} = 0.01$ were selected from 299.2 ± 7.8 pb^{-1} of integrated luminosity collected by ZEUS in the period 2004-2007. The subjet variables defined for this analysis were E_T^{sbj}/E_T^{jet}, $\eta^{sbj} - \eta^{jet}$, $|\phi^{sbj} - \phi^{jet}|$, β^{sbj}, α_{23}, γ^{sbj} and $\eta_{low}^{sbj} - \eta^{jet}$.

Normalised differential cross sections as functions of these variables were measured. The data show that the three subjets tend to have similar transverse energies and that the subjet with lowest transverse energy tends to be in forward direction. This is consistent with the effects of color coherence between the initial and final states. To further check this prediction, measurements of normalised differential cross sections as functions of $\eta_{low}^{sbj} - \eta^{jet}$ were performed in different regions of η^{jet} in order to check that the lowest transverse energy subjet tends to be in the forward part of jet also in regions where $\eta^{jet} < 0$. It is observed that the subjets tend to be

close to each other in the $\eta - \phi$ plane. An adequate description of the data is given by the $\mathcal{O}(\alpha_s^3)$ pQCD calculations.

The sensitivity of the cross sections to different color configurations was studied by comparing the measured distributions to the predictions at LO ($\mathcal{O}(\alpha_s^2)$) based on the underlying gauge symmetries $SU(3)$ and $U(1)^3$ as well as a scenario in which $C_F = 0$. The data disfavor the scenario with $C_F = 0$. Some differences are observed between the data and the predictions of $U(1)^3$ in the distribution of β^{sbj}. The measurements are best described by the calculations which include the admixture of the color configurations as predicted by $SU(3)$.

10.3 Final remarks

The results presented in this thesis demonstrate that perturbative QCD calculations at next-to-leading order are able to describe the internal structure of jets. They also highlight that the pattern of parton radiation in general and the colour flow in particular are observable in certain regions of phase space. Thus, the measurements of subjet topology presented here demonstrate the feasibility of investigating the internal structure of jets using subjets with experimental data and pave the way for the use of subjets in hadron-hadron collisions, such as those that will be soon available at the LHC, as a new means to search for new heavier particles decaying into (sub)jets.

Resumen y conclusiones

En este capítulo se presenta un resumen de los resultados y conclusiones más relevantes del trabajo presentado.

Los dos análisis presentados corresponden a muestras de producción inclusiva de jets en el régimen de corrientes neutras en DIS en las cuales $Q^2 > 125$ GeV^2 en colisiones ep en HERA medidas por ZEUS. Las muestras de jets consisten en aquellos jets cuya energía transversa cumple que $E_T^{jet} > 14$ GeV y pseudorapidez $-1 < \eta^{jet} < 2.5$ y fueron reconstruidos en el sistema de referencia del laboratorio con el algoritmo k_T-cluster en su modo inclusivo y longitudinalmente invariante. Los subjets fueron reconstruidos como las estructuras análogas a jets que resultan de la re-aplicación del algoritmo de reconstrucción sobre los objetos previamente asociados a un jet habiendo modificado el parámetro de resolución y_{cut}.

10.4 Análisis de dos subjets

En este análisis, se consideraron aquellos jets con exactamente dos jets a la escala de resolución $y_{cut} = 0.05$ en una muestra de 81.7 ± 1.9 pb^{-1} de luminosidad integrada correspondiente al período 1998-2000.

Se midieron secciones eficaces diferenciales normalizadas como funciones de las variables de subjet E_T^{sbj}/E_T^{jet}, $\eta^{sbj} - \eta^{jet}$, $|\phi^{sbj} - \phi^{jet}|$ y α^{sbj}, que son sensibles al patrón de radiación partónica. Los datos mostraron, por una parte, que los subjets tienden a tener energías transversas similares y que el subjet con la energía transversa más alta tiende a estar en la parte trasera del jet, lo cual es compatible con los efectos de coherencia de color, por los cuales la radiación partónica suave tiende a emitirse principalmente hacia el haz de protones desde el punto de vista del jet. Además, se observó que los subjets tienden a estar cerca uno del otro en el plano $\eta - \phi$.

Los cálculos de pQCD NLO, realizados con el programa DISENT, fueron capaces de reproducir correctamente estos aspectos de la radiación partónica, mostrando que pQCD es capaz de describir la topología de los subjets observada en los datos. Además, se observó que las distribuciones de subjets están mejor descritas por cálculos para jets provenientes de una pareja quark-gluon ($q \to qg$) que para aquellos provenientes de una pareja quark-antiquark ($g \to \bar{q}q$), lo cual es compatible con la predicción NLO según la cual el 82% de los jets provienen de una pareja quark-gluon.

Se estudió también la evolución de las secciones eficaces diferenciales normalizadas con la escala de la energía. Se observó poca dependencia con la energía transversa de los jets, lo cual es compatible con el hecho de que la dependencia con la escala de la energía es logarítmica.

Las secciones eficaces normalizadas fueron estudiadas en diferentes regiones de η^{jet} para confirmar la predicción de que si los efectos de coherencia de color están presentes, el subjet de menos E_T sería principalmente emitido hacia la zona del haz del protón incluso en la región donde $\eta^{jet} < 0$.

La evolución con Q^2 muestra que la distribución en E_T^{sbj}/E_T^{jet} apenas varía, pero sí se observa alguna dependencia en el resto de variables. Estas dependencias están correctamente descritas por los cálculos NLO y se entienden como una combinación de dos efectos: la fracción de jets inducidos por gluones y quarks cambia con Q^2, y además la forma de las distribuciones para jets inducidos por quarks y por gluones también cambia. Efectos similares se pueden observar en la evolución de las secciones eficaces con x.

Con el objetivo de investigar más profundamente los cambios observados en la forma de las distribuciones, se realizaron comparaciones de cálculos LO y NLO. Las diferencias entre los cálculos demuestran que las correcciones radiativas de NLO QCD son responsables de estas variaciones en la forma y por tanto necesarias para describir los datos.

10.5 Análisis de tres subjets

En este análisis, aquellos jets con tres subjets a la escala de resolución $y_{cut} = 0.01$ fueron seleccionados de 299.2 ± 7.8 pb^{-1} de luminosidad integrada obtenida por ZEUS durante 2004-2007. Las variables definidas para este análisis son E_T^{sbj}/E_T^{jet}, $\eta^{sbj} - \eta^{jet}$, $|\phi^{sbj} - \phi^{jet}|$, β^{sbj}, α_{23}, γ^{sbj} y $\eta_{low}^{sbj} - \eta^{jet}$.

Se obtuvieron secciones eficaces diferenciales normalizadas como función de estas variables. Los datos muestran que los subjets tienden a tener energías transversas similares y que los subjets con la energía transversa más baja tienden a estar en la parte delantera del jet. Esto es consistente con la presencia de efectos de coherencia de color entre los estados inicial y final. Para comprobar esta predicción más profundamente, se estudió la distribución en $\eta_{low}^{sbj} - \eta^{jet}$ como función de η^{jet}, y se comprobó que efectivamente el subjet de menos E_T apunta hacia el haz de protones incluso en el caso en el que $\eta^{jet} < 0$. También se observó que los subjets tienden a estar cerca en el plano $\eta - \phi$. Los cálculos NLO ($\mathcal{O}(\alpha_s^3)$), realizados con el programa NLOJET++, describen satisfactoriamente la topología de los subjets observada en los datos.

La sensibilidad de las secciones eficaces a distintas configuraciones de color fue estudiada mediante comparaciones de las distribuciones medidas con predicciones LO ($\mathcal{O}(\alpha_s^2)$) basadas en los grupos de simetría gauge $SU(3)$ y $U(1)^3$, así como en un escenario en el cual el factor de color C_F vale cero. Los datos desfavorecen

el escenario en el cual $C_F = 0$. Se observan algunas diferencias entre los datos y las predicciones de $U(1)^3$ en la distribución de β^{sbj}. En general, las medidas están mejor descritas por los cálculos en los cuales las configuraciones de color están implementadas de acuerdo con las predicciones $SU(3)$.

10.6 Conclusiones finales

Los resultados presentados en esta tesis doctoral demuestran que los cálculos de QCD perturbativa al siguiente orden son capaces de describir la estructura interna de jets. Así mismo, se enfatiza que el patrón de radiación partónica en general y el flujo de color en particular son observables en ciertas regiones del espacio de fases. Por lo tanto, las medidas de topología de subjets presentadas aquí demuestran la factibilidad de investigar la estructura interna de jets mediante subjets con datos experimentales, y sirven de guía para el uso de subjets como un nuevo medio de búsqueda de partículas masivas en colisiones hadrón hadrón, como las que pronto tendrán lugar en el LHC.

Chapter 11

Appendix

11.1 Theoretical uncertainties for the two-subjet analysis

In this section, the remaining plots from section 5.5, in which the theoretical uncertainties are discussed, are shown.

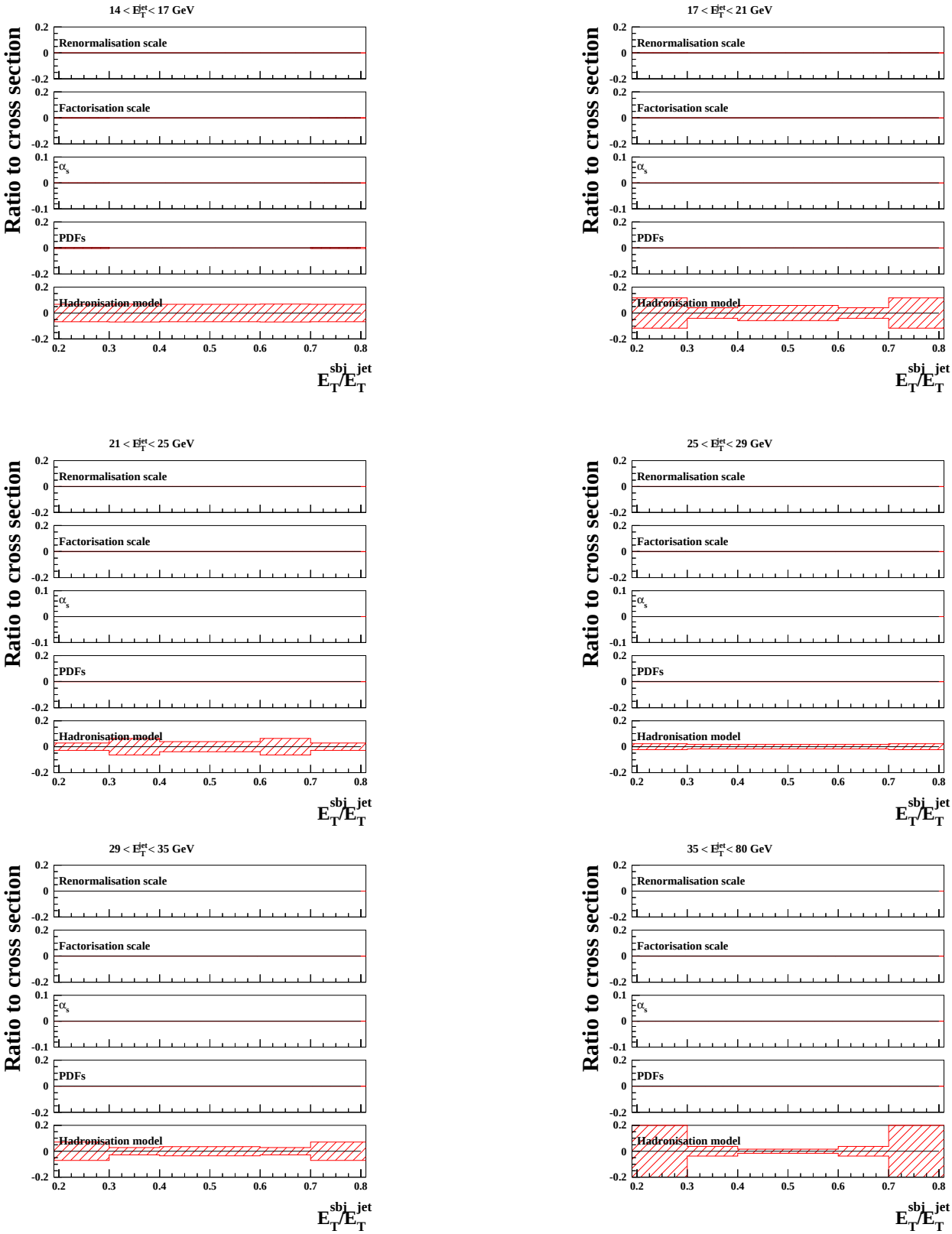

Figure 11.1: Relative theoretical uncertainties of the normalised differential cross-section calculations for the inclusive production of jets with exactly two subjets at $y_{cut} = 0.05$ as functions of E_T^{sbj}/E_T^{jet} in regions of E_T^{jet}.

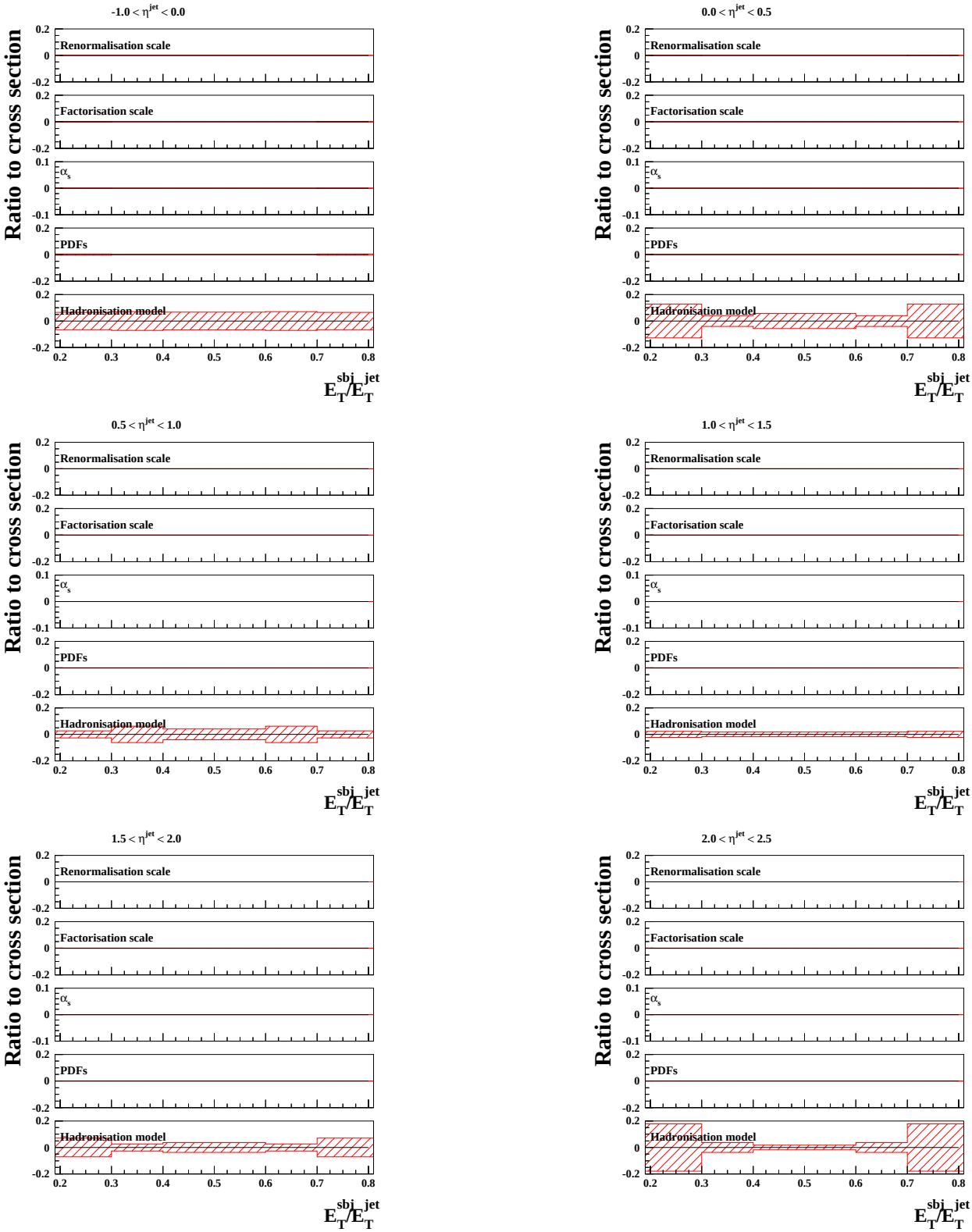

Figure 11.2: Relative theoretical uncertainties of the normalised differential cross-section calculations for the inclusive production of jets with exactly two subjets at $y_{cut} = 0.05$ as functions of E_T^{sbj}/E_T^{jet} in regions of η^{jet}.

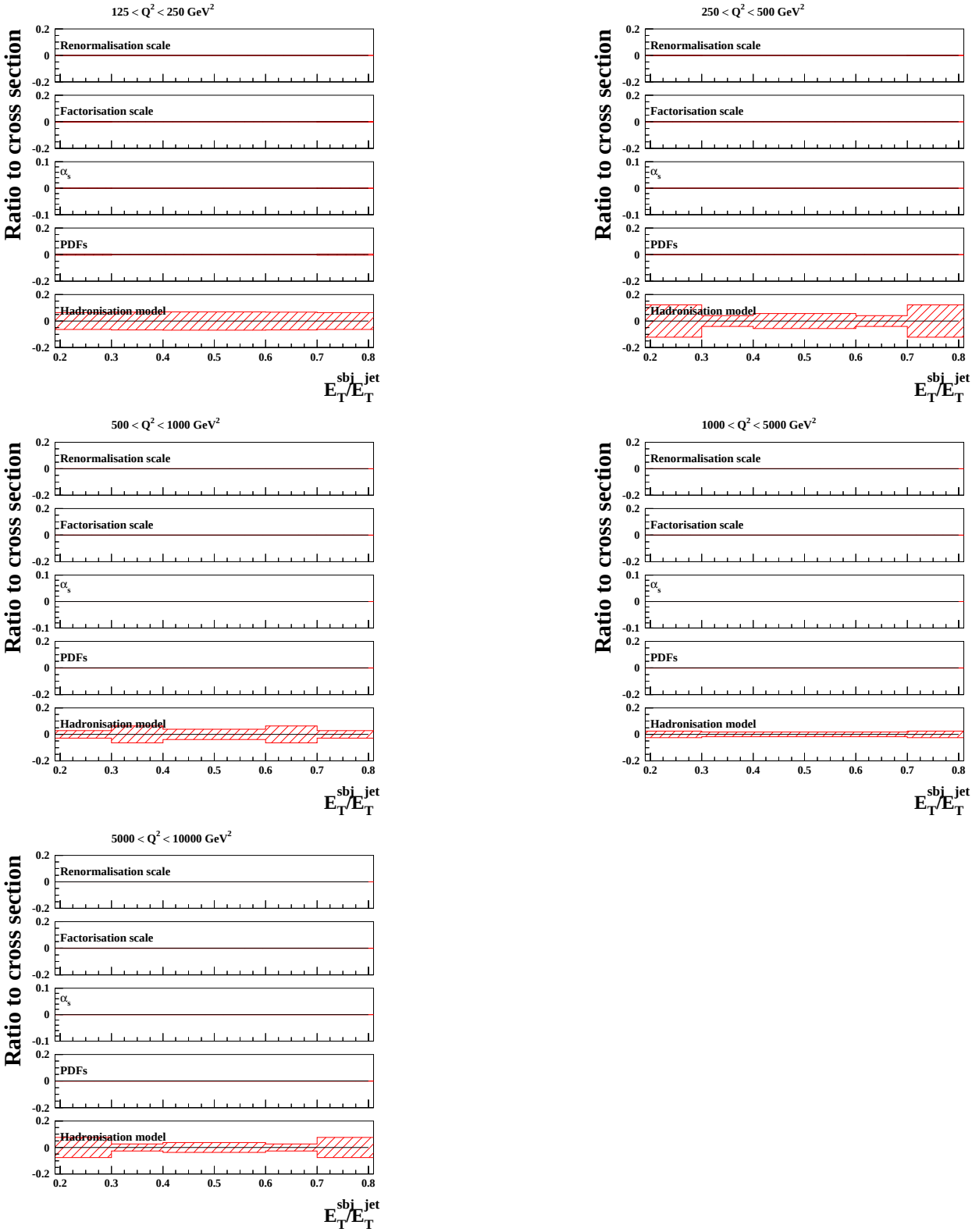

Figure 11.3: Relative theoretical uncertainties of the normalised differential cross-section calculations for the inclusive production of jets with exactly two subjets at $y_{cut} = 0.05$ as functions of E_T^{sbj}/E_T^{jet} in regions of Q^2.

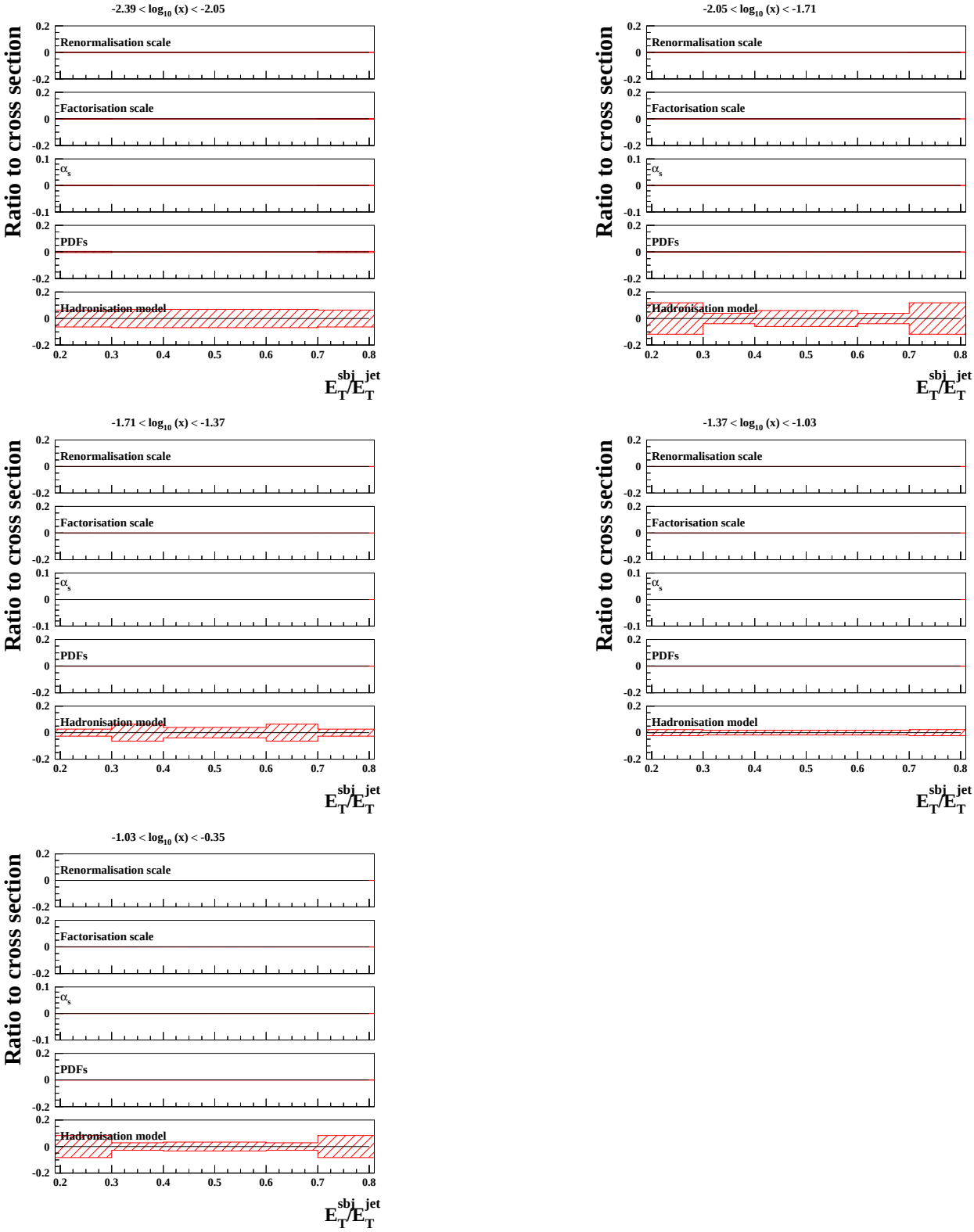

Figure 11.4: Relative theoretical uncertainties of the normalised differential cross-section calculations for the inclusive production of jets with exactly two subjets at $y_{cut} = 0.05$ as functions of E_T^{sbj}/E_T^{jet} in regions of x.

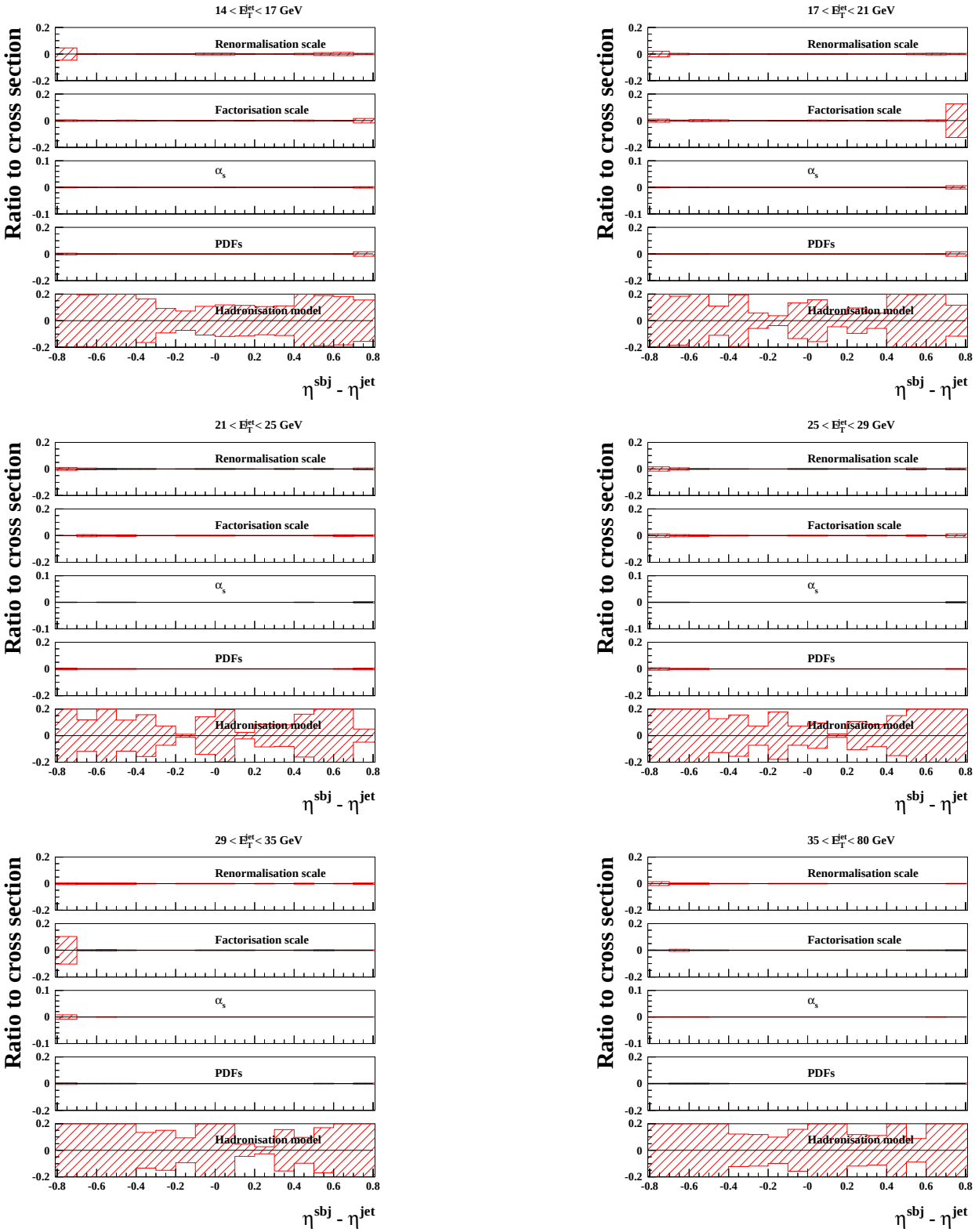

Figure 11.5: Relative theoretical uncertainties of the normalised differential cross-section calculations for the inclusive production of jets with exactly two subjets at $y_{cut} = 0.05$ as functions of $\eta^{sbj} - \eta^{jet}$ in regions of E_T^{jet}.

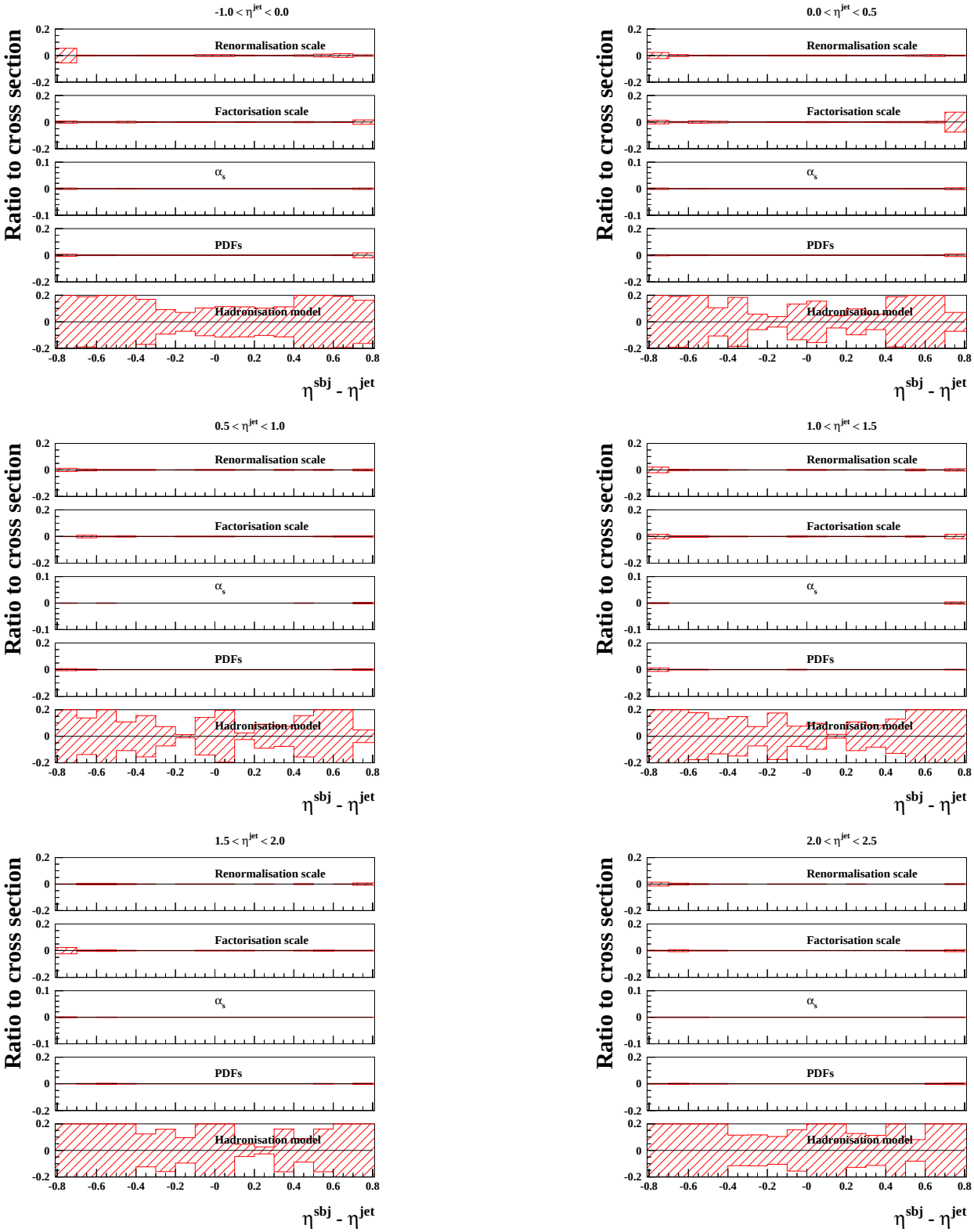

Figure 11.6: Relative theoretical uncertainties of the normalised differential cross-section calculations for the inclusive production of jets with exactly two subjets at $y_{cut} = 0.05$ as functions of $\eta^{sbj} - \eta^{jet}$ in regions of η^{jet}.

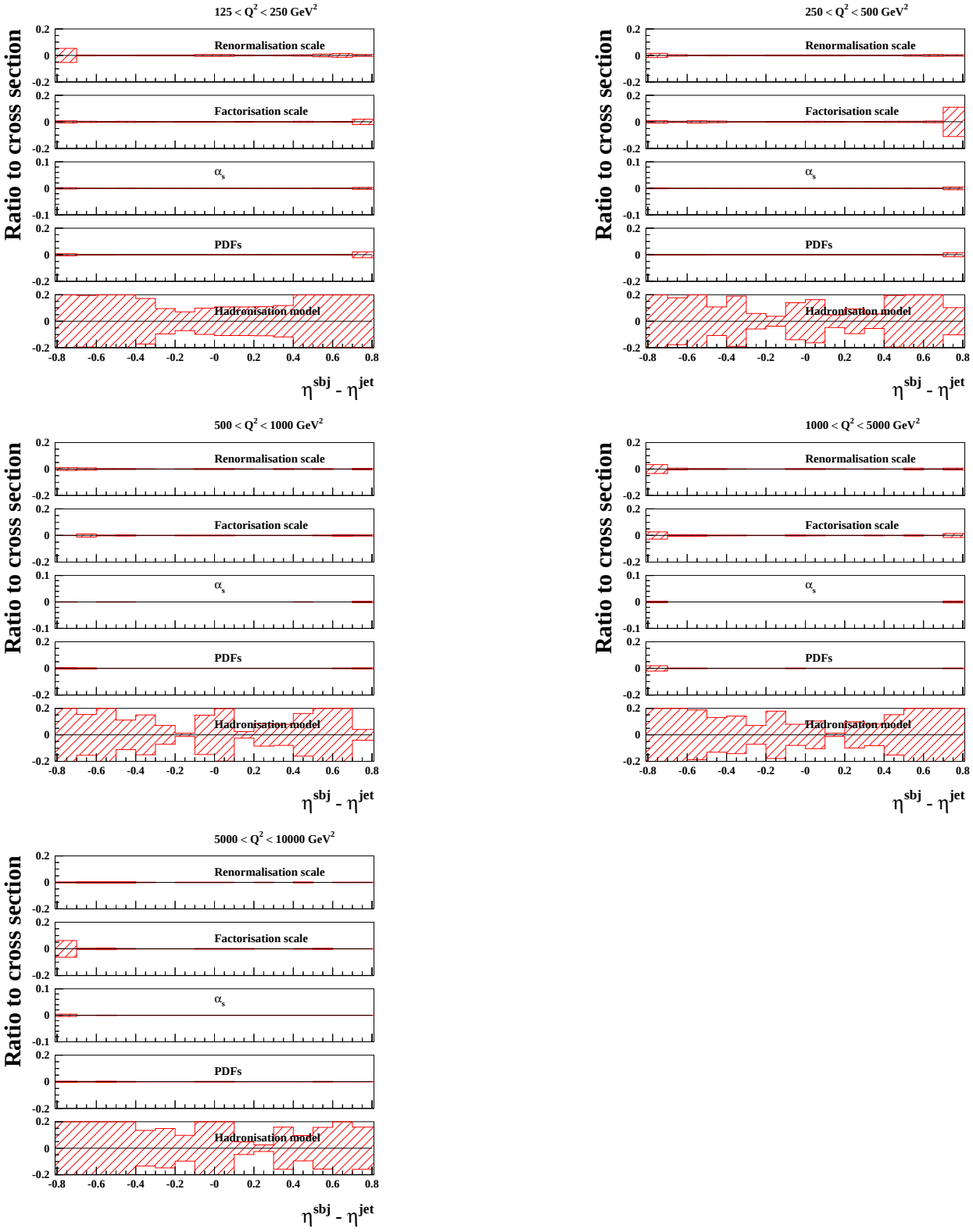

Figure 11.7: Relative theoretical uncertainties of the normalised differential cross-section calculations for the inclusive production of jets with exactly two subjets at $y_{cut} = 0.05$ as functions of $\eta^{sbj} - \eta^{jet}$ in regions of Q^2.

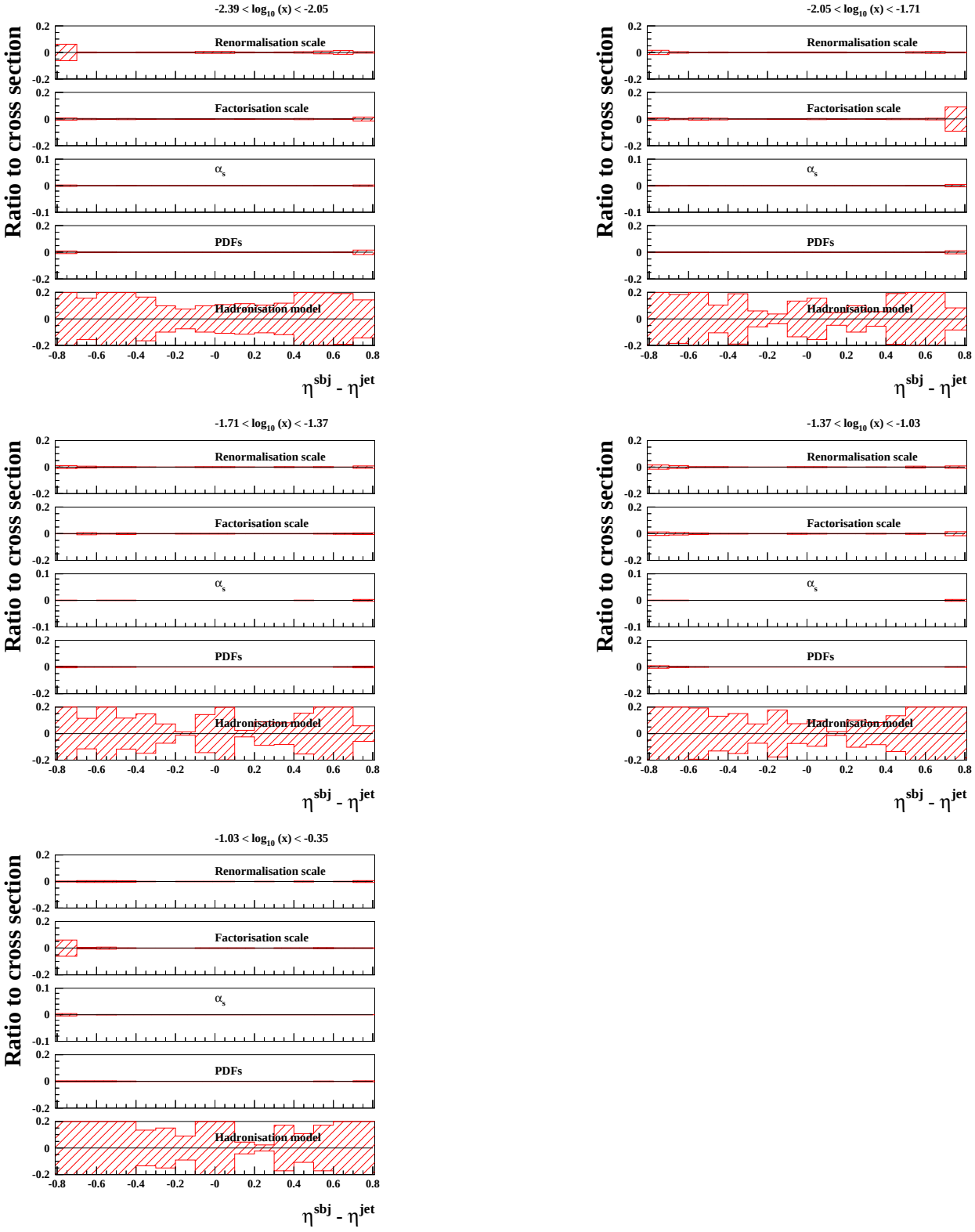

Figure 11.8: Relative theoretical uncertainties of the normalised differential cross-section calculations for the inclusive production of jets with exactly two subjets at $y_{cut} = 0.05$ as functions of $\eta^{sbj} - \eta^{jet}$ in regions of x.

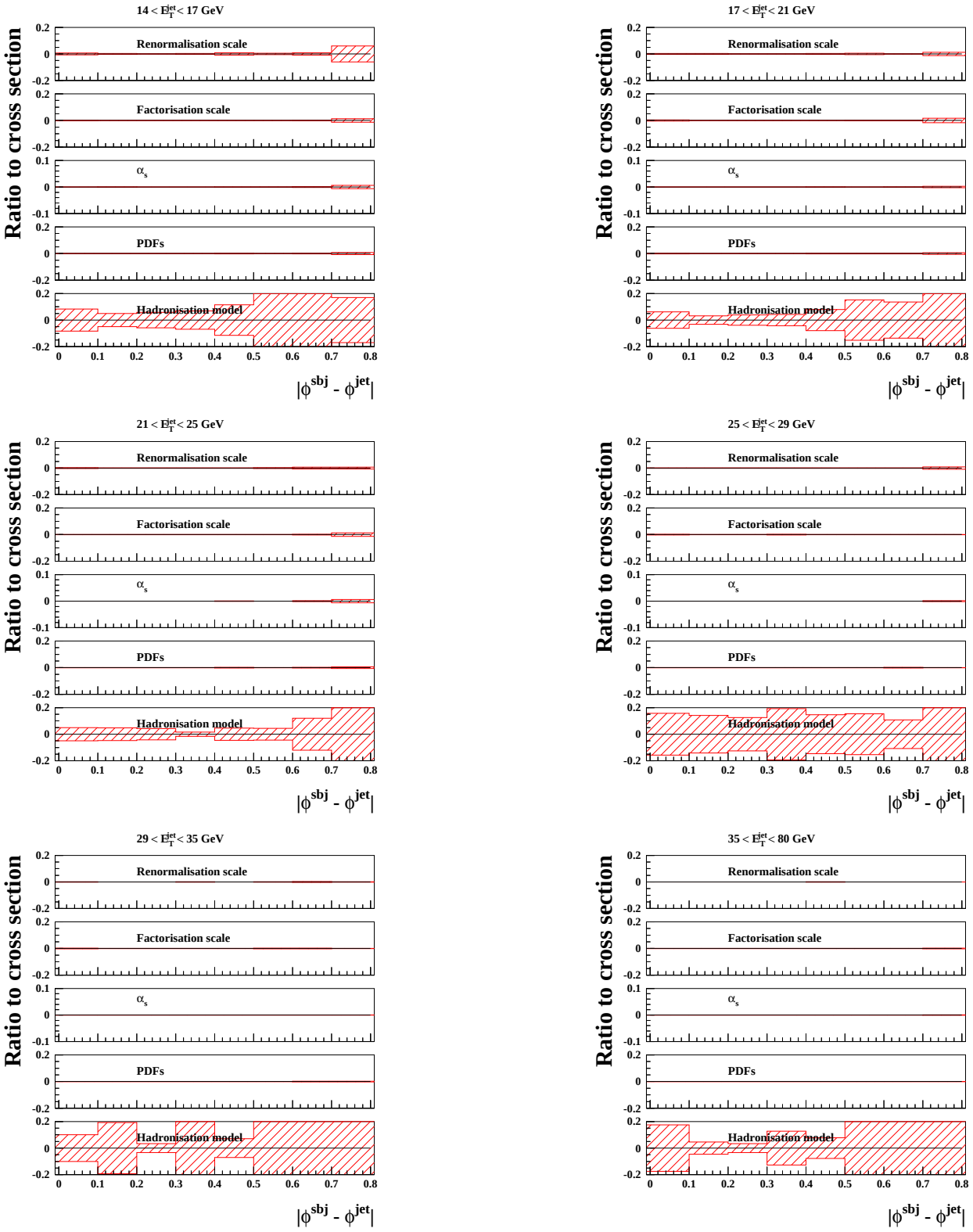

Figure 11.9: Relative theoretical uncertainties of the normalised differential cross-section calculations for the inclusive production of jets with exactly two subjets at $y_{cut} = 0.05$ as functions of $|\phi^{sbj} - \phi^{jet}|$ in regions of E_T^{jet}.

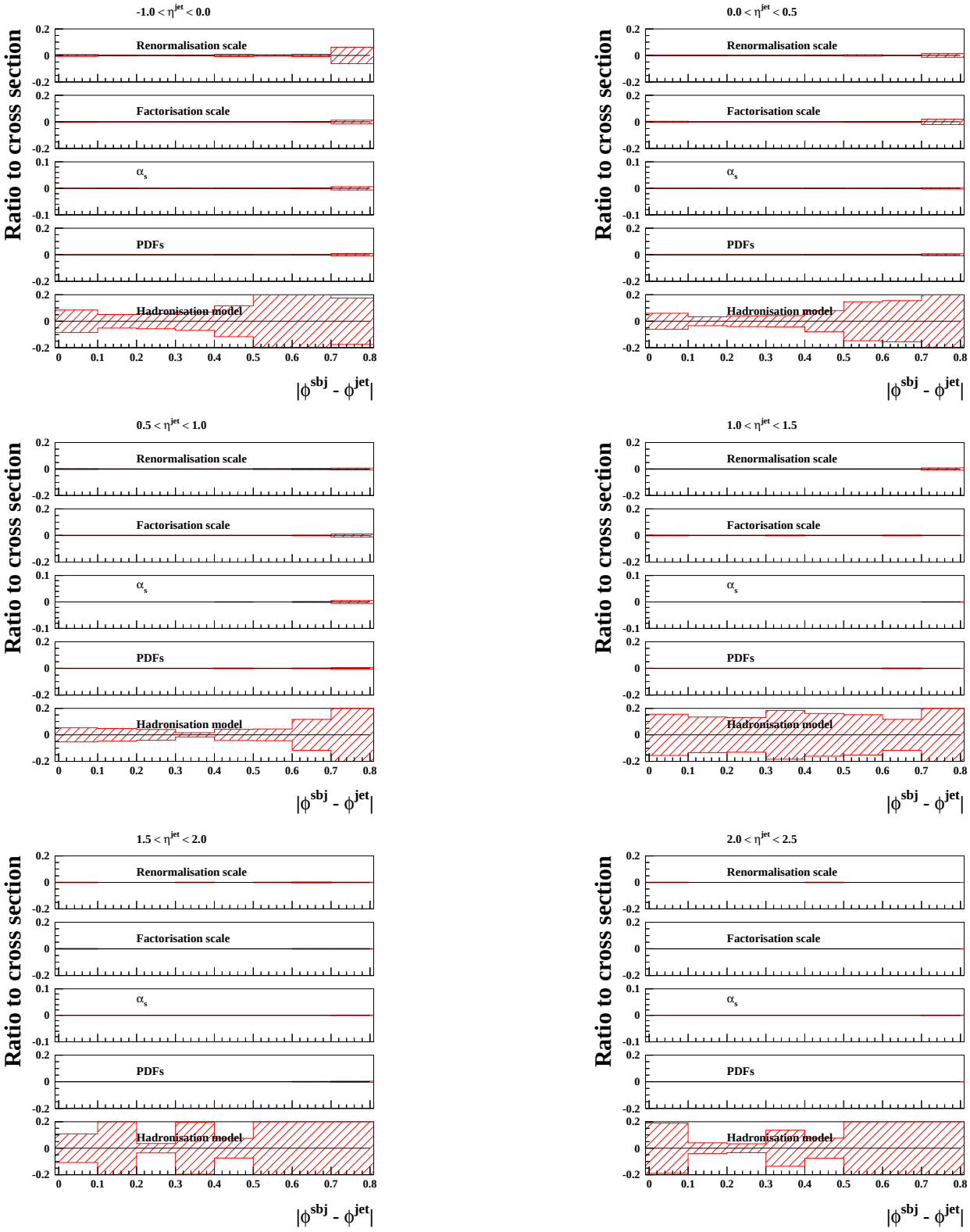

Figure 11.10: Relative theoretical uncertainties of the normalised differential cross-section calculations for the inclusive production of jets with exactly two subjets at $y_{cut} = 0.05$ as functions of $|\phi^{sbj} - \phi^{jet}|$ in regions of η^{jet}.

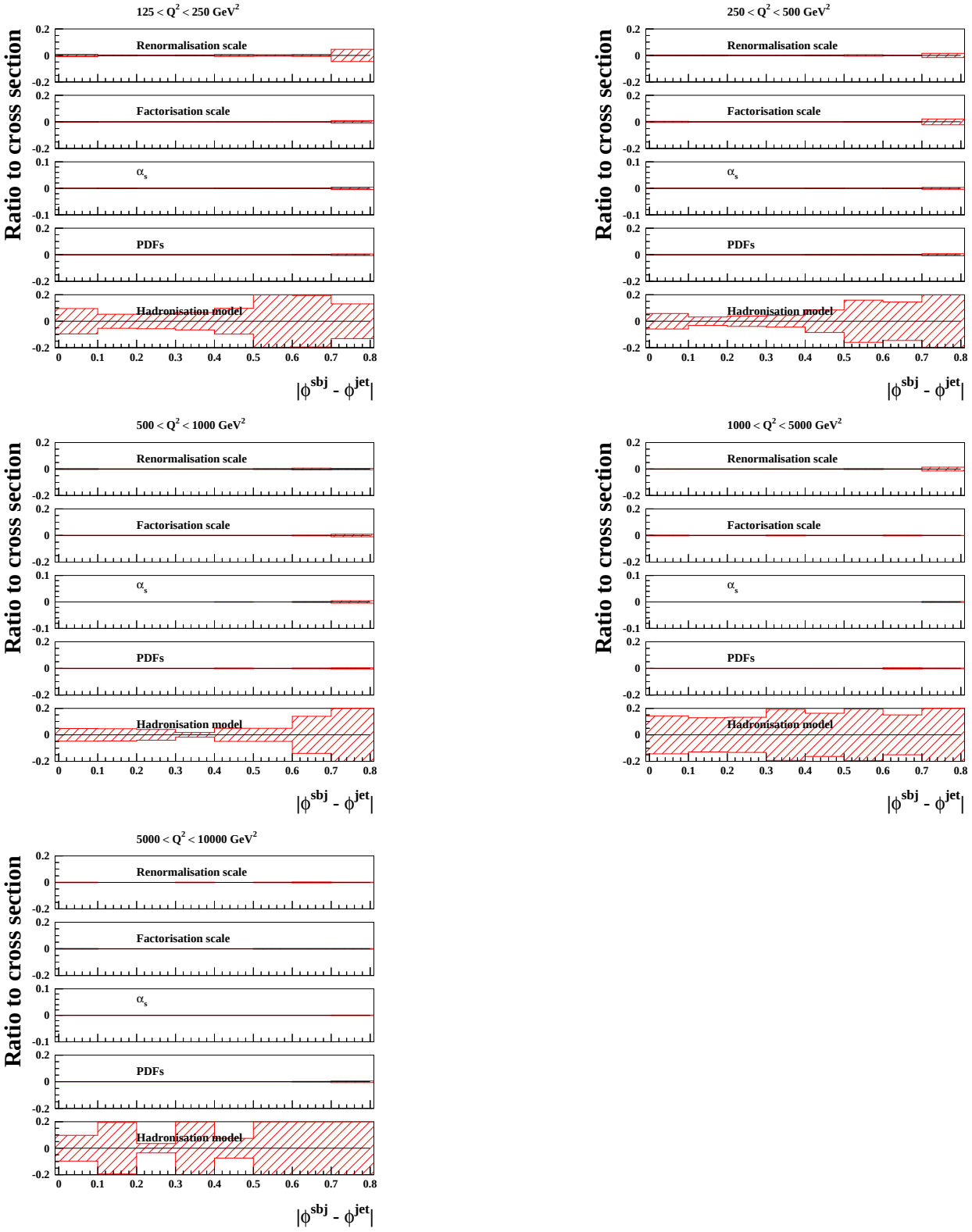

Figure 11.11: Relative theoretical uncertainties of the normalised differential cross-section calculations for the inclusive production of jets with exactly two subjets at $y_{cut} = 0.05$ as functions of $|\phi^{sbj} - \phi^{jet}|$ in regions of Q^2.

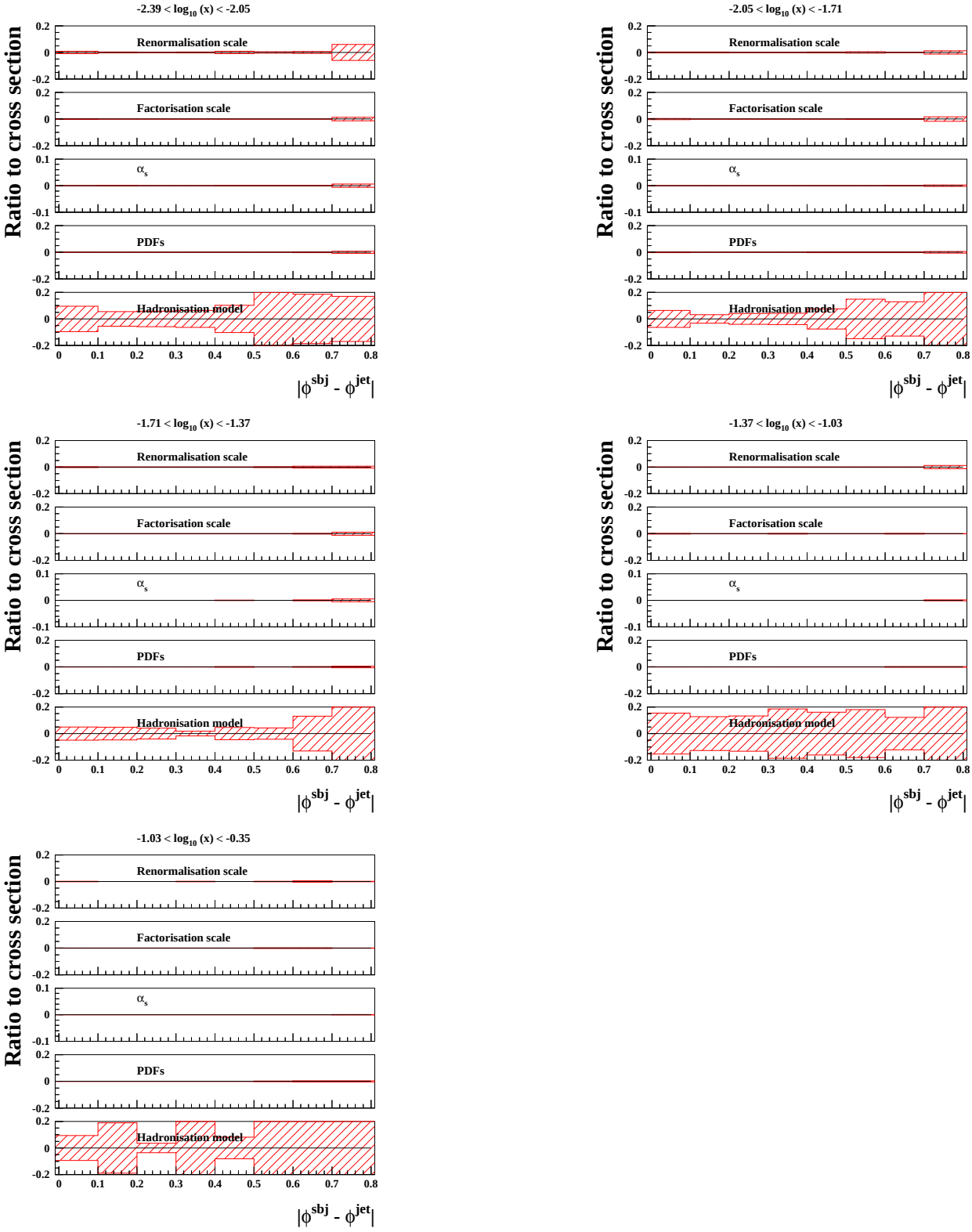

Figure 11.12: Relative theoretical uncertainties of the normalised differential cross-section calculations for the inclusive production of jets with exactly two subjets at $y_{cut} = 0.05$ as functions of $|\phi^{sbj} - \phi^{jet}|$ in regions of x.

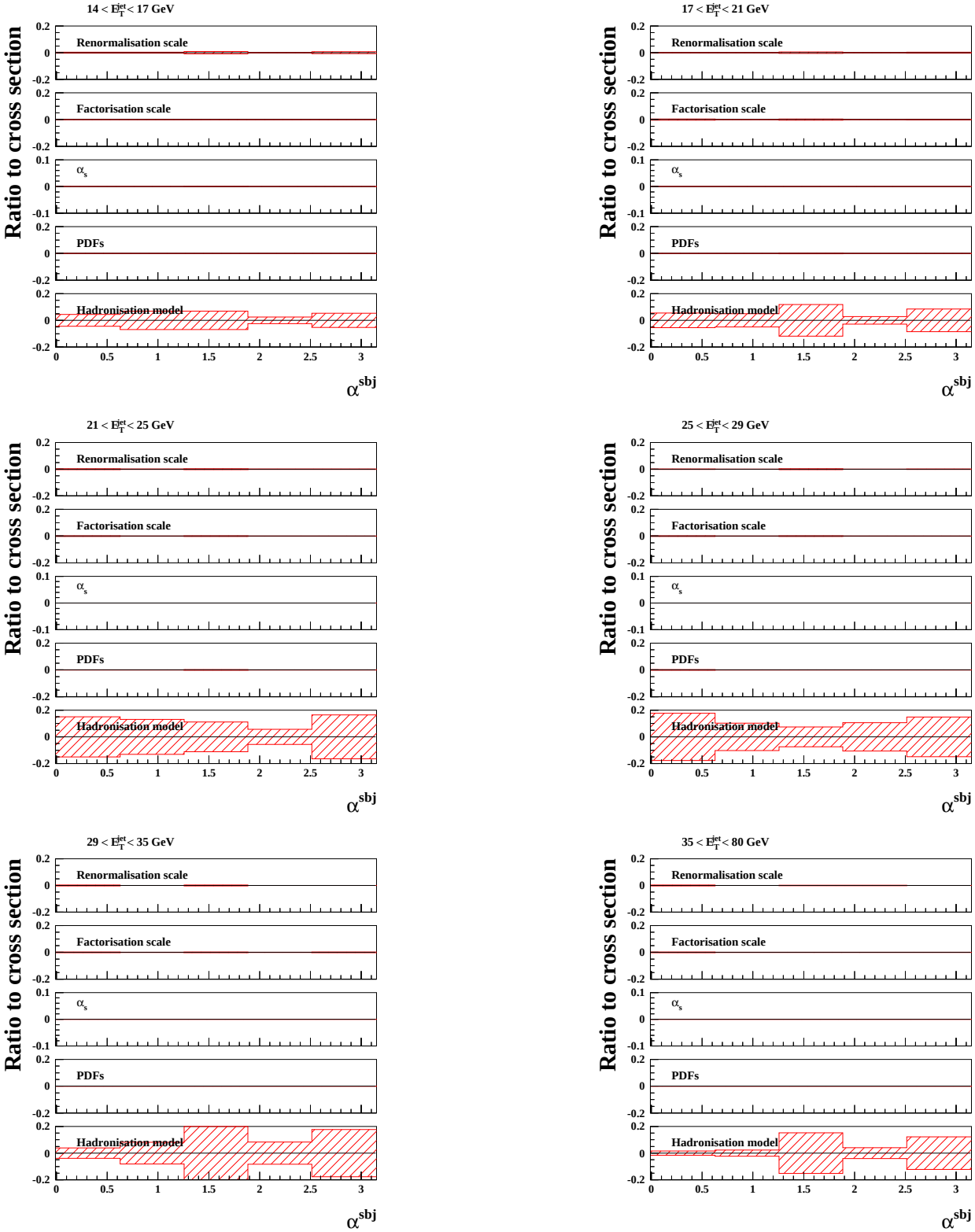

Figure 11.13: Relative theoretical uncertainties of the normalised differential cross-section calculations for the inclusive production of jets with exactly two subjets at $y_{cut} = 0.05$ as functions of α^{sbj} in regions of E_T^{jet}.

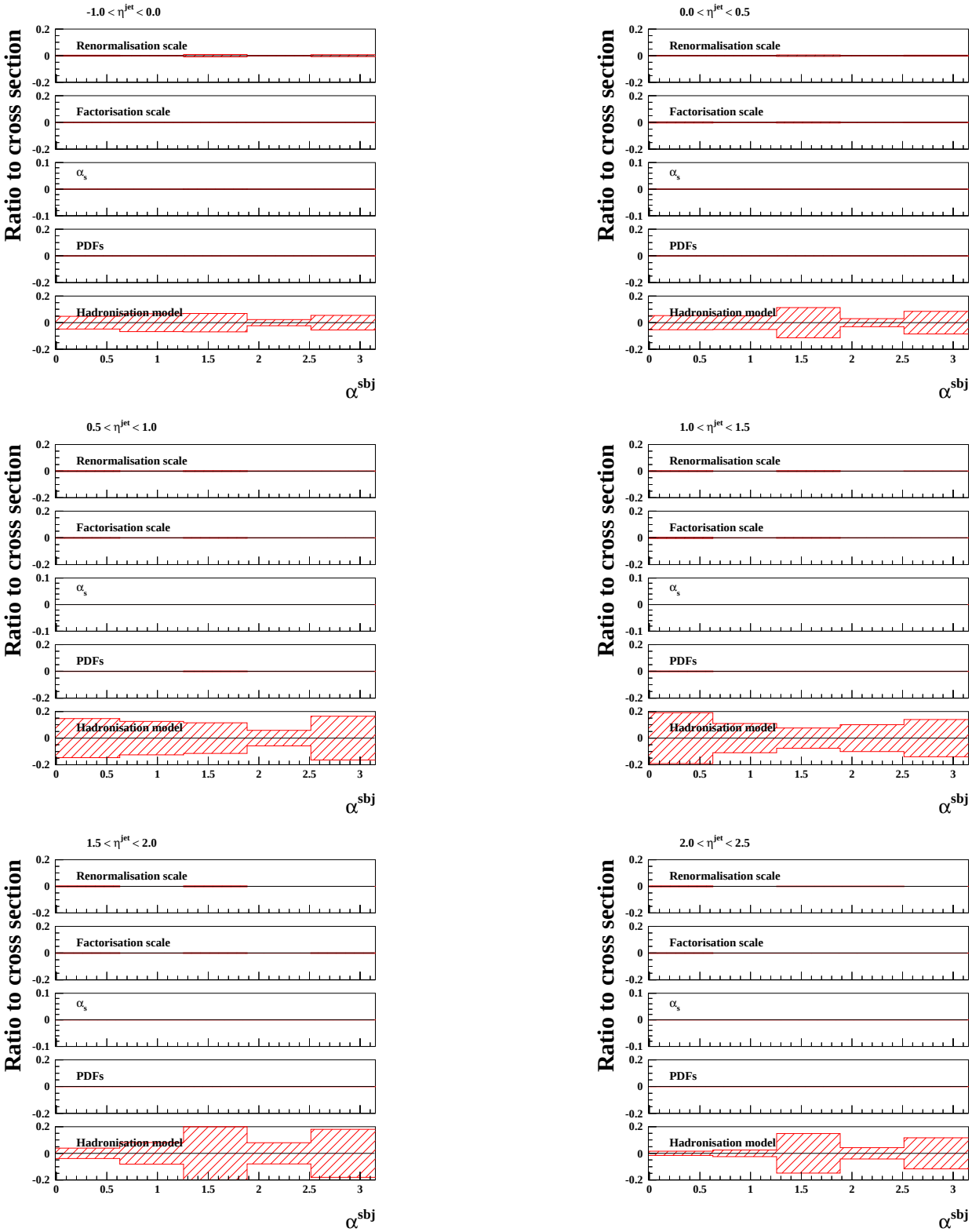

Figure 11.14: Relative theoretical uncertainties of the normalised differential cross-section calculations for the inclusive production of jets with exactly two subjets at $y_{cut} = 0.05$ as functions of α^{sbj} in regions of η^{jet}.

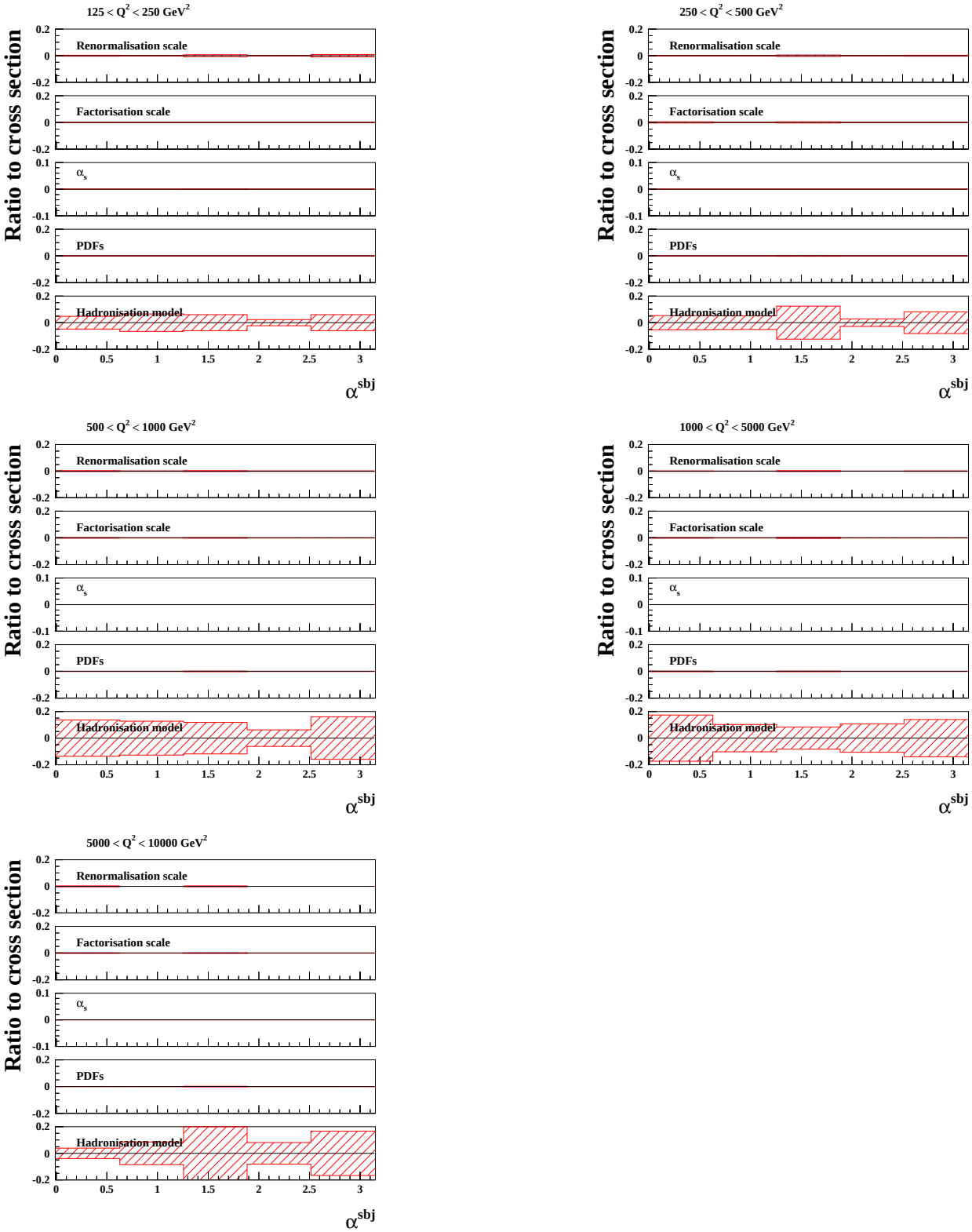

Figure 11.15: Relative theoretical uncertainties of the normalised differential cross-section calculations for the inclusive production of jets with exactly two subjets at $y_{cut} = 0.05$ as functions of α^{sbj} in regions of Q^2.

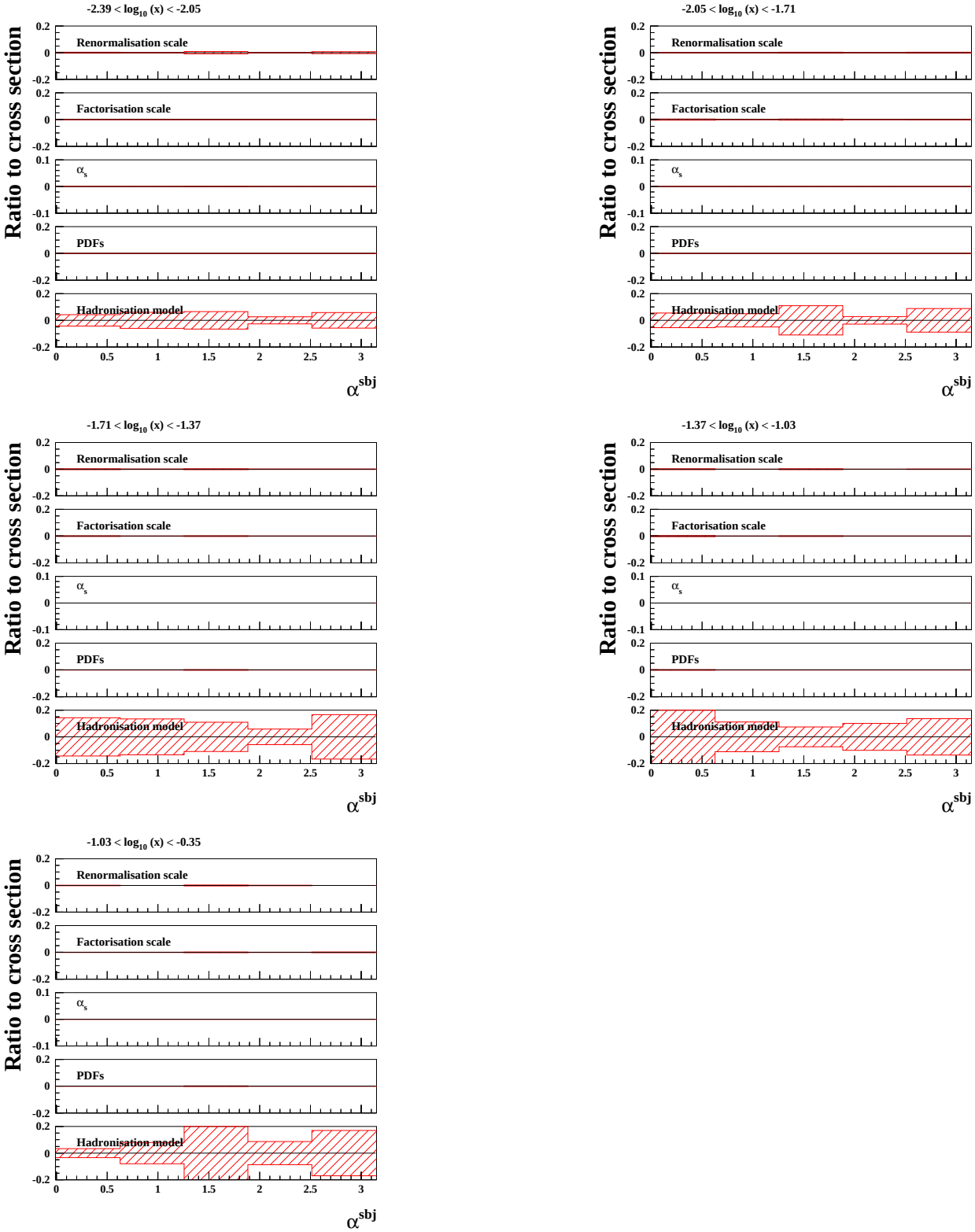

Figure 11.16: Relative theoretical uncertainties of the normalised differential cross-section calculations for the inclusive production of jets with exactly two subjets at $y_{cut} = 0.05$ as functions of α^{sbj} in regions of x.

11.2 Evolution of the acceptance correction factors. Two-subjet analysis

In this section, the remaining plots from section 8.1.1 are shown. In figures 11.17 to 11.20 the ratio of the normalised distributions at hadron level over those at detector level is shown in different regions of E_T^{jet}, η^{jet}, Q^2 and x. As can be observed, the corrections generally modify the shape by less than 20% except for $\eta^{sbj} - \eta^{jet}$ (see Fig. 11.18), for which the correction factors are bigger for some bins; however, it should be noted that in those bins the data statistics is low.

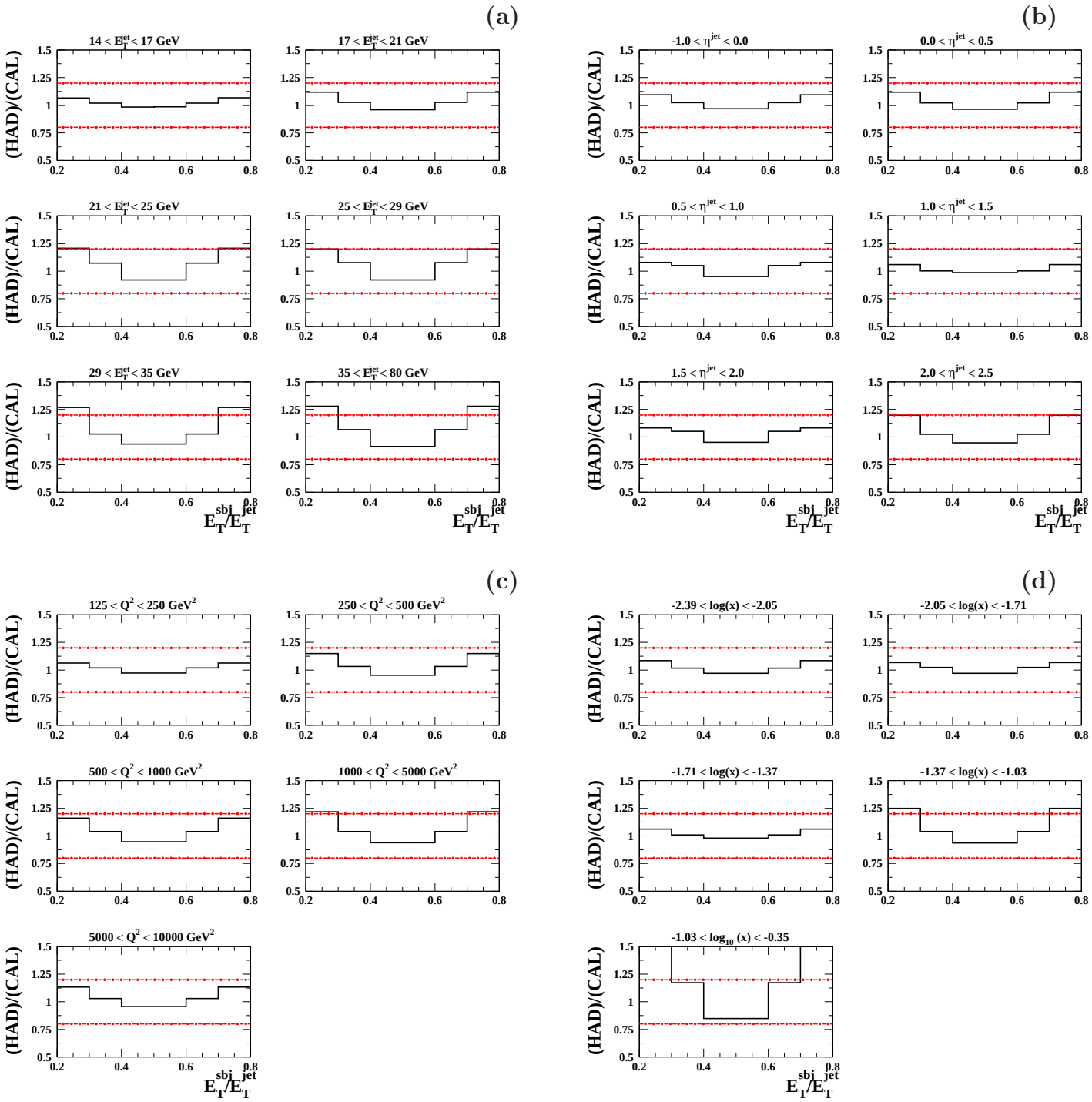

Figure 11.17: The ratio of the normalised distributions for E_T^{sbj}/E_T^{jet} at hadron level over those at detector level in regions of a) E_T^{jet}, b) η^{jet}, c) Q^2 and d) x. The horizontal dot-dashed lines represent changes of 20%.

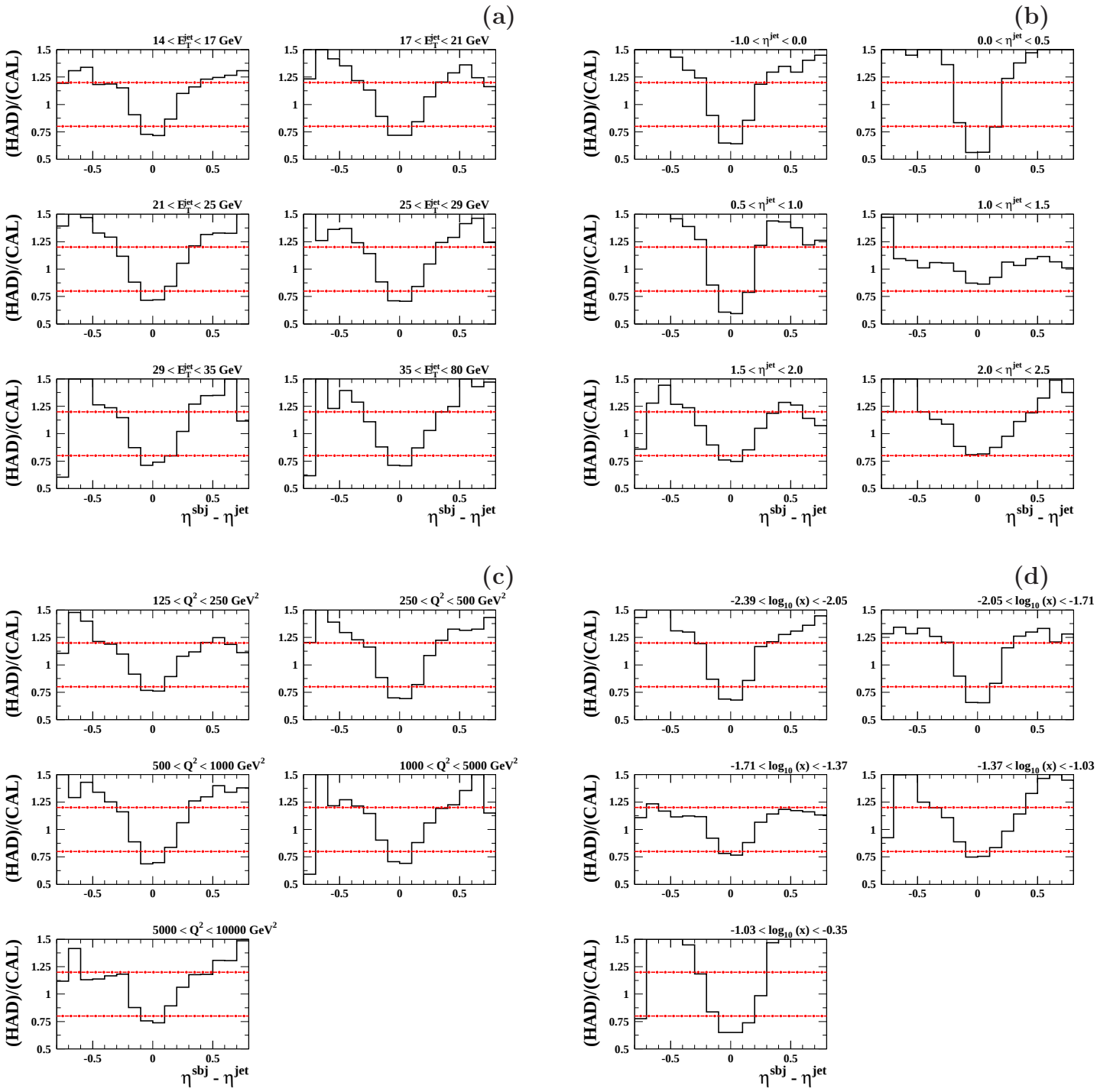

Figure 11.18: The ratio of the normalised distributions at hadron level over those at detector level as a function of $\eta^{sbj} - \eta^{jet}$ in regions of a) E_T^{jet}, b) η^{jet}, c) Q^2 and d) x. The red dashed lines represent a deviation from unity of 20%.

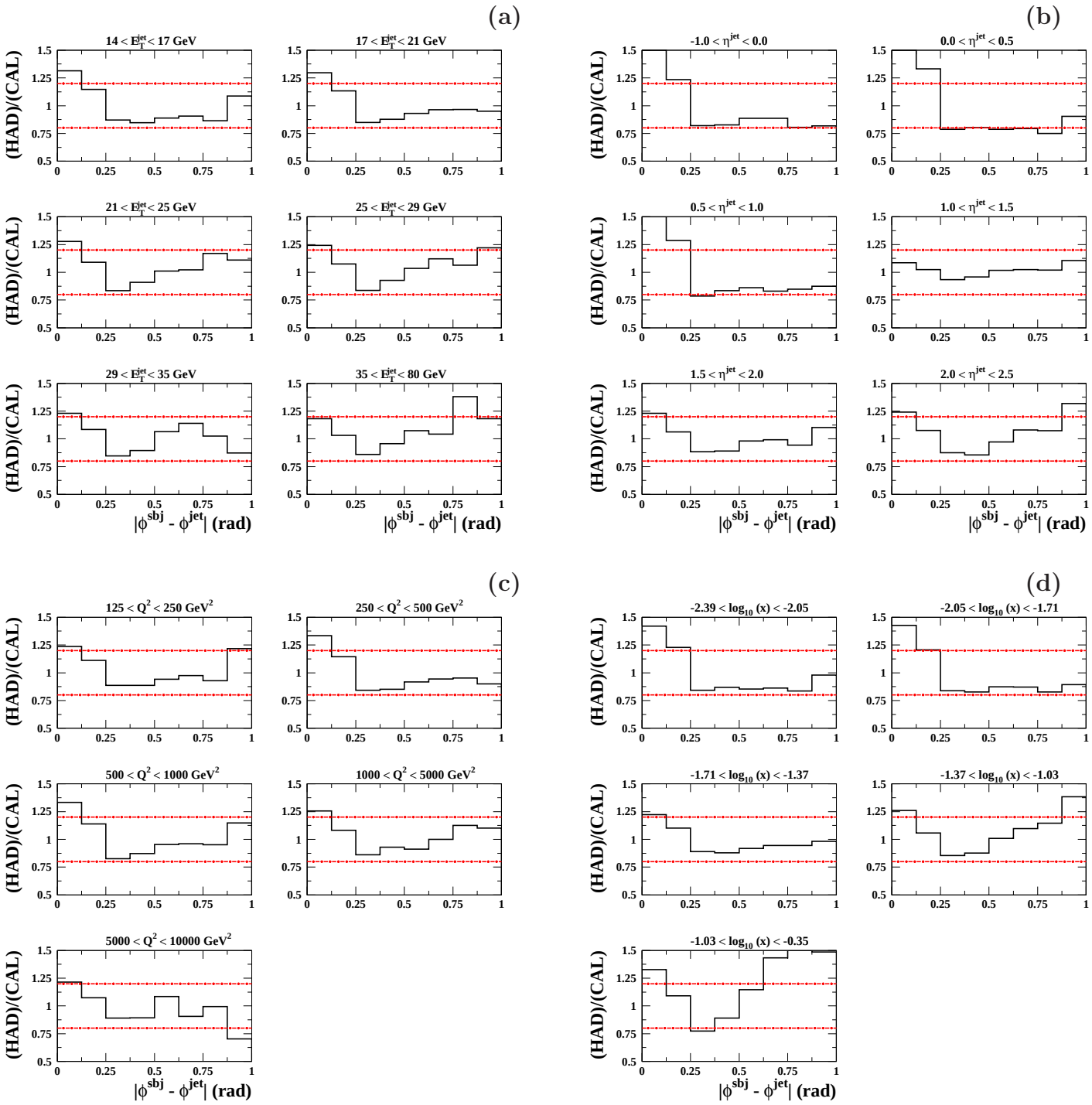

Figure 11.19: The ratio of the normalised distributions at hadron level over those at detector level as a function of $|\phi^{sbj} - \phi^{jet}|$ in regions of a) E_T^{jet}, b) η^{jet}, c) Q^2 and d) x. The red dashed lines represent a deviation from unity of 20%.

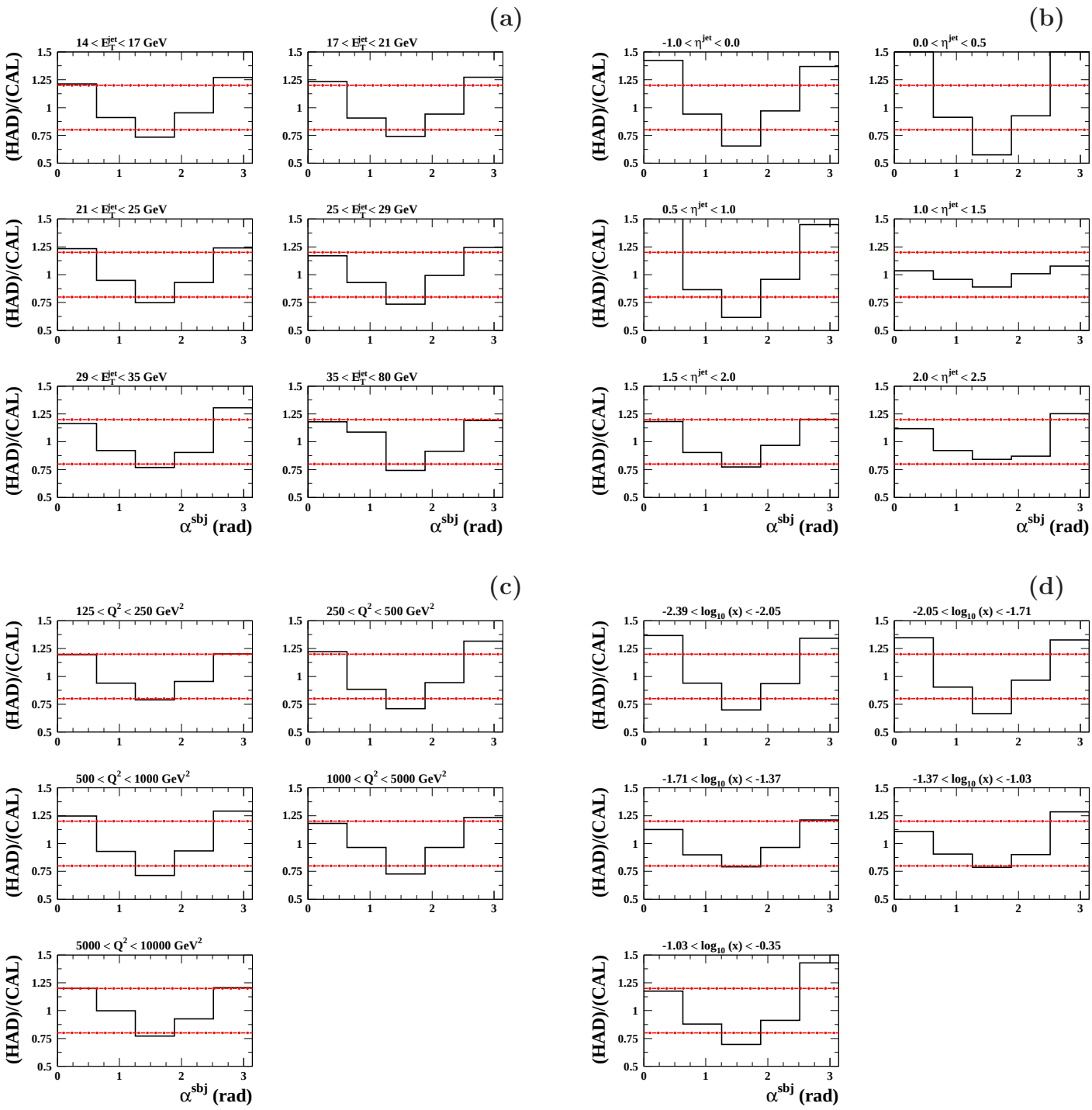

Figure 11.20: The ratio of the normalised distributions at hadron level over those at detector level as a function of α^{sbj} in regions of a) E_T^{jet}, b) η^{jet}, c) Q^2 and d) x. The red dashed lines represent a deviation from unity of 20%.

11.3 Parton-to-hadron corrections. Two-subjet analysis

Figures 11.21 to 11.24 show the remaning plots that were omitted in section 8.1.3. These illustrate the parton-to-hadron correction factors in regions of E_T^{jet}, η^{jet}, Q^2 and x.

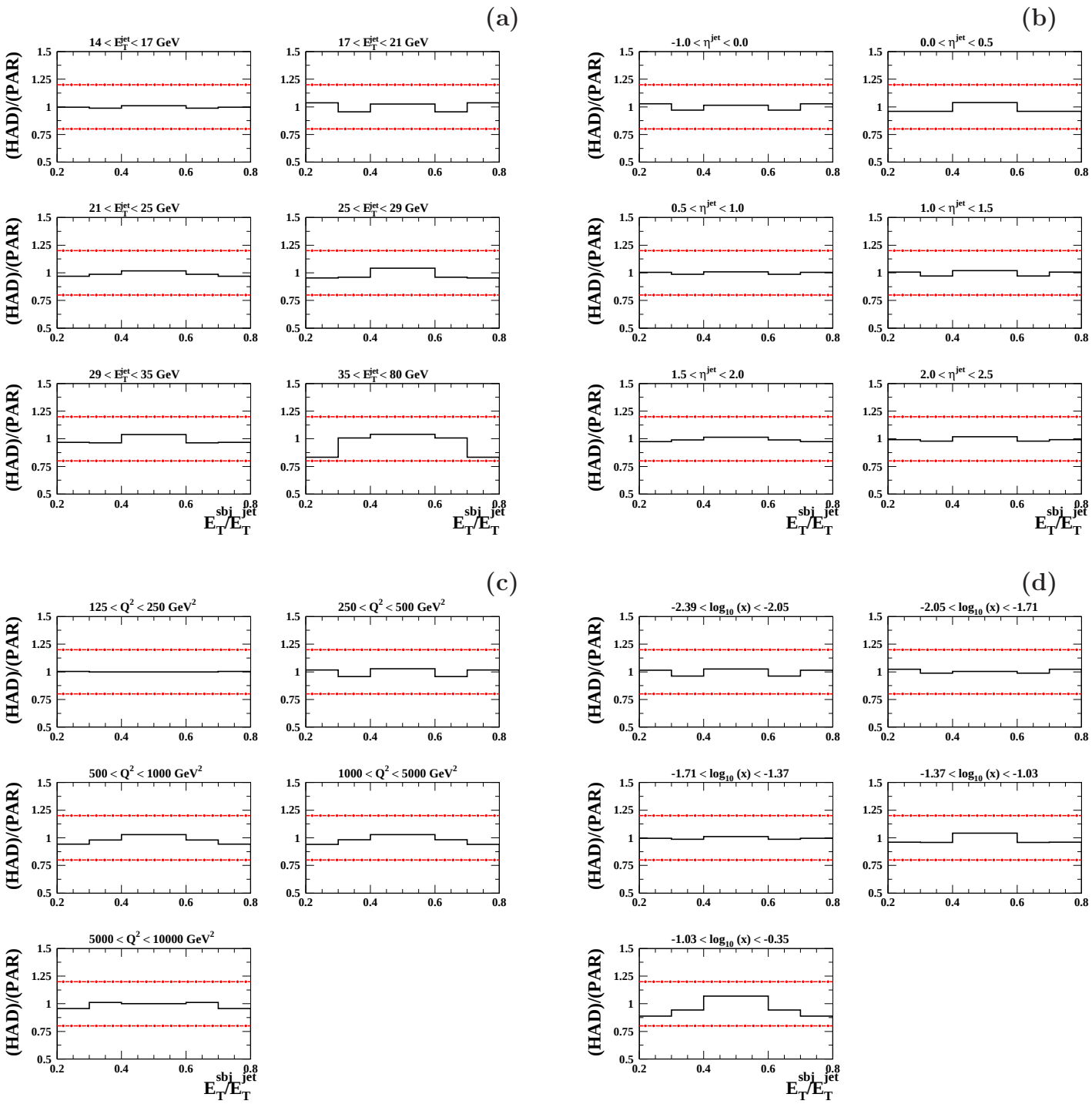

Figure 11.21: The ratio of the normalised distributions at hadron level over those at parton level as a function of E_T^{sbj}/E_T^{jet} in different regions of a) E_T^{jet}, b) η^{jet}, c) Q^2 and d) x. The red dashed lines represent a deviation from unity of 20%.

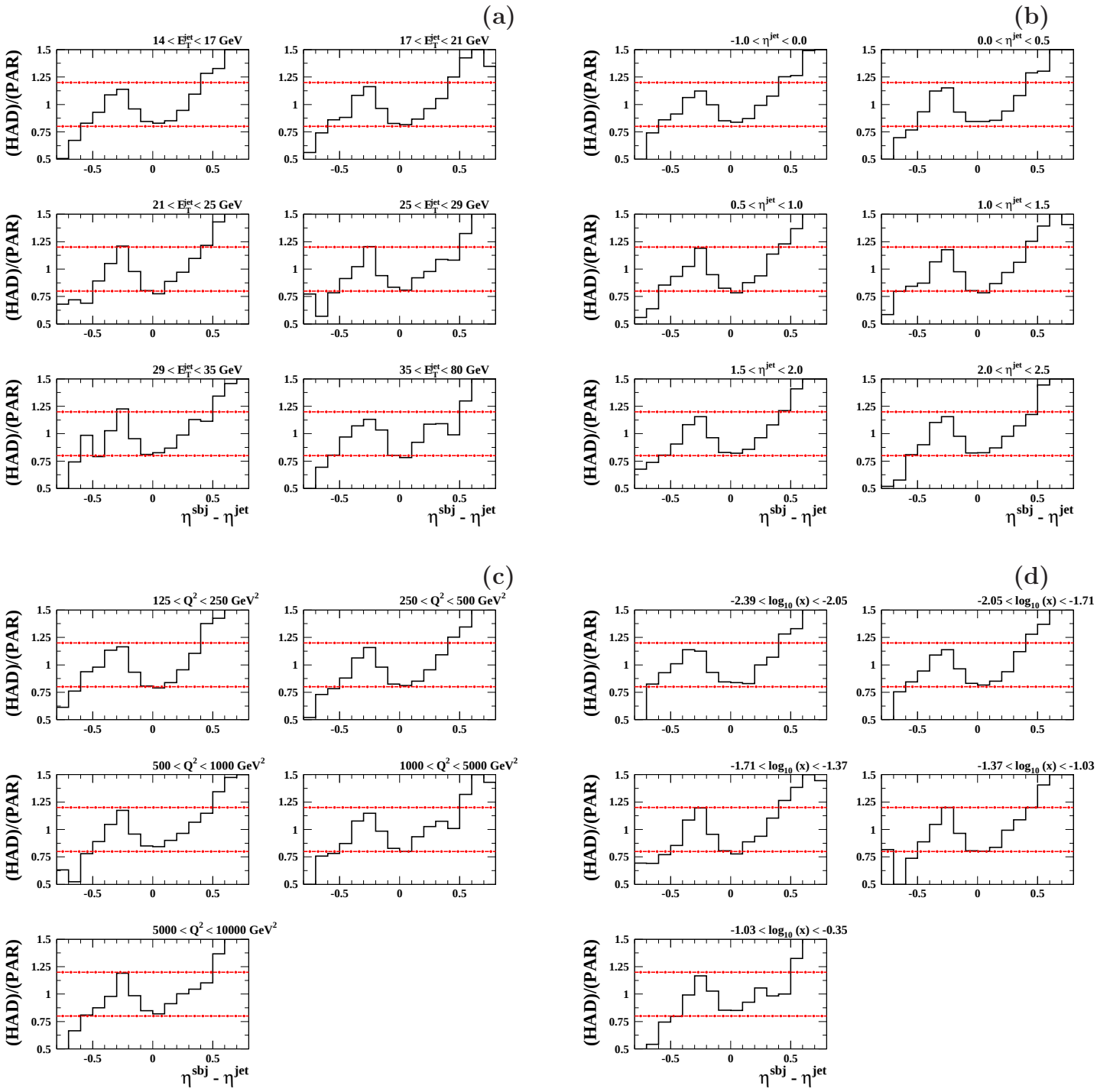

Figure 11.22: The ratio of the normalised distributions at hadron level over those at parton level as a function of $\eta^{sbj} - \eta^{jet}$ in regions of a) E_T^{jet}, b) η^{jet}, c) Q^2 and d) x. The red dashed lines represent a deviation from unity of 20%.

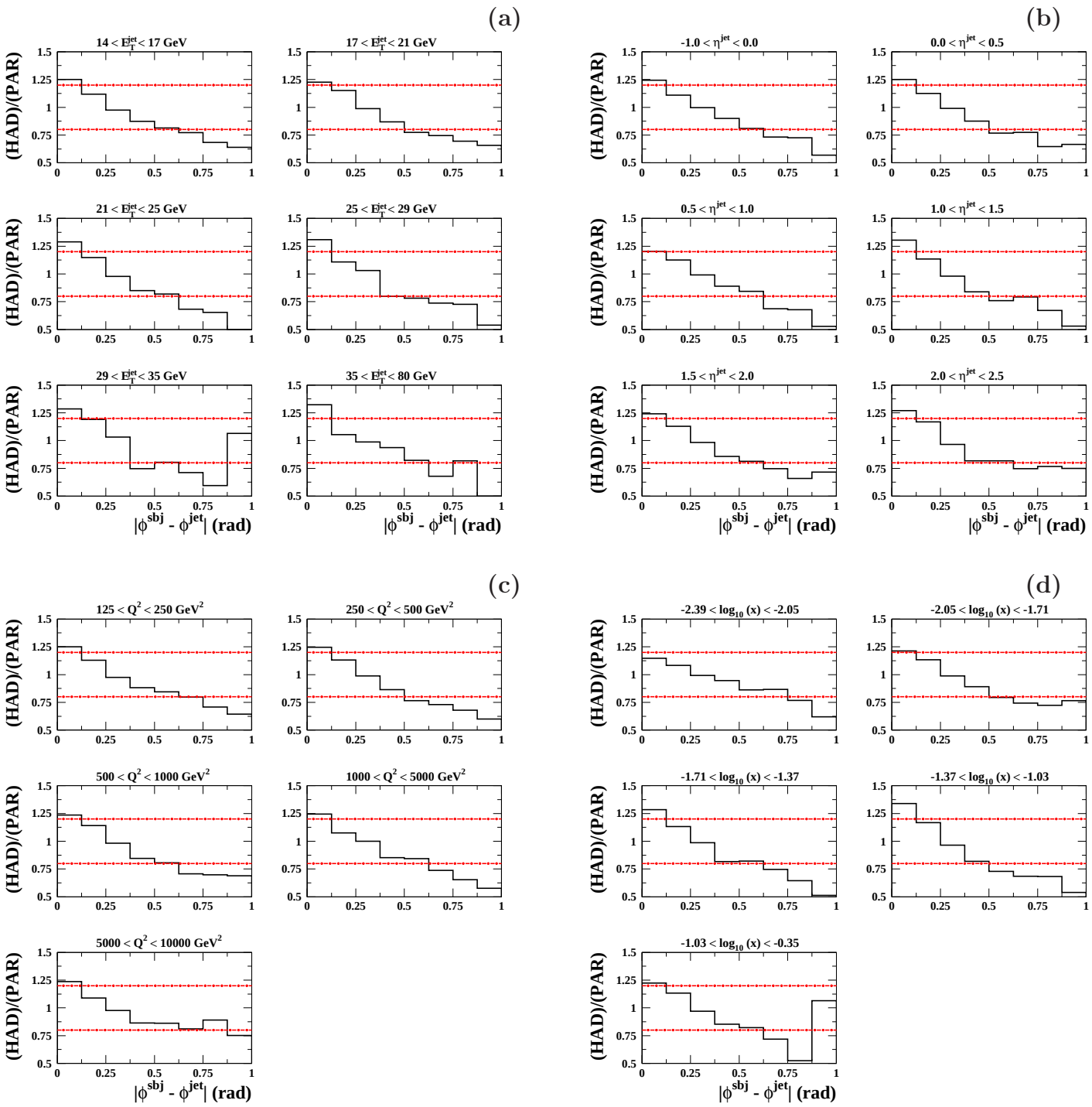

Figure 11.23: The ratio of the normalised distributions at hadron level over those at parton level as a function of $|\phi^{sbj} - \phi^{jet}|$ in regions of a) E_T^{jet}, b) η^{jet}, c) Q^2 and d) x. The red dashed lines represent a deviation from unity of 20%.

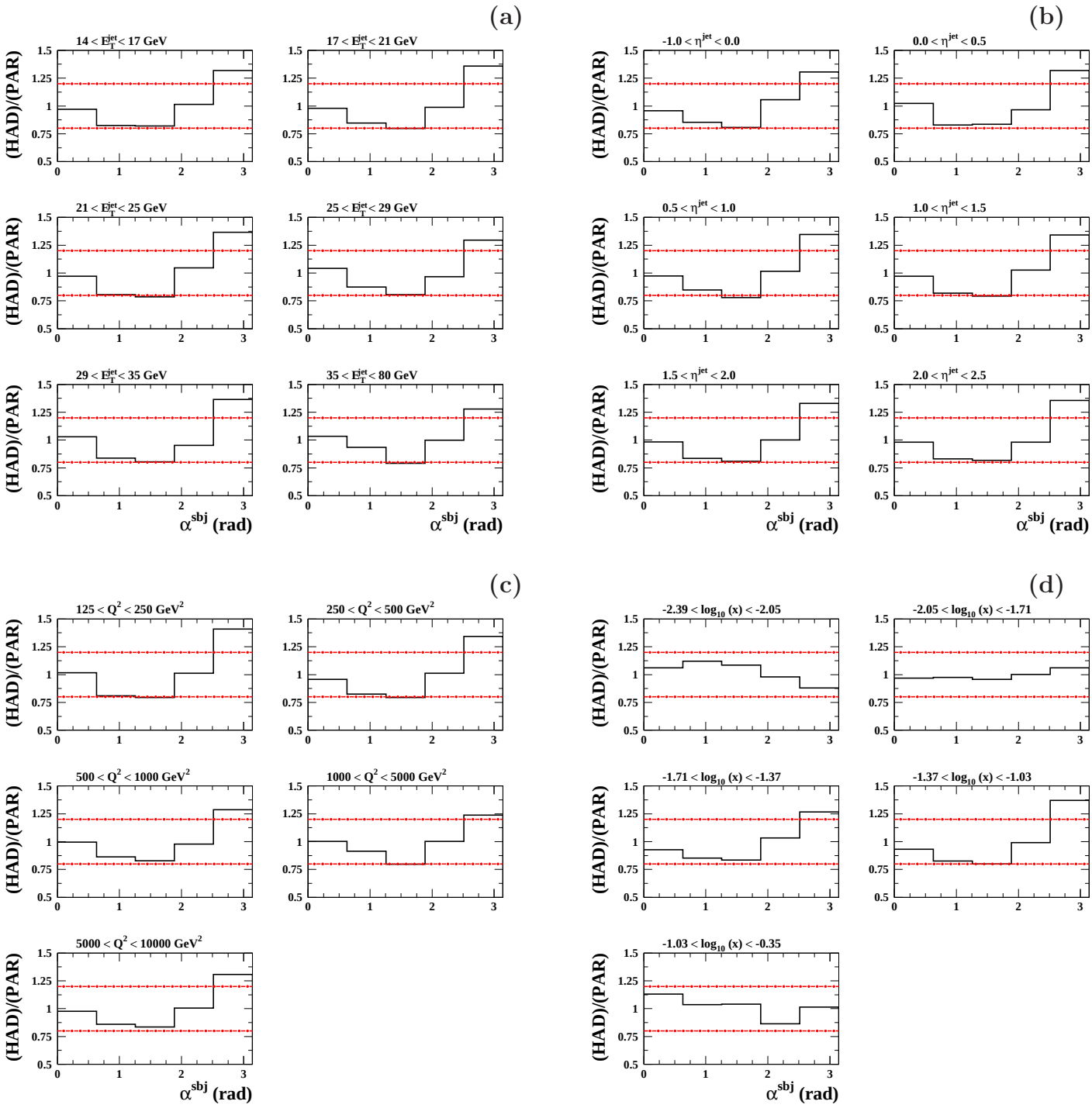

Figure 11.24: The ratio of the normalised distributions at hadron level over those at parton level as a function of α^{sbj} in regions of a) E_T^{jet}, b) η^{jet}, c) Q^2 and d) x. The red dashed lines represent a deviation from unity of 20%.

11.4 Systematic uncertainties. Two-subjet analysis

Figures 11.25 to 11.56 show the relative systematic and statistical uncertainties of the normalised differential cross sections in regions of E_T^{jet}, η^{jet}, Q^2 and x for all the subjet variables.

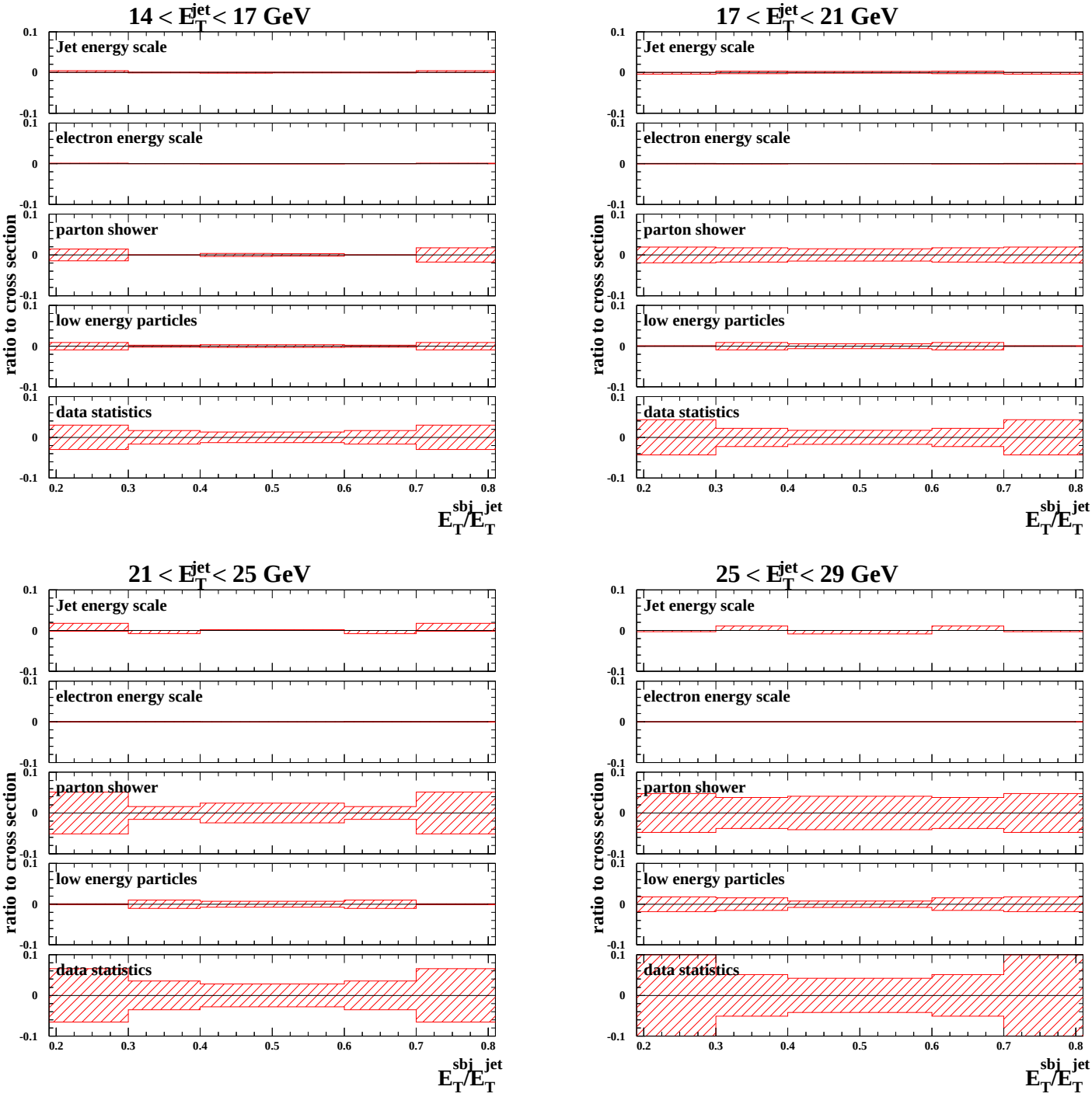

Figure 11.25: Relative systematic and statistical uncertainties of the normalised differential cross sections as functions of E_T^{sbj}/E_T^{jet} in different regions of E_T^{jet}.

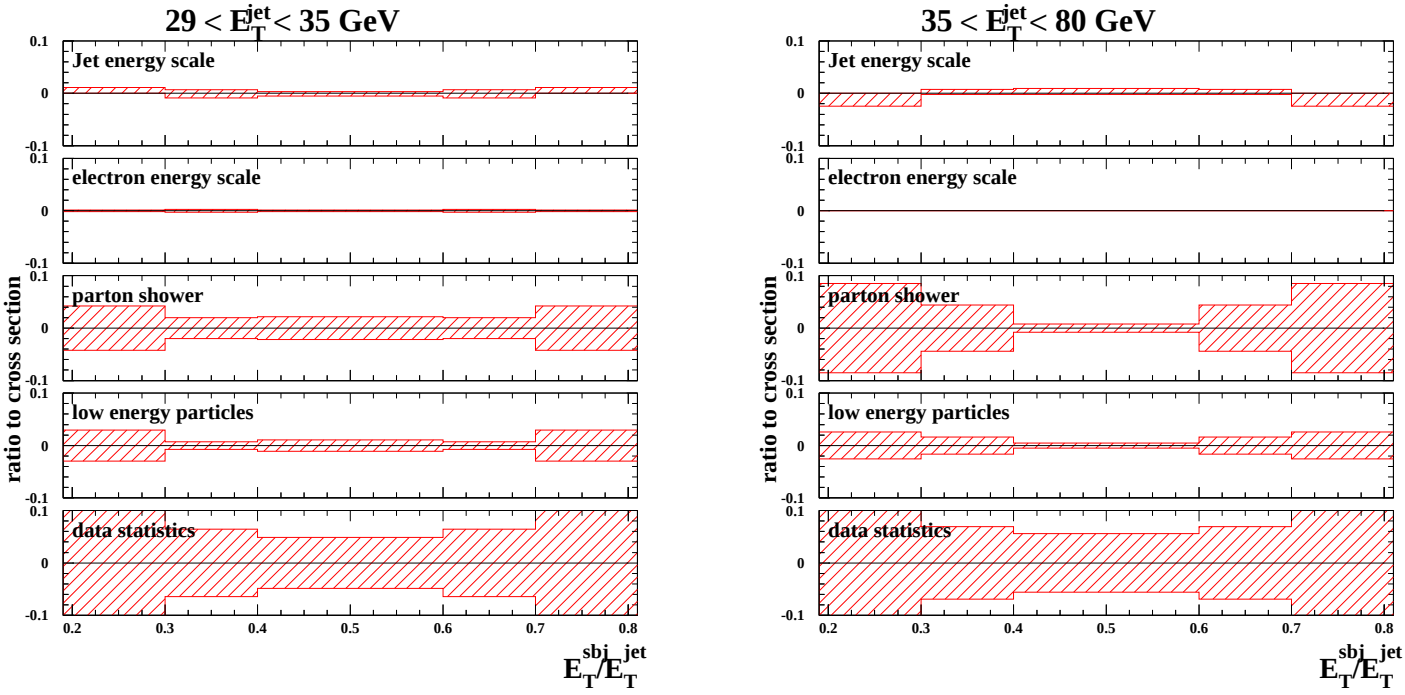

Figure 11.26: Relative systematic and statistical uncertainties of the normalised differential cross sections as functions of E_T^{sbj}/E_T^{jet} in different regions of E_T^{jet}.

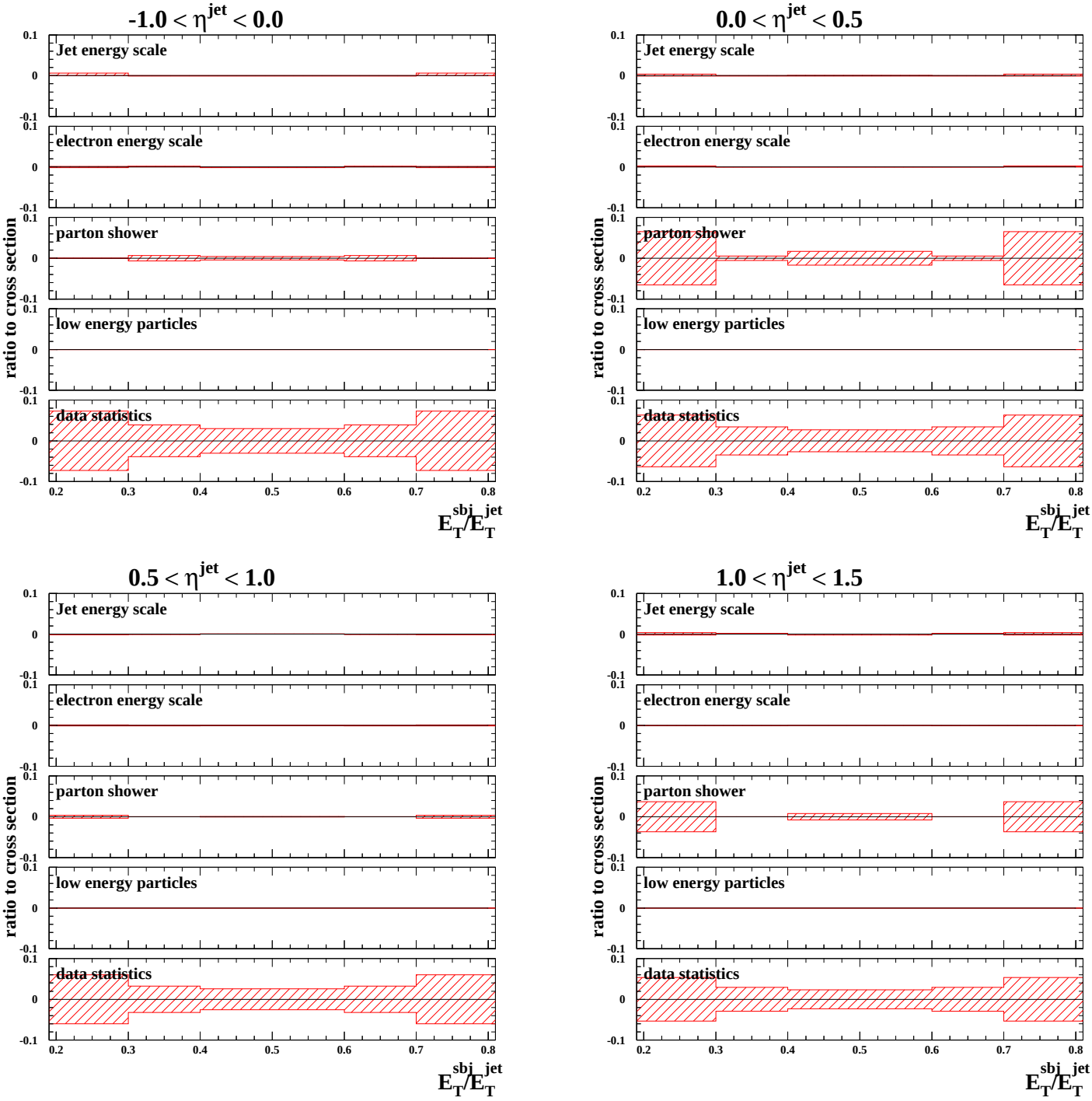

Figure 11.27: Relative systematic and statistical uncertainties of the normalised differential cross sections as functions of E_T^{sbj}/E_T^{jet} in different regions of η^{jet}.

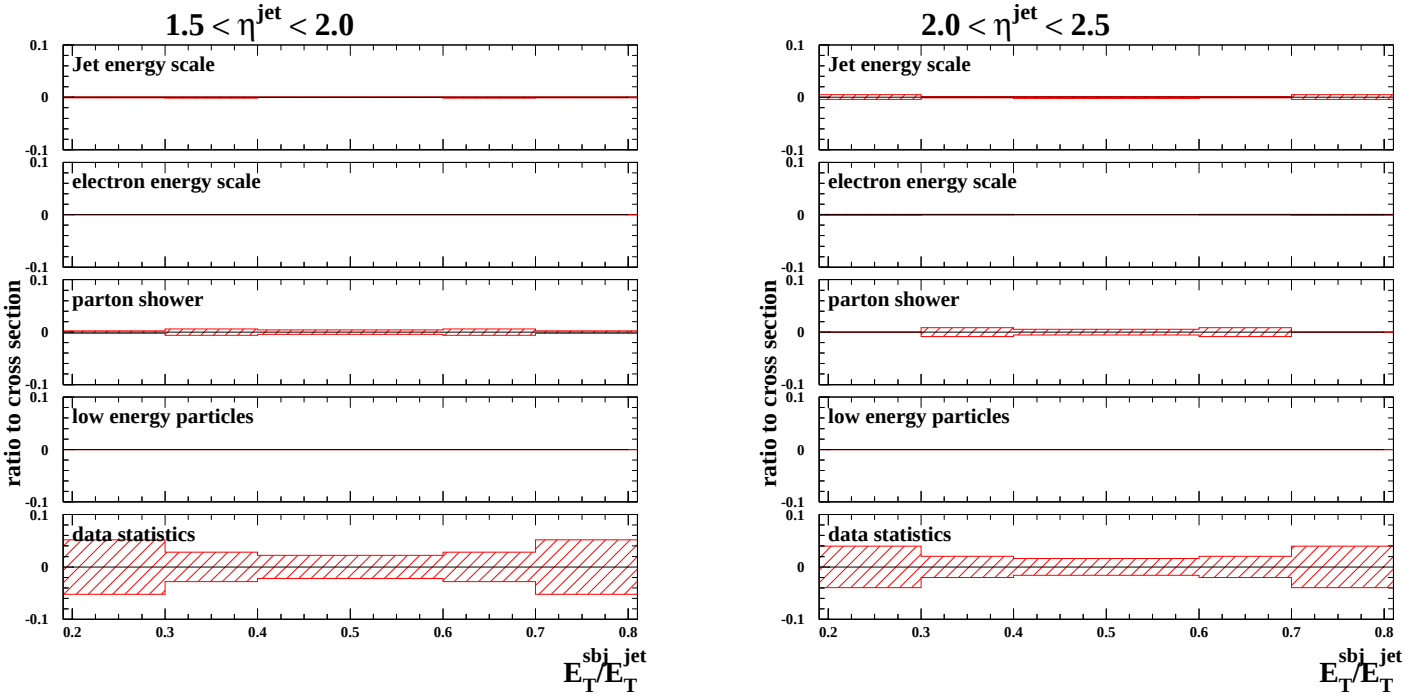

Figure 11.28: Relative systematic and statistical uncertainties of the normalised differential cross sections as functions of E_T^{sbj}/E_T^{jet} in different regions of η^{jet}.

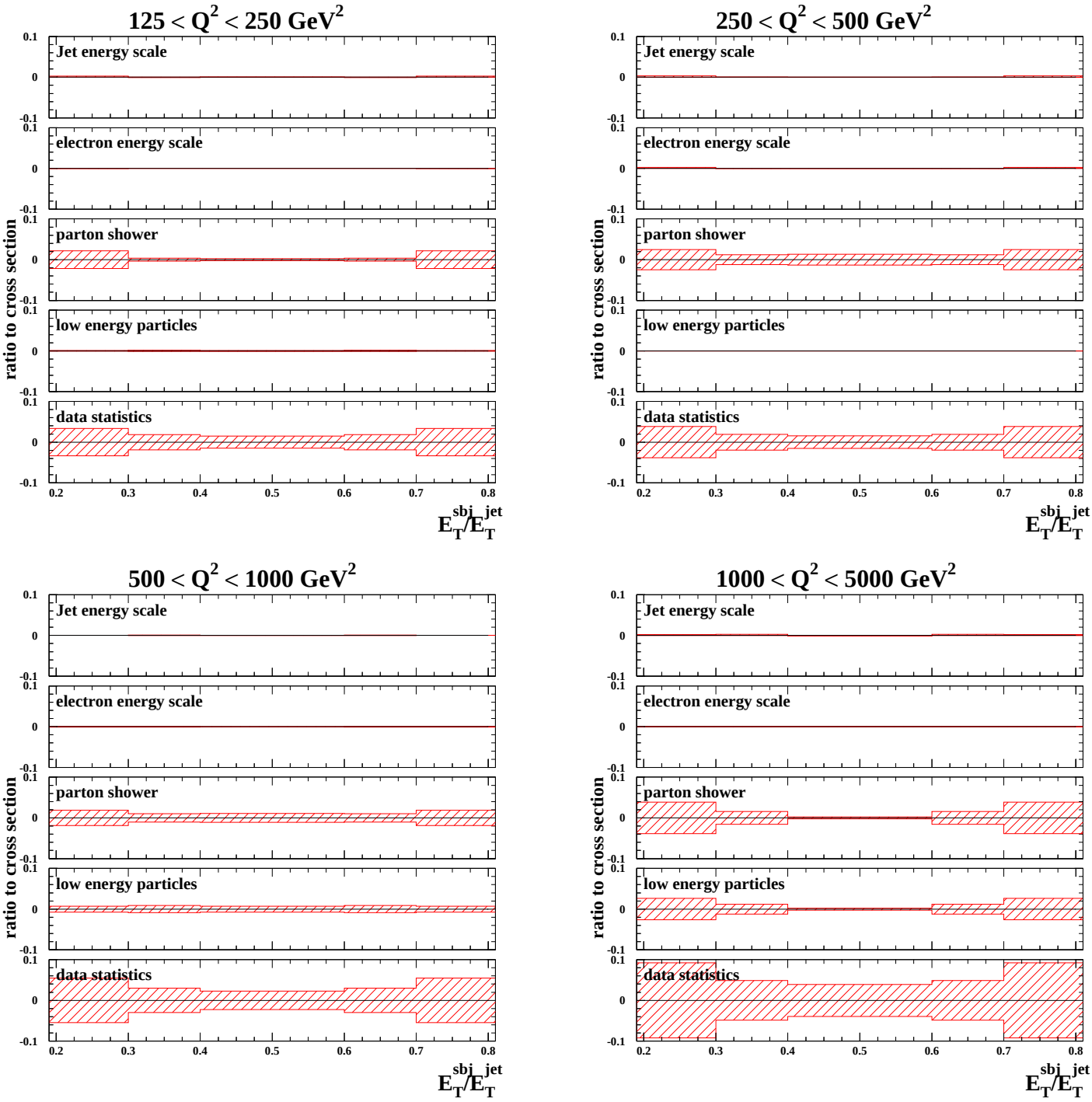

Figure 11.29: Relative systematic and statistical uncertainties of the normalised differential cross sections as functions of E_T^{sbj}/E_T^{jet} in different regions of Q^2.

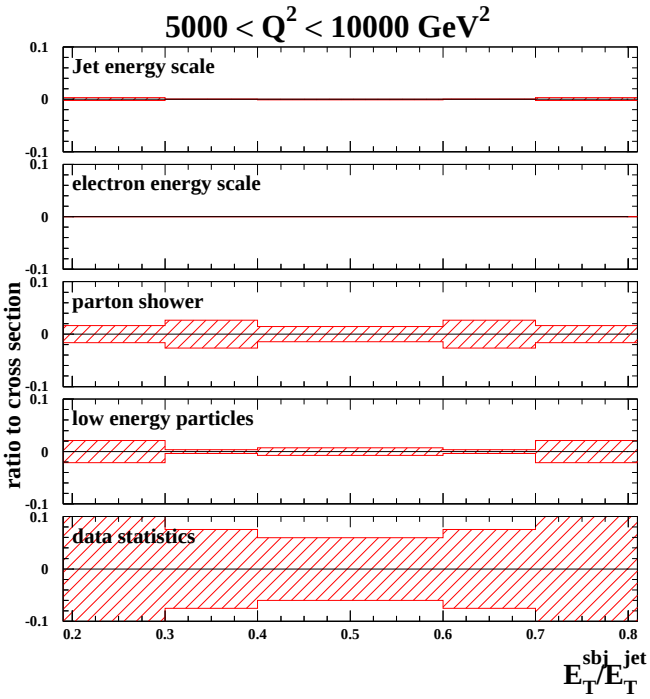

Figure 11.30: Relative systematic and statistical uncertainties of the normalised differential cross sections as functions of E_T^{sbj}/E_T^{jet} in different regions of Q^2.

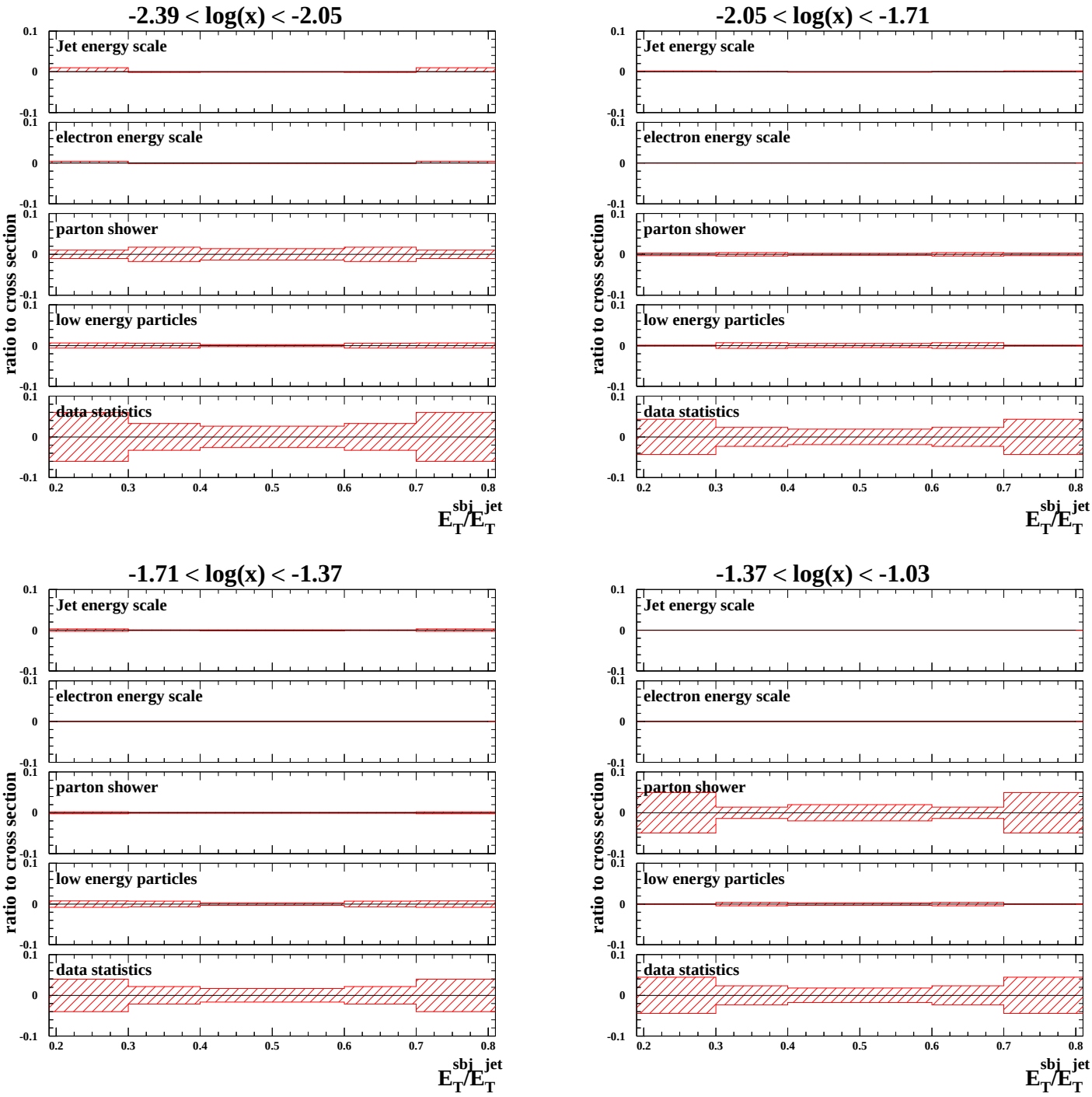

Figure 11.31: Relative systematic and statistical uncertainties of the normalised differential cross sections as functions of E_T^{sbj}/E_T^{jet} in different regions of x.

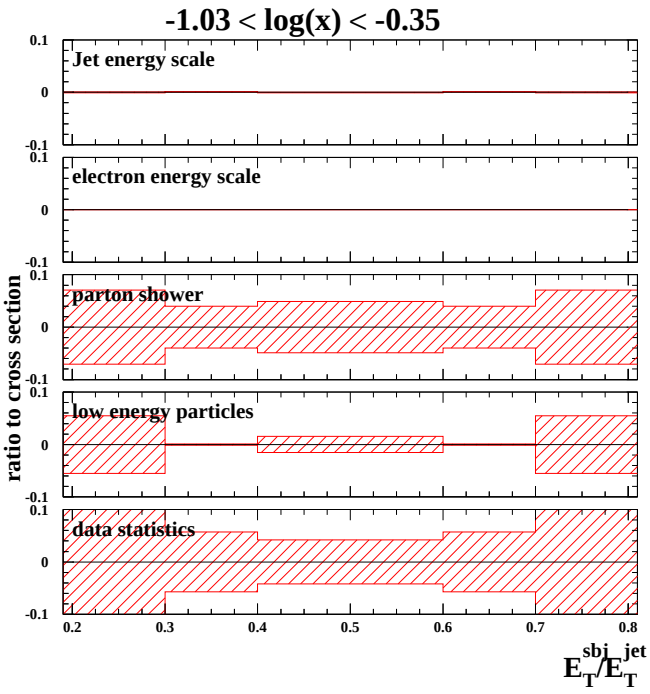

Figure 11.32: Relative systematic and statistical uncertainties of the normalised differential cross sections as functions of E_T^{sbj}/E_T^{jet} in different regions of x.

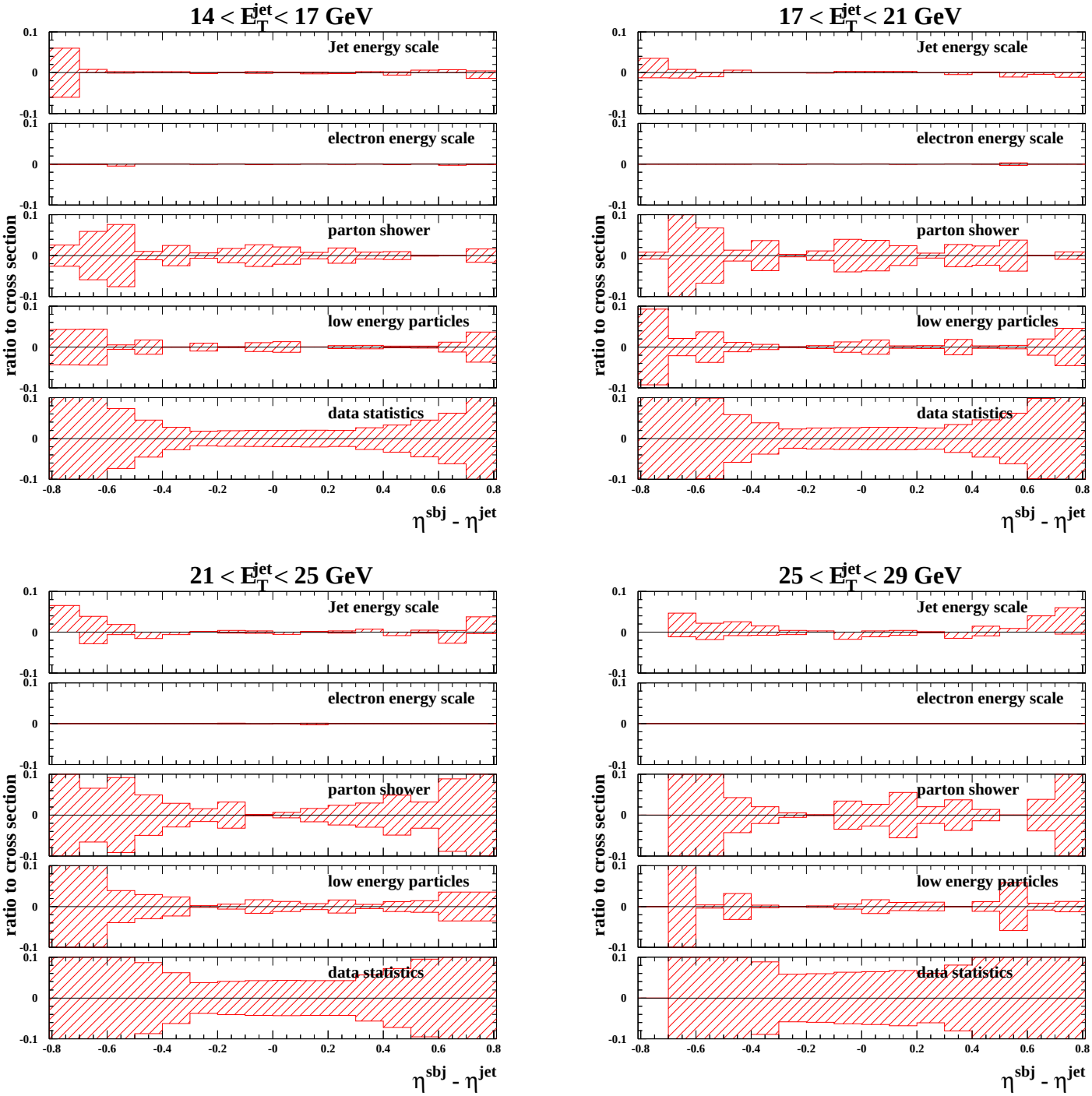

Figure 11.33: Relative systematic and statistical uncertainties of the normalised differential cross sections as functions of $\eta^{sbj} - \eta^{jet}$ in different regions of E_T^{jet}.

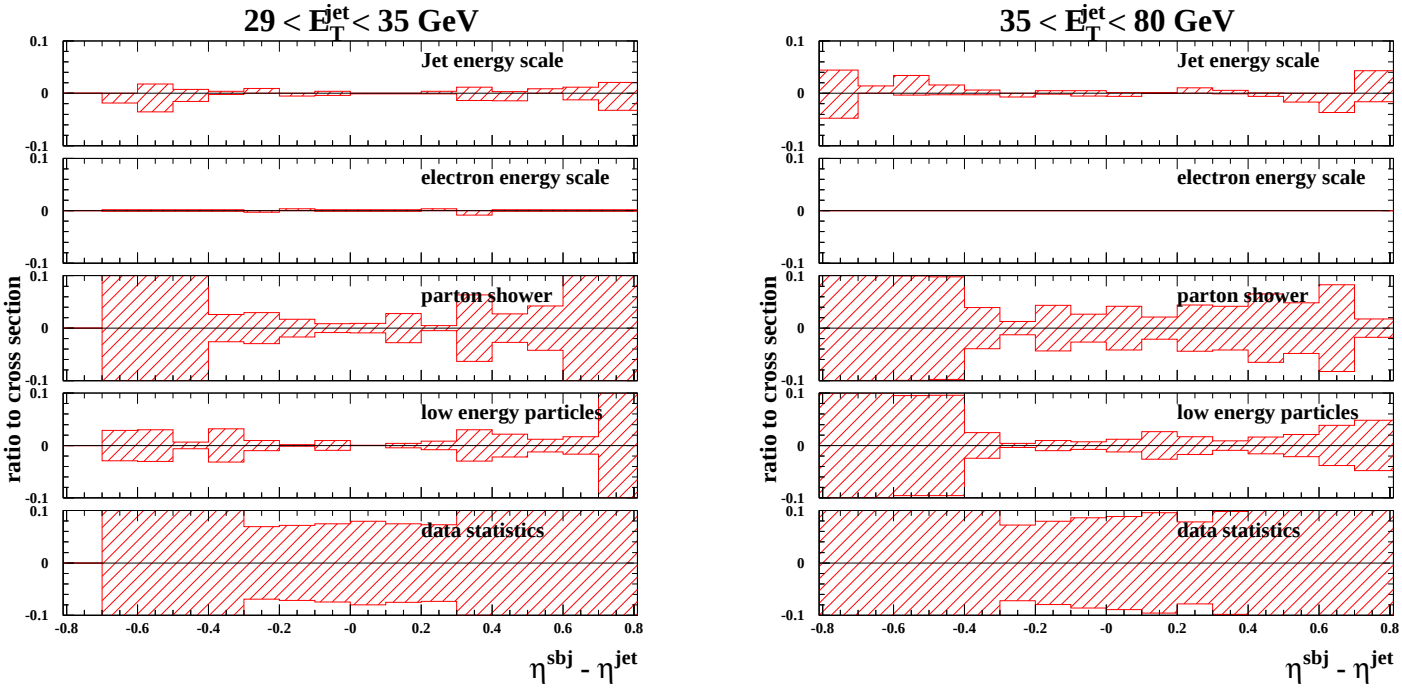

Figure 11.34: Relative systematic and statistical uncertainties of the normalised differential cross sections as functions of $\eta^{sbj} - \eta^{jet}$ in different regions of E_T^{jet}.

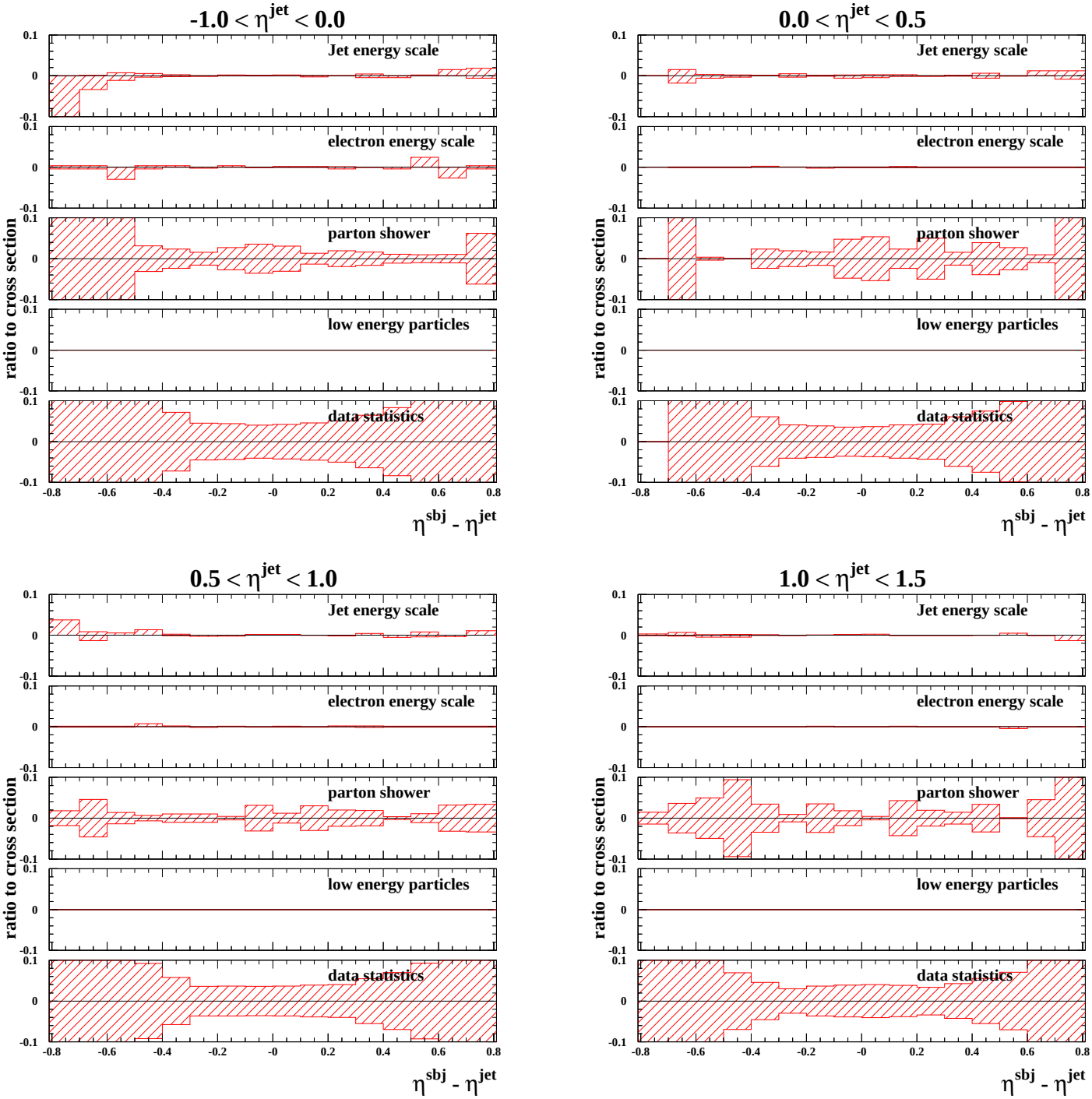

Figure 11.35: Relative systematic and statistical uncertainties of the normalised differential cross sections as functions of $\eta^{sbj} - \eta^{jet}$ in different regions of η^{jet}.

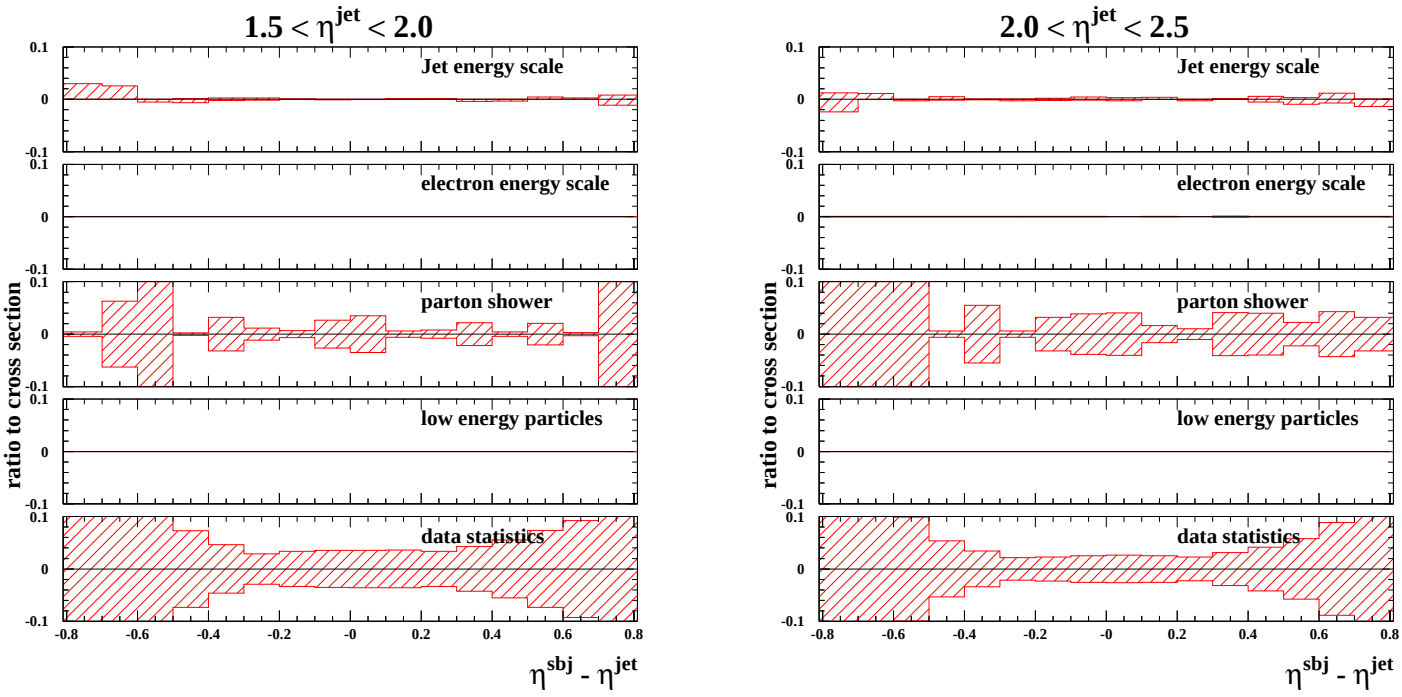

Figure 11.36: Relative systematic and statistical uncertainties of the normalised differential cross sections as functions of $\eta^{sbj} - \eta^{jet}$ in different regions of η^{jet}.

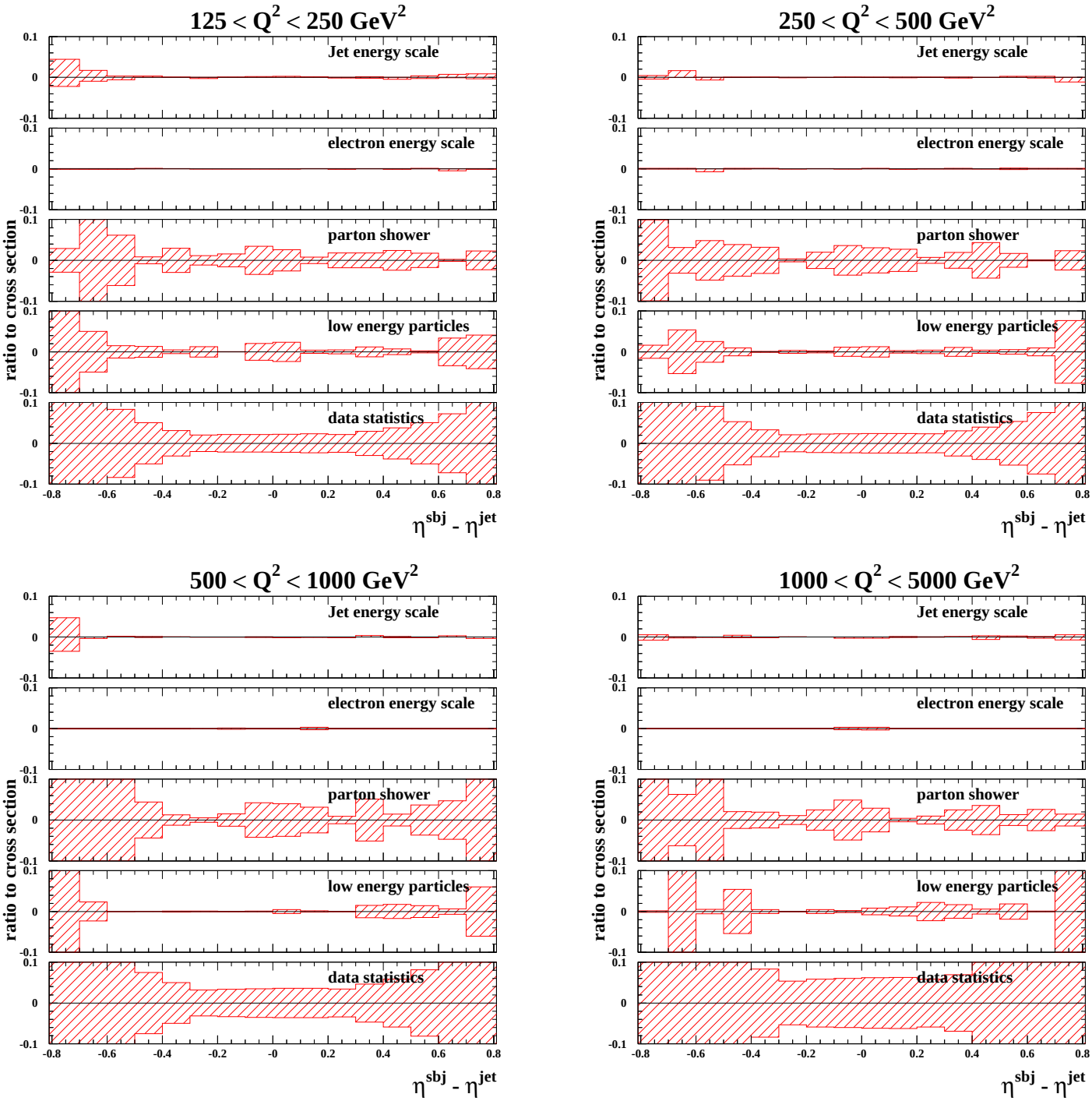

Figure 11.37: Relative systematic and statistical uncertainties of the normalised differential cross sections as functions of $\eta^{sbj} - \eta^{jet}$ in different regions of Q^2.

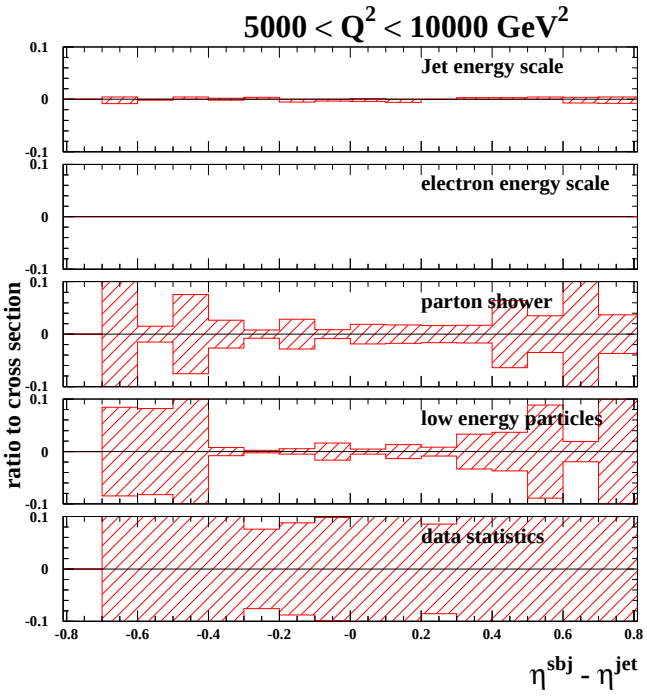

Figure 11.38: Relative systematic and statistical uncertainties of the normalised differential cross sections as functions of $\eta^{sbj} - \eta^{jet}$ in different regions of Q^2.

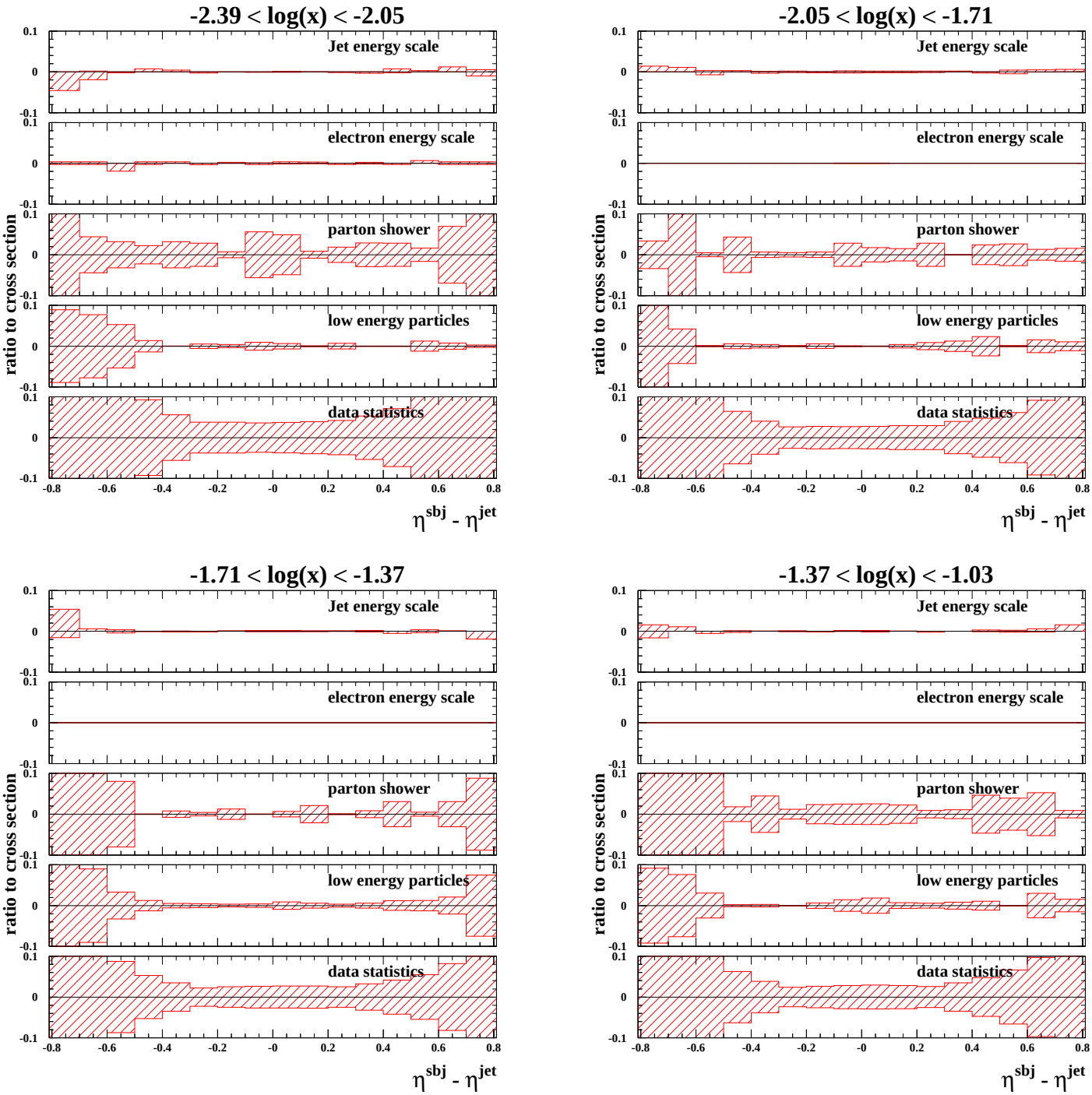

Figure 11.39: Relative systematic and statistical uncertainties of the normalised differential cross sections as functions of $\eta^{sbj} - \eta^{jet}$ in different regions of x.

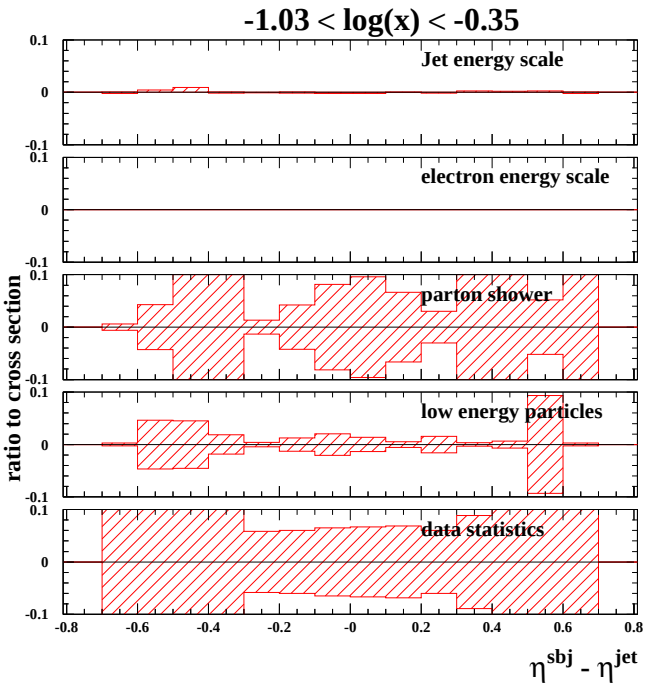

Figure 11.40: Relative systematic and statistical uncertainties of the normalised differential cross sections as functions of $\eta^{sbj} - \eta^{jet}$ in different regions of x.

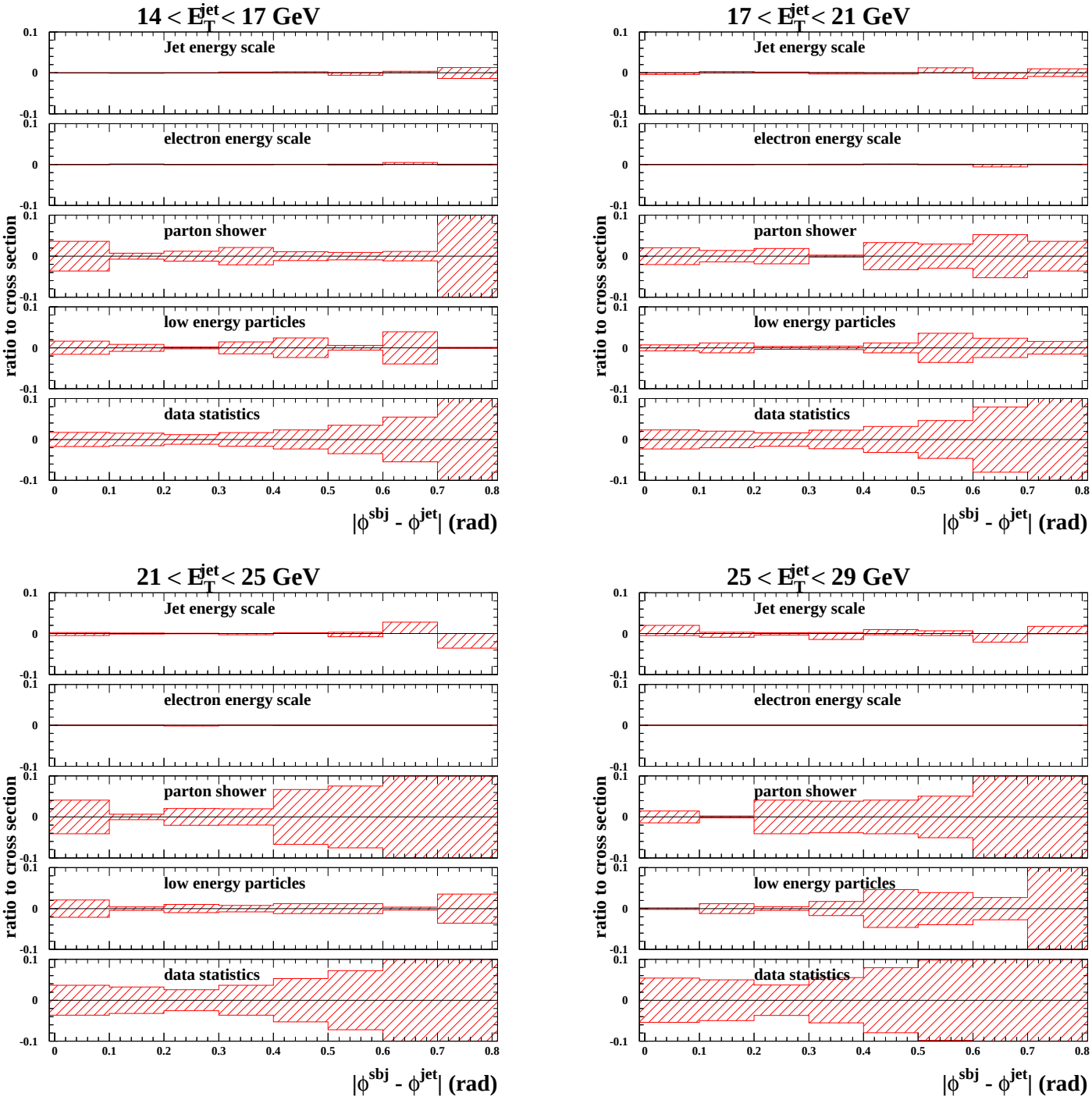

Figure 11.41: Relative systematic and statistical uncertainties of the normalised differential cross sections as functions of $|\phi^{sbj} - \phi^{jet}|$ in different regions of E_T^{jet}.

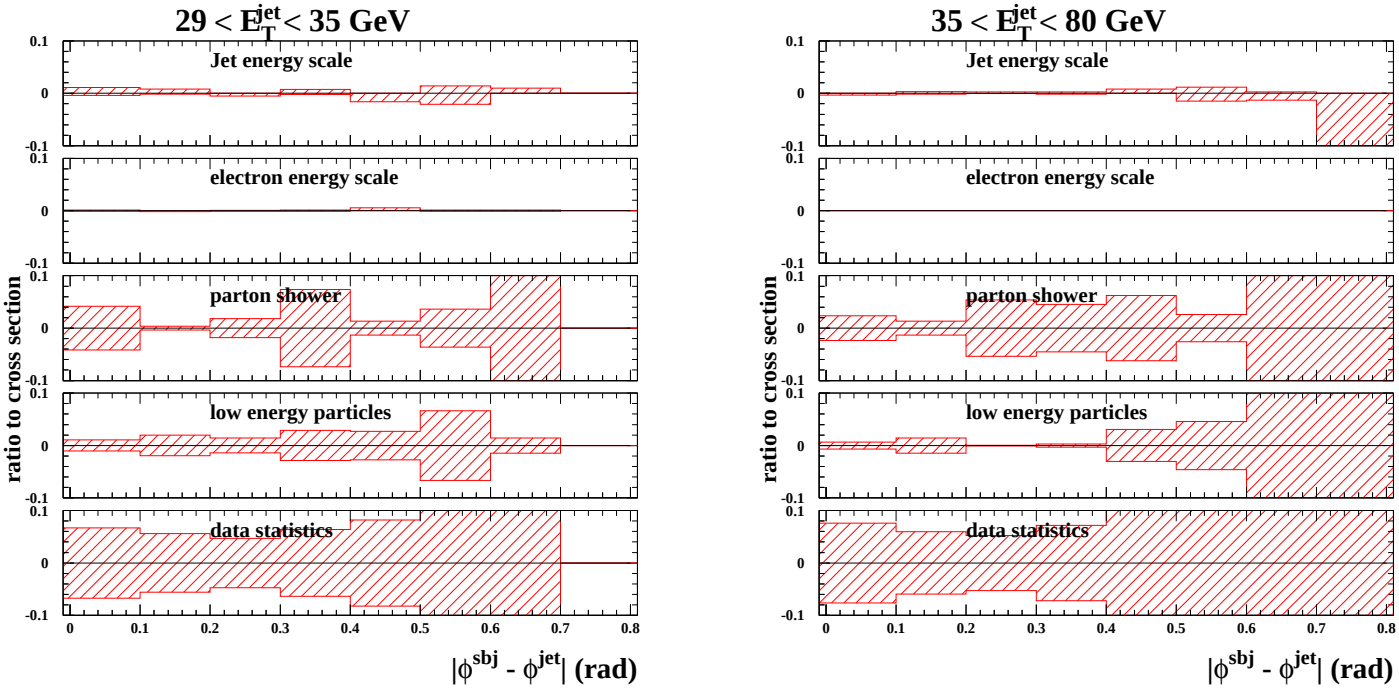

Figure 11.42: Relative systematic and statistical uncertainties of the normalised differential cross sections as functions of $|\phi^{sbj} - \phi^{jet}|$ in different regions of E_T^{jet}.

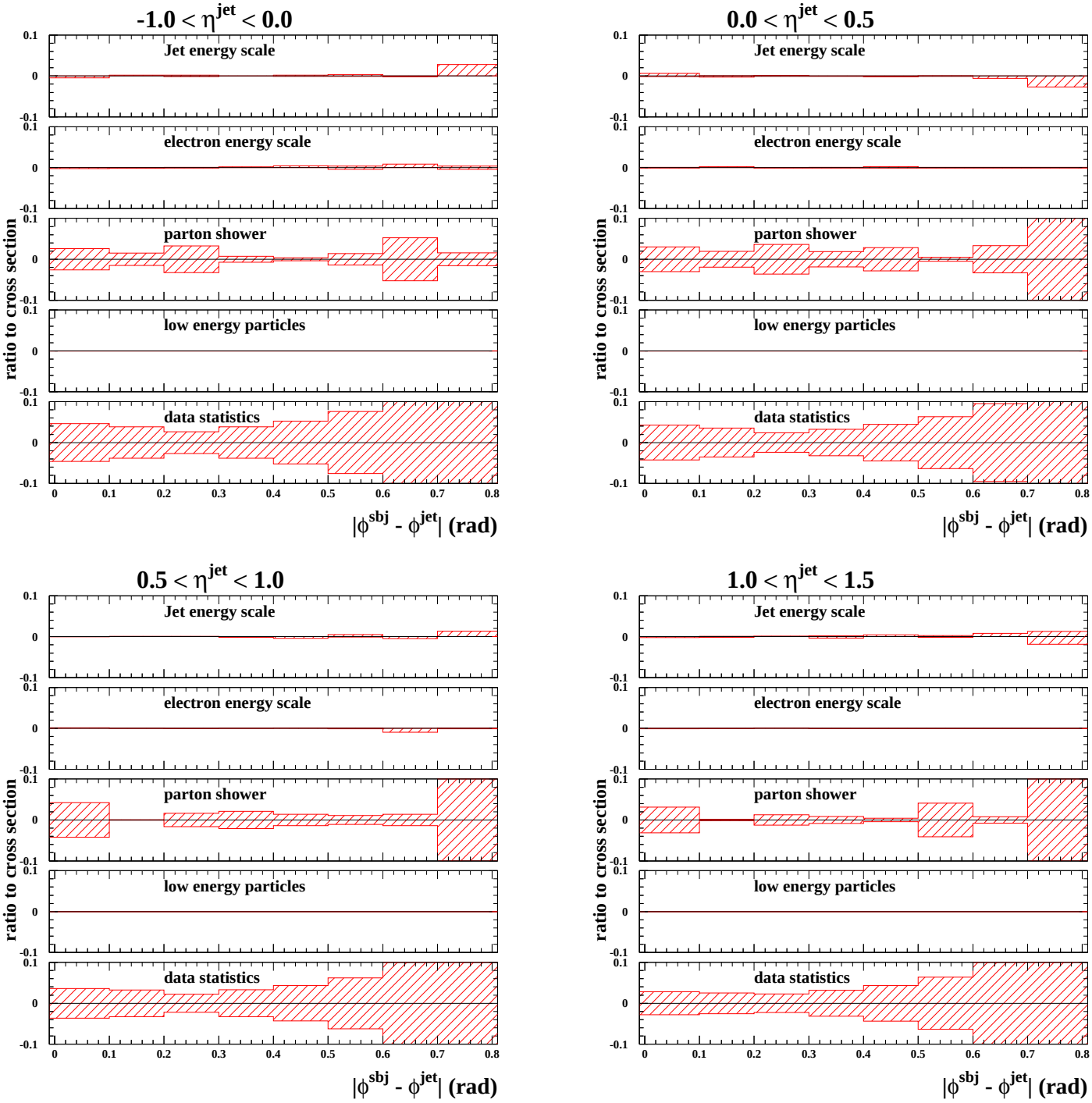

Figure 11.43: Relative systematic and statistical uncertainties of the normalised differential cross sections as functions of $|\phi^{sbj} - \phi^{jet}|$ in different regions of η^{jet}.

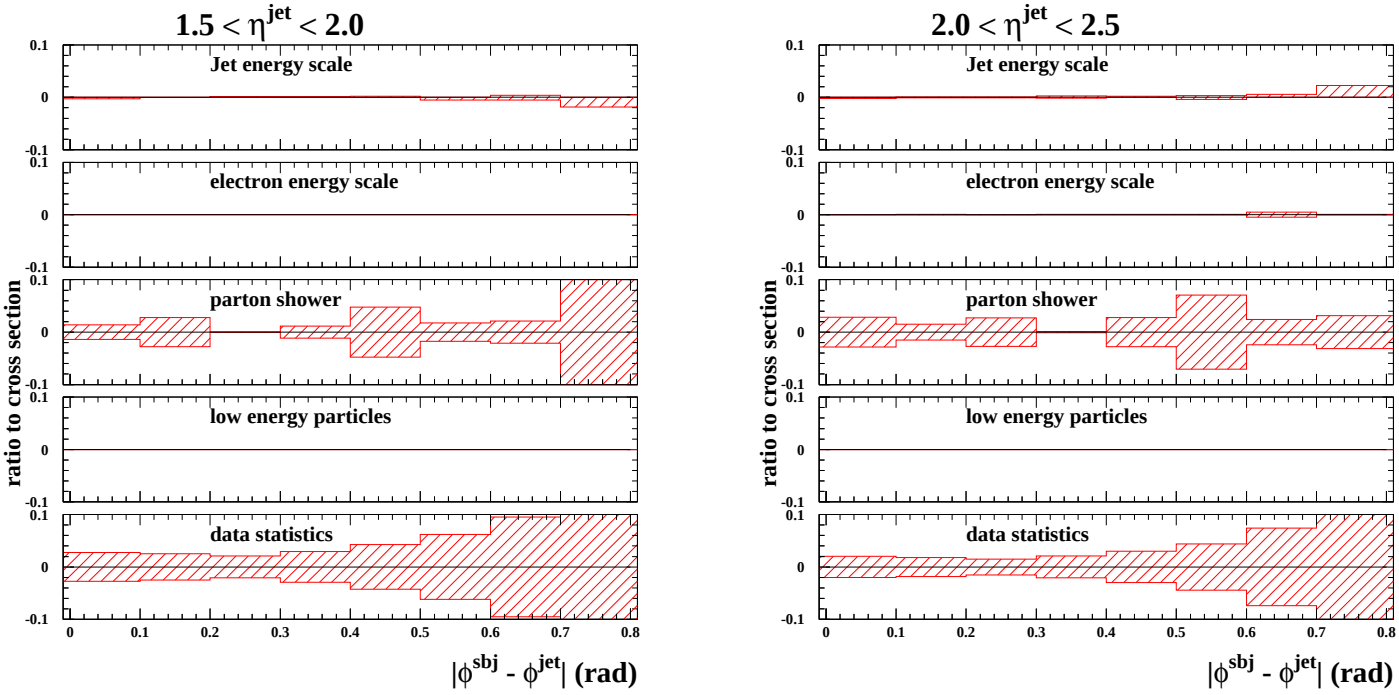

Figure 11.44: Relative systematic and statistical uncertainties of the normalised differential cross sections as functions of $|\phi^{sbj} - \phi^{jet}|$ in different regions of η^{jet}.

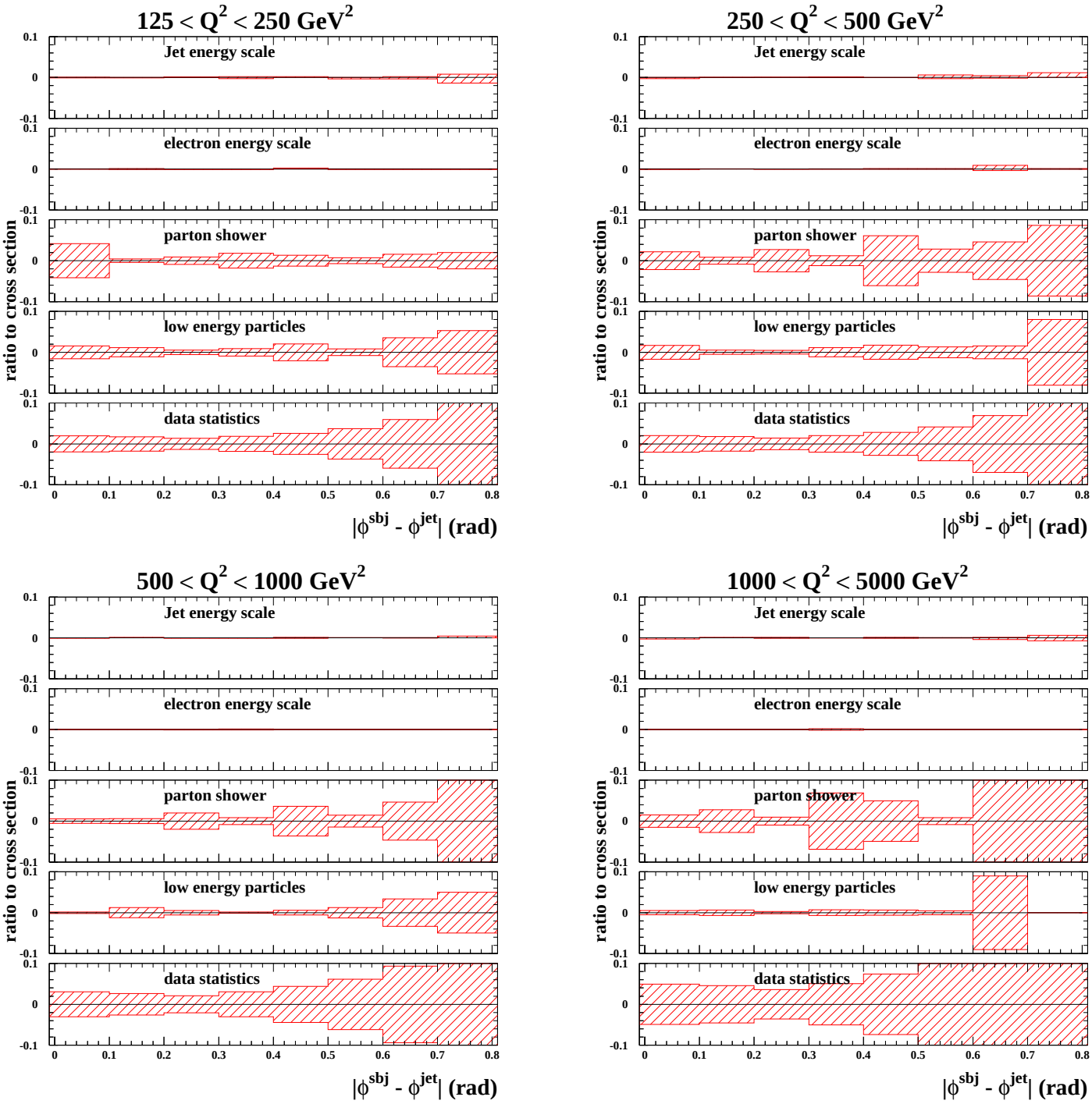

Figure 11.45: Relative systematic and statistical uncertainties of the normalised differential cross sections as functions of $|\phi^{sbj} - \phi^{jet}|$ in different regions of Q^2.

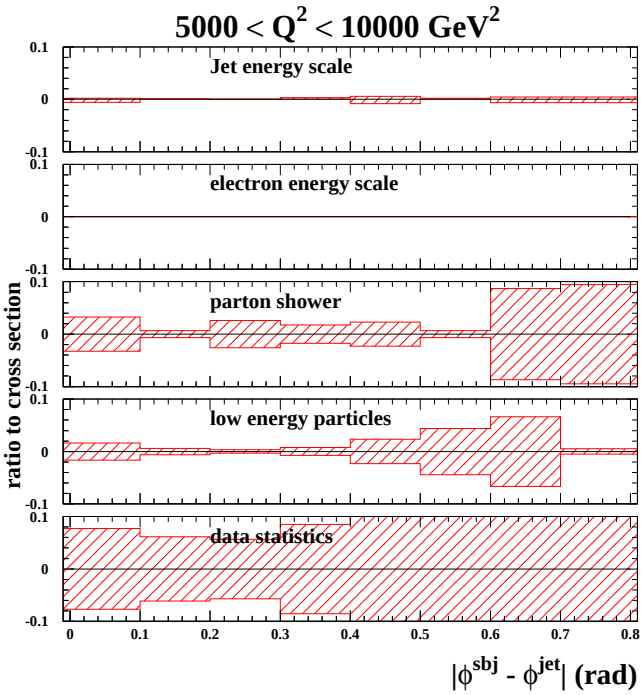

Figure 11.46: Relative systematic and statistical uncertainties of the normalised differential cross sections as functions of $|\phi^{sbj} - \phi^{jet}|$ in different regions of Q^2.

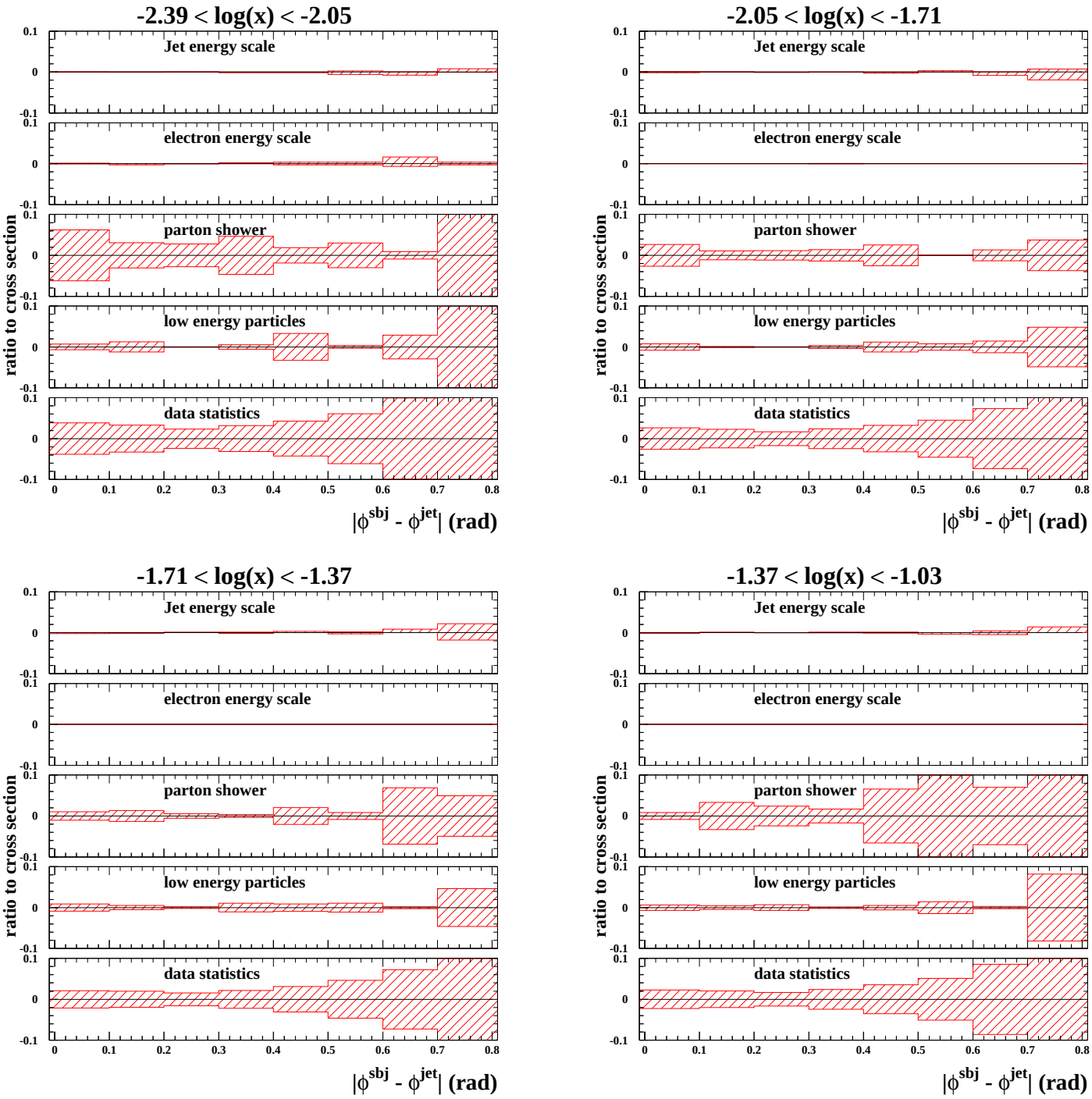

Figure 11.47: Relative systematic and statistical uncertainties of the normalised differential cross sections as functions of $|\phi^{sbj} - \phi^{jet}|$ in different regions of x.

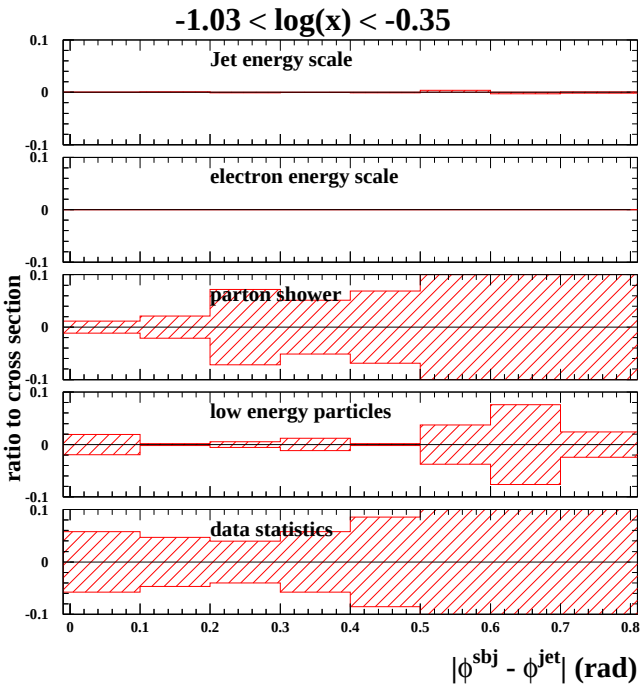

Figure 11.48: Relative systematic and statistical uncertainties of the normalised differential cross sections as functions of $|\phi^{sbj} - \phi^{jet}|$ in different regions of x.

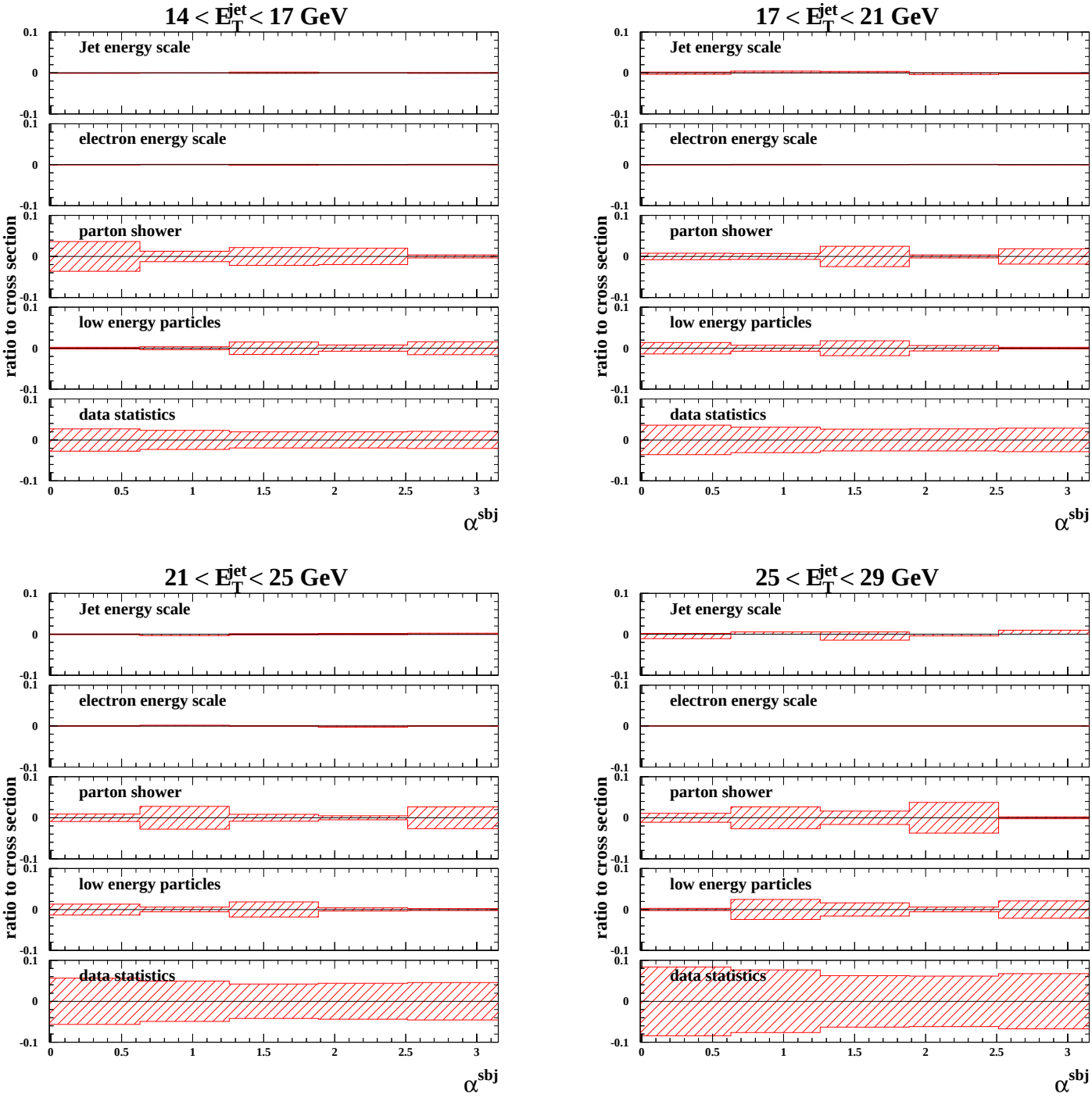

Figure 11.49: Relative systematic and statistical uncertainties of the normalised differential cross sections as functions of α^{sbj} in different regions of E_T^{jet}.

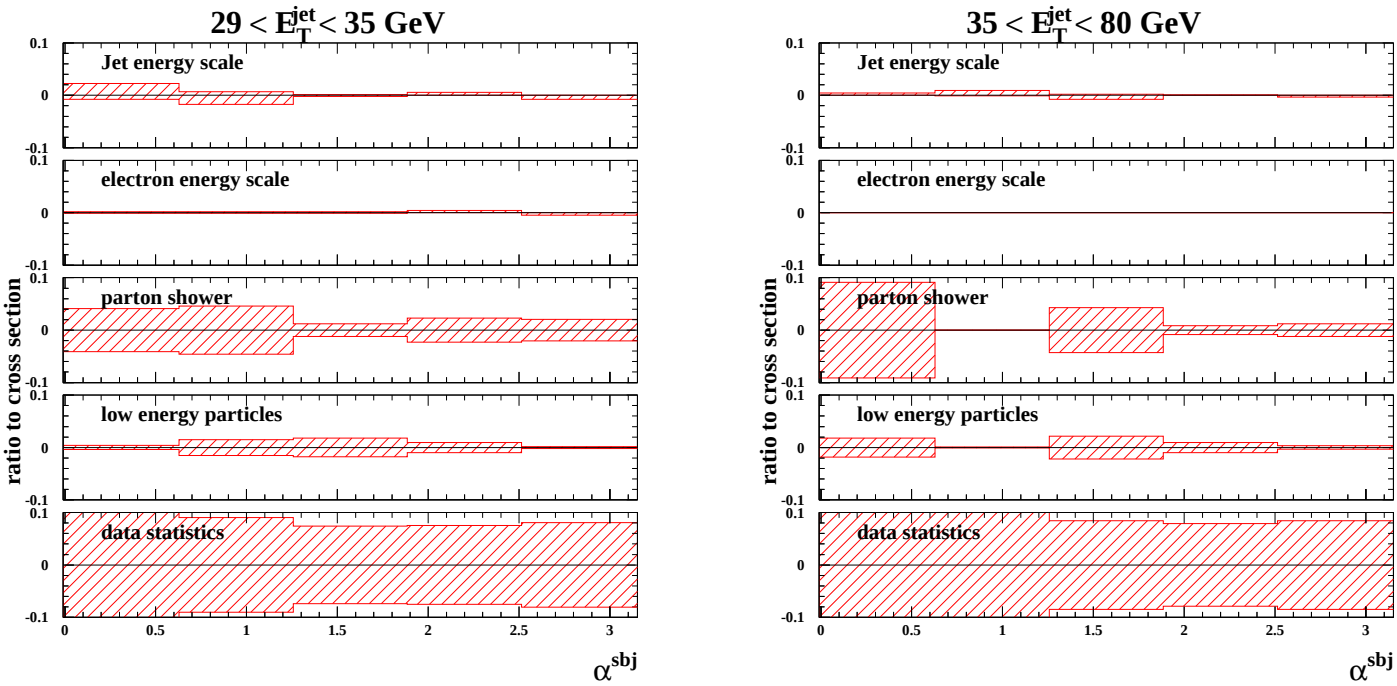

Figure 11.50: Relative systematic and statistical uncertainties of the normalised differential cross sections as functions of α^{sbj} in different regions of E_T^{jet}.

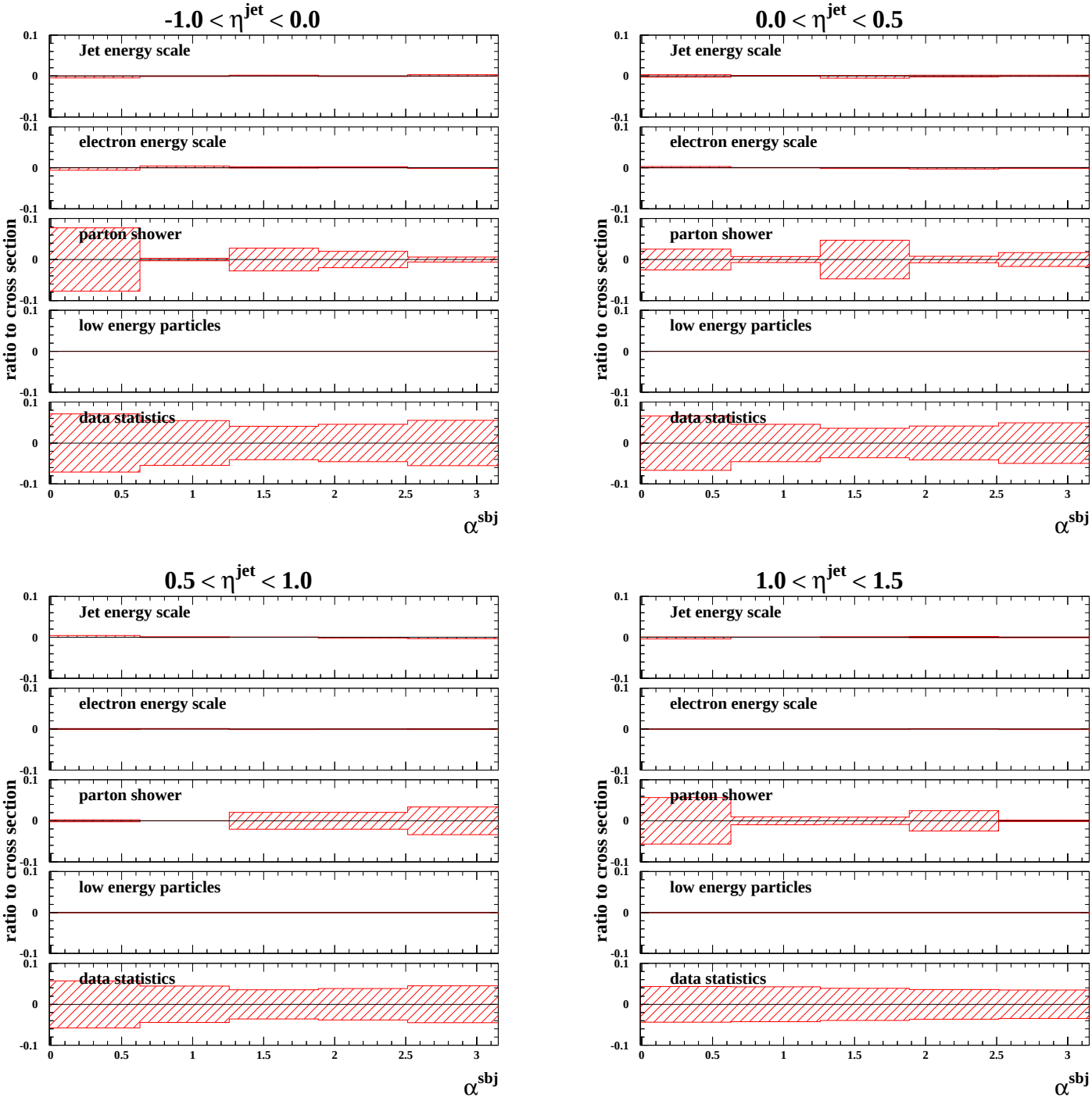

Figure 11.51: Relative systematic and statistical uncertainties of the normalised differential cross sections as functions of α^{sbj} in different regions of η^{jet}.

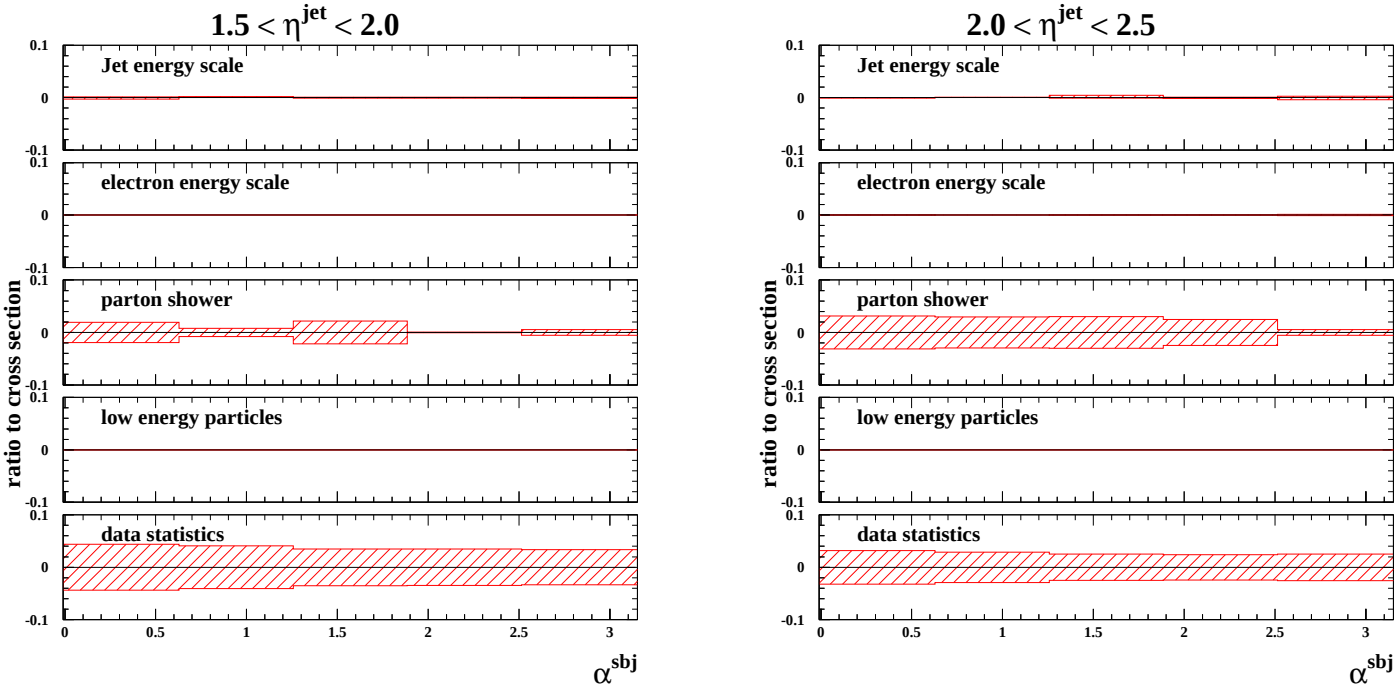

Figure 11.52: Relative systematic and statistical uncertainties of the normalised differential cross sections as functions of α^{sbj} in different regions of η^{jet}.

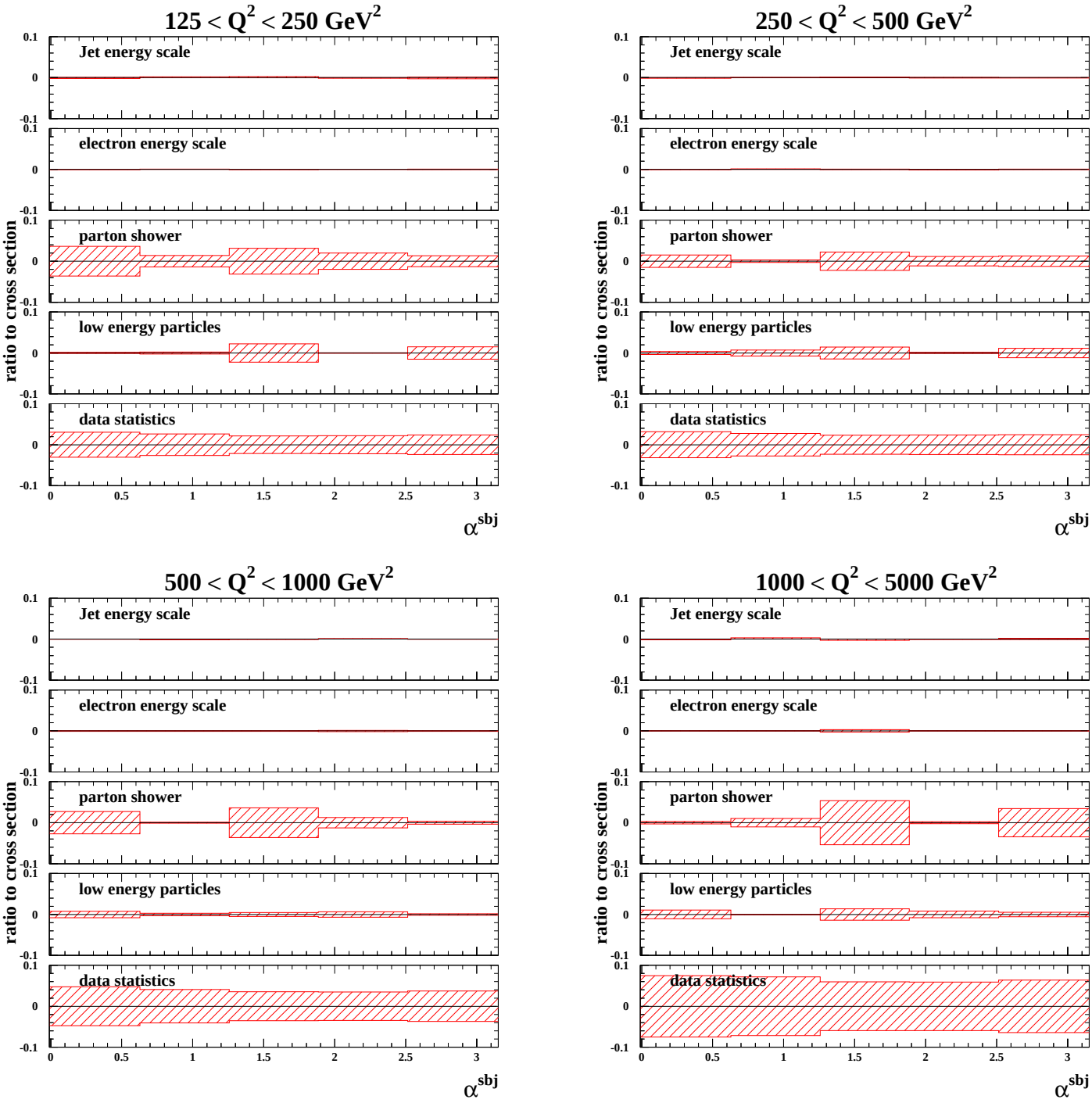

Figure 11.53: Relative systematic and statistical uncertainties of the normalised differential cross sections as functions of α^{sbj} in different regions of Q^2.

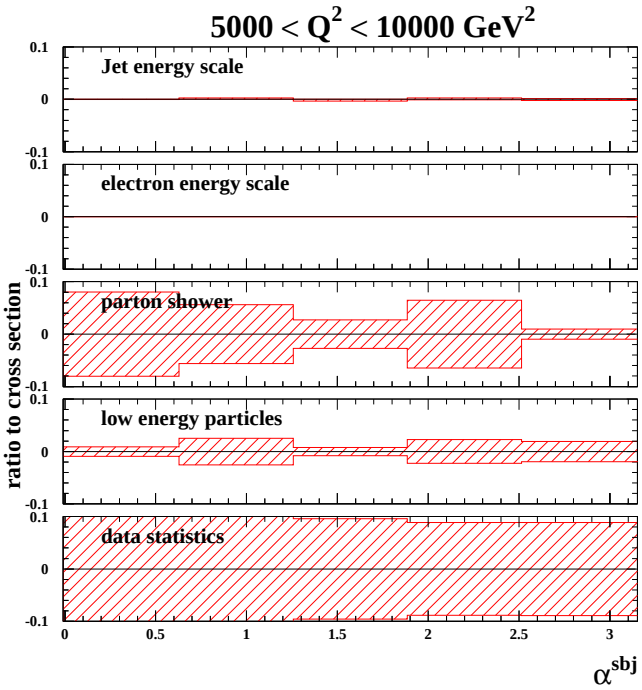

Figure 11.54: Relative systematic and statistical uncertainties of the normalised differential cross sections as functions of α^{sbj} in different regions of Q^2.

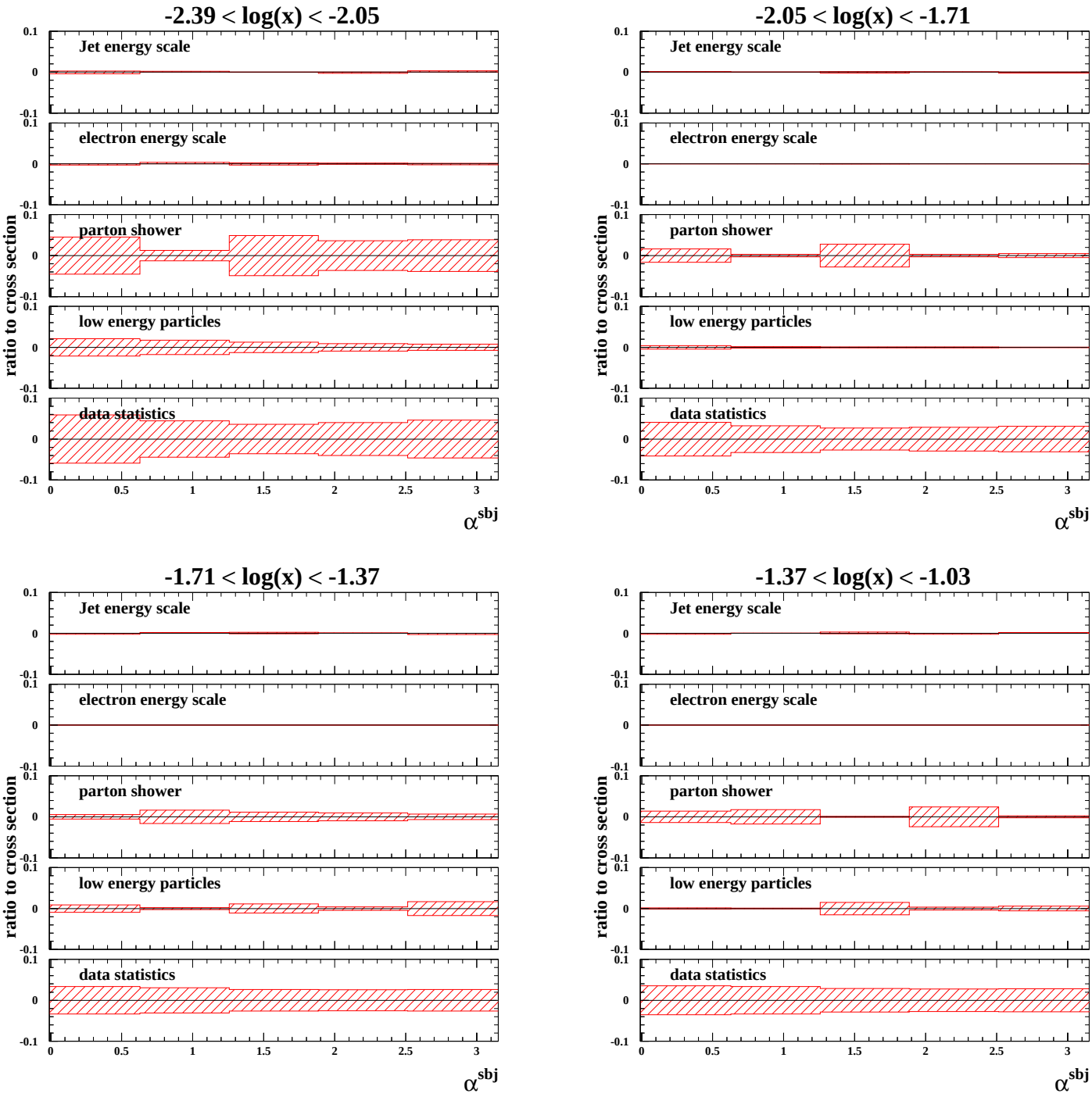

Figure 11.55: Relative systematic and statistical uncertainties of the normalised differential cross sections as functions of α^{sbj} in different regions of x.

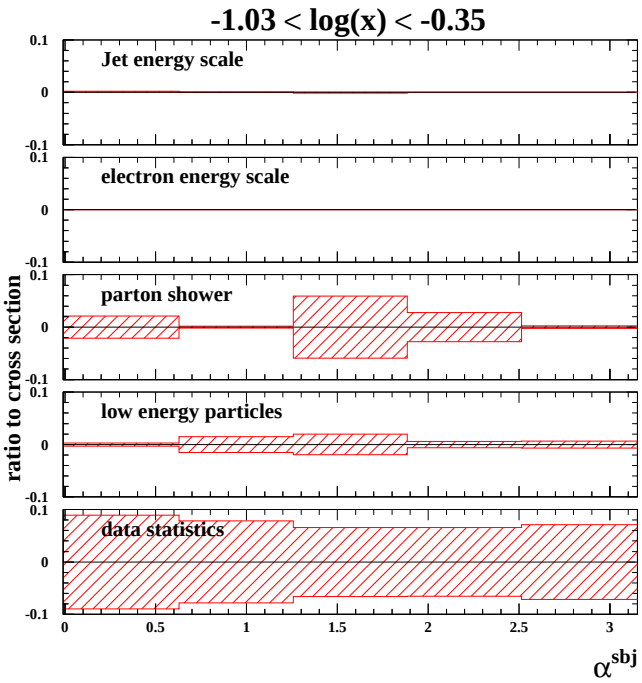

Figure 11.56: Relative systematic and statistical uncertainties of the normalised differential cross sections as functions of α^{sbj} in different regions of x.

References

[1] ZEUS Coll., S. Chekanov et al., Phys. Rev. **D 67**, 012007 (2003).

[2] ZEUS Coll., S. Chekanov et al., Eur. Phys. J. **C 42**, 1 (2005).

[3] V.N. Gribov and L.N. Lipatov, Sov. J. Nucl. Phys. **15**, 438 (1972).

[4] L.N. Lipatov, Sov. J. Nucl. Phys. **20**, 94 (1975).

[5] G. Parisi, *Proc. of the 11th Rencontre de Moriond*, J. Tran Thanh Van (ed.), Vol. 3, p. 83. Flaine, France (1976).

[6] Yu.L. Dokshitzer, Sov. Phys. JETP **46**, 641 (1977).

[7] G. Altarelli and G. Parisi, Nucl. Phys. **B 126**, 298 (1977).

[8] A.D. Martin et al., Eur. Phys. J. **C 23**, 73 (2002).

[9] J. Pumplin et al., JHEP **0207**, 012 (2002).

[10] Yu.L. Dokshitzer, V.A. Khoze, A.H. Mueller and S.I. Troyan, *Basics of Perturbative QCD*. Ed. J. Tran Thanh Van, Editions Frontiéres, Gif-sur-Yvette, (1991).

[11] V.A. Khoze and W. Ochs, Int. J. Mod. Phys. **A 12**, 2949 (1997).

[12] S. Catani et al., Nucl. Phys. **B 406**, 187 (1993).

[13] S.D. Ellis and D.E. Soper, Phys. Rev. **D 48**, 3160 (1993).

[14] UA1 Coll., G. Arnison et al., Phys. Lett. **B 123**, 115 (1983).

[15] M. Jiménez, *Tests of color dynamics and precision measurements of $\alpha_s(M_Z)$ using jet production in DIS with the ZEUS detector at HERA*. Ph.D. Thesis, Universidad Autónoma de Madrid, Spain, 2008. (Unpublished).

[16] ZEUS Coll., S. Chekanov et al., Phys. Lett. **B 649**, 12 (2007).

[17] J.E. Huth et al., *Research Directions for the Decade. Proc. of Summer Study on High Energy Physics, 1990*, E.L. Berger (ed.), p. 134. World Scientific (1992). Also in preprint FERMILAB-CONF-90-249-E.

[18] R.P. Feynman, *Photon-Hadron Interactions*. Benjamin, New York, (1972).

[19] K.H. Streng, T.F. Walsh and P.M. Zerwas, Z. Phys. **C 2**, 237 (1979).

[20] Ya.I. Azimov, Yu.L. Dokshitzer, V.A. Khoze and S.I. Troyan, Z. Phys. **C 27**, 65 (1985).

[21] Ya.I. Azimov, Yu.L. Dokshitzer, V.A. Khoze and S.I. Troyan, Z. Phys. **C 31**, 213 (1986).

[22] S. Catani et al., Nucl. Phys. **B 383**, 419 (1992).

[23] M.H. Seymour, Nucl. Phys. **B 421**, 545 (1994).

[24] M.H. Seymour, Phys. Lett. **B 378**, 279 (1996).

[25] J.R. Forshaw and M.H. Seymour, JHEP **9909**, 009 (1999).

[26] ZEUS Coll., S. Chekanov et al., Phys. Lett. **B 558**, 41 (2003).

[27] O. González, *Precise determinations of the strong coupling constant at HERA*. Ph.D. Thesis, Universidad Autónoma de Madrid, Spain, 2002. DESY-THESIS-2002-020.

[28] ZEUS Coll., S. Chekanov et al., Phys. Lett. **B 531**, 9 (2002).

[29] ZEUS Coll., S. Chekanov et al., Eur. Phys. J. **C 23**, 615 (2002).

[30] ZEUS Coll., J. Breitweg et al., Phys. Lett. **B 443**, 394 (1998).

[31] ZEUS Coll., J. Breitweg et al., Phys. Lett. **B 507**, 70 (2001).

[32] ZEUS Coll., S. Chekanov et al., Phys. Lett. **B 547**, 164 (2002).

[33] ZEUS Coll., S. Chekanov et al., Eur. Phys. J. **C 23**, 13 (2002).

[34] ZEUS Coll., S. Chekanov et al., Phys. Lett. **B 560**, 7 (2003).

[35] ZEUS Coll., S. Chekanov et al., Eur. Phys. J. **C 31**, 149 (2003).

[36] ZEUS Coll., S. Chekanov et al., Nucl. Phys. **B 765**, 1 (2007).

[37] ZEUS Coll., S. Chekanov et al., Preprint DESY-08-100 (hep-ex/0808.3783), DESY, 2008.

[38] H1 Coll., C. Adloff et al., Phys. Lett. **B 515**, 17 (2001).

[39] H1 Coll., C. Adloff et al., Eur. Phys. J. **C 19**, 289 (2001).

[40] H1 Coll., C. Adloff et al., Eur. Phys. J. **C 19**, 429 (2001).

[41] H1 Coll., C. Adloff et al., Eur. Phys. J. **C 25**, 13 (2002).

[42] H1 Coll., C. Adloff et al., Phys. Lett. **B 542**, 193 (2002).

[43] H1 Coll., C. Adloff et al., Eur. Phys. J. **C 29**, 497 (2003).

[44] H1 Coll., A. Aktas et al., Phys. Lett. **B 639**, 21 (2006).

[45] H1 Coll., A. Aktas et al., Phys. Lett. **B 653**, 134 (2007).

[46] C. Glasman, *Proc. of the 13th International Workshop on Deep Inelastic Scattering*, S.R. Dasu and W.H. Smith (eds.), p. 689. Madison, USA (2005). Also in preprint hep-ex/0506035.

[47] ZEUS Coll., S. Chekanov et al., Eur. Phys. J. **C 63**, 527 (2009).

[48] ZEUS Coll., *Three-subjet distributions in neutral current deep inelastic scattering.* ZEUS-prel-09-007, International Europhysics Conference on High Energy Physics, Krakow, Poland, 2009.

[49] S. Catani and M.H. Seymour, Nucl. Phys. **B 485**, 291 (1997). Erratum in Nucl. Phys. **B 510** (1998) 503.

[50] Z. Nagy and Z. Trocsanyi, Phys. Rev. Lett. **87**, 082001 (2001).

[51] ALEPH Coll., R. Alemany et al., Phys. Lett. **B 284**, 151 (1992).

[52] ALEPH Coll., R. Barate et al., Z. Phys. **C 76**, 1 (1997).

[53] ALEPH Coll., A. Heister et al., Eur. Phys. J. **C 27**, 1 (2003).

[54] DELPHI Coll., P. Abreu et al., Phys. Lett. **B 255**, 466 (1991).

[55] DELPHI Coll., P. Abreu et al., Z. Phys. **C 59**, 357 (1993).

[56] DELPHI Coll., P. Abreu et al., Phys. Lett. **B 414**, 401 (1997).

[57] DELPHI Coll., P. Abreu et al., Phys. Lett. **B 449**, 383 (1999).

[58] L3 Coll., B. Adeva et al., Phys. Lett. **B 248**, 227 (1990).

[59] OPAL Coll., M.Z. Akrawy et al., Z. Phys. **C 49**, 49 (1991).

[60] OPAL Coll., R. Akers et al., Z. Phys. **C 65**, 367 (1995).

[61] OPAL Coll., G. Abbiendi et al., Eur. Phys. J. **C 20**, 601 (2001).

[62] S. Kluth, Nucl. Phys. Proc. Suppl. **133**, 36 (2004).

[63] HERMES Coll., *Technical Design Report*, 1993.

[64] HERA-B Coll., *Technical Design Report*. DESY-PRC 95/01.

[65] DESY, *Annual Report*, 1994.

[66] ZEUS Coll., M. Derrick et al., Phys. Lett. **B 293**, 465 (1992).

[67] ZEUS Coll., U. Holm (ed.), *The ZEUS Detector*. Status Report (unpublished), DESY (1993), available on `http://www-zeus.desy.de/bluebook/bluebook.html`.

[68] A. Polini et al., Nucl. Inst. Meth. **A 581**, 656 (2007).

[69] N. Harnew et al., Nucl. Inst. Meth. **A 279**, 290 (1989).

[70] B. Foster et al., Nucl. Phys. Proc. Suppl. **B 32**, 181 (1993).

[71] B. Foster et al., Nucl. Inst. Meth. **A 338**, 254 (1994).

[72] M. Derrick et al., Nucl. Inst. Meth. **A 309**, 77 (1991).

[73] A. Andresen et al., Nucl. Inst. Meth. **A 309**, 101 (1991).

[74] A. Caldwell et al., Nucl. Inst. Meth. **A 321**, 356 (1992).

[75] A. Bernstein et al., Nucl. Inst. Meth. **A 336**, 23 (1993).

[76] H. Bethe and W. Heitler, Proc. Roy. Soc. Lond. **A146**, 83 (1934).

[77] J. Andruszków et al., Preprint DESY-92-066, DESY, 1992.

[78] ZEUS Coll., M. Derrick et al., Z. Phys. **C 63**, 391 (1994).

[79] J. Andruszków et al., Acta Phys. Pol. **B 32**, 2025 (2001).

[80] M. Helbich et al., Nucl. Inst. Meth. **A 565**, 572 (2006).

[81] C. Youngman, *The ZEUS Data Acquisition System*. DESY 92-150A.

[82] W.H. Smith et al., *The ZEUS Trigger System*. ZEUS-note 89-084.

[83] W.H. Smith, K. Tokushuku and L.W. Wiggers, *Proc. Computing in High-Energy Physics (CHEP), Annecy, France, Sept. 1992*, C. Verkerk and W. Wojcik (eds.), p. 222. CERN, Geneva, Switzerland (1992). Also in preprint DESY 92-150B.

[84] H. Uigterwall, *The Global Second Level Trigger for ZEUS*. Ph.D. Thesis, University of Amsterdam, 1992.

[85] S.M. Fisher et al., *ADAMO: User's guide*. CERN, 1993.

[86] R. Brun et al., GEANT3, Technical Report CERN-DD/EE/84-1, CERN, 1987.

[87] L.A.T. Bauerdick et al.. DESY-95-236, 1995.

[88] Y. Azimov et al., Phys. Lett. **B 165**, 147 (1985).

[89] G. Gustafson, Phys. Lett. **B 175**, 453 (1986).

[90] G. Gustafson and U. Pettersson, Nucl. Phys. **B 306**, 746 (1988).

[91] B. Andersson et al., Z. Phys. **C 43**, 625 (1989).

[92] L. Lönnblad, Comp. Phys. Comm. **71**, 15 (1992).

[93] L. Lönnblad, Z. Phys. **C 65**, 285 (1995).

[94] G. Ingelman, A. Edin and J. Rathsman, Comp. Phys. Comm. **101**, 108 (1997).

[95] B. Andersson et al., Phys. Rep. **97**, 31 (1983).

[96] B.R. Webber, Nucl. Phys. **B 238**, 492 (1984).

[97] J. Pumplin et al., Phys. Rev. **D 65**, 014013 (2001).

[98] S. Bethke, Prog. Part. Nucl. Phys. **58**, 351 (2007).

[99] H. Plothow-Besch, Comp. Phys. Comm. **75**, 396 (1993).

[100] H.L. Lai et al., Eur. Phys. J. **C 12**, 375 (2000).

[101] A. Kwiatkowski, H. Spiesberger and H.-J. Möhring, Comp. Phys. Comm. **69**, 155 (1992).

[102] H. Spiesberger, *An Event Generator for ep Interactions at HERA Including Radiative Processes (Version 4.6)*, 1996, available on `http://www.desy.de/~hspiesb/heracles.html`.

[103] K. Charchuła, G.A. Schuler and H. Spiesberger, Comp. Phys. Comm. **81**, 381 (1994).

[104] H. Spiesberger, HERACLES *and* DJANGOH*: Event Generation for ep Interactions at HERA Including Radiative Processes*, 1998, available on `http://wwwthep.physik.uni-mainz.de/~hspiesb/djangoh/djangoh.html`.

[105] T. Sjöstrand, Comp. Phys. Comm. **82**, 74 (1994).

[106] T. Sjöstrand et al., Comp. Phys. Comm. **135**, 238 (2001).

[107] T. Sjöstrand, Comp. Phys. Comm. **39**, 347 (1986).

[108] T. Sjöstrand and M. Bengtsson, Comp. Phys. Comm. **43**, 367 (1987).

[109] H. Abramowicz, A. Caldwell and R. Sinkus, Nucl. Inst. Meth. **A 365**, 508 (1995).

[110] R. Sinkus and T. Voss, Nucl. Inst. Meth. **A 391**, 360 (1997).

[111] S. Bentvelsen, J. Engelen and P. Kooijman, *Proc. of the Workshop on Physics at HERA*, W. Buchmüller and G. Ingelman (eds.), Vol. 1, p. 23. Hamburg, Germany, DESY (1992).

[112] M. Wing (on behalf of the ZEUS Coll.), *Proc. of the 10th International Conference on Calorimetry in High Energy Physics*, R. Zhu (ed.), p. 767. Pasadena, USA (2002). Also in preprint hep-ex/0206036.

[113] ZEUS Coll., S. Chekanov et al., Eur. Phys. J. **C 21**, 443 (2001).

Acknowledgements

La gente a la que la que me gustaría nombrar en este capítulo se divide en dos grandes grupos. En primer lugar esta la gente gracias a la cual este trabajo ha sido posible y en el otro la gente a pesar de la cual este trabajo ha sido posible.

En el primer grupo están, destacados en cabeza y a algunos minutos del pelotón, Juan y Claudia. De hecho debería incluirlos en un grupo aparte, en el de "gente sin la cual este trabajo sería inconcebible". Creo que suele ser el caso que en una colaboración laboral que dura algunos años se tengan lo que normalmente se denomina "sus más y sus menos". En mi caso no puedo decir de ninguna manera que haya habido "menos", todo este tiempo ha sido una sucesion continua de "mases". Claro que esa es mi perspectiva... Aunque sea injusto para con el resto de cosas que tanto Juan como Claudia han hecho por mí (horas y horas de explicaciones, aclaraciones, sugerencias, burocracia, invitaciones a cenar y un largo etc.), me gustaría nombrar especialmente las cuatro (o cinco? ya no sé) veces que Juan se ha leído el borrador entero de la tesis, línea a línea, figura a figura, con el único objetivo de que fuera presentada en las mejores condiciones.

De la misma manera que al final de la tesis doctoral los directores escriben cartas de recomendación para sus estudiantes, quisiera que este capítulo (este párrafo, debería de decir) hiciera las veces de carta de recomendación para Juan y Claudia en su faceta de directores de tesis.

En segundo lugar me gustaría agradecer al grupo de física de altas energías de la UAM el apoyo que me han brindado todo este tiempo, and I mean it. El compromiso con la formación de futuros estudiantes y el apoyo proporcionado es un ejemplo de lo que debería ser toda tesis doctoral.

Como dije al principio, y pasando a un tono mas desenfadado, ahora querría nombrar a la gente a pesar de la cual el trabajo ha salido adelante. En este caso tambien hay algún ganador. Marcos, cansino de las personas, se lleva el primer premio. Voy al despacho, ahí esta el pesao, voy al gimasio, y oh sorpresa, ahí sigue el cansino. Salgo por ahí y veeenga, otra vez el Marcos dando la lata, y así sustantivamente varios años. Menos mal que te has pirao al CERN a que te dé el

aire un poco porque ya no sabía dónde meterme. Manolo, no te escondas, que tú tampoco has ayudado nada a que la tesis saliera adelante, venga a hablarme del barça y del tenis. No te habré dicho veces que no me gusta el deporte? que no veo el fútbol? hombre ya. Por no hablar de las veces en las que te negaste absurdamente a comer en la cantina (por qué?) y te empeñaste en ir a La Sepia. Anda ya.

Ana, a ti te quiero dar las gracias por incluirme en tu capítulo de agradecimientos en tu tesis. Por lo demás, no tengo tampoco nada que agradecerte. El tiempo que me has hecho perder intentando que pronuncies bien Altona, Reeperbahn, Schanze, o que no confudieras "Acropolis" con "Apocalipsis" ya nunca volverá. Nunca. Marcel Proust por mucho menos escribió 3000 páginas de un libro llamado "En busca del tiempo perdido", menos mal que no te conoció.

A los de la UAM, tengo que reconocer que algún que otro cable con los problemas de los cursos de doctorado me echasteis, pero es que erais unos pesaos de no callaros ni un minuto en el 512 y de hacer largas las sobremesas. Bueno venga, gracias pero con la boca pequeña.

Tom, we gotta spend another weekend in Berlin before we get too old, thanks for all the acid jokes (to use an euphemism...) and keep them coming. Jerome, thanks for all the hard work teaching me the three cvs commands needed for the software thing.

Fuera del ámbito doctoril me gustaría nombrar a algunos individuos.

Nidia y Maria Paz, pa qué incluiros en este capítulo si no lo vais a leer? Ahí os quedáis. Agorer!

Und ich danke euch auch, all meine liebe Mitbewohner. Es war echt cool mit euch diese vier Jahre zusammen zu wohnen. Als ich nach Deutschland kam konnte ich mir nicht vorstellen dass so eine schöne WG haben würde! Anja, Britta, Hanna, Max, Stefan, Katrin, Ayleen, Simone und Florian: bis bald!

Clara, qué te pasa en la cabeza? Ah, que necesitas un vondolio? Ara mismo. Vete a trabajar con Omino Bianco anda.

Gracias a mis padres (y esto sí va en serio), que me inculcaron desde pequeño el interés por aprender todo tipo de cosas, y que creo que es la principal causa en la intrincada y enmarañada cadena de causas y consecuencias que culminan, de momento, en esta tesis. Ah, y a mi abuela, que hace el mejor arroz con leche del mundo.

Por último, un beso para Rocío, que lleva aguantándome algo más de dos años, cosa que yo la verdad no entiendo ;). Muakas!